

# Episodic outflow feedback in low-mass star formation

INAUGURAL-DISSERTATION

zur  
Erlangung des Doktorgrades  
der Mathematisch-Naturwissenschaftlichen Fakultät  
der Universität zu Köln



vorgelegt von

**Paul Rohde**  
aus Köln, Deutschland

Köln, 2021

Berichterstatter (Gutachter):  
Prof. Dr. Stefanie Walch-Gassner  
Prof. Dr. Peter Schilke

Vorsitzender der Kommission:  
Prof. Dr. David Gross

Tag der mündlichen Prüfung:  
21. Juli 2021

*Für Annika*



## ABSTRACT

---

Protostellar outflows are a ubiquitous signpost of star formation. Even the youngest and most embedded sources launch outflows that entrain ambient core material, significantly altering the whole accretion phase of protostars. Thereby outflows reduce the star formation efficiency and determine the final stellar mass. By extracting angular momentum outflows allow the stars to accrete mass from their surrounding accretion discs. In the case of low-mass star formation, outflows are considered to be the most important feedback mechanism. Observations of long chains of outflow bullets show that outflow feedback is episodic rather than continuous. How episodic outflow feedback impacts the evolution and outcome of star formation is still not fully understood. This thesis contains three publications addressing the impact of episodic outflow feedback on the star formation process and the fossil information carried by the outflows. Using an episodic, sub-grid outflow model in a total of 111 numerical smoothed particle hydrodynamics simulations are performed to follow the star formation process through the early stages. These simulations contain a resolution and parameter study showing that episodic outflow feedback is highly self-regulating. Episodic protostellar outflows entrain about ten times their initially ejected mass, thereby approximately halving the star formation efficiency, resulting in a shifted stellar initial mass function. Protostellar outflows affect how the stars accrete by promoting disc accretion over radial accretion. The promoted disc accretion enhances the fraction of equal-mass twin binaries to a fraction in good agreement with observations. Simulations without outflow feedback form more stars and higher-order multiple systems, which predominantly break apart into binary systems. Outflow feedback enhances the stability of higher-order multiple systems such that the resulting multiplicity statistics are in good agreement with observations. Since the accretion of gas and the launching of outflows are highly connected, protostellar outflows carry fossil records of the launching protostar's accretion history. Hubble wedges in position-velocity diagrams correspond to episodically ejected outflow bullets that have not yet interacted with the cavity wall. Using the kinematic information carried by the outflow and especially by the bullets, it is possible to estimate stellar accretion rates. Dynamical ages of outflows and individual bullets give an estimate of the protostellar age and a history of outburst events. The outflow opening angle and activity help to differentiate between evolutionary stages. This information combined allows a reconstruction of the launching protostars accretion history. Episodic outflows significantly shape the evolution and morphology of the star formation process and should therefore be considered when studying star formation.

## ZUSAMMENFASSUNG

---

Protostellare Ausflüsse, Outflows genannt, sind ein eindeutiges Zeichen aktiver Sternentstehung. Selbst die jüngsten und eingebettetsten Protosterne stoßen Outflows aus, die umgebendes Kernmaterial mitreißen und so die gesamte Akkretionsphase von Protosternen erheblich beeinflussen. Auf diese Weise reduzieren Outflows die Effizienz der Sternentstehung und bestimmen die finale Sternmasse. Durch die Extraktion von Drehimpuls ermöglichen Outflows den Protosternen Masse aus ihren umgebenden Scheiben zu akkretieren. Bei massearmer Sternentstehung gelten Outflows als der wichtigste Feedback Mechanismus. Beobachtungen langer Ketten von Ausflusskugeln, engl. Outflow Bullets, zeigen, dass Outflow Feedback eher episodisch als kontinuierlich ist. Wie episodische Outflows den Prozess der Sternentstehung und dessen Ausgang im Detail beeinflusst, ist noch umstritten. Diese Arbeit enthält drei wissenschaftliche Publikationen, die sich mit der Auswirkung von episodischem Outflow-Feedback auf den Sternentstehungsprozess und die fossilen Informationen, die von den Outflows mitgetragen werden, beschäftigen. Unter Verwendung eines episodischen Outflowmodells werden insgesamt 111 numerische "Smoothed Particle Hydrodynamic" Simulationen durchgeführt, um den Sternentstehungsprozess durch die ersten Phasen zu verfolgen. Diese Simulationen beinhalten eine Auflösungs- und Parameterstudie, wobei die Letztere zeigt, dass episodisches Outflow Feedback in hohem Maße selbstregulierend ist. Episodische protostellare Outflows reißen etwa das Zehnfache ihrer ursprünglich Masse mit sich, wodurch sich die Sternentstehungseffizienz ungefähr halbiert, was zu einer verschobenen stellaren Anfangsmassefunktion führt. Outflows beeinflussen, wie die Sterne akkretieren, indem sie die Scheibenakkretion gegenüber der radialen Akkretion fördern. Ein höherer Anteil an Scheibenakkretion erhöht den Anteil der Zwillingsterne mit fast gleicher Masse, sodass dieser gut mit Beobachtungen übereinstimmt. Simulationen ohne Outflow Feedback bilden mehr Sterne und Mehrfachsysteme höherer Ordnung, welche überwiegend zu Doppelsternsystemen auseinanderbrechen. Outflow Feedback erhöht die Stabilität von Mehrfachsystemen höherer Ordnung, sodass die resultierende Vielfachheitsstatistik in guter Übereinstimmung mit Beobachtungen ist. Da die Akkretion von Gas und das Emitieren von Outflows eng miteinander verknüpft sind, tragen protostellare Outflows die Akkretionsgeschichte des emittierenden Protosterns mit sich. Hubble-Wedges in Positions-Geschwindigkeits Diagrammen entsprechen episodisch emittierten Outflow Bullets, die noch nicht mit der Hohlraumwand interagiert haben. Mit Hilfe der kinematischen Informationen, die der Outflow und insbesondere die Bullets tragen, ist es möglich, stellare Akkretionsraten abzuschätzen. Mittels dynamischer Alter der Outflows lässt sich das Alter der Protosterne abschätzen. Der Öffnungswinkel und die Aktivität des Outflows helfen bei der Unterscheidung zwischen Entwicklungsstadien. Diese Informationen kombiniert erlauben die Rekonstruktion der Akkretionsgeschichte des Protosterns. Episodische Outflows prägen maßgeblich die Entwicklung und Morphologie des sternentstehungs Prozess und sollten daher bei deren Untersuchung berücksichtigt werden.

# CONTENTS

1	INTRODUCTION	1
1.1	Core collapse	2
1.2	Accretion disc	4
1.3	Episodic accretion	5
1.4	Outflow launching	7
1.5	Outflows	10
2	SMOOTHED PARTICLE HYDRODYNAMICS	14
2.1	Euler Equations	15
2.2	Basic SPH formulation	15
2.3	Smoothing kernel	16
2.4	Smoothing length	17
2.5	Euler equation in SPH formulation	17
2.6	Artificial viscosity	18
2.7	Gravity	19
2.8	Radiative heating and cooling	21
2.9	Time integration	23
2.10	Timesteps	23
2.11	Sink particles	24
2.12	Alternatives to SPH	25
3	THE RESEARCH	27
4	PAPER I	30
5	PAPER II	49
6	PAPER III	69
7	SUMMARY AND CONCLUSION	90
7.1	Summary	90
7.2	Conclusion	93
7.3	Outlook	94

# List of Figures

1	Central temperature against central density for a collapsing $1 M_{\odot}$ core with 3000 AU radius. The different phases of the core collapse, as well as the formation of the first and second core are highlighted. The figure is taken with the permission from the Springer-Nature publisher from <a href="#">Rosen et al. (2020)</a> , based on <a href="#">Bhandare et al. (2018)</a> . . . . .	3
2	Zooming in on the HH212 outflow. Panel (a) shows the outflow on parsec scale ( <a href="#">Reipurth et al., 2019</a> ). (b) Zooming in to individual outflow bullets and the leading shock front ( <a href="#">McCaughrean et al., 2002</a> ). (c) The jet and bullets traced by SiO and CO ( <a href="#">McCaughrean et al., 2002</a> ; <a href="#">Lee et al., 2015</a> ). (d) Accretion disc and the central 1000 AU of the jet ( <a href="#">Lee et al., 2017</a> ). (e) Zooming in on the accretion disc with arrows indication the direction of rotation ( <a href="#">Lee et al., 2017</a> ). This composite work is taken from <a href="#">Lee (2020)</a> with the permission from the Springer-Nature publisher. . . . .	8
3	Sketch of the X-wind launching model based on figure 1 from <a href="#">Shu et al. (2000)</a> showing the funnel flows onto the protostar and the X-winds being launched. . . . .	9
4	Two panels from Fig.10 in <i>Paper I</i> showing the position-velocity relation's time evolution of an outflow lobe from the turbulent setup simulation. Letters A to F mark the position of individual outflow bullets. The black line corresponds to the Hubble law relation. Bullets that have decelerated at the leading shock front lie on the linear relation, whereas those that have not lie above the line. . . . .	90
5	Normalised distribution of mass ratios, $q$ , between the secondary, $M_{\star-s}$ , and primary component, $M_{\star-p}$ , of binary systems for the simulations with (orange) and without outflow feedback (blue). Simulations with outflow feedback have a significantly higher fraction of equal mass, $q > 0.95$ , twin binaries. The original figure is found in <i>Paper II</i> . . . . .	91
6	Estimated (orange) and true accretion history (blue) of a simulation presented in <i>Paper III</i> . Estimating the current accretion rate, the dynamical age of outflow bullets, and their corresponding accretion rate allows it to reconstruct the accretion history. The spacing of the outburst events and the episodic and background accretion rate resembles the underlying simulation. For the estimates, an ejection velocity of $30 \text{ km s}^{-1}$ and an outburst duration of 50 yr is assumed. . . . .	92

## INTRODUCTION

---

Since the dawn of time, we are bothered by the question of how these bright lights in the sky got there in place. For a long period, it was believed that the gas forming a star simply collapses under its own gravity, knowing just one direction – towards the forming star. During the last few decades, the discovery of bright spots, called "Herbig-Haro objects", strung on a long chain that emerges from the forming star, questioned this picture. It turns out that the simple picture of a one-way road to star formation is not appropriate, and instead, a large fraction of gas approaching the star is re-ejected in energetic and often parsec scale outflows.

If we want to understand the process of star formation, it is essential to take stellar feedback into account, especially protostellar outflows. Protostellar outflow feedback, albeit being the least energetic, is the first rung on a ladder of different feedback mechanisms. Basically all stars launch protostellar outflows from their earliest moment of birth. Thereby protostellar outflows regulate the star formation process by ejecting and entraining a significant fraction of gas that otherwise would end up in the star and therefore decisively influence the distribution of stellar masses that we observe today. The gas that actually accretes onto the protostar does so because outflows carry away angular momentum from the star-disc system. This accretion process turns out to be highly episodic, causing the outflow to be episodic too. The episodic ejection of gas manifests as individual outflow bullets, which can be observed as long chains of Herbig–Haro objects. The spacing and kinematics of these bullets might carry fossil information of the launching protostars accretion history.

This thesis contains three scientific publications that discuss the morphology and importance of protostellar outflow feedback in low-mass star formation. In this chapter, I will introduce the reader to the star formation process, following the collapse from filaments to dense cores and down to the protostellar embryo. There, I will describe how the gas accretes onto the young protostar via an accretion disc, focusing on episodic accretion bursts. I will discuss current theories on how this accretion process causes the ejection of protostellar jets and winds, as well as their morphology and impact on the larger scale envelope.

## 1.1

## CORE COLLAPSE

Star formation occurs in dense cores, which tend to be concentrated in filaments (Shu & Adams, 1987; André et al., 2014; Könyves et al., 2020; Beuther et al., 2021; Zhang et al., 2021). Filaments are elongated, often parsec long, dense gas structures that form from a larger scale clump or molecular cloud (Vázquez-Semadeni et al., 2019). Prestellar cores might form through fragmentation along the filament (Könyves et al., 2015) or especially clustered at junction points of multiple filaments or sub-filaments (Clarke et al., 2020; Zhang et al., 2020). The distribution of core masses can be described with the core mass function (CMF), which has a power-law tail towards high mass cores (O'Neill et al., 2021; Takemura et al., 2021). The forming prestellar cores are rather spherical compared to the elongated filaments, and their density distribution can be approximated by a Bonner–Ebert sphere (Bonnor, 1956; Ebert, 1957; Vázquez-Semadeni et al., 2019; Könyves et al., 2020). If these cores become Jeans unstable,

$$M_C > M_{\text{JEANS}} = \sqrt{\frac{1}{\rho_C} \left( \frac{k T_C}{G \mu} \right)^3}, \quad (1.1)$$

they start to collapse due to self-gravity and eventually form stars (Jeans, 1902). Here,  $G$  is the gravitational constant,  $\mu$  the mean mass of a molecule and  $M_{\text{JEANS}}$  the corresponding Jeans mass. The core properties,  $M_C$ ,  $\rho_C$ , and  $T_C$  denote the core's mass, density and temperature.

The process of forming a young protostar out of a dense core covers an enormous range of physical scales. A prestellar core with a typical size of 0.01 - 0.1 pc collapses into a stellar object with a typical size of a few  $R_{\odot} \sim 10^{-8}$  pc. Similarly, the density increases from the typical core density of  $10^{-19}$  g cm $^{-3}$  to about  $10^{-2}$  g cm $^{-3}$  in the protostar. This evolution can be divided into three phases (Larson, 1969). The *first phase*, called "isothermal collapse", covers the density regime of  $10^{-19}$  g cm $^{-3}$  to  $10^{-13}$  g cm $^{-3}$ . During this collapse, gravitational potential energy that is converted to thermal energy via compression is radiated away, mostly by dust grains and hydrogen molecules (Schulz, 2012). Since the density is low, the core is optically thin to far infrared dust cooling, and the radiation can escape from the core. Thus, the core is approximately isothermal and the temperature stays almost constant at 10 K. Since the thermal energy is radiated away, there is no significant pressure gradient that could stop the core from contracting, resulting in an almost free-fall collapse.

This runaway collapse remains as long as the gas is able to radiate away the energy released by contraction (Ward-Thompson & Whitworth, 2011). Once densities exceed  $10^{-13}$  g cm $^{-3}$ , the gas becomes optically thick, and the cooling radiation can no longer be radiated away (Larson, 1969). Since the radiation is trapped, the gas heats up, which causes a pressure gradient, eventually balancing gravity. This object in hydro-static equilibrium is then called a "first core" (Fig. 1). Envelope gas continues to fall onto the first core with almost free-fall velocity causing a shock front at the boundary layer. While the mass of the first core grows, its radius decreases.

The *second phase* is called "adiabatic collapse" since the first core now contracts adiabatically

$$T \propto \rho^{\gamma_{\text{ACTUAL}} - 1} \quad (1.2)$$

with an adiabatic index  $\gamma_{\text{ACTUAL}} \sim 5/3$ . An adiabatic index of  $\gamma_{\text{ACTUAL}} > 4/3$  is needed to stabilise the core. As the temperature rises, the  $\text{H}_2$  rotational and vibrational degrees of freedom become excited, lowering  $\gamma_{\text{ACTUAL}}$  to  $\sim 7/5$  (Bodenheimer, 2011; Arce & Sargent, 2004) (Fig. 1). The adiabatic contraction phase continues until the central density reaches  $\sim 10^{-8} \text{ g cm}^{-3}$ .

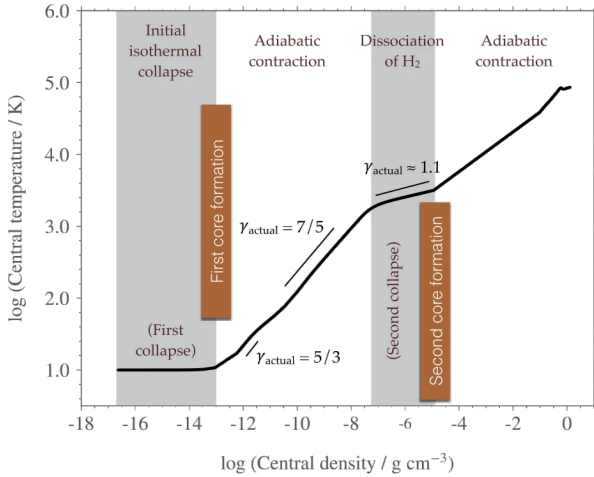


Figure 1: Central temperature against central density for a collapsing  $1 M_{\odot}$  core with 3000 AU radius. The different phases of the core collapse, as well as the formation of the first and second core are highlighted. The figure is taken with the permission from the Springer-Nature publisher from Rosen et al. (2020), based on Bhandare et al. (2018).

(Rosen et al., 2020). The resulting dense object within the first core is called the "second core", surrounded by a second shock front.

As the molecular hydrogen starts to deplete, the adiabatic index rises to  $\gamma_{\text{ACTUAL}} = 5/3$ , and the second core reaches hydro-static equilibrium again. As the gas of the first core falls onto the second core, the second core expands, and the first shock front disappears (Larson, 1969). At the same time, the temperature of the second core exceeds  $2 \cdot 10^4 \text{ K}$  and Hydrogen starts to ionise. The ionisation again causes the adiabatic index to decrease, but not below the critical value of  $\gamma = 4/3$  (Larson, 1969). Thus the core stays in hydro-static equilibrium and does not undergo a third collapse phase. By the time the hydrogen is almost completely ionised, the first core is mostly depleted and the second core has reached a density of  $10^{-2} \text{ g cm}^{-3}$  and a mass of  $\sim 0.01 M_{\odot}$  (Bodenheimer, 2011). Vaytet & Haugbølle (2017) find, using a grid of 1D simulations, that the formation of the first and second core is not significantly altered by varying density distributions and core masses of up to  $8 M_{\odot}$ .

The second core now enters the *third phase*, called "accretion phase", where it accretes the greatest part of its final mass. During this phase, the forming star's energy is dominated by contraction and accretion, which is radiated away from the surface (Bodenheimer, 2011). Dust grains in the envelope absorb and re-emit the

When the central temperature exceeds 2000 K,  $\text{H}_2$  starts to dissociate. The dissociation energy of  $\text{H}_2$  is 4.48 eV, a multiple of the thermal energy of 0.25 eV at  $T = 2000 \text{ K}$  (Bodenheimer, 2011). Energy released by the contraction is almost completely spent to dissociate  $\text{H}_2$ . Therefore, the temperature rises only slowly with a  $\gamma_{\text{ACTUAL}} \sim 1.1$  below the critical value of  $4/3$  (Schulz, 2012). Similar to the isothermal phase, the pressure gradient can no longer balance gravity, and the central region of the first core collapses a second time. The second collapse is much shorter than the isothermal collapse phase, a few hundred years compared to some  $10^4$  years, and ends when almost the entire  $\text{H}_2$  in the central region is dissociated at a density of  $\sim 10^{-5} \text{ g cm}^{-3}$

radiation of the star, which is now observable in the infrared regime (Larson, 1969). From now on, the second core is referred to as a protostar until hydrogen-burning sets in and the star formation process is completed. Since the outer parts of the envelope are, till now, almost unaffected and still at low densities of  $\sim 10^{-19} \text{ g cm}^{-3}$ , the accretion phase takes a few  $10^5$  years to complete (Evans et al., 2009).

## 1.2

### ACCRETION DISC

Collapsing cores generally have some level of initial turbulence and have therefore a net rotation associated with angular momentum (Gaudel et al., 2020). This rotation does not significantly alter the collapse and formation of the first core (Schulz, 2012), as described in the previous section, except for slowing down the collapse (Tomida et al., 2013). However, what significantly changes is how the protostar accretes gas from the envelope. Around the time of the second core formation, the first core condensates into an accretion disc around the central protostar due to angular momentum conservation (Gaudel et al., 2020; Xu & Kunz, 2021). These accretion discs are often observed to be differentially rotating with a velocity profile close to Kepler rotation (e.g. Hone et al., 2019; Yen et al., 2019; Reynolds et al., 2021)

$$v(r) = \sqrt{\frac{GM_\star}{r}}. \quad (1.3)$$

Here,  $M_\star$  is the mass of the central object, and  $r$  is the radius in the disc. Accretion onto the star occurs mostly via the accretion disc as the gas spirals inwards (Dunham et al., 2014).

Accretion discs play an essential role in redistributing the angular momentum of the inwards spiralling gas to the accretion disc's outskirts and, therefore, allow the central protostar to accrete. One of several mechanisms to redistribute angular momentum are gravitational instabilities. The Toomre Q parameter (Toomre, 1964)

$$Q = \frac{c_s \kappa}{\pi G \Sigma} \quad (1.4)$$

is an indicator of how prone a differentially rotating disc is to gravitational instabilities. Here,  $c_s$  is the sound speed,  $\kappa$  the epicyclic frequency (equivalent to the angular frequency for Keplerian rotation) and  $\Sigma$  is the surface density of the disc. The colder and denser the disc, the lower the Toomre Q parameter and the higher the chance for gravitational instabilities. Toomre Q parameter between 1.3 and 1.5 are associated with spiral waves, which efficiently redistribute angular momentum due to gravitational torques (Schulz, 2012; Lee et al., 2020; Xu & Kunz, 2021). This allows the disc to accrete mass onto the star and therefore to stabilise. If Q nevertheless falls below  $Q = 1$ , the accretion disc might fragment, eventually leading to a multiple system or a planetary companion.

Typical collapsing cores are not only rotating but they are also threaded by magnetic fields (Troland & Crutcher, 2008; Kandori et al., 2018). Numerical magneto-hydrodynamics (MHD) simulations have found that magnetic fields profoundly impact the formation of accretion discs (Wurster & Li, 2018). The earliest simulations only consider ideal MHD where field lines are perfectly frozen into the gas leading to the "magnetic braking catastrophe" (Li et al., 2014). When also ignoring turbulence, magnetic braking is so efficient in removing angular momentum that,

depending on the magnetic field strength, no disks at all or only small ones form (Seifried et al., 2011; Commerçon et al., 2012; Bate et al., 2014).

However, accounting for non-ideal MHD effects and using less idealised initial conditions mitigate the magnetic braking catastrophe to some extent. Non-ideal MHD effects, such as Hall effect, Ohmic resistivity, and ambipolar diffusion, reduce the efficiency of magnetic braking (see the reviews by Li et al., 2014 and Wurster & Li, 2018). Turbulence and the resulting misalignment of the magnetic field with the angular momentum axis further reduce the efficiency of magnetic braking (Seifried et al., 2013, 2015; Wurster et al., 2016; Gray et al., 2018; Wurster & Li, 2018; Wurster et al., 2019). Combining non-ideal MHD and, more importantly, less idealised initial conditions, Wurster et al. (2019) find that accretion discs of 10 - 80 AU form independent of the initial magnetic field strength. Maury et al. (2019) find that observed discs are rather small during their early evolution, with most discs being smaller than 60 AU, favouring collapse models that include magnetic fields.

Once the accretion disc has formed, magnetic fields stabilise the disc against gravitational instabilities. Therefore, the Toomre Q parameter (Eq. 1.4) is modified to account for magnetic fields (Kim & Ostriker, 2001; Wurster & Bate, 2019)

$$Q_M = \frac{\kappa \sqrt{c_s^2 + v_A^2}}{\pi G \Sigma}. \quad (1.5)$$

Here,  $v_A$  is the Alfvén velocity. If the accretion disc's inner parts are sufficiently ionised, magnetic fields might trigger the magnetorotational instability (MRI), which transports angular momentum outwards (Velikhov, 1959; Chandrasekhar, 1960; Stone et al., 2000; Audard et al., 2014). Another mechanism associated with magnetic fields that rearranges angular momentum in the accretion disc are protostellar winds and jets. The launching mechanism of winds and jets are discussed in Section 1.4.

### 1.3 EPISODIC ACCRETION

During the protostellar phase, a significant fraction of the stellar luminosity is due to accretion luminosity. Observations show that average accretion rates inferred from the luminosity of protostars does not match with typical stellar masses and accretion time scales (Kenyon et al., 1990; Kenyon & Hartmann, 1995; Evans et al., 2009). Assuming typical stellar masses and accretion time scales, the accretion luminosity of a  $0.25 M_\odot$  star with the size of  $3 R_\odot$  would be  $\sim 25 L_\odot$ , much higher than the median luminosity observed (Dunham et al., 2014). The other way around, accretion rates inferred by the observed luminosities of  $\sim 10^{-7} M_\odot \text{ yr}^{-1}$  are too low to reach typical stellar masses during the deeply embedded phase (Dunham et al., 2014). A possible solution to this so-called "luminosity problem" is that the accretion onto protostars is not continuous, but episodic (Kenyon & Hartmann, 1995). A scenario where a significant fraction of the stellar mass is accreted in short bursts could explain why most of the stars are usually observed to have low luminosities and still grow to typical stellar masses in a reasonable amount of time.

Today, there is considerable evidence that accretion onto protostars is indeed episodic. Protostars that undergo the most prominent accretion bursts are called "FU Orionis" (FUor) stars. FUors are observed to undergo some ten years lasting accretion bursts where their accretion rate quickly rises to a few  $10^{-4} M_\odot \text{ yr}^{-1}$ ,

followed by a  $10^3 - 10^4$  years lasting quiescent phase with typical accretion rates of  $\sim 10^{-7} M_{\odot} \text{ yr}^{-1}$  (Audard et al., 2014; Safron et al., 2015; Fehér et al., 2017; Takami et al., 2019; Pérez et al., 2020; Takagi et al., 2020). FUors' more frequent and less intense outbursting counterparts are called "EXors" (Stock et al., 2020). EXors quasi-periodically undergo phases of high accretion every few years, albeit there is no clear distinction between the two classes (Audard et al., 2014).

By observing the same source over several years, it is possible to study the brightening and fading due to episodic accretion bursts (Hillenbrand et al., 2018; Fischer et al., 2019; Szegedi-Elek et al., 2020; Takagi et al., 2020; Hillenbrand et al., 2021). Lucas et al. (2020) find a low-mass Class I protostar that between 2004 and 2019 shows a strong outburst with luminosity rising to some  $10^2 L_{\odot}$  corresponding to an accretion rate of  $10^{-4} M_{\odot} \text{ yr}^{-1}$ . In 2019 the burst was already fading, indicating a duration of the burst of at least 13 years.

An indirect method of confirming episodic accretion is by studying the chemical composition of the protostellar envelope. Simulations suggest that the luminosity burst have a long-lasting impact on the chemical composition by sublimating molecules from the dust grains and expanding the so-called "snow line" to larger radii (Rab et al., 2017; Molyarova et al., 2018; Vorobyov et al., 2018). Observations of CO isotopologues and the H<sub>2</sub>O snow lines confirm this behaviour (Hsieh et al., 2018, 2019; Sharma et al., 2020). Using chemical modelling, Anderl et al. (2020) suggest that the chemical abundances of C<sup>19</sup>O and N<sub>2</sub>H<sup>+</sup> around the very low luminosity object IRAM 04191+1522 can be explained by an increase of the present-day luminosity by a factor of 150 a couple of hundred years ago. Another indirect signpost of episodic accretion is the spacing and dynamics of episodic outflow bullets (Sicilia-Aguilar et al., 2020; Nony et al., 2020). Episodic outflow bullets and how to predict the corresponding accretion bursts will be discussed in Section 1.5 and *Paper III*.

Episodic accretion bursts might play a significant role in regulating the fragmentation of accretion discs (Audard et al., 2014). If the cooling time scale of the accretion disc is comparable to or smaller than the time between outbursts, the accretion disc is prone to fragmentation (Stamatellos & Whitworth, 2009). Once a companion star formed, the time scale between outbursts is reduced, and further fragmentation is reduced (Stamatellos et al., 2012). Lomax et al. (2014, 2016) find that episodic accretion is necessary to reproduce the observed ratio of brown dwarfs to H-burning stars as well as the correct position of the peak of the stellar initial mass function (IMF).

The relative importance of various possible outburst triggers is still highly debated. One of these suggested trigger mechanisms is the thermal instability. Suppose a massive planet in the accretion disc blocks the gas from reaching the central protostar, then mass piles up in front of the planet. This compressed gas heats up, which might trigger the thermal instability, allowing the gas to bypass the planet (Audard et al., 2014).

Similarly, the combination of MRI and Gravitational instabilities (GI) can function as an outburst trigger (Kadam et al., 2020). GIs allow the gas to spiral inwards from the outskirts of the accretion disc (Machida & Basu, 2019). The gas potentially piles up in the inner part of the accretion disc and heats up. Once the temperature is high enough to cause ionisation, the MRI triggers. If active, the MRI effectively transports angular momentum outwards and allows the gas to pass the innermost few AU, causing a rapid outburst (Audard et al., 2014). Zhu et al. (2009a,b, 2010) develop a model that assumes the MRI to be the trigger for FU-Orion like episodic accretion bursts. Building upon this model, Stamatellos et al. (2012) develop a

sub-grid model emulating the episodic accretion behaviour of FUors, which will be used in this work.

Another possible outburst trigger mechanism is disc fragmentation (Vorobyov & Basu, 2015). If the Accretion disc is gravitationally unstable with a Toomre Q value  $< 1$ , then the disc might fragment in addition to forming spiral arms. Especially in the early phase, these fragments often do not survive and are instead accreted onto the protostar, causing a massive outburst (Audard et al., 2014). Observations by Takami et al. (2019) and Sharma et al. (2020) favour the fragmentation trigger mechanism.

All the outburst trigger mechanism discussed so far are caused by instabilities in the accretion disc. These instabilities might also be triggered externally, such as by the accretion of a gas clump onto the accretion disc (Kuffmeier et al., 2018), the interaction with a close binary star (Kuruwita et al., 2020) or the flyby of a star in a star cluster (Cuello et al., 2020). All of these trigger mechanisms might cause luminosity outbursts as observed in FUors – to distinguish between them and study which mechanism might dominate in certain environments is one of today's open topics. Vorobyov et al. (2021) perform numerical simulations with different accretion burst trigger and find that deviations from a Keplerian disc might allow distinguishing between different trigger mechanism.

## 1.4

### OUTFLOW LAUNCHING

During gravitational collapse, magnetic field lines threading the initial core are dragged with the inwards moving gas in an hourglass shape (Schleuning, 1998; Maury et al., 2018). These magnetic fields play an essential role in launching protostellar outflows. The details of how protostellar jets and winds are launched are still debated. However, the consensus is that gravitational potential energy is converted into kinetic energy via magneto-centrifugal acceleration (Frank et al., 2014; Lee, 2020).

Blandford & Payne (1982) propose a mechanism how ordered magnetic fields threading an accretion disc might launch disc-winds. There, the magnetic field line's footpoints are frozen in the accretion disc and rotate with it. Due to the hourglass shape, the field lines bend towards the outer end of the accretion disc. Particles are dragged along these field lines and behave like "beads on a rigid wire". If the angle between the field lines and the rotation axis is larger than  $30^\circ$ , the particles are accelerated centrifugally. However, Seifried et al. (2012) showed that the  $30^\circ$  angle is not a strict threshold. At larger distances from the driving source, the ejected gas inertia causes the field lines to become increasingly toroidal. The resulting pressure gradient then further collimates the disc-wind (Seifried et al., 2012).

Since the angular velocity stays constant while the particles move along the "wire", they carry away angular momentum. This is especially important since the angular momentum extracted from the disc allows the gas in the disc to accrete onto the protostar, thus mitigating the "angular momentum problem" (Bodenheimer, 1995; Matt & Pudritz, 2005; Ward-Thompson & Whitworth, 2011). Recent observations find signs of rotation in outflows and therefore corroborate the magneto-centrifugal driven wind model (Chen et al., 2016; Zhang et al., 2016; Lee et al., 2017; Tabone et al., 2017; Hirota et al., 2017; Louvet et al., 2018; Zhang et al., 2018; López-Vázquez et al., 2020; de Valon et al., 2020; Tabone et al., 2020). Lee et al.

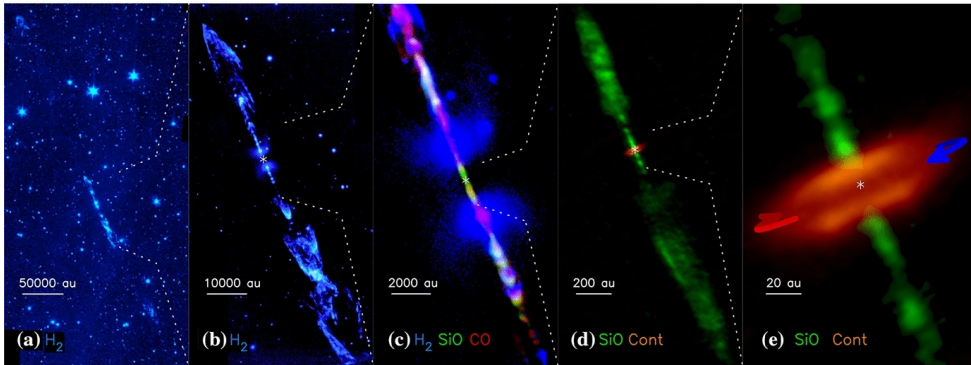


Figure 2: Zooming in on the HH 212 outflow. Panel (a) shows the outflow on parsec scale (Reipurth et al., 2019). (b) Zooming in to individual outflow bullets and the leading shock front (McCaughrean et al., 2002). (c) The jet and bullets traced by SiO and CO (McCaughrean et al., 2002; Lee et al., 2015). (d) Accretion disc and the central 1000 AU of the jet (Lee et al., 2017). (e) Zooming in on the accretion disc with arrows indication the direction of rotation (Lee et al., 2017). This composite work is taken from Lee (2020) with the permission from the Springer-Nature publisher.

(2017) find a magnetic lever arm in HH212 (Fig.2), the ratio of specific angular momentum in the jet and launching region, of  $\lambda \sim 3.2$ .

In the magneto-centrifugal wind model, the ejection velocity is a few times the Keplerian velocity at the launching region, decreasing with larger launching radii (Bally, 2016). Models that assume this kind of magneto-centrifugal outflow driving mechanism, operating in an extended region up to large disc radii, are called "disc-wind" models. Disc-wind models have been studied and extended, e.g. to account for non-ideal MHD effects and the magneto-rotational instability, by numerous authors (Wardle & Koenigl, 1993; Li, 1995, 1996; Ferreira, 1997; Casse & Ferreira, 2000; Salmeron et al., 2007; Königl et al., 2010; Leung & Ogilvie, 2020). Recent observations find signs of disc-wind launching (Zhang et al., 2018; Jiménez-Serra et al., 2020; Moscadelli et al., 2021), suggesting launching radii of a few AU (Moscadelli et al., 2021).

Next to the disc-wind models, there is a second model called "X-winds" (Shu et al., 1994; Mohanty & Shu, 2009). In contrast to disc-winds, X-winds are launched in a narrow region of the inner accretion disc (Frank et al., 2014). Ghosh & Lamb (1978) argue that the accretion disc is truncated at the co-rotation radius where the angular velocity of the accretion disc equals the angular velocity of the protostellar surface (Fig. 3). The accretion onto the protostar instead occurs via funnel flows along closed field lines (Fig. 3). These funnel flows are anchored at the stellar surface in so-called "hot-spots" (Fig. 3), covering up to 10% of the protostellar surface (Audard et al., 2010; Lorenzetti et al., 2012). Koenigl (1991) suggests that these funnel flows efficiently transport angular momentum into the inner parts of the accretion disc and therefore allow the protostar to stay below the break-up angular velocity. Shu et al. (1994) combine these funnel flows with the magneto-rotational launching model to the X-wind model. On the one hand, the gas at the co-rotation radius gains angular momentum through the funnel flows and therefore moves outwards. On the other hand, gas at the footpoints of the magnetic field lines, associated with magneto-rotational launching (Fig. 3), lose angular momentum and move inwards. Shu et al. (1994) find a steady-state solution where both effects balance each other. Consequently, gas and field lines become squeezed into a small region at the inner

truncation radius, called "X-region" (Fig. 3; [Shu et al., 2000](#)). The X-region is expected to be  $\sim R_{\odot}$  wide at the disc inner truncation radius of  $\sim 10 R_{\odot}$  corresponding to  $\sim 0.05$  AU ([Cai, 2009](#)).

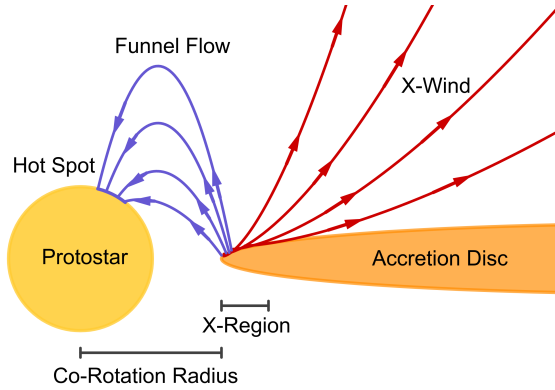


Figure 3: Sketch of the X-wind launching model based on figure 1 from [Shu et al. \(2000\)](#) showing the funnel flows onto the protostar and the X-winds being launched.

models can be ruled out so far. [Lee et al. \(2017\)](#) find for the jet in HH 212 (Fig. 2) launching region of  $\sim 0.04$  AU, as predicted by the X-wind model, whereas [Moscadelli et al. \(2021\)](#) find for an outflow in IRAS 21078+5211 a launching radius of  $\sim 2.2$  AU, corresponding to the disc-wind model.

Some outflow observations can not be explained with a fast collimated jet alone ([Lee et al., 2002](#); [Arce & Sargent, 2004](#); [Sicilia-Aguilar et al., 2020](#)). [Arce et al. \(2007\)](#) suggest a combination of a collimated high-velocity jet and a low-velocity wide-angle disc wind. [Shang et al. \(2006, 2020\)](#) present a model that combines the characteristics of a collimated jet with a wide-angle wind, based on the X-wind model. Both the X-wind and the disc-wind launching mechanism predict some kind of low-velocity wide-angle wind ([Lee, 2020](#)). In the X-wind model, these winds are also generated in the X-region at the inner edge of the accretion disc. In contrast, the disc wind model predicts that these wide-angle winds are generated further out in the disc.

At sufficiently large distances from the launching point, [Shu et al. \(1995\)](#) show that the in spherical coordinates almost radially ejected X-wind becomes collimated. The density distribution of the X-wind approaches a cylindrical configuration proportional to

$$\rho_w \propto 1 / (r \sin(\theta))^2, \quad (1.6)$$

where  $\rho_w$  is the density of the wind and  $\theta$  the angle of the flow with respect to the axis. [Matzner & McKee \(1999\)](#) show that this is not only the case for X-winds, but for any momentum conserving MHD wind in a power-law density distribution. Moreover, they show that these winds naturally resemble the mass-velocity relation's power-law exponent of  $\gamma = -2$ , close to the observed value of  $\gamma = -1.8$  ([Arce et al., 2007](#); [Liu et al., 2017](#)). Assuming that the wind is ejected almost radially

To determine whether the disc-wind or X-wind model is the main outflow launching mechanism is one of the current central challenges ([Lee et al., 2000](#)). Since in the X-wind model jets are launched at smaller radii than in the disc-wind model, both models predict a different amount of specific angular momentum carried away by the outflow. Recent high-resolution studies are able to measure the angular momentum in outflows and eventually differentiate between both launching models by estimating a launching region ([Anderson et al., 2003](#)). However, none of the

it follows from Eq. 1.6 that

$$\rho_w v_w^2 \propto 1 / (r \sin(\theta))^2, \quad (1.7)$$

with  $v_w$  being the wind velocity. [Matzner & McKee \(1999\)](#) argue that the angular force distribution,  $P(\mu)$ , must be flat for  $\mu \rightarrow 0$  and therefore approximate the distribution with

$$P(\mu) \simeq \frac{1}{\ln(2/\theta_0) (1 + \theta_0^2 - \mu^2)}, \quad (1.8)$$

where  $\theta_0$  is a parameter over which the distribution is flattened and  $\mu = r \cos(\theta)$ . This so called "wind-driven shell" model has been adapted by numerous authors in sub-grid models to eject outflows at a sufficiently large distance from the actual launching point (e.g. [Cunningham et al., 2011](#); [Offner & Arce, 2014](#); [Kuiper et al., 2015](#); [Tanaka et al., 2018](#); [Grudić et al., 2020](#), or *PaperI*).

## 1.5 OUTFLOWS

Despite the huge progress that has been made in understanding protostellar outflows since their first observations (e.g. [Snell et al., 1980](#)), there still remain many challenges. The launching of outflows and how they interact with their environment, e.g. by disrupting the core, are still not fully understood. A better understanding of outflows becomes even more desirable considering that outflows are ubiquitous ([Frank et al., 2014](#); [Bally, 2016](#); [Podio et al., 2020](#)). Outflow feedback is observed for almost all protostars, starting as early as Class 0 when the accretion rates are high ([Hirano et al., 2010](#); [Plunkett et al., 2015](#); [Busch et al., 2020](#); [Vazzano et al., 2021](#)) and continuing until the early Class II phase when accretions rates diminish ([Lee, 2020](#)). Outflows are observed for all protostellar masses from low-mass brown dwarfs ([Riaz et al., 2017](#); [Whelan et al., 2018](#); [Riaz & Bally, 2021](#)) up to massive stars where outflows are assumed to be a scaled-up version of their low-mass counterparts ([Carrasco-González et al., 2010](#); [Ellerbroek et al., 2013](#); [Caratti o Garatti et al., 2015](#); [Kölligan & Kuiper, 2018](#); [Rodríguez et al., 2021](#)).

Protostellar outflows consist of multiple components. The central part of the outflow is the collimated jet. The jet reaches extremely high velocities of 50 - 160 km s<sup>-1</sup> during the Class 0 phase and up to several 100 km s<sup>-1</sup> at later stages ([Anglada et al., 2007](#); [Hartigan et al., 2011](#); [Bally, 2016](#); [Lee, 2020](#)). The collimated jet associated with HH 212 (Fig. 2) has a velocity of 100 – 200 km s<sup>-1</sup> ([Podio et al., 2015](#)). These high velocities indicate that the jet is launched from the innermost part of the accretion disc, either through the disc-wind or X-wind launching mechanism (Section 1.4).

During the Class 0 phase, jets are mostly molecular and observed in infrared molecular line emission from CO, SiO, SO, H<sub>2</sub>, H<sub>2</sub>O, and HO ([Arce et al., 2007](#); [Frank et al., 2014](#); [Bally, 2016](#)). As SiO is a dense shock tracer it allows one to study the launching and collimation zone at the innermost 10<sup>4</sup> AU ([Lee, 2020](#)). The jet's molecular abundances are higher than in the envelope ([Lee et al., 2018](#); [Bjerkeli et al., 2019](#)). One possible explanation for these high molecular abundances is that in the launching region, elements such as C, Si, S and O are released from the grains and then, once ejected, quickly form molecules due to the high jet densities ([Glassgold et al., 1991](#); [Millan-Gabet et al., 2007](#)). During the Class I and II phases, the jet becomes increasingly atomic ([Sperling et al., 2021](#)), and the ionisation fraction

increases. Therefore, the more evolved jets are usually traced by O, H $\alpha$ , SII, NII and OI. Close to the launching region, the jets are ionised and therefore radiate free-free emission at centimetre wavelength (Anglada et al., 2018; Lee, 2020).

Protostellar jets are often observed to be surrounded by low-velocity wide-angle winds (Zhang et al., 2016; Maud et al., 2018; Zhang et al., 2019; Fernández-López et al., 2020; Pascucci et al., 2020; Zinchenko et al., 2020; Jhan & Lee, 2021). These winds have typical velocities of up to 50 km s<sup>-1</sup> (Zhang et al., 2019) and are less dense and collimated than the jet component. Hirota et al. (2017) and Louvet et al. (2018) find, using CO and SiO observations, low-velocity wide-angle winds with associated launching radii of  $\sim 20$  AU. Wide-angle disc winds that are launched further out in the accretion disc remove angular momentum there and allow the gas to reach the jet component's launching region (Lee et al., 2021, or the review by Lee, 2020). Podio et al. (2020) find an onion-like shell structure around the jet, where the inner  $\sim 10^\circ$  are traced by SiO, the intermediate  $\sim 10^\circ - 15^\circ$  are traced by SO, surrounded by a layer of CO up to  $\sim 25^\circ$ , similar to the results by Tabone et al. (2017). Lee et al. (2021) observe in HH 212 (Fig. 2) a rotating wide-angle disc wind in SO, interacting with the central jet component. This wide-angle disc wind is launched at radii between  $\sim 4$  and 40 AU in the accretion disc (see also Tabone et al., 2020). Zhang et al. (2017, 2019) detect signs that the wide-angle wind in the HH 46/47 outflow is episodic, similar to the collimated jet.

In the region where the jet hits the ambient medium a leading bow shock forms (Cerqueira et al., 2021). At the far side of the bow shock, a forward shock accelerates, compresses and heats the ambient medium. Where the jet hits the bow shock, a reverse shock front forms that decelerates, compresses and heats the jet material (Bally, 2016). The working surface in between these two shocks is dense and hot (Cerqueira et al., 2021). Depending on the shock velocity and density, the bow shock can be observed with ionised species, such as [SII], [OI], [OII] and [OIII] (Bally, 2016), or with dense shock tracers, such as SiO, SO and H<sub>2</sub> (Lee, 2020). The high-pressure gas between the two shock layers is pressed sideways and interacts with the ambient medium (Arce et al., 2007). This sideways motion of the gas results in broad wings surrounding the jet (Fig. 2 b).

The launching of protostellar jets is strongly connected to the accretion of gas (Section 1.4). Since the accretion of protostars is episodic rather than continuous, the launching of jets is episodic too (Vorobyov et al., 2018; Machida & Basu, 2019; Sicilia-Aguilar et al., 2020). The rapidly ejected high-velocity gas interacts with the slower cavity gas to form bow shocks along the jet axis. These intermediate bow shocks – often called "outflow bullets" – are similar to the leading bow shock and show wings that redirects the gas into sideways motion (Tafalla et al., 2017; Jhan & Lee, 2021). Outflow bullets are a frequently observed characteristic of protostellar outflows (e.g. Cheng et al., 2019; Tychoniec et al., 2019; Vazzano et al., 2021), and most often traced by shock tracers such as SiO, SO and CO (Lefèvre et al., 2017; Jhan & Lee, 2021; Lee et al., 2021). An example of outflow bullets can be seen in Fig. 2. In position-velocity diagrams, outflow bullets – in this context often called "Hubble Wedges" – stand out as high-velocity fingers from the otherwise linear position-velocity relation (Bachiller et al., 1990; Lada & Fich, 1996; Arce & Goodman, 2001; Wang et al., 2014, 2019; Nony et al., 2020). The spacing and velocity of the outflow bullets give insight into the accretion and ejection behaviour of their launching protostars (Bally, 2016; Lee, 2020). A frequently observed characteristic of episodic outflows is a bimodality of the time scale between two ejection events (Jhan & Lee, 2021, or the review by Lee 2020). Vorobyov et al. (2018) find a spa-

cing between bullets corresponding to quiescent phases between ejection events of  $\sim 10^3 - 10^4$  years and substructure within these bullets of  $\sim 10 - 100$  years. Once these outflow bullets break out of their dense core and are observable in the optical spectrum, they are referred to as "Herbig-Haro" objects, often spanning parsec scale long chains (Reipurth et al., 1997, 1998; Cortes-Rangel et al., 2020; Ferrero et al., 2020; Movsessian et al., 2021).

Outflows are confined by cavity walls, which are compressed layers of dense gas. These cavity walls are mostly molecular (Bally, 2016) and might cause an enhancement of complex molecule formation (Arce et al., 2008; Drozdovskaya et al., 2015). The cavities interior is filled with low-velocity, low-density entrained gas. Sideways moving gas, redirected from the leading and intermediate bow shocks, together with the wide-angle wind, hit and compress the cavity wall. Therefore, the cavity wall moves almost perpendicular to the outflow axis and widens over time (Arce & Sargent, 2006; Seale & Looney, 2008; Velusamy et al., 2014; Hsieh et al., 2017).

Another evolutionary trend of outflows – besides widening of the cavities and becoming increasingly atomic and ionised – is a diminishing outflow activity with evolutionary stage (Curtis et al., 2010; Yıldız et al., 2015; Bally, 2016; Mottram et al., 2017; Vazzano et al., 2021; Podio et al., 2021; Sperling et al., 2021). Tanabe et al. (2019) find in a sample of 44 outflows with an average dynamical age of 3.8 kyr an average mass-loss rate of  $1.7 \times 10^{-5} M_{\odot} \text{ yr}^{-1}$ . Combining observational results for young outflows of many authors, Lee (2020) find mass-loss of  $\sim 10^{-6} M_{\odot} \text{ yr}^{-1}$  for Class 0 sources. During the Class I and II phase these mass-loss rates decrease to  $\sim 10^{-10} M_{\odot} \text{ yr}^{-1}$  (Ellerbroek et al., 2013; Lee, 2020). This decrease in outflow activity is correlated with an diminishing accretion rate from  $\sim 10^{-5}$  during Class 0 phase to  $\sim 10^{-9} M_{\odot} \text{ yr}^{-1}$  during Class II phase (Ellerbroek et al., 2013; Lee, 2020). While the mass-loss and accretion rate decrease with evolutionary stage, the ratio of both, namely the ejection efficiency, stays rather constant at  $\sim 0.1$  in good agreement with predictions from the launching models (Shu et al., 1988; Pelletier & Pudritz, 1992; Calvet et al., 1993; Hartmann & Calvet, 1995; Ellerbroek et al., 2013; Bally, 2016; Lee, 2020).

Outflow feedback has a tremendous impact on the star formation processes it accompanies. Protostellar outflows are the first rung of a ladder of increasingly impactful feedback mechanism (Bally, 2016). Especially for cores and clouds forming mostly low-mass stars, where other feedback mechanisms such as stellar winds, ionising radiation or supernovae do not come into play, protostellar outflows are the dominant feedback mechanism, (e.g. Nakamura & Li, 2007; Hansen et al., 2012; Federrath et al., 2014; Krumholz et al., 2014; Li et al., 2018; Cunningham et al., 2018). Outflows inject a significant amount of energy and momentum on scales of a few AU to several parsecs (Arce et al., 2007).

On core scales, the initially ejected jet and wide-angle wind entrain secondary envelope material, unbinding up to  $\sim 50\%$  of the initial core mass (Lee et al., 2000; Arce et al., 2007; Machida & Matsumoto, 2012). The associated outflow lobes block the accretion from these directions onto the protostar, therefore reducing the accretion rate onto the protostar (Guszejnov et al., 2021). Since outflow feedback is accretion powered, the reduction in accretion rate causes a feedback loop resulting in self-regulated outflow feedback (Myers, 2008; Federrath et al., 2014). The injected energy and momentum might disperse the core and terminate the whole accretion process (Myers, 2008; Zhang et al., 2016; Bally, 2016). Overall, outflow feedback reduces the core-to-star efficiency to about 0.25 - 0.5 (Zhang et al., 2016; Tabone

[et al., 2017](#)).

On molecular cloud scales, the impact of outflow feedback depends on the size of the cloud. In smaller clouds, outflow feedback is sufficient to sustain the level of turbulence, delay collapse and even disrupt the whole cloud ([Matzner & Jumper, 2015](#); [Drabek-Maunder et al., 2016](#); [Feddersen et al., 2020](#); [Guszejnov et al., 2021](#)). However, this is probably not the case for more massive giant molecular clouds ([Arce et al., 2010](#); [Nakamura & Li, 2014](#); [Tanabe et al., 2019](#); [Li et al., 2020](#); [Guszejnov et al., 2021](#)). [Guszejnov et al. \(2021\)](#) find that outflows disrupt accretion flows and trigger star formation leading to a more realistic initial mass function.

## SMOOTHED PARTICLE HYDRODYNAMICS

---

Smooth Particle Hydrodynamics (SPH) is a numerical technique independently developed by [Lucy \(1977\)](#) and [Gingold & Monaghan \(1977\)](#) to solve astrophysical problems. Today, modern SPH formulations find use in a broad range of fields such as engineering or geophysics ([Springel, 2010](#); [Lind et al., 2020](#)). The unique feature of SPH is that the gas is discretised in a finite number of particles – the "P" in SPH – with a fixed mass. In a Lagrangian fashion, these particles are advected with the flow and store gas properties, such as energy and momentum. The Lagrangian frame of reference has some benefits compared to grid-based Eulerian methods. Particles moving with the flow naturally cause a high resolution in dense regions. Especially for star formation simulations with a huge dynamic range in density, this property is very convenient. Since the mass of a particle never changes, mass is naturally conserved in SPH simulations. Moreover, momentum and angular momentum are conserved too. In principle, even energy and entropy are conserved, but only if viscosity is neglected. One of the biggest drawbacks of SPH is that viscosity must be added artificially, which is a major error source. In the following, I give a brief overview of the SPH technique with a focus on the implementation in `GANDALF` ([Hubber et al., 2018](#)).

## 2.1

## EULER EQUATIONS

The "H" in SPH stands for hydrodynamics, referring to the goal of solving the equations of hydrodynamics, often called "Euler equations". These equations describe the flow of gases, such as in star forming regions. Considering inviscid gases and no additional force terms, the Euler equations in the Lagrangian form read as

$$\frac{d\rho}{dt} + \rho \nabla \mathbf{v} = 0, \quad (2.1)$$

$$\frac{d\mathbf{v}}{dt} + \frac{\nabla P}{\rho} = 0, \quad (2.2)$$

$$\frac{du}{dt} + \frac{P}{\rho} \nabla \mathbf{v} = 0. \quad (2.3)$$

Where  $d/dt = \partial/\partial t + \mathbf{v} \nabla$  is the convective derivative. Each of these equations covers a fundamental conservation law, respectively mass, momentum and energy. Except for some special cases, there are no analytical solutions to this problem. Therefore, to evolve the gas in time, this system of differential equations must be solved numerically. One of these numerical methods often used in modern astrophysics is Smooth Particle Hydrodynamics.

## 2.2

## BASIC SPH FORMULATION

The "S" in SPH refers to smoothing the properties carried by the SPH particles. A kernel,  $W$ , is used to smooth a property,  $A$ , defined at the particles' positions,  $\mathbf{r}'$ , into a continuous field, defined at any position,  $\mathbf{r}$ ,

$$\langle A(\mathbf{r}) \rangle = \int_V A(\mathbf{r}') W(|\mathbf{r} - \mathbf{r}'|, h) dV. \quad (2.4)$$

Here,  $h$  refers to the smoothing length on which the kernel,  $W$ , operates. Since in SPH the gas is modelled by a finite number of particles, the volume integral is approximated by the sum over all particles

$$\langle A(\mathbf{r}) \rangle = \sum_j^{n_{\text{PART}}} A(\mathbf{r}_j) W(|\mathbf{r} - \mathbf{r}_j|, h) \frac{M_{\text{PART}}}{\rho_j}. \quad (2.5)$$

The volume element,  $dV$ , is replaced by the associated volume of an SPH particle, e.g. the mass of a particle divided by its density  $M_{\text{PART}}/\rho_j$ .

The summation over all particles is similar to a Monte-Carlo integration; increasing the number of particles reduces the integration error (Dehnen & Aly, 2012). Since the particles are at least in the close vicinity of  $\mathbf{r}$  roughly equally spaced, the accuracy is significantly better than for a random distribution in a Monte-Carlo integration. Theoretically, SPH is a second-order algorithm (Monaghan, 2005). However, the somewhat irregular particle distribution causes the convergence order to drop to 1.1 - 1.8 (Quinlan et al., 2006; Lind et al., 2020).

The field variable  $A$  can be any property carried by the SPH particles. For the density, Eq. 2.5 takes the convenient form

$$\langle \rho(\mathbf{r}) \rangle = \sum_j^{n_{\text{PART}}} M_{\text{PART}} W(|\mathbf{r} - \mathbf{r}_j|, h), \quad (2.6)$$

only dependent on the particles' positions and masses. Vector-fields,  $\mathbf{B}$ , are computed in the same way

$$\langle \mathbf{B}(\mathbf{r}) \rangle = \sum_j^{n_{\text{PART}}} \mathbf{B}(\mathbf{r}_j) W(|\mathbf{r} - \mathbf{r}_j|, h) \frac{M_{\text{PART}}}{\rho_j}. \quad (2.7)$$

Another convenient property of the SPH formulation is that derivatives of field variables simply become derivatives of the kernel  $\nabla W(\mathbf{r} - \mathbf{r}_i, h)$ , which are in general pre-calculated,

$$\langle \nabla A(\mathbf{r}) \rangle = \sum_j^{n_{\text{PART}}} A(\mathbf{r}_j) \nabla W(|\mathbf{r} - \mathbf{r}_j|, h) \frac{M_{\text{PART}}}{\rho_j}. \quad (2.8)$$

### 2.3

#### SMOOTHING KERNEL

The kernel used in Eq. 2.4-2.8 can be any function that satisfies the following conditions. The kernel must (i) be normalised

$$\int_V W(|\mathbf{r} - \mathbf{r}'|, h) dV = 1, \quad (2.9)$$

(ii) be at least two times differentiable and (iii) approximate a Dirac  $\delta$ -function as the smoothing length tends towards zero

$$\lim_{h \rightarrow 0} W(|\mathbf{r} - \mathbf{r}'|, h) = \delta(|\mathbf{r} - \mathbf{r}'|). \quad (2.10)$$

Additionally, it is beneficial if the kernel has a finite support. In contrast to the historically used Gaussian (Gingold & Monaghan, 1977), kernels with finite support cut the computational cost by just considering the particle in the close vicinity. For a kernel with finite support Eq. 2.5 becomes

$$\langle A(\mathbf{r}) \rangle = \sum_j^{n_{\text{NEIB}}} A(\mathbf{r}_j) W(|\mathbf{r} - \mathbf{r}_j|, h) \frac{M_{\text{PART}}}{\rho_j}, \quad (2.11)$$

where  $n_{\text{NEIB}}$  is the number of neighbours within the kernel instead of all particles. Thereby, particles far away from  $\mathbf{r}$  do not influence local properties such as density or temperature.

A frequently used kernel is the M4 kernel

$$W(r, h) = \frac{1}{\pi h^3} \begin{cases} 1 - \frac{3}{2}s^2 + \frac{3}{4}s^3 & \text{if } 0 \leq s < 1 \\ \frac{1}{4}(2-s)^3 & \text{if } 1 \leq s \leq 2 \\ 0 & \text{if } s > 2 \end{cases}. \quad (2.12)$$

The M4 kernel fulfils the above mentioned conditions and has a finite support of

two smoothing length,  $s \equiv r/h < 2$ . The first spacial derivative is

$$\frac{dW(r,h)}{dr} = \frac{1}{\pi h^4} \begin{cases} -3s + \frac{9}{4}s^2 & \text{if } 0 \leq s < 1 \\ \frac{3}{4}(2-s)^2 & \text{if } 1 \leq s \leq 2 \\ 0 & \text{if } s > 2 \end{cases} . \quad (2.13)$$

An alternative to the M4 kernel is the Quintic kernel that utilises a higher-order spline and extends to  $3h$ . These spline kernels suffer from a phenomenon called "pair-instability", causing particles to stick at each other when the number of particles in the kernel exceeds a certain threshold. Wendland kernels avoid this problem and are therefore a viable alternative (Dehnen & Aly, 2012).

## 2.4

### SMOOTHING LENGTH

The smoothing length defines on which spatial scales the smoothing kernel operates. Thereby, the smoothing length, in combination with the choice of the kernel, determine the spatial resolution. A larger smoothing length results in a lower error due to noise. However, there is a trade-off between noise and spatial resolution. In addition, too large smoothing length might trigger the above-mentioned pair-instability.

Historically the smoothing length used to be fixed for all particles. However, moving to individual smoothing length opens up the full potential of adaptive refinement (Monaghan, 2002). The idea is to keep the number of particles within the kernel roughly constant. This is equivalent to assuming a constant mass within the kernel

$$\rho h_i^3 = \eta M_{\text{PART}} . \quad (2.14)$$

Here,  $\eta$  is a parameter used to scale the number of neighbours. Since the definition of the smoothing length,

$$h_i = \eta \left( \frac{M_{\text{PART}}}{\rho_i} \right)^{\frac{1}{3}} , \quad (2.15)$$

depends on the density and the density itself is a function of the smoothing length (Eq. 2.6), both are found iteratively. In Hubber et al. (2018) the default  $\eta = 1.2$  resulting in on average 58 neighbours for the M4 kernel (Price & Monaghan, 2004).

## 2.5

### EULER EQUATION IN SPH FORMULATION

To numerically solve the Euler equations (Eq. 2.1 - 2.3), one needs a discretised version of these equation that are formulated using SPH quantities. The mass conservation equation can be ignored since the mass of SPH particles never changes, and therefore Eq. 2.1 is fulfilled anyway.

Springel & Hernquist (2002) propose a "grad-h" formulation of SPH, which is also adopted by Hubber et al. (2018), where they discretise the corresponding Lag-

rangian

$$\mathcal{L}_{\text{SPH}} = \sum_j^{n_{\text{PART}}} M_{\text{PART}} \left( \frac{1}{2} v_j^2 - u_j \right), \quad (2.16)$$

with  $v_j$  and  $u_j$  being the velocity and internal energy of particle  $j$ . From this Lagrangian they derive a SPH version of the momentum equation (Eq. 2.2)

$$\frac{dv_i}{dt} = - \sum_j^{n_{\text{NEIB}}} M_{\text{PART}} \left( \frac{P_i}{\Omega_i \rho_i^2} \nabla W(r_{ij}, h_i) + \frac{P_j}{\Omega_j \rho_j^2} \nabla W(r_{ij}, h_j) \right) \quad (2.17)$$

and the energy equation (Eq. 2.3)

$$\left. \frac{du_i}{dt} \right|_{\text{COMP}} = \frac{P_i}{\Omega_i \rho_i^2} \sum_j^{n_{\text{NEIB}}} M_{\text{PART}} v_{ij} \cdot \nabla W(r_{ij}, h_i). \quad (2.18)$$

Here,  $\Omega_i$  denotes a correction factor that accounts for variable smoothing length of particle  $i$ 's neighbours,  $r_{ij} = |\mathbf{r}_{ij}| = |\mathbf{r}_i - \mathbf{r}_j|$  and  $v_{ij} = v_i - v_j$ . Since the SPH version of the Euler equations is directly derived from Lagrangian mechanics, energy, momentum and angular momentum conservation is guaranteed. However, additional modifications, e.g. individual particle timesteps, may cause that actual conservation is not achieved in practice (Hubber et al., 2018).

## 2.6

### ARTIFICIAL VISCOSITY

The SPH formulation, including the Euler equations (Eq. 2.1 - 2.3), discussed so far is completely inviscid. Viscosity is especially important for an accurate description of shocks, e.g. in protostellar outflows, to allow the conversion of kinetic into thermal energy. To correctly describe viscous fluids one would need to solve the Navier-Stokes equation, and there are SPH formulations that do exactly that (Sijacki & Springel, 2006). However, the more common approach is to add artificial viscosity terms to the Euler equations. Hubber et al. (2018) add an additional force term to the momentum equation (Eq. 2.17)

$$\left. \frac{dv_i}{dt} \right|_{\text{VISC}} = \sum_j^{n_{\text{NEIB}}} \frac{M_{\text{PART}}}{\bar{\rho}_{ij}} \alpha v_{\text{SIG}} \mu_{ij} \nabla \bar{W}(r_{ij}, h_i, h_j) \quad (2.19)$$

and a corresponding source term to the energy equation (Eq. 2.18)

$$\begin{aligned} \left. \frac{du_i}{dt} \right|_{\text{VISC}} &= - \sum_j^{n_{\text{NEIB}}} \frac{M_{\text{PART}}}{\bar{\rho}_{ij}} \frac{\alpha v_{\text{SIG}} \mu_{ij}^2}{2} \hat{\mathbf{r}}_{ij} \cdot \nabla \bar{W}(r_{ij}, h_i, h_j) \\ &+ \sum_j^{n_{\text{NEIB}}} \frac{M_{\text{PART}}}{\bar{\rho}_{ij}} \alpha v'_{\text{SIG}} (u_i - u_j) \hat{\mathbf{r}}_{ij} \cdot \nabla \bar{W}(r_{ij}, h_i, h_j), \end{aligned} \quad (2.20)$$

such that the energy is conserved (Monaghan, 1997). The heating and cooling rates due to compression (Eq. 2.18) and viscosity follows as

$$\left. \frac{du_i}{dt} \right|_{\text{HYDRO}} = \left. \frac{du_i}{dt} \right|_{\text{COMP}} + \left. \frac{du_i}{dt} \right|_{\text{VISC}}. \quad (2.21)$$

Since the viscous force between particle  $i$  and  $j$  is antisymmetric, momentum and angular momentum are still conserved. Here,

$$\bar{W}(r_{ij}, h_i, h_j) = \frac{W(r_{ij}, h_i) + W(r_{ij}, h_j)}{2}, \quad (2.22)$$

is a symmetrized kernel,  $\bar{\rho}_{ij} = (\rho_i + \rho_j)/2$  denotes the mean density,  $\mu_{ij} = \min(0, \mathbf{v}_{ij} \cdot \mathbf{r}_{ij})$  and  $\hat{\mathbf{r}}_{ij} = \mathbf{r}_{ij}/r_{ij}$ . The signal speed for the artificial viscosity is

$$v_{\text{SIG}} = c_i + c_j - \beta \mathbf{v}_{ij} \cdot \hat{\mathbf{r}}_{ij} \quad (2.23)$$

and

$$v'_{\text{SIG}} = |\mathbf{v}_{ij} \cdot \hat{\mathbf{r}}_{ij}| \quad (2.24)$$

for the artificial conductivity with  $c_i$  the isothermal sound speed of particle  $i$ . The strength of the artificial viscosity is regulated by the parameters  $\beta = 2\alpha$  of unity order (Morris & Monaghan, 1997).

This artificial viscosity description allows SPH to capture shocks but comes with the drawback that now inviscid flows are modelled incorrectly. To mitigate this problem, most SPH codes incorporate time-dependent viscosity switches. The switch used in this work was proposed by Cullen & Dehnen (2010). Each particle has its own time-dependent  $\alpha_i$  viscosity parameter. If the particle encounters a shock,  $\alpha_i$  rises to a predefined value and decays afterwards. Compared to previous methods, the switch by Cullen & Dehnen (2010) reduces unwanted artificial viscosity in accretion discs much more efficiently.

## 2.7 GRAVITY

The star formation process is mainly driven by the self-gravity. However, the implementation of self-gravity is not trivial; simply computing the gravitational acceleration between all particles

$$\left. \frac{d\mathbf{v}_i}{dt} \right|_{\text{GRAV}} = - \sum_j^{n_{\text{PART}}} \frac{G M_{\text{PART}} \hat{\mathbf{r}}_{ij}}{r_{ij}^2} \quad (2.25)$$

is generally not an option for two reasons. The first reason is that this would result in a computationally expensive  $O(\mathcal{N}^2)$  problem, which will be discussed later. The second reason is that if two particles lie within a smoothing kernel, the gravitational force needs to account for the smoothing to avoid numerical artefacts. Price & Monaghan (2007) propose a method that accounts for kernel smoothed gravity and does not break any conservation properties. Just as one may derive the momentum equation (Eq. 2.17) from the Lagrangian, the same may be done to determine the gravitational acceleration. Price & Monaghan (2007) formulate an additional gravity term that is added to the SPH Lagrangian (Eq. 2.16)

$$\mathcal{L}_{\text{GRAV}} = \sum_i^{n_{\text{PART}}} M_{\text{PART}} \psi_i \quad (2.26)$$

with the gravitational potential

$$\psi_i = -\frac{G}{2} \sum_j^{n_{\text{PART}}} M_{\text{PART}} \frac{\phi(r_{ij}, h_i) + \phi(r_{ij}, h_j)}{2}. \quad (2.27)$$

Here,  $\phi$  is the gravitational potential kernel, which is derived by integrating the the gravitational force kernel

$$\phi(r, h) = \int \phi'(r, h) dr. \quad (2.28)$$

The gravitational force kernel itself is obtained from the smoothing kernel,  $W(r, h)$ , as

$$\phi'(r, h) = \frac{4\pi}{r^2} \int_0^r W(r, h) r' dr'. \quad (2.29)$$

For  $W(r, h)$  being the M4 kernel (Eq. 2.12) the gravitational force and potential kernels take the form

$$\phi'(r, h) = \begin{cases} h^{-2} \left( \frac{4}{3} s - \frac{6}{5} s^3 + \frac{1}{2} s^4 \right) & \text{if } 0 \leq s < 1 \\ h^{-2} \left( \frac{8}{3} s - 3 s^2 + \frac{6}{5} s^3 - \frac{1}{6} s^4 - \frac{1}{15 s^3} \right) & \text{if } 1 \leq s < 2 \\ r^{-2} & \text{if } s \geq 2 \end{cases} \quad (2.30)$$

and

$$\phi(r, h) = \begin{cases} h^{-1} \left( \frac{2}{3} s^2 - \frac{3}{10} s^4 + \frac{1}{10} s^5 - \frac{7}{5} \right) & \text{if } 0 \leq s < 1 \\ h^{-1} \left( \frac{4}{3} s^2 - s^3 + \frac{3}{10} s^4 - \frac{1}{30} s^5 - \frac{8}{5} + \frac{1}{15 s} \right) & \text{if } 1 \leq s < 2 \\ -r^{-1} & \text{if } s \geq 2 \end{cases}. \quad (2.31)$$

From the modified Lagrangian (Eq. 2.16 and 2.26) the additional acceleration due to self-gravity can be derived as

$$\begin{aligned} \left. \frac{d\mathbf{v}_i}{dt} \right|_{\text{GRAV}} &= -G \sum_j^{n_{\text{PART}}} M_{\text{PART}} \frac{\phi'(r_{ij}, h_i) + \phi'(r_{ij}, h_j)}{2} \hat{\mathbf{r}}_{ij} \\ &- \frac{G}{2} \sum_j^{n_{\text{PART}}} M_{\text{PART}} \left( \frac{\xi_i}{\Omega_i} \nabla W_i(r_{ij}, h_i) + \frac{\xi_j}{\Omega_j} \nabla W_i(r_{ij}, h_j) \right). \end{aligned} \quad (2.32)$$

The factor  $\xi_i$  is derived as

$$\xi_i = \frac{\partial h_i}{\partial \rho_i} \sum_j^{n_{\text{NEIB}}} M_{\text{PART}} \frac{\partial \phi(r_{ij}, h_i)}{\partial h_i}. \quad (2.33)$$

Eq. 2.32 describes the acceleration of a particle due to the gravitational attraction of all other particles in the simulation. The difference to the hydrodynamical forces is that gravity has an infinite range, which manifests as a non zero term in gravitational force kernel for  $s > 2$  (Eq. 2.30). For state of the art simulations with many particles, this  $O(\mathcal{N}^2)$  scaling behaviour is disadvantageous and would cause high computational costs. Therefore, modern codes approximate the attraction of a distant group of particles on the gravitational acceleration of particle  $i$ . Instead of computing the acceleration to all of these particles individually, one only considers

their combined mass at their centre of mass position.

The most common way to determine which particles can be approximated as a group and which must be taken care of individually is a tree. Trees are hierarchical data structures where the highest level combines references to all elements, here particles, and splits them subsequently into smaller groups, called "nodes". Frequently used trees are KD-trees (Bentley, 1975) or Barnes-Hut trees (Barnes & Hut, 1986). A KD-tree subsequently divides the simulation domain in two such that each half, called "children", contains the same number of particles. The division repeats multiple time with the splitting alternating along the  $x$ ,  $y$  and  $z$ -axis. The highest level node is called the "root", whereas the bottom nodes are called "leaves".

When computing the gravitational force, one "walks the tree" down from the root towards the leaves and evaluates at each node whether all particles in this domain can be approximated with a single point mass or if the node must be broken up further. A possible opening criterion that a node at a distance  $d$  with size  $s$  has to fulfil is

$$\frac{s}{d} \leq \theta_{\text{MAX}}, \quad (2.34)$$

where  $\theta_{\text{MAX}}$  is a pre-defined maximum opening angle. The smaller the maximum opening angle, the more nodes are opened up, and the approximation approaches the exact solution.

Using such a tree structure reduces the computational complexity of self-gravity from  $O(\mathcal{N}^2)$  to  $O(\mathcal{N} \log(\mathcal{N}))$ . Moreover, the tree is also used to find the neighbours of a given particle efficiently for other calculations.

## 2.8

### RADIATIVE HEATING AND COOLING

So far, the gas internal energy is only affected by compression (Eq. 2.18) and viscous heating (Eq. 2.20). However, radiative heating (e.g. from stars, the background radiation field or cosmic rays) as well as radiative deexcitation of molecules, atoms and ions and black body radiation from dust, are the main regulators of the interstellar mediums (ISM) temperature. To correctly treat the effects of radiation, one would need to solve the full radiative transfer (RT) equation, which is not feasible with current computation resources. There are SPH-RT methods that approximate radiative transfer (e.g. Pawlik & Schaye, 2008; Grond et al., 2019; Chan et al., 2021), but they are still computationally expensive and complex to implement.

On the other hand, the most straightforward way to approximate the ISM's thermal behaviour is to use a barotropic equation of state (EOS). There, the gas temperature and pressure depends only on the density. The barotropic EOS combines an isothermal EOS for low-density, optically thin regions with an adiabatic EOS for dense, optically thick regions (e.g. Masunaga & Inutsuka, 2000). However, the barotropic EOS is often a strong oversimplification, e.g. disc fragmentation is not well captured.

To obtain a more appropriate description of the gas thermodynamics compared to a simple barotropic EOS, without the need to perform the full radiative transfer, I implemented the method by Stamatellos et al. (2007) into GANDALF to capture thermal and radiative effects. This method computes heating and cooling rates for each particle individually just from their local density, temperature and gravitational potential. The gravitational potential,  $\psi_i$ , is already calculated (Eq. 2.27) and

represents the particle's larger-scale environment.

To better differentiate between optically thin and thick regions, [Stamatellos et al. \(2007\)](#) introduce a pseudo-cloud around each SPH particle. The density and temperature profile of this pseudo cloud are modelled with a polytrope of index  $n = 2$ . The particle's position in the cloud is not fixed, instead it may take any position within this pseudo-cloud (for a use full illustration see figure 1 and 2 in [Stamatellos et al., 2007](#)). For each position of the SPH particle within the pseudo cloud, the parameter of the pseudo cloud are adjusted such that the density and temperature at the position within the pseudo cloud match that of the generating SPH particle. Dependent on the particle's density and gravitational potential, a mass weighted, pseudo-mean column-density,  $\bar{\Sigma}_i$  is estimated by integrating from any possible position within the pseudo-cloud to its edge

$$\bar{\Sigma}_i = \zeta_n \left( \frac{-\psi_i \rho_i}{4 \pi G} \right)^{\frac{1}{2}}. \quad (2.35)$$

Here,  $\zeta_n$  is precomputed factor, dependent on the polytropic index  $n$ , with  $\zeta_2 = 0.368$  as the default value. In a similar way pseudo-mean opacities,  $\bar{\kappa}_R(\rho, T)$  are precomputed and stored in a look-up table.

The relation between internal energy and temperature depends on many factors. [Stamatellos et al. \(2007\)](#) assume the gas consists of 70 % hydrogen and 30 % helium, for which they compute the fraction of molecular, atomic and ionised particles using the Saha equation (e.g. [Black & Bodenheimer, 1975](#)). The internal energy description accounts for ionisation and dissociation, for rotational and vibrational degrees of freedom and optical depth effects such as ice and metal grains and electron scattering. The internal energy depends only on the density and temperature,  $u_i(\rho_i, T_i)$ , and is stored as a pre-calculated lookup table.

With the pseudo-mean column density (Eq. 2.35) and opacity the additional heating or cooling due to radiation can be written as

$$\left. \frac{du_i}{dt} \right|_{\text{RAD}} = \frac{4 \sigma_{\text{SB}} (T_0^4(\mathbf{r}_i) - T_i^4)}{\bar{\Sigma}_i^2 \bar{\kappa}_R(\rho_i, T_i) + \kappa_P^{-1}(\rho_i, T_i)} \quad (2.36)$$

Here,  $\sigma_{\text{OB}}$  is the Stefan-Boltzmann constant and  $\kappa_P(\rho_i, T_i)$  is the Planck-mean opacity. The background temperature,  $T_0$ , is defined as

$$T_0^4(\mathbf{r}) = (10 \text{ K})^4 + \sum_s^{n_*} \frac{L_{*,s}}{16 \pi \sigma_{\text{OB}} |\mathbf{r} - \mathbf{r}_{*,s}|^2} \quad (2.37)$$

and accounts for the background radiation field as well as the pseudo background temperature field caused by the luminosity,  $L_{*,s}$ , of the stars in the simulation,  $n_*$ . In *Paper II* the stellar evolution model by [Offner et al. \(2009\)](#) is introduced to compute the luminosity of each star.

Instead of adding Eq. 2.36 to the energy equation (Eq. 2.21), which would cause very small timesteps, [Stamatellos et al. \(2007\)](#) propose a different scheme to update the internal energy. First an equilibrium temperature,  $T_{\text{EQUI}}$ , where the heating and cooling from compression and viscosity (Eq. 2.21) balance the heating and cooling from radiation (Eq. 2.36), is computed from

$$\left. \frac{du_i}{dt} \right|_{\text{HYDRO}} + \frac{4 \sigma_{\text{SB}} (T_0^4(\mathbf{r}_i) - T_{\text{EQUI}}^4)}{\bar{\Sigma}_i^2 \bar{\kappa}_R(\rho_i, T_{\text{EQUI}}) + \kappa_P^{-1}(\rho_i, T_{\text{EQUI}})} = 0. \quad (2.38)$$

Then, a thermalization timescale is estimated as

$$t_{\text{THERM},i} = (u_{\text{EQU},i} - u_i) \left( \left. \frac{du_i}{dt} \right|_{\text{HYDRO}} + \left. \frac{du_i}{dt} \right|_{\text{RAD}} \right)^{-1}, \quad (2.39)$$

where  $u_{\text{EQU},i} = u(\rho_i, t_{\text{EQU},i})$  is the tabulated internal energy for the equilibrium temperature. Finally the internal energy is updated as

$$u_i(t + \Delta t) = u_i(t) \exp\left(-\frac{\Delta t}{t_{\text{THERM},i}}\right) + u_{\text{EQU},i} \left(1 - \exp\left(-\frac{\Delta t}{t_{\text{THERM},i}}\right)\right). \quad (2.40)$$

Here,  $t$  is the simulation time and  $\Delta t$  the timestep.

This method is very efficient since it requires only local SPH quantities that are either already computed or tabulated. Therefore, it is a good compromise between a computationally more expensive radiative transfer code and a simple barotropic EOS.

## 2.9

### TIME INTEGRATION

Section 2.8 describes the time integration of the energy equation (Eq. 2.18). The momentum equation (Eq. 2.17) with the additional terms due to viscosity (Eq. 2.19) and gravity (Eq. 2.32) are integrated using a second-order Leap-Frog kick-drift-kick (KDK) scheme. Particle  $i$ 's position and velocity at step  $n$  are updated by the KDK scheme as

$$\mathbf{r}_i^{n+1} = \mathbf{r}_i^n + \mathbf{v}_i^n \Delta t + \frac{1}{2} \mathbf{a}_i^n \Delta t^2, \quad (2.41)$$

$$\mathbf{v}_i^{n+1} = \mathbf{v}_i^n + \frac{1}{2} (\mathbf{a}_i^n + \mathbf{a}_i^{n+1}) \Delta t. \quad (2.42)$$

Here, the acceleration is only computed once, but is taken into account at the beginning,  $\mathbf{a}_i^n$ , and at the end of a timestep,  $\mathbf{a}_i^{n+1}$ , which effectively halves the timestep  $\Delta t$ . The KDK scheme is symplectic and therefore comes with a bound energy error, which is especially use full for self-gravitating gas, e.g. in an accretion disc, as it prevents the orbits from drifting.

## 2.10

### TIMESTEPS

SPH codes a use Courant (CFL) condition,

$$\Delta t_i = f_c \frac{h_i}{c_i + |\nabla \mathbf{v}_i| + \epsilon}, \quad (2.43)$$

to limit the timesteps such that SPH particles can not cross their smoothing kernel in less than a timestep. Here,  $f_c = 0.15$  is a free parameter with the constraint that  $f_c < 1$  and  $\epsilon$  is a small number to prevent divisions by zero. As an addition to the

CFL condition, GANDALF uses an acceleration timestep limiter (Hubber et al., 2011),

$$\Delta t_i = f_A \frac{h_i}{\sqrt{|a_i|} + \epsilon}, \quad (2.44)$$

limiting the the timesteps in regions with high accelerations, e.g. in the vicinity of sink particles. Again,  $f_A = 0.075$  is a free parameter. The last condition used in GANDALF is an energy rate timestep limiter,

$$\Delta t_i = f_U u_i \left( \frac{du_i}{dt} + \epsilon \right)^{-1}, \quad (2.45)$$

with  $f_U = 0.4$ . The ideal timestep of a particle is the smallest of these three timesteps. Reducing  $f_C$ ,  $f_A$  or  $f_U$  makes the simulation more stable, but increases the computational cost.

Ideal timesteps might differ greatly between different particles. Particles sitting in the simulation's outskirts usually have much larger ideal timesteps than particles close to a sink. To not evaluate these particles more often than necessary, most SPH codes make use of block timestepping. In GANDALF, each particle is updated with its own timestep, which is a binary multiple

$$\Delta t_l = 2^l \Delta t_{\text{MIN}} \quad \text{with } l \in [0, 1, 2, \dots, l_{\text{MAX}}]. \quad (2.46)$$

of the smallest time step in the simulation,  $\Delta t_{\text{MIN}}$ . Accordingly, particle  $i$ 's block timestep is the largest  $\Delta t_l$  that is smaller than its ideal timestep (Eq. 2.43 - 2.45). Assuming  $l_{\text{MAX}} = 9$  is the highest allowed timestep level, then a particle on the lowest level receives  $2^{l_{\text{MAX}}} = 512$  times more updates than a particle on the highest level.

Neighbouring particles are only allowed to have a timestep level difference of  $\Delta l = 1$  to avoid situations where a particle with a long individual timestep does not react to an incoming shock front. At the end of a full timestep  $\Delta t_{\text{MAX}} = 2^{l_{\text{MAX}}} \Delta t_{\text{MIN}}$  all particles are at the same timestep and can be synchronised.

## 2.11

### SINK PARTICLES

During the gravitational collapse in which stars form out of dense cores, the density continuously increases. In the SPH formulation, high mass densities correspond to a high density of SPH particles. Due to the CFL timestep criterion (Eq. 2.43), this leads to continuously decreasing timesteps until it becomes infeasible to continue the simulation. Bate et al. (1995) propose sink particles to mitigate this problem. They replace gravitationally bound, dense objects with a single unsmoothed sink particle and therefore limit the timestep. Sink particles are unsmoothed and interact only gravitationally with the rest of the simulation. Neighbouring bound particles might be accreted onto the sink, thereby transferring their mass, momentum and angular momentum onto the sink particle.

Once a sink accretes particles, they are not able to leave the sink ever again. To avoid situations in which a particle would later leave the dense region again, certain requirements for the formation of sinks, and the accretion of particles onto it, must be fulfilled. These requirements may differ between SPH codes. Here, I focus on the ones proposed by Hubber et al. (2013) that are implemented in GANDALF. For

an SPH particle to turn into a sink particle, it must

- have a density greater than a pre-defined threshold density,  $\rho_{\text{SINK}}$ .
- have the lowest gravitational potential (Eq. 2.27) among all neighbours.
- not have an overlapping smoothing kernel with another sink particle.
- have a density greater than  $\rho_{\text{HILL}}$ . Where

$$\rho_{\text{HILL}} = -\frac{3(\mathbf{r}_{is} \cdot \mathbf{a}_{is})}{\pi G r_{is}^2} \quad (2.47)$$

with  $i$  the candidate particle,  $s$  an already existing sink particle and  $\mathbf{a}_{is}$  the acceleration between the two. This criterion ensures that if a sink particle forms in another sink particle's vicinity, the new one dominates the gravitational attraction.

- be able to collapse within a free fall time,  $\tau_{\text{FF},i}$ , before reaching another sink particle,  $s$ , corresponding to (Clarke et al., 2017)

$$\tau_{\text{FF},i} < \frac{r_{is}}{\hat{\mathbf{r}}_{is} \mathbf{v}_{is}}, \quad (2.48)$$

$$\rho_i > \frac{3\pi}{32G} \left( \frac{\hat{\mathbf{r}}_{is} \mathbf{v}_{is}}{r_{is}} \right)^2. \quad (2.49)$$

In previous implementations of sink particles, the accretion criteria are only that the SPH particle is within the accretion radius of the sink and gravitationally bound to it. Almost all particles within the accretion radius are immediately accreted, leaving an empty void around the sink as a consequence. The lack of particles causes an artificial pressure towards the sink. Hubber et al. (2013) propose a sub-grid model mitigating this problem. Particles are not accreted directly but slowly over time such that the vicinity of the sink is not empty, improving the hydrodynamical behaviour of the gas surrounding the sinks.

For this work, sink particles also serve as star particles; each sink is considered to be a single star. In *Paper I* and *Paper II*, I will introduce several additional sub-grid models that all operate on the sinks.

## 2.12

### ALTERNATIVES TO SPH

Historically SPH and finite-volume grid codes are the two options used in astrophysical simulations. Both have different strengths and weaknesses. Grid codes do not conserve angular and linear momentum at the same time, and the grid axis might lead to artefacts. Adaptive mesh refining codes, such as FLASH (Fryxell et al., 2000) mitigate the lack of adaptive resolution. Advantages of grid codes compared to SPH codes are the high accuracy and fast convergence due to high-order Riemann solvers. Moreover, there is no need for artificial viscosity since Riemann solvers accurately capture shocks with substantial dissipation.

In recent years, methods evolved that try to combine the advantages of Eulerian grid and Lagrangian SPH codes. Moving mesh (MM) codes, such as `AREPO` (Weinberger et al., 2020), advance particles in a Lagrangian fashion and therefore have a similar adaptive resolution as SPH. These particles are the base of a finite-volume Voronoi grid. Similar to standard grid codes, Riemann solvers compute fluxes at the cell boundaries with high precision. The unstructured grid adapts to interfaces and prevents grid artefact. However, the Voronoi tessellation is computationally expensive and angular momentum is not conserved.

An alternative to moving mesh codes are mesh-less finite-volume (MFV) or finite-mass (MFM) codes that are somewhat closer to SPH codes than MM codes (Hopkins, 2015). There, the volume associated with a given particle is computed using a kernel function instead of the Voronoi tessellation for MM codes. The difference is that in MFM interfaces are smooth, and a volume element at the boundary belongs partially to more than one particle, whereas MM codes have a sharp partition (see Fig. 1 in Hopkins, 2015, for an intuitive visualisation). Compared to MM, the MFM method features angular momentum conservation at the cost of higher noise. Hubber et al. (2018) find (similar to Hopkins (2015) for the `GIZMO` code) that the MFM implementation in `GANDALF` is superior to the SPH method. They find that MFM, compared to SPH, has better convergence properties, is better at shock capturing, less noisy and does not need artificial viscosity. I performed the simulations in this work with pure grad-h SPH because the implementation of MFM in `GANDALF` was not yet available when I started.

THE RESEARCH

---

Protostellar outflows are a ubiquitous signpost of the star formation process (Podio et al., 2020) emerging already during the earliest stages of star formation (Busch et al., 2020; Vazzano et al., 2021). While the outflow carves out a cavity (Duncan et al., 2021) that widens over time (Hsieh et al., 2017), the initially ejected gas *entrains* secondary core material (Zhang et al., 2017). Therefore, outflow feedback reduces the *star formation efficiency* to about 50% (Machida & Hosokawa, 2013; Tabone et al., 2017) in a *self-regulated* manner (Cunningham et al., 2018) and shifts the peak of the *IMF* closer to observed values (Bate, 2012; Guszejnov et al., 2021). Numerous authors are working on numerical simulations to study the launching of protostellar outflows as well as their impact on the envelope (Banerjee et al., 2007; Seifried et al., 2012; Price et al., 2012; Bate et al., 2014; Tomida et al., 2015; Offner & Chaban, 2017; Li et al., 2018; Cunningham et al., 2018; Machida & Basu, 2019; Rosen et al., 2020; Guszejnov et al., 2021). However, none of these works focuses especially on episodic outflow feedback.

As the accretion of protostars is observed to be episodic (Takagi et al., 2020), such are the outflows (Jhan & Lee, 2021; Lee et al., 2021), since both processes are highly connected (Vorobyov et al., 2018; Machida & Basu, 2019; Sicilia-Aguilar et al., 2020). Episodic outflow bullets stand out in observed *position-velocity* diagrams as high-velocity *Hubble Wedges* (Arce & Goodman, 2001; Wang et al., 2019; Nony et al., 2020). How these wedges relate to the linear position-velocity relation in terms of an evolutionary sequence is of great interest.

Since the accretion and ejection of gas are linked, outflows carry fossil records of the *accretion history* (Nony et al., 2020). Observers use kinematic information of the outflows and their bullets to infer stellar properties, such as the accretion rate (Li et al., 2020). *Dynamical ages* of outflows and their bullets (Zhang et al., 2005; Downes & Cabrit, 2007; Mottram et al., 2017; Li et al., 2020), the decline in *outflow activity* (Curtis et al., 2010; Yıldız et al., 2015; Vazzano et al., 2021) and the *widening of outflow cavities* (Arce & Sargent, 2006; Hsieh et al., 2017) might give a glimpse on the protostellar age or evolutionary stage. While these methods are frequently used, it is still unclear how accurate they are.

Only about half of the field stars are single stars like our sun; all other stars are in binary or even higher-order multiple systems (Raghavan et al., 2010). The *multiplicity* fraction during the early stage of star formation is even higher (Duchêne et al., 2007; Pineda et al., 2015; Tobin et al., 2016; Shan et al., 2017; Duchêne et al., 2018; Tobin et al., 2018; Kounkel et al., 2019). Therefore, most stars do not form in isolation but in a multiple system. Since only binary systems are genuinely stable, it is of great interest which factors influence the chances of higher-order multiple systems to stay intact or break apart. Binary systems are observed to occur frequently as so-called "*twin*" binaries where both components have roughly the same mass (Lucy, 2006; Simon & Obbie, 2009; Kounkel et al., 2019). The influence of episodic outflow feedback on the stability of multiple systems and the occurrence of twin binaries has not been studied so far.

This thesis aims to better understand the impact of episodic outflow feedback on the evolution and outcome of low-mass star formation. A new episodic outflow feedback model for SPH simulations is developed, extended and tested. Using this new model, simulations with and without episodic outflow feedback are compared to study the impact of outflow feedback on the star formation process. In the last step, the simulated outflows are used to test the accuracy of widely used methods to infer protostellar ages and accretion rates from these outflows. The main work of this thesis is presented in three publications which I will introduce in the following. The full publications are provided in Chapter 4, 5, and 6. In Chapter 7, I shortly summarise and discuss the results and give an outlook for further investigation.

*Paper I - Evolution of Hubble wedges in episodic protostellar outflows* (Rohde et al., MNRAS, 483, 2563, 2019)

The focus of this paper is to introduce the newly developed sub-grid, episodic outflow feedback model. An ensemble of 19 simulations of  $1 M_{\odot}$  rotating cores with a singular isothermal sphere (Shu, 1977) density distribution are performed. These simulations differ in model parameters as well as mass resolutions. In order to compare episodic and continuous outflow feedback, three additional simulations with continuous outflow feedback are presented. The publication covers an extensive resolution and parameter study of the new outflow model. The simulations with varying model parameter are used to discuss whether episodic outflow feedback is *self-regulating*. To study the influence of episodic outflow feedback in a more realistic environment, an additional simulation of a  $2.7 M_{\odot}$  core with a density distribution proportional to a Bonnor–Ebert sphere and an initially turbulent velocity field is presented (Bonnor, 1956; Ebert, 1957). This simulation is used to compare the simulated mass-velocity and *position-velocity* relation to observations and study *Hubble wedges* which are characteristic for episodic outflows.

*Paper II - The impact of episodic outflow feedback on stellar multiplicity and the star formation efficiency* (Rohde et al., MNRAS, 500, 3594, 2021)

The goal of the second paper is to study the influence of episodic outflow feedback on the outcome of the star formation process, such as the *multiplicity*, the *star formation efficiency* and the peak of the *IMF*. To model outflow feedback more accurately, the sub-grid outflow model presented in *Paper I* is improved by including a stellar evolution model that allows for a more realistic description of the ejection velocity and angular momentum extraction. A large ensemble of 88 simulations of  $1 M_{\odot}$  cores with varying initial conditions, such as the core radius and virial ratio as well as the turbulent mode and seed, are used to study the influence of these initial conditions on the star formation process. The simulation ensemble consists of 44 simulations without outflow feedback and 44 identical simulations but with episodic outflow feedback. These two samples are then compared in terms of *star formation efficiency*, *IMF*, *stellar multiplicity* and the fraction of *twin binaries*. For the simulations with outflow feedback, the *entrainment* factor and outflowing gas mass are analysed with a focus on the question of whether outflow feedback is *self-regulating*.

---

*Paper III - Protostellar Outflows: a window to the past* (Rohde et al., MNRAS, 510, 2552, 2022)

The focus of the third paper is to find out whether protostellar outflows can be used to infer the launching protostar's age, accretion history and evolutionary stage. For the sample of simulations with outflow feedback from *Paper II* the outflow lobes are detected using a k-means algorithm. Episodic outflow bullets within these lobes are extracted with the help of an OPTICS algorithm. For these extracted lobes and bullets *dynamical ages* are computed with four widely used methods. These four methods, together with a newly developed method that takes into account two subsequent outflow bullets, are compared to the underlying simulations in terms of accuracy. Outflow mass, momentum and energy rates, indicating the *outflow activity*, are computed using these dynamical ages to predict the launching protostar's evolutionary stage. Similarly, the *widening of outflow cavities* is studied with a focus on the accuracy of predicting the protostellar age. The outflows and bullets are used to predict continuous and episodic accretion rates, and the accuracy of these estimates is discussed. Finally, *Paper III* showcases how this information can be combined to reconstruct the *accretion history* of a protostar.

4

PAPER I

---



## Evolution of Hubble wedges in episodic protostellar outflows

P. F. Rohde,<sup>1</sup> S. Walch,<sup>1</sup> D. Seifried,<sup>1</sup> A. P. Whitworth,<sup>2</sup> S. D. Clarke<sup>1</sup> and D. A. Hubber<sup>3</sup>

<sup>1</sup>*Physikalisches Institut, Universität zu Köln, Zùlpicher Str. 77, D-50937 Köln, Germany*

<sup>2</sup>*School of Physics and Astronomy, Cardiff University, Cardiff CF24 3AA, UK*

<sup>3</sup>*Universitäts-Sternwarte München, Scheinerstraße 1, D-81679 München, Germany*

Accepted 2018 November 30. Received 2018 November 30; in original form 2018 August 23

### ABSTRACT

Young low-mass protostars undergo short phases of high accretion and outburst activity leading to lumpy outflows. Recent observations have shown that the position–velocity and mass–velocity diagrams of such outflows exhibit individual bullet-like features; some of these bullets subscribe to a ‘Hubble Law’ velocity relation, and others are manifest as ‘Hubble wedges’. In order to explore the origin of these features, we have developed a new episodic outflow model for the SPH code GANDALF, which mimics the accretion and ejection behaviour of FU-Ori-type stars. We apply this model to simulations of star formation, invoking two types of initial conditions: spherically symmetric cores in solid-body rotation with  $\rho \propto r^{-2}$ , and spherically symmetric turbulent cores with density proportional to the density of an Bonnor–Ebert sphere. For a wide range of model parameters, we find that episodic outflows lead to self-regulation of the ejected mass and momentum, and we achieve acceptable results, even with relatively low resolution. Using this model, we find that recently ejected outflow bullets produce a ‘Hubble wedge’ in the position–velocity relation. However, once such a bullet hits the leading shock front, it decelerates and aligns with older bullets to form a ‘Hubble-law’. Bullets can be identified as bumps in the mass–velocity relation, which can be fit with a power-law,  $dM/dv_{\text{RAD}} \propto v_{\text{RAD}}^{-1.5}$ .

**Key words:** stars: formation – stars: protostars – stars: winds, outflows.

### 1 INTRODUCTION

In the *core accretion* scenario for star formation, collapsing dense cores form protostars, and these protostars are usually surrounded by accretion discs (e.g. Shu & Adams 1987; Tan et al. 2014, and references therein). However, the observed luminosities of such protostars, and therefore by implication also their accretion rates, are typically much lower than one would expect, given their masses and formation time-scales, and assuming steady accretion; this mismatch is called ‘the luminosity problem’ (Kenyon et al. 1990, 1994; Kenyon & Hartmann 1995). The luminosity problem can be mitigated if the accretion from the disc onto the protostar is episodic, with a large fraction of the accretion occurring in short intense events called outbursts (Offner & McKee 2011; Dunham & Vorobyov 2012; Cesaroni et al. 2018; Hsieh et al. 2018; Ibryamov, Semkov & Peneva 2018; Kuffmeier et al. 2018). Such outbursts are observed in FU-Orionis-type stars (FUOrs), which undergo a rapid increase in accretion rate, from  $\sim 10^{-7} M_{\odot} \text{ yr}^{-1}$  to  $\sim 10^{-4} M_{\odot} \text{ yr}^{-1}$ , for a period of order 10 years (Herbig 1966; Hartmann & Kenyon 1985;

Hartmann et al. 1989; Audard et al. 2014; Safron et al. 2015; Fehér et al. 2017). The cause of this behaviour is still debated, but one possibility is the interplay of gravitational and magnetorotational instabilities (MRI; Balbus & Hawley 1991) in the disc (e.g. Zhu, Hartmann & Gammie 2009a; Zhu et al. 2010a; Stamatellos, Whitworth & Hubber 2011b; Kuffmeier et al. 2018). Using a large ensemble of Smoothed Particle Hydrodynamics (SPH) simulations Lomax, Whitworth & Hubber (2016a,b) conclude that episodic accretion is necessary to reproduce the observed stellar initial mass function and the ratio of brown dwarfs to hydrogen-burning stars.

Most, possibly all, forming protostars launch fast bipolar outflows (see, e.g., the reviews of Arce et al. (2007); Frank et al. (2014); Bally (2016), or the recent results from Samal et al. (2018)). The inference is that, during the collapse, gravitational energy is converted into kinetic and magnetic energy, which then drives and collimates the outflow, either through magnetic pressure or magnetocentrifugal forces (Blandford & Payne 1982; Lynden-Bell 2003; Pudritz et al. 2007; Machida, Inutsuka & Matsumoto 2008; Seifried et al. 2012; Frank et al. 2014; Bally 2016). The outflow removes a significant fraction of the angular momentum from the star–disc system, enabling the gas in the accretion disc to reach the central protostar (Konigl & Pudritz 2000; Pudritz et al. 2007). Since the

\* E-mail: rohde@ph1.uni-koeln.de (PFR); seifred@ph1.uni-koel.de (SW)

outflows are accretion-driven and the accretion is episodic, outflows are episodic too (Reipurth 1989; Hartigan, Edwards & Ghandour 1995; Hartmann 1997; König & Pudritz 2000; Arce et al. 2007; Hennebelle et al. 2011; Kuiper, Yorke & Turner 2015; Bally 2016; Choi et al. 2017; Cesaroni et al. 2018).

The collimated, high-velocity jet is usually traced by shock-excited  $\text{H}_2$  in the early embedded phase, and later by  $\text{H}\alpha$ ,  $[\text{S II}]$ ,  $[\text{N II}]$ , and  $\text{O I}$  (see, e.g. the review by Bally 2016). These jets have velocities ranging from  $\sim 10 \text{ km s}^{-1}$  to  $\sim 150 \text{ km s}^{-1}$ , and carve out narrow channels (Mundt & Fried 1983; Bally 2016; Liu et al. 2018). In addition, the jets are surrounded by low-velocity, wide-angle winds, with velocities up to  $\sim 30 \text{ km s}^{-1}$ . These winds are launched further out in the accretion disc (Cabrit, Raga & Gueth 1997; Bellocche et al. 2002; Lee et al. 2002; Arce et al. 2007; Frank et al. 2014). The collimated jet and the low-velocity, wide-angle wind entrain secondary, low-density, molecular gas, leading to a molecular outflow, mainly traced by  $\text{CO}$  and to a lesser extent by  $\text{SiO}$  (Arce et al. 2007). Lines from  $\text{SO}$  and  $\text{SO}_2$  trace gas that has been entrained by the wide-angle wind (Tabone et al. 2017). The outflow terminates in a bow shock, where it collides with the ambient medium (the leading shock front), thus forming a shock-compressed layer of gas. Changes in the ejection rate, caused by sudden accretion events, lead to the formation of bullets and internal working surfaces, which are shocked layers between the fast ejecta and the gas in the outflow cavity. More evolved outflows break out of their parental core or cloud and form parsec-scale outflows, traced by chains of Herbig–Haro objects. In some cases, these chains extend to over 10 per cent, e.g. HH 131 with an extent of 17 per cent (Reipurth, Bally & Devine 1997; Reipurth, Devine & Bally 1998). The velocities and spacings of these chains of Herbig–Haro objects allow one to constrain the episodic accretion history of the launching protostar.

A common relation observed in protostellar outflows is a linear position–velocity (PV) relation, i.e. a ‘Hubble Law’, in which the velocity of the outflowing gas increases linearly with distance from the source (Lada & Fich 1996). Recent observations show that the PV diagram also exhibits so called ‘Hubble Wedges’ of high-velocity emission, caused by the bow shocks of individual outflow bullets (Bachiller et al. 1990; Arce & Goodman 2001; Tafalla et al. 2004; Santiago-García et al. 2009; Wang et al. 2014).

In addition, spectral line observations of molecular outflows show a power-law mass–velocity (MV) relation

$$\frac{dM}{dv_{\text{RAD}}} \propto v_{\text{RAD}}^{-\gamma}, \quad (1)$$

as first reported by Kuiper, Zuckerman & Rodríguez Kuiper (1981). While some objects show a single power-law MV relation, others can only be fit with a broken power-law (Lada & Fich 1996; Davis et al. 1998; Ridge & Moore 2001; Birks, Fuller & Gibb 2006; Stojimirović, Snell & Narayanan 2008; Qiu et al. 2011; Mao, Yang & Lu 2014; Plunkett et al. 2015; Liu et al. 2017). In these cases, the low-velocity component has a shallow slope (i.e. low  $\gamma_\ell$ ), and the high-velocity component has a much steeper slope (i.e.  $\gamma_h \gg \gamma_\ell$ ).

Matzner & McKee (1999) show analytically that, for an idealized continuous hydrodynamical outflow,  $\gamma_\ell = 2$ , independent of the outflow velocity, density, or temperature. However, observations and simulations show that  $\gamma_\ell$  can range from  $\sim 1$  to  $\sim 3$  with a mode of  $\gamma_\ell \simeq 1.8$  (Lada & Fich 1996; Richer et al. 2000; Arce et al. 2007; Plunkett et al. 2015; Liu et al. 2017; Li, Klein & McKee 2018). Arce & Goodman (2001) find that episodic outflows can lead to a much steeper relation, with  $\gamma_\ell \sim 2.7$ . Using 1.3 mm waveband continuum and molecular line observations, Qiu & Zhang (2009) detect jumps in the MV relation of the outflows in the high-mass

star-forming region HH 80–81, and attribute these to molecular bullets, caused by episodic outflow events.

In the last decade, the challenge of simulating protostellar outflows self-consistently has been tackled by a number of authors (Machida, Inutsuka & Matsumoto 2009; Hennebelle et al. 2011; Price, Tricco & Bate 2012; Seifried et al. 2012; Machida & Hosokawa 2013; Bate, Tricco & Price 2014; Machida 2014; Tomida 2014; Tomida, Okuzumi & Machida 2015; Lewis & Bate 2017). Machida et al. (2009) and Machida (2014) are able to reproduce the two outflow components in high-resolution Magneto-hydrodynamics (MHD) simulations of collapsing Bonnor–Ebert spheres. However, resolving the jet launching region,  $r_{\text{LAUNCH}} \sim R_\odot$ , and at the same time following the outflow on parsec scales, over  $> 10^5$  yrs, is not presently feasible computationally. Hence, these simulations are limited either to short simulation times, or to low jet velocities. An alternative approach is to invoke an almost resolution-independent sub-grid model (Nakamura & Li 2007; Cunningham et al. 2011; Federrath et al. 2014; Myers et al. 2014; Offner & Arce 2014; Peters et al. 2014; Kuiper et al. 2015; Offner & Chaban 2017; Li et al. 2018). In this study, we introduce a sub-grid model which – for the first time – focuses on the time-variability of the outflows by mimicking the accretion behaviour of FUor-type stars.

The paper is organized as follows. In Section 2, we describe the computational method, introduce the sub-grid outflow model, and define the simulation setups. In Section 3, we compare episodic and continuous outflow feedback, and discuss the results of our resolution and parameter studies, based on simulations where the initial conditions are spherically symmetric cores in solid-body rotation with  $\rho \propto r^{-2}$ . In Section 4, we present the results of simulations where the initial conditions are a spherically symmetric turbulent core with density proportional to the density of a Bonnor–Ebert sphere, in particular concentrating on the PV and MV relations. The results are discussed in Section 5, and in Section 6 we summarize our results.

## 2 COMPUTATIONAL METHODS AND SETUP

### 2.1 SPH code GANDALF

We use the highly object orientated ‘grad-h’ SPH code GANDALF (Hubber, Rosotti & Booth 2018), which is based on the SPH code SEREN (Hubber et al. 2011). GANDALF offers different integration schemes, and we have chosen the second-order Leapfrog KDK scheme for our simulations. We use hierarchical block time-stepping to reduce the computational cost.

GANDALF can treat the thermodynamics of the gas in several ways, for example with simple isothermal, polytropic, or barotropic equations of state. Here, we invoke the approximate algorithm due to Stamatellos et al. (2007), which uses the density,  $\rho_i$ , temperature,  $T_i$ , and gravitational potential,  $\Phi_i$ , of each SPH particle  $i$ , to estimate a mean optical depth, which is then used to compute the local heating and cooling rates. The algorithm takes into account the opacity changes due to ice mantle melting and sublimation of dust, and the switch from dust opacity to molecular line opacity; it also captures the changes of specific heat due to dissociation and ionization of H and He.

To minimize the shortcomings of SPH in capturing shocks, we use the artificial viscosity formulation of Morris & Monaghan (1997), complemented by the time-dependent artificial viscosity switch of Cullen & Dehnen (2010).

## 2.2 Episodic accretion model

Modelling outflow feedback is crucial for star formation simulations, since outflow cavities significantly reduce the amount of gas that can be accreted onto the forming protostar, thus lowering the star formation efficiency (see, e.g. the review by Frank et al. 2014). Self-consistent outflow simulations suffer from the extremely high spatial and temporal resolution required to resolve the jet-launching region. To bypass this problem, we treat the collapse of the core explicitly only up to the sink creation density,  $\rho_{\text{SINK}} = 10^{-10} \text{ g cm}^{-3}$ ; thereafter, we assume that a protostar forms and insert a sink particle of radius  $r_{\text{SINK}} \sim 1 \text{ AU}$  (Bate, Bonnell & Price 1995). We use an improved treatment of sink particles, in which SPH particles that are flagged to be assimilated by a sink particle are not assimilated instantaneously, but instead are assimilated smoothly over a few time steps. Consequently, the sink particle's surroundings are not suddenly evacuated, and this improves the hydrodynamics in the vicinity of the sink (Hubber, Walch & Whitworth 2013). In addition, the rate of inflow onto the sink,  $dM_{\text{SINK}}/dt|_{\text{INFLOW}}$  is more smoothly varying.

Following Stamatellos, Whitworth & Hubber (2012) we divide the mass of the sink particle,  $M_{\text{SINK}}(t)$ , into the mass of the central protostar,  $M_*(t)$ , and the mass of an unresolved inner accretion disc,  $M_{\text{IAD}}(t)$ ,

$$M_*(t) = M_{\text{SINK}}(t) - M_{\text{IAD}}(t). \quad (2)$$

In addition, we keep track of the angular momentum of the unresolved central protostar,  $L_*(t)$ , and the inner accretion disk (IAD),  $L_{\text{IAD}}(t)$ ,

$$L_*(t) = L_{\text{SINK}}(t) - L_{\text{IAD}}(t). \quad (3)$$

Mass and angular momentum accreted onto the sink particle are first stored in the IAD. In order to treat the episodic accretion from the IAD onto the central protostar, and the resulting accretion luminosity, we use the sub-grid episodic accretion module developed by Stamatellos et al. (2012), based on an analytical description of FUor-type stars due to Zhu et al. (2009a, 2010a), in which episodic accretion is regulated by the interplay between gravitational instability and magneto-rotational instability (MRI).

In the absence of outflow, the rate of growth of the central protostar has just two contributions,

$$\frac{dM_*}{dt} = \frac{dM}{dt}\Big|_{\text{BG}} + \frac{dM}{dt}\Big|_{\text{MRI}}. \quad (4)$$

The first one is the background accretion rate,  $dM/dt|_{\text{BG}} = 10^{-7} M_{\odot} \text{ yr}^{-1}$ , allowing a small amount of mass to reach the central protostar even if the MRI is not active.

The second contribution,  $dM/dt|_{\text{MRI}}$ , represents the enhanced accretion rate enabled by the MRI during an outburst. It can exceed  $dM/dt|_{\text{BG}}$  by many orders of magnitude, but only during short outbursts of MRI activity. Following Zhu, Hartmann & Gammie (2010b) we assume

$$\frac{dM}{dt}\Big|_{\text{MRI}} = 5 \times 10^{-4} M_{\odot} \text{ yr}^{-1} \left( \frac{\alpha_{\text{MRI}}}{0.1} \right). \quad (5)$$

Here,  $\alpha_{\text{MRI}}$  is the Shakura–Sunyayev parameter (Shakura & Sunyayev 1973) for the effective disc viscosity due to the MRI. Simulations and observations suggest that  $0.01 < \alpha_{\text{MRI}} < 0.4$  (King, Pringle & Livio 2007). We use  $\alpha_{\text{MRI}} = 0.1$  as the default value, and vary it between  $\alpha_{\text{MRI}} = 0.05$  and  $\alpha_{\text{MRI}} = 0.2$ . Zhu et al. (2009b, 2010b) estimate

that the duration of an MRI outburst is

$$\Delta t_{\text{MRI}} \approx 0.25 \text{ kyr} \left( \frac{\alpha_{\text{MRI}}}{0.1} \right)^{-1} \left( \frac{M_*(t)}{0.2 M_{\odot}} \right)^{2/3} \left( \frac{dM/dt|_{\text{IAD}}}{10^{-5} M_{\odot} \text{ yr}^{-1}} \right)^{1/9}. \quad (6)$$

Hence, the total mass deposited on the protostar during a typical MRI accretion outburst is of order

$$\begin{aligned} \Delta M_{\text{MRI}}(t) &= \Delta t_{\text{MRI}}(t) \frac{dM}{dt}\Big|_{\text{MRI}} \\ &= 0.13 M_{\odot} \left( \frac{M_*(t)}{0.2 M_{\odot}} \right)^{2/3} \left( \frac{dM/dt|_{\text{IAD}}}{10^{-5} M_{\odot} \text{ yr}^{-1}} \right)^{1/9}. \end{aligned} \quad (7)$$

Stamatellos et al. (2012) assume that, as soon as the mass of the inner accretion disc exceeds the mass for a typical MRI event, the temperature of the inner accretion disc has become high enough for thermal ionization to activate the MRI. Hence, an outburst is triggered if

$$M_{\text{IAD}}(t) > \Delta M_{\text{MRI}}(t). \quad (8)$$

In the absence of outflow, the rate at which the IAD grows is given by

$$\frac{dM_{\text{IAD}}}{dt} = \frac{dM_{\text{SINK}}}{dt}\Big|_{\text{INFLOW}} - \frac{dM}{dt}\Big|_{\text{BG}} - \frac{dM}{dt}\Big|_{\text{MRI}}. \quad (9)$$

In addition, we impose a lower limit on the mass of the IAD,  $M_{\text{IAD}}(t) > M_{\text{MIN}} = 0.025 M_{\odot}$ , to ensure that the direction of the associated angular momentum,  $L_{\text{IAD}}$ , does not vary too much from one time-step to the next.

## 2.3 Outflow feedback model

Observations and theoretical predictions suggest that a fraction  $f_{\text{EJECT}} \sim 0.1 - 0.4$  of the gas accreted by a protostar is ejected in bipolar outflows (Crowell, Hartmann & Avrett 1987; Shu et al. 1988; Pelletier & Pudritz 1992; Calvet, Hartmann & Kenyon 1993; Hartmann & Calvet 1995; but see also the review by Bally 2016). We set  $f_{\text{EJECT}} = 0.1$  as the default value. To determine the rate of outflow at the current time  $t$ , following a time-step  $\Delta t$ , we first compute the mass available for outflow,

$$\Delta M_{\text{AVAIL}}(t) = \Delta M_{\text{AVAIL}}(t - \Delta t) + f_{\text{EJECT}} [M_*(t) - M_*(t - \Delta t)]. \quad (10)$$

If the outflow model is used in combination with the episodic accretion model (see Section 2.2), particles are only ejected if the MRI is active (equation (8)). Particles that would be ejected during a quiescent phase make up only a few per cent compared to the outburst and are thus ejected with the particles of the outburst to improve the hydrodynamical behaviour of the outflow. If  $\Delta M_{\text{AVAIL}}(t) > 4m_{\text{SPH}}$  we inject  $4N(t)$  SPH particles, where

$$N(t) = \text{floor} \left( \frac{\Delta M_{\text{AVAIL}}(t)}{4m_{\text{SPH}}} \right), \quad (11)$$

and reduce  $\Delta M_{\text{AVAIL}}(t)$  accordingly,

$$\Delta M_{\text{AVAIL}}(t) \rightarrow \Delta M_{\text{AVAIL}}(t) - 4Nm_{\text{SPH}}. \quad (12)$$

In Equation (11), the `floor()` operation returns the next lower natural number, and  $m_{\text{SPH}}$  is the mass of a single SPH particle.

The SPH particles driving the outflow are injected in a cone around the angular momentum axis of the IAD, which is defined by the unit vector  $\hat{e}_{\text{IAD}}(t) = L_{\text{IAD}}(t)/|L_{\text{IAD}}(t)|$ . They are injected in groups of four (labelled  $n = 1, 2, 3, 4$ ), simultaneously and symmetrically (see below), first in order to ensure conservation

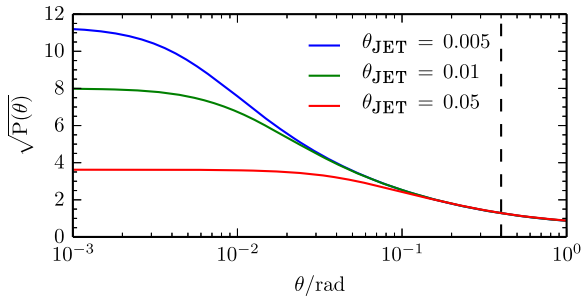


**Figure 1.** The outflow density distribution,  $\sqrt{P(\theta)}$ , giving the probability that a particle is injected at polar angle  $\theta$  (equation (14)), for three different effective opening angles  $\theta_{\text{JET}}$ . The dotted line shows the default value for the maximum polar angle,  $\theta_{\text{WIND}} = 0.4$ .

of linear momentum, and secondly in order to cancel unwanted angular momentum (i.e. angular momentum that is not parallel or antiparallel to  $\hat{e}_{\text{IAD}}(t)$ ). In a spherical–polar coordinate system, where the sink particle is at the origin and the polar axis is parallel to  $\hat{e}_{\text{IAD}}(t)$ , the position of the first injected SPH particle in a group of four is given by  $\mathbf{r}_1'' = (r, \theta, \phi)$ , with radius  $r \in [r_{\text{MIN}}, r_{\text{MIN}} + 2 \text{ AU}]$ , polar angle  $\theta \in [0, \theta_{\text{WIND}}]$ , and azimuthal angle  $\phi \in [0, 2\pi]$ . (All position vectors and velocity vectors in this coordinate system are distinguished by double primes, e.g.  $\mathbf{r}_1''$ .)

$r_{\text{MIN}}$  is a purely numerical parameter, giving the smallest radius from which the SPH particles representing the outflow can be injected without incurring prohibitively short time-steps. It has default value  $r_{\text{MIN}} = 10 \text{ AU}$  (i.e.  $\sim 10r_{\text{SINK}}$ ; see Section 3.3.5) and must be distinguished from  $r_{\text{LAUNCH}}$ , which is the much smaller – and unresolved – radius from which the outflow is assumed to originate (see below).  $\theta_{\text{WIND}}$  is the opening angle of the wide-angle wind, with default value  $\theta_{\text{WIND}} = 0.4 \text{ rad}$  (see Section 3.3.1).  $r$  and  $\phi$  are drawn randomly from uniform distributions in their respective ranges, but the distribution of  $\theta$  values is more complicated.

The distribution of  $\theta$  determines the relative mass fractions injected in the jet- and wind-components of the outflow. Like Cunningham et al. (2011), Offner & Arce (2014), and Kuiper et al. (2015), we use the force distribution derived by Matzner & McKee (1999) for a hydrodynamical outflow at scales far larger than the launching region,

$$P(\theta) \propto r^2 \rho v^2 \simeq \left[ \ln \left( \frac{2}{\theta_{\text{JET}}} \right) (\sin^2(\theta) + \theta_{\text{JET}}^2) \right]^{-1}. \quad (13)$$

Here,  $\theta_{\text{JET}}$  is the jet opening angle, i.e. it determines how collimated the jet component is. We assume that the density and velocity distributions at the base of the outflow satisfy

$$\rho_{\text{INJECT}}(\theta) \propto P^{1/2}(\theta), \quad (14)$$

$$|v_{\text{INJECT}}(\theta)| \propto P^{1/4}(\theta). \quad (15)$$

Therefore, we draw  $\theta$  randomly from the distribution  $P^{1/2}(\theta)$  in the range  $\theta \in [0, \theta_{\text{WIND}}]$ . This distribution is illustrated in Fig. 1 for representative values of  $\theta_{\text{JET}}$ .

The shape of the outflow is controlled by  $\theta_{\text{JET}}$  and  $\theta_{\text{WIND}}$ . Decreasing  $\theta_{\text{JET}}$  leads to a more collimated outflow; more particles are injected close to the outflow axis, and they are injected with

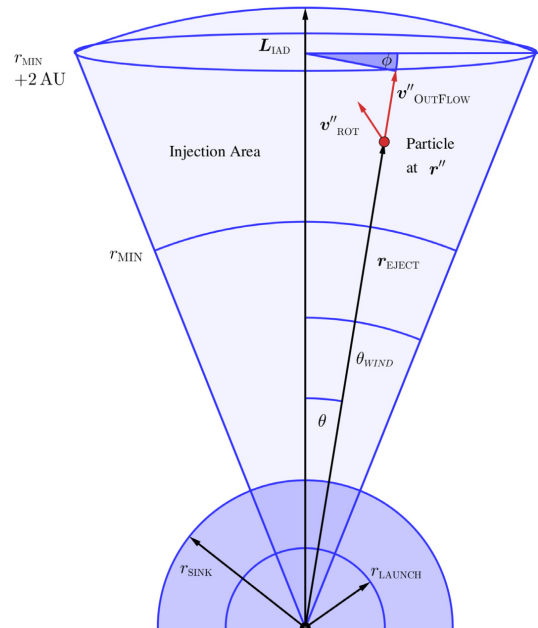


**Figure 2.** Sketch of the outflow configuration, in the spherical polar coordinate system where the sink particle is at rest at the origin and the polar axis is parallel to  $\mathbf{L}_{\text{IAD}}$ .

higher velocities, making the jet component stronger with respect to the low-velocity wind component (see Section 3.3.3). Increasing  $\theta_{\text{WIND}}$  leads to a wider outflow, affecting a larger volume, with more particles being injected in the low-velocity wind component (see Section 3.3.1).

The outflow velocity is scaled to the Keplerian velocity at  $r_{\text{LAUNCH}}$ , i.e.  $(GM_*/r_{\text{LAUNCH}})^{1/2}$ . Since we do not treat the evolution of the stellar radius (cf. Offner et al. 2009),  $r_{\text{LAUNCH}}$  is a free parameter, with the default value  $r_{\text{LAUNCH}} = 0.07 \text{ AU}$ . We emphasize that  $r_{\text{LAUNCH}} \ll r_{\text{SINK}} \ll r_{\text{MIN}}$ ; in other words, the SPH particles representing the outflow are injected much further out ( $\geq r_{\text{MIN}}$ ) than where the outflow is assumed to originate ( $r_{\text{LAUNCH}}$ ). The outflow velocity,  $\mathbf{v}_{\text{OUT1}}''$ , points in the same direction as the position vector  $\mathbf{r}_1''$  (Fig. 2), i.e.

$$\mathbf{v}_{\text{OUT1}}'' = \left( \frac{GM_*(t)}{r_{\text{LAUNCH}}} \right)^{1/2} P^{1/4}(\theta) \frac{\mathbf{r}_1''}{|\mathbf{r}_1''|}, \quad (16)$$

where  $P(\theta)$  is the force distribution (see equation (13)).

We add to  $\mathbf{v}_{\text{OUT1}}''$  a rotational velocity component,  $\mathbf{v}_{\text{ROT1}}''$ , which removes angular momentum from the IAD (see Fig. 2). About 90 per cent of the associated angular momentum must be removed from the gas that reaches the protostar, so that its rotation speed matches observations and stays below the break-up limit (Herbst et al. 2007). However, the physical mechanisms by which angular momentum is redistributed in a protostellar core are not fully understood and are not resolved in our simulations. The amount of angular momentum carried away by each SPH particle in the outflow is given by

$$\ell_{\text{SPH}}(t) = f_{\text{AngMom}} |\mathbf{L}_{\text{IAD}}(t)| \frac{m_{\text{SPH}}}{\Delta M_{\text{MRI}}(t)}, \quad (17)$$

where  $f_{\text{AngMom}} = 0.9$ . This ensures that the angular momentum of the protostar is a few per cent of the break-up angular momentum for a  $10R_{\odot}$  protostar of the same mass. The rotational velocity component in the outflow (e.g. Launhardt et al. 2009; Chen et al. 2016; Lee et al. 2017; Tabone et al. 2017) is then given by

$$\mathbf{v}_{\text{ROT.1}}'' = \mathbf{r}_1'' \times \boldsymbol{\omega}(t), \quad (18)$$

with

$$\boldsymbol{\omega}(t) = \frac{\ell_{\text{SPH}}(t)}{m_{\text{SPH}} \sin^2(\theta) r^2} \hat{\mathbf{e}}_{\text{IAD}}(t), \quad (19)$$

and the additional constraint that

$$v_{\text{ROT.1}}'' \leq \left( \frac{GM_{\star}(t)}{r_{\text{LAUNCH}}} \right)^{1/2}, \quad (20)$$

to ensure that the outflow velocity field is not dominated by rotation. If the resulting angular momentum that can be carried away by the outflow is smaller than  $L_{\text{IAD}}$ , the rest remains in the IAD and is available for the next time-step. The total velocity of the injected SPH particle is

$$\mathbf{v}_1'' = \mathbf{v}_{\text{OUT.1}}'' + \mathbf{v}_{\text{ROT.1}}''. \quad (21)$$

To compensate for the fact that part of the injected angular momentum is not parallel to  $\hat{\mathbf{e}}_{\text{IAD}}(t)$ , we inject a second SPH particle at position  $\mathbf{r}_2'' = (r, \theta, \phi + \pi)$ , and we compute its velocity, analogously to the first particle, i.e.

$$\mathbf{v}_{\text{OUT.2}}'' = \left( \frac{GM_{\star}(t)}{r_{\text{LAUNCH}}} \right)^{1/2} P^{1/4}(\theta) \frac{\mathbf{r}_2''}{|\mathbf{r}_2''|}, \quad (22)$$

$$\mathbf{v}_{\text{ROT.2}}'' = \mathbf{r}_2'' \times \boldsymbol{\omega}(t), \quad (23)$$

$$\mathbf{v}_2'' = \mathbf{v}_{\text{OUT.2}}'' + \mathbf{v}_{\text{ROT.2}}''; \quad (24)$$

otherwise, angular momentum is not conserved (Hubber et al. 2013).

The positions and velocities of particles 1 and 2 are then rotated, using a fast quaternion rotation scheme, into a frame in which the coordinate axes are parallel to those in the simulation frame, but with the origin still at the sink particle i.e.  $\mathbf{r}_n'' \rightarrow \mathbf{r}'_n$  and  $\mathbf{v}_n'' \rightarrow \mathbf{v}'_n$ , for  $n = 1$  and 2. (All position vectors and velocity vectors in this frame are distinguished by single primes, e.g.  $\mathbf{r}'_n$ .)

To obtain a bipolar outflow, and ensure conservation of linear momentum, we inject two further SPH particles, at positions  $\mathbf{r}'_3 = -\mathbf{r}'_1$  and  $\mathbf{r}'_4 = -\mathbf{r}'_2$ , and with velocities  $\mathbf{v}'_3 = -\mathbf{v}'_1$  and  $\mathbf{v}'_4 = -\mathbf{v}'_2$ . The net angular and linear momenta carried away by the set of four particles are then

$$|\Delta \mathbf{L}_{\text{TOTAL}}(t)| = m_{\text{SPH}} \left| \sum_{n=1}^{n=4} \{\mathbf{r}'_n \cdot \mathbf{v}'_n\} \right| \leq 4 \ell_{\text{SPH}}(t), \quad (25)$$

$$|\Delta \mathbf{p}_{\text{TOTAL}}(t)| = m_{\text{SPH}} \sum_{n=1}^{n=4} \{\mathbf{v}'_n\} = 0. \quad (26)$$

Finally, the particles are shifted into the simulation frame, with final positions and velocities

$$\mathbf{r}_n = \mathbf{r}'_n + \mathbf{r}_{\text{SINK}}, \quad (27)$$

$$\mathbf{v}_n = \mathbf{v}'_n + \mathbf{v}_{\text{SINK}}. \quad (28)$$

**Table 1.** The model parameters, with their default values, and the ranges over which we vary them in Section 3.3.

Model parameter	Default value	Range
$r_{\text{MIN}}$	20 AU	10 AU to 30 AU
$r_{\text{LAUNCH}}$	0.07 AU	0.047 AU to 0.140 AU
$\theta_{\text{WIND}}$	0.4 rad	0.2 rad to 0.4 rad
$\theta_{\text{JET}}$	0.01	0.005 to 0.05
$f_{\text{EJECT}}$	0.1	0.05 to 0.2
$f_{\text{AngMom}}$	0.9	—
$M_{\text{MIN}}$	$0.025 M_{\odot}$	—

If more than four particles are injected ( $N(t) > 1$ , equation 11), this process is repeated until the positions and velocities of all the new SPH particles in the outflow have been computed. Finally, if SPH particles have been injected ( $N(t) > 0$ ), the masses and angular momenta of the sink particle and its two constituent parts (the central protostar and the IAD) must be adjusted, according to

$$M_{\text{SINK}}(t) \rightarrow M_{\text{SINK}}(t) - 4N(t)m_{\text{SPH}}, \quad (29)$$

$$M_{\star}(t) \rightarrow M_{\star}(t) - 4N(t)m_{\text{SPH}}, \quad (30)$$

$$M_{\text{IAD}}(t) = M_{\text{SINK}}(t) - M_{\star}(t), \quad (31)$$

$$\mathbf{L}_{\text{SINK}}(t) \rightarrow \mathbf{L}_{\text{SINK}}(t) - \Delta \mathbf{L}_{\text{TOTAL}}(t), \quad (32)$$

$$\mathbf{L}_{\star}(t) \rightarrow \mathbf{L}_{\star}(t) + \frac{(1 - f_{\text{AngMom}})}{f_{\text{AngMom}}} \Delta \mathbf{L}_{\text{TOTAL}}(t), \quad (33)$$

$$\mathbf{L}_{\text{IAD}}(t) = \mathbf{L}_{\text{SINK}}(t) - \mathbf{L}_{\star}(t). \quad (34)$$

The model parameters are summarized in Table 1.

## 2.4 Simulation setup

In all simulations, the initial conditions are spherically symmetric, and consist of a dense core, embedded in a low-density envelope. In the following, we consider two different initial density profiles.

For the simulations presented in Section 3 (hereafter the *Rotating Setup*), we construct the initial core from a singular isothermal sphere (SIS; Shu 1977), i.e.  $\rho_{\text{SIS}}(r) = c_s^2/2\pi Gr^2$ , truncated at  $R_{\text{CORE}} = 0.015$  pc; the mass of the truncated SIS is  $M = 2c_s^2 R_{\text{CORE}}^2/G = 0.25 M_{\odot}$ , and the density at its boundary is  $\rho_{\text{SIS}}(R_{\text{CORE}}) = 4.0 \times 10^{-19} \text{ g cm}^{-3}$ . Next, we increase the density of the truncated SIS by a factor of 4, so that its mass is  $M_{\text{CORE}} = 1 M_{\odot}$ , and it is no longer supported against self-gravity. Finally, we set it in solid body rotation with angular frequency  $\omega = 1.35 \times 10^{-12} \text{ s}^{-1}$ , so that it collapses to form an accretion disc with radius of order  $\sim 150$  AU.

For the simulations presented in Section 4 (hereafter the *Turbulent Setup*), we construct the initial core from a Bonnor–Ebert sphere (BES; Bonnor 1956; Ebert 1957), since this may be a more realistic density profile than an SIS (Whitworth et al. 1996). The BES has central density  $\rho_{\text{CENTRAL}} = 5 \times 10^{-19} \text{ g cm}^{-3}$ ; it is truncated at  $R_{\text{CORE}} = 0.058$  pc, and the mass inside this radius is  $1.35 M_{\odot}$ . Next, we increase the density of the truncated BES by a factor of 2, so

that its mass is  $M_{\text{CORE}} = 2.70 M_{\odot}$ , and it is no longer in hydrostatic equilibrium. Finally, we add a turbulent velocity field with the virial ratio

$$\alpha_{\text{VIRIAL}} = \frac{2(E_{\text{TURB}} + E_{\text{THERM}})}{E_{\text{GRAV}}} = 0.85 \quad (35)$$

and the power spectrum

$$P_{\lambda} \propto \lambda^4 \text{ for } \lambda \in [\lambda_{\text{MIN}}, \lambda_{\text{MAX}}], \quad (36)$$

similar to Walch et al. (2010). The scale of the largest, thus the most energetic, turbulent mode is set to  $\lambda_{\text{MAX}} = 2 R_{\text{CORE}}$  (Walch, Whitworth & Girichidis 2012). The scale of the smallest mode is  $\lambda_{\text{MIN}} = 1/64 R_{\text{CORE}}$ .

The masses and radii of these cores resemble typical pre-stellar cores that will preferentially form low-mass protostars massive enough to launch outflows that have a significant impact on the core and envelope (Motte et al. 2001; André et al. 2014).

The dense cores are embedded in an envelope with low and uniform density,  $\rho_{\text{ENVELOPE}} = 10^{-23} \text{ g cm}^{-3}$ . The outer radius of the envelope is set to  $R_{\text{ENVELOPE}} = 1 \text{ pc}$ , in order to study multiple outflow bullets propagating simultaneously through the envelope. In the Rotating Setup, the mass of the envelope (between  $R_{\text{CORE}}$  and  $R_{\text{ENVELOPE}}$ ) is  $M_{\text{ENVELOPE}} = 0.62 M_{\odot}$ , and hence  $M_{\text{TOTAL}} = 1.62 M_{\odot}$ . In the Turbulent Setup, the mass of the envelope is  $M_{\text{ENVELOPE}} = 1.20 M_{\odot}$ , and hence  $M_{\text{TOTAL}} = 3.90 M_{\odot}$ . In both setups, the initial temperature is  $T = 10 \text{ K}$  everywhere, and the corresponding isothermal sound speed is  $c_s = 0.19 \text{ km s}^{-1}$ .

### 3 THE ROTATING SETUP

In order to illustrate the main features of core evolution, Fig. 3 shows the column density from Run 8 with the Rotating Setup (i.e. EPISODIC:400, see Table 2), at three different times. The first panel, at 2.4 kyr, shows how the first outflow event carves out a narrow cavity. In the second panel, at 4 kyr, the outflows break out of the parental dense core. In the third panel, at 16 kyr, one sees multiple bullets propagating in a bipolar outflow. Since the outflow becomes longer as it evolves, the panels in Fig. 3 have different scales, as shown by the scale bars.

In the following, we explore the effects of changing the numerical parameters (Section 3.1); of switching from episodic to continuous outflows (Section 3.2); and of changing the model parameters (Section 3.3). The parameters for all the runs are given in Table 2. For each run, only one parameter is changed from its default value; the default value is the value for the fiducial case (Run 6, see Table 2).

We are particularly concerned with the amount of mass and momentum escaping from the core and its envelope. An SPH particle,  $n$ , at radius  $r_n$  (measured from the centre of mass), is deemed to have escaped if its radial velocity,  $v_{\text{RAD},n}$ , exceeds a notional escape velocity, i.e.

$$v_{\text{RAD},n} > v_{\text{ESCAPE}} = \left( \frac{2GM_{\text{TOTAL}}}{r_n} \right)^{1/2}. \quad (37)$$

A typical value for the escape velocity at  $r = 0.1 \text{ pc}$  is  $v_{\text{ESCAPE}} \sim 0.37 \text{ km s}^{-1}$  (where we recall that, for the Rotating Setup,  $M_{\text{TOTAL}} = 1.62 M_{\odot}$ ).

Specifically, we evaluate, as a function of time, (i) the mass of the sink,  $M_{\text{SINK}}(t)$ ; (ii) the total mass carried away by all the escaping SPH particles (i.e. those that have been injected in groups of four, plus ambient SPH particles that have become entrained in the flow),

i.e.

$$M_{\text{TOTAL}}(t) = \sum_{n=1}^{n=N_{\text{TOTAL}}(t)} \{m_n\}, \quad (38)$$

where  $N_{\text{TOTAL}}(t)$  is the total number of SPH particles to date that satisfy equation (37); (iii) the total momentum carried away by the escaping SPH particles *in the outflow* (i.e. just those SPH particles that have been injected in groups of four following an accretion outburst),

$$P_{\text{OUTFLOW}}(t) = \sum_{n=1}^{n=N_{\text{OUTFLOW}}(t)} \{m_n v_{\text{RAD},n}\}, \quad (39)$$

where  $N_{\text{OUTFLOW}}(t)$  is the total number of injected SPH particles that satisfy equation (37); and (iv) the total momentum carried away by all the escaping SPH particles, i.e.

$$P_{\text{TOTAL}}(t) = \sum_{n=1}^{n=N_{\text{TOTAL}}(t)} \{m_n v_{\text{RAD},n}\}. \quad (40)$$

#### 3.1 Varying the numerical parameters

The Outflow Feedback Model involves two purely numerical parameters, the number of SPH particles representing the core,  $\mathcal{N}_{\text{CORE}}$ , and the density above which sink particles are created,  $\rho_{\text{SINK}}$ . In this section, we explore how the results change when one or other of these numerical parameters is changed from its default value (i.e. Run 6:  $\mathcal{N}_{\text{CORE}} = 10^5$ ,  $\rho_{\text{SINK}} = 10^{-10} \text{ g cm}^{-3}$ ). In each of Runs 4 through 10, (see Table 2), all the physical parameters are held at their default values:  $\theta_{\text{WIND}} = 0.4 \text{ rad}$ ,  $r_{\text{LAUNCH}} = 0.07 \text{ AU}$ ,  $\theta_{\text{JET}} = 0.01 \text{ rad}$ ,  $f_{\text{EJECT}} = 0.1$ ,  $r_{\text{MIN}} = 20 \text{ AU}$  and  $\alpha_{\text{MRI}} = 0.1$ .

##### 3.1.1 Mass resolution

In Runs 4 through 8 (Table 2), the sink creation density is held constant (at  $\rho_{\text{SINK}} = 10^{-10} \text{ g cm}^{-3}$ ) and the number of SPH particles in the core increases from  $\mathcal{N}_{\text{CORE}} \simeq 2.5 \times 10^4$  (Run 4) to  $\mathcal{N}_{\text{CORE}} \simeq 4 \times 10^5$  (Run 8). Consequently, the mass of an SPH particle,  $m_{\text{SPH}} = M_{\odot}/\mathcal{N}_{\text{CORE}}$ , decreases along this sequence from  $m_{\text{SPH}} \simeq 4 \times 10^{-5} M_{\odot}$  (Run 4) to  $m_{\text{SPH}} \simeq 2.5 \times 10^{-6} M_{\odot}$  (Run 8). The minimum mass that can be resolved is  $M_{\text{RES}} \sim 100 m_{\text{SPH}}$ , and therefore decreases from  $M_{\text{RES}} \sim 4 \times 10^{-3} M_{\odot}$  (Run 4) to  $M_{\text{RES}} \sim 2.5 \times 10^{-4} M_{\odot}$  (Run 8).

Fig. 4 shows the evolution of  $M_{\text{SINK}}(t)$  and  $M_{\text{TOTAL}}(t)$  (top left-hand panel) and  $P_{\text{OUTFLOW}}(t)$  and  $P_{\text{TOTAL}}(t)$  (bottom left-hand panel), obtained with different  $\mathcal{N}_{\text{CORE}}$ . There are some systematic changes with increasing  $\mathcal{N}_{\text{CORE}}$ , and the results are therefore not strictly converged, even at the highest  $\mathcal{N}_{\text{CORE}}$ ; in particular, the downtime between outbursts tends to be somewhat shorter with higher  $\mathcal{N}_{\text{CORE}}$ , especially at late times.

However, the overall behaviour is not strongly dependent on  $\mathcal{N}_{\text{CORE}}$ . (i) At all times, the mass of the sink particle,  $M_{\text{SINK}}(t)$  varies by less than a few per cent (see also Hubber et al. 2013). (ii) At late times ( $t \gtrsim 30 \text{ kyr}$ ), the total mass ( $M_{\text{TOTAL}}(t)$ ) and momentum ( $P_{\text{TOTAL}}(t)$ ) escaping from the core and its envelope, vary with  $\mathcal{N}_{\text{CORE}}$  (which changes by a factor of 8) by at most 20 per cent. (iii) In all the simulations, the delay between successive outburst events increases with time; this is because the mass required to trigger an outburst ( $\Delta M_{\text{MRI}}(t)$ , equation (7)) increases, and the rate at which the IAD grows ( $dM_{\text{IAD}}/dt$ ) decreases, as the inflow rate from the outer parts of the core declines.

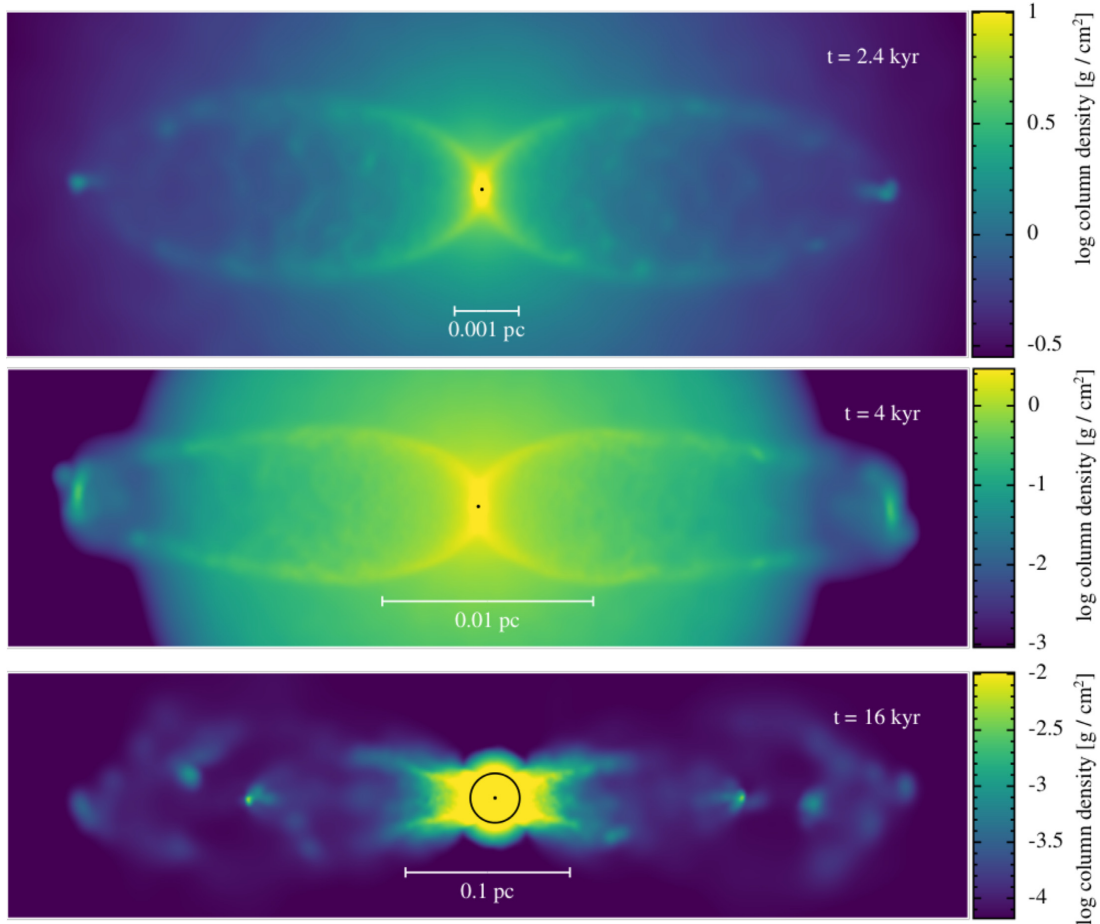


**Figure 3.** False-colour images of the column-density in run EPISODIC:400 at times  $t = 2.4$  kyr,  $t = 4$  kyr and  $t = 16$  kyr. The spatial scale increases from top to bottom, and the circle in the bottom panel shows the initial radius of the dense core (0.015 pc). The first panel shows the outflow cavity shortly after the first outflow event. In the second panel, the outflow breaks out of the dense core. Multiple bullets forming a chain of Herbig–Haro-like objects are seen in the third panel.

### 3.1.2 Sink creation

In Runs 6, 9 and 10 (see Table 2), the number of SPH particles in the core is held constant (at  $\mathcal{N}_{\text{CORE}} = 10^5$ ; hence  $m_{\text{SPH}} = 10^{-5} M_{\odot}$  and  $M_{\text{RES}} = 10^{-3} M_{\odot}$ ) and the sink creation density is decreased from  $\rho_{\text{SINK}} = 10^{-10} \text{ g cm}^{-3}$  (Run 6) through  $\rho_{\text{SINK}} = 10^{-11} \text{ g cm}^{-3}$  (Run 9) to  $\rho_{\text{SINK}} = 10^{-12} \text{ g cm}^{-3}$  (Run 10). Along this sequence, the sink radius increases from  $r_{\text{SINK}} = 0.9 \text{ AU}$  (Run 6) through  $r_{\text{SINK}} = 2.0 \text{ AU}$  (Run 9) to  $r_{\text{SINK}} = 4.3 \text{ AU}$  (Run 10).

Fig. 4 shows the evolution of  $M_{\text{SINK}}(t)$  and  $M_{\text{TOTAL}}(t)$  (top right-hand panel), and  $P_{\text{OUTFLOW}}(t)$  and  $P_{\text{TOTAL}}(t)$  (bottom right-hand panel), obtained with different  $\rho_{\text{SINK}}$ . There are some systematic changes with increasing  $\rho_{\text{SINK}}$ , and the results are therefore not strictly converged, even at the highest  $\rho_{\text{SINK}}$ . In particular, the downtime between outbursts is longer with lower  $\rho_{\text{SINK}}$ . However, the overall behaviour is not strongly dependent on  $\rho_{\text{SINK}}$ . (i) At all times, the mass of the sink particle,  $M_{\text{SINK}}(t)$  varies by less than a few per cent. (ii) In all the simulations, the downtime between successive outburst events increases with time. (iii) At late times ( $t \gtrsim 30 \text{ kyr}$ ), as  $\rho_{\text{SINK}}$  changes by a factor of 100, the total mass

escaping from the core and its envelope,  $M_{\text{TOTAL}}(t)$ , varies by at most 10 per cent; and the total momentum escaping,  $P_{\text{TOTAL}}(t)$ , by at most 20 per cent.

### 3.1.3 Synopsis

Low  $\mathcal{N}_{\text{CORE}}$  means not having to follow so many SPH particles (but at the price of coarser mass resolution), and low  $\rho_{\text{SINK}}$  means not having to follow the SPH particles to such high densities, and hence with such short timesteps (but at the price of excising the detailed dynamics at these high densities). On both counts this reduces computing requirements. Since our outburst model produces approximately converged results with low  $\mathcal{N}_{\text{CORE}}$  and low  $\rho_{\text{SINK}}$  – modulo slightly longer downtimes between outburst events – we conclude that it can be used in larger scale simulations of star formation (e.g. Clarke et al. 2017), where the computing requirements with higher  $\mathcal{N}_{\text{CORE}}$  and/or higher  $\rho_{\text{SINK}} = 10^{-10} \text{ g cm}^{-3}$  might not be feasible.

**Table 2.** Parameters for the runs performed with the Rotating Setup (Section 2.4). Reading left to right, the columns give the run number, the run ID, the feedback mechanism, the number of particles in the core ( $\mathcal{N}_{\text{CORE}}$ ), the sink formation density ( $\rho_{\text{SINK}}$ ), the wind opening angle ( $\theta_{\text{WIND}}$ ), the launching radius ( $r_{\text{LAUNCH}}$ ), the jet opening angle ( $\theta_{\text{JET}}$ ), the fraction of the gas accreted by a protostar that is ejected in bipolar outflows ( $f_{\text{EJECT}}$ ), the minimum radius at which the SPH particles representing the outflow are injected ( $r_{\text{MIN}}$ ), and the Shakura–Sunyaev viscosity parameter for MRI viscosity ( $\alpha_{\text{MRI}}$ ).

#	Run	Feedback	$\frac{\mathcal{N}_{\text{CORE}}}{10^3}$	$\frac{\rho_{\text{SINK}}}{\text{g cm}^{-3}}$	$\frac{\theta_{\text{WIND}}}{\text{radian}}$	$\frac{r_{\text{LAUNCH}}}{\text{AU}}$	$\frac{\theta_{\text{JET}}}{\text{radian}}$	$f_{\text{EJECT}}$	$\frac{r_{\text{MIN}}}{\text{AU}}$	$\alpha_{\text{MRI}}$
1	CONT:100	Continuous	100	$10^{-10}$	0.4	0.07	0.01	0.1	20	0.1
2	CONT:200	Continuous	200	$10^{-10}$	0.4	0.07	0.01	0.1	20	0.1
3	CONT:400	Continuous	400	$10^{-10}$	0.4	0.07	0.01	0.1	20	0.1
4	EPISODIC:25	Episodic	25	$10^{-10}$	0.4	0.07	0.01	0.1	20	0.1
5	EPISODIC:50	Episodic	50	$10^{-10}$	0.4	0.07	0.01	0.1	20	0.1
6	EPISODIC:100	Episodic	100	$10^{-10}$	0.4	0.07	0.01	0.1	20	0.1
7	EPISODIC:200	Episodic	200	$10^{-10}$	0.4	0.07	0.01	0.1	20	0.1
8	EPISODIC:400	Episodic	400	$10^{-10}$	0.4	0.07	0.01	0.1	20	0.1
9	RHO SINK:11	Episodic	100	$10^{-11}$	0.4	0.07	0.01	0.1	20	0.1
10	RHO SINK:12	Episodic	100	$10^{-12}$	0.4	0.07	0.01	0.1	20	0.1
11	THETA WIND:0.6	Episodic	100	$10^{-10}$	0.6	0.07	0.01	0.1	20	0.1
12	THETA WIND:0.2	Episodic	100	$10^{-10}$	0.2	0.07	0.01	0.1	20	0.1
13	RLAUNCH:14	Episodic	100	$10^{-10}$	0.4	0.14	0.01	0.1	20	0.1
14	RLAUNCH:047	Episodic	100	$10^{-10}$	0.4	0.047	0.01	0.1	20	0.1
15	THETA JET:0.05	Episodic	100	$10^{-10}$	0.4	0.07	0.05	0.1	20	0.1
16	THETA JET:0.005	Episodic	100	$10^{-10}$	0.4	0.07	0.005	0.1	20	0.1
17	FEJECT:0.2	Episodic	100	$10^{-10}$	0.4	0.07	0.01	0.2	20	0.1
18	FEJECT:0.05	Episodic	100	$10^{-10}$	0.4	0.07	0.01	0.05	20	0.1
19	RMIN:30	Episodic	100	$10^{-10}$	0.4	0.07	0.01	0.1	30	0.1
20	RMIN:10	Episodic	100	$10^{-10}$	0.4	0.07	0.01	0.1	10	0.1
21	ALPHAMRI:0.2	Episodic	100	$10^{-10}$	0.4	0.07	0.01	0.1	20	0.2
22	ALPHAMRI:0.05	Episodic	100	$10^{-10}$	0.4	0.07	0.01	0.1	20	0.05

### 3.2 Comparison between episodic and continuous outflows

Here, we compare and contrast episodic outflow feedback with continuous outflow feedback. The continuous feedback runs (Runs 1–3, Table 2) equate the accretion rate onto the protostar ( $dM_*/dt$ ) to the accretion rate onto the sink particle ( $dM_{\text{SINK}}/dt$ ) – rather than using the sub-grid model of Stamatellos, Hubber & Whitworth (2011a) and obtaining episodic accretion rate onto the protostar; we reiterate that in the episodic approach particles are only ejected during an outburst (see Section 2.3). The continuous feedback runs use  $\mathcal{N}_{\text{CORE}} \simeq 10^5$  (Run 1),  $\mathcal{N}_{\text{CORE}} \simeq 2 \times 10^5$  (Run 2), and  $\mathcal{N}_{\text{CORE}} \simeq 4 \times 10^5$  (Run 3); all other parameters have their default values. The results are compared with the episodic accretion Runs 6 and 7.

Fig. 5 shows the evolution of  $M_{\text{SINK}}(t)$  and  $M_{\text{TOTAL}}(t)$  (top panel), and  $P_{\text{OUTFLOW}}(t)$  and  $P_{\text{TOTAL}}(t)$  (bottom panel), obtained with continuous and episodic outflows. There is no evidence that the runs with continuous outflows have converged with increasing  $\mathcal{N}_{\text{CORE}}$  – particularly as regards the momentum carried away from the core (blue, , and black lines on the bottom panel of Fig. 5) – and therefore we cannot safely draw any conclusions regarding the physics of continuous outflows. The reason for non-convergence is that the continuous outflows are not properly resolved.

To be properly resolved, the SPH particles near the axis of the outflow must have neighbour-lists which contain exclusively SPH particles that are also in the outflow (and *all* SPH particles in the outflow must have neighbour-lists which contain at least a significant fraction of SPH particles that are also in the outflow). In other words, the SPH particles in the outflow must interact hydrodynamically with one another. With continuous outflow, the rate at which outflow SPH particles are launched may be so low that this requirement is not met; successively ejected outflow SPH particles may be too far apart. The SPH particles in the outflow will only interact hydrodynamically with one another if they have very low-mass, and

therefore are very numerous, specifically

$$m_{\text{SPH}} < \frac{\dot{M}_* f_{\text{EJECT}} (4\pi/3) r_{\text{MIN}}}{4 \bar{N}_{\text{NEIB}} \pi \theta_{\text{JET}}^2 v_{\text{LAUNCH}}} \quad (41)$$

$$< 7 \times 10^{-6} M_{\odot} \left( \frac{\dot{M}_*}{10^{-6} M_{\odot} \text{ yr}^{-1}} \right) \left( \frac{v_{\text{LAUNCH}}}{100 \text{ km s}^{-1}} \right)^{-1}. \quad (42)$$

To obtain the second expression, we have substituted the default values for  $f_{\text{EJECT}} = 0.1$ ,  $r_{\text{MIN}} = 20 \text{ AU}$ , and  $\theta_{\text{JET}} = 0.01 \text{ rad}$ . The factor 4 in the denominator derives from the fact that we launch outflow SPH particles in groups of four.  $\bar{N}_{\text{NEIB}}$  is the mean number of neighbours, and we have substituted  $\bar{N}_{\text{NEIB}} = 50$ . In the runs with continuous outflow,  $\dot{M}_*$  is usually much smaller than  $10^{-6} M_{\odot} \text{ yr}^{-1}$ , and the launch speed,  $v_{\text{LAUNCH}}$  is usually  $\gtrsim 100 \text{ km s}^{-1}$ . Consequently, convergence requires  $\mathcal{N}_{\text{CORE}} \gtrsim 10^6$  SPH particles per  $M_{\odot}$ .

A further issue affecting the runs with continuous outflow is that the high velocity of the launched SPH particles greatly reduces the time-step for these particles and for all those with which they interact, even indirectly – in particular, those that get entrained in the outflow early on. Even though the code uses individual particle time steps, many particles have short time steps, throughout the simulation, and hence the computing requirements are very demanding. In contrast, the runs with episodic outflow only require these short timesteps for brief periods during and immediately after an outburst.

### 3.3 Varying the physical parameters

The Outflow Feedback Model involves six physical parameters, and their values are poorly constrained by observation or theory. In this section, we explore how the results change when these parameters are increased or decreased from their default values (i.e. those in the fiducial Run 6, EPISODIC:100:  $\theta_{\text{WIND}} = 0.4 \text{ rad}$ ,  $r_{\text{LAUNCH}} = 0.07 \text{ AU}$ ,

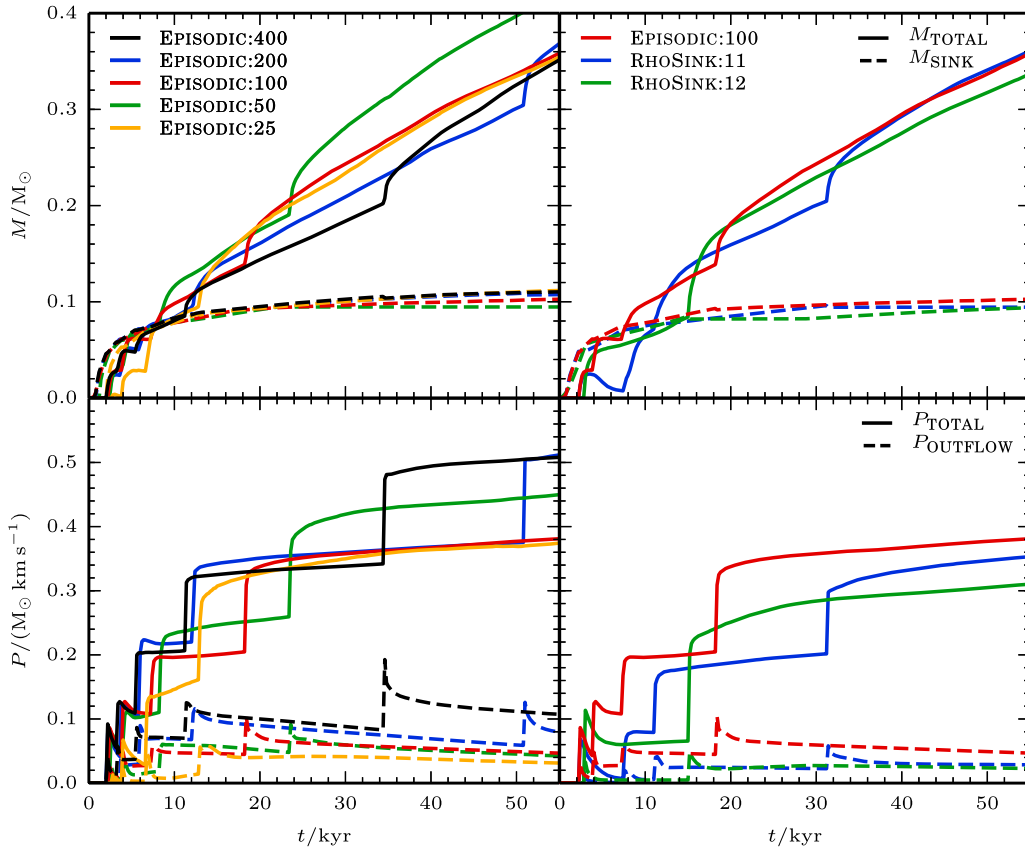


**Figure 4.** The top panels display the evolution of the sink mass ( $M_{\text{SINK}}(t)$ , dashed lines) and the total mass carried away by all the escaping SPH particles ( $M_{\text{TOTAL}}(t)$ , solid lines). The bottom panels display the evolution of the momentum carried away by the escaping outflow SPH particles alone ( $P_{\text{OUTFLOW}}(t)$ , dashed lines), and by all the escaping SPH particles (i.e. including ambient SPH particles entrained in the flow;  $P_{\text{TOTAL}}(t)$ , solid lines). The left-hand panels show the results obtained with different numbers of SPH particles, and hence different mass-resolution, viz. ( $\mathcal{N}_{\text{CORE}} \cdot M_{\text{RES}}$ ) = ( $2.5 \times 10^4, 4 \times 10^{-3} M_{\odot}$ ), yellow; ( $5 \times 10^4, 2 \times 10^{-3} M_{\odot}$ ), green; ( $10^5, 10^{-3} M_{\odot}$ ), red; ( $2 \times 10^5, 5 \times 10^{-4} M_{\odot}$ ), blue; ( $4 \times 10^5, 2.5 \times 10^{-4} M_{\odot}$ ), black – corresponding to Runs 4, 5, 6, 7, and 8, respectively. The right-hand panels show the results obtained with different sink creation densities,  $\rho_{\text{SINK}} = 10^{-10} \text{ g cm}^{-3}$ , red;  $10^{-11} \text{ g cm}^{-3}$ , blue;  $10^{-12} \text{ g cm}^{-3}$ , green – corresponding to Runs 6, 9, and 10, respectively.

$\theta_{\text{JET}} = 0.01 \text{ rad}$ ,  $f_{\text{EJECT}} = 0.1$ ,  $r_{\text{MIN}} = 20 \text{ AU}$ , and  $\alpha_{\text{MRI}} = 0.1$ ). In each of Runs 11 through 22 (see Table 2), only one physical parameter is changed from its default value, and the numerical parameters are held at their default values, i.e.  $\mathcal{N}_{\text{CORE}} = 10^5$  (hence  $m_{\text{SPH}} = 10^{-5} M_{\odot}$  and  $M_{\text{RES}} = 10^{-3} M_{\odot}$ ) and  $\rho_{\text{SINK}} = 10^{-10} \text{ g cm}^{-3}$ .

### 3.3.1 The wind opening angle, $\theta_{\text{WIND}}$

We consider three wind opening angles,  $\theta_{\text{WIND}} = 0.6 \text{ radian}$  (Run 11),  $0.4 \text{ radian}$  (fiducial Run 6) and  $0.2 \text{ radian}$  (Run 12); the evolution of  $M_{\text{SINK}}(t)$  and  $M_{\text{TOTAL}}(t)$  is shown in the top left-hand panel of Fig. 6, and the evolution of  $P_{\text{OUTFLOW}}(t)$  and  $P_{\text{TOTAL}}(t)$  in the top left-hand panel of Fig. 7. If we analyse the results at the end of the simulation,  $t_{\text{END}}$ , then, as  $\theta_{\text{WIND}}$  is decreased from  $0.6 \text{ radian}$  to  $0.2 \text{ radian}$  (i.e. by a factor of 3), there is very little change in  $M_{\text{SINK}}(t_{\text{END}})$  ( $\lesssim 1$  per cent), but the amount of mass escaping,  $M_{\text{TOTAL}}(t_{\text{END}})$ , has increased by  $\sim 25$  per cent; and the amount of momentum escaping,  $P_{\text{TOTAL}}(t_{\text{END}})$ , has increased by  $\sim 100$  per cent. This seemingly counterintuitive result arises because it is the relatively fast narrow jet, rather than the relatively slow wide-angle wind, that does most of

the damage to the core; as  $\theta_{\text{WIND}}$  is decreased, an increasing fraction of the outflow is concentrated in the jet.

### 3.3.2 The launch radius, $r_{\text{LAUNCH}}$

We consider three launch radii,  $r_{\text{LAUNCH}} = 0.14 \text{ AU}$  (Run 13),  $0.07 \text{ AU}$  (fiducial Run 6), and  $0.047 \text{ AU}$  (Run 14; this last value fits the observations of Lee et al. (2017)). The evolution of  $M_{\text{SINK}}(t)$  and  $M_{\text{TOTAL}}(t)$  is shown in the top right-hand panel of Fig. 6, and the evolution of  $P_{\text{OUTFLOW}}(t)$  and  $P_{\text{TOTAL}}(t)$  in the top right-hand panel of Fig. 7. Smaller values of  $r_{\text{LAUNCH}}$  equate to higher outflow velocities (see equation (16)), and consequently, all other things being equal, more vigorous feedback. However, as  $r_{\text{LAUNCH}}$  is decreased, the outburst frequency decreases and the downtime between outbursts lengthens; since outbursts produce abrupt changes in  $M_{\text{TOTAL}}$  and  $P_{\text{TOTAL}}$ , this makes quantitative comparison difficult. If we make the comparison at  $\sim 32 \text{ kyr}$ , when all three runs have experienced the same number of outbursts, then, as  $r_{\text{LAUNCH}}$  is decreased from  $0.14 \text{ AU}$  to  $0.047 \text{ AU}$  (i.e. by a factor of 3),  $M_{\text{SINK}}$  decreases by  $\sim 21$  per cent,  $M_{\text{TOTAL}}$  increases by  $\sim 56$  per cent, and  $P_{\text{TOTAL}}$  increases by  $\sim 81$  per cent. By the end of the simulation,

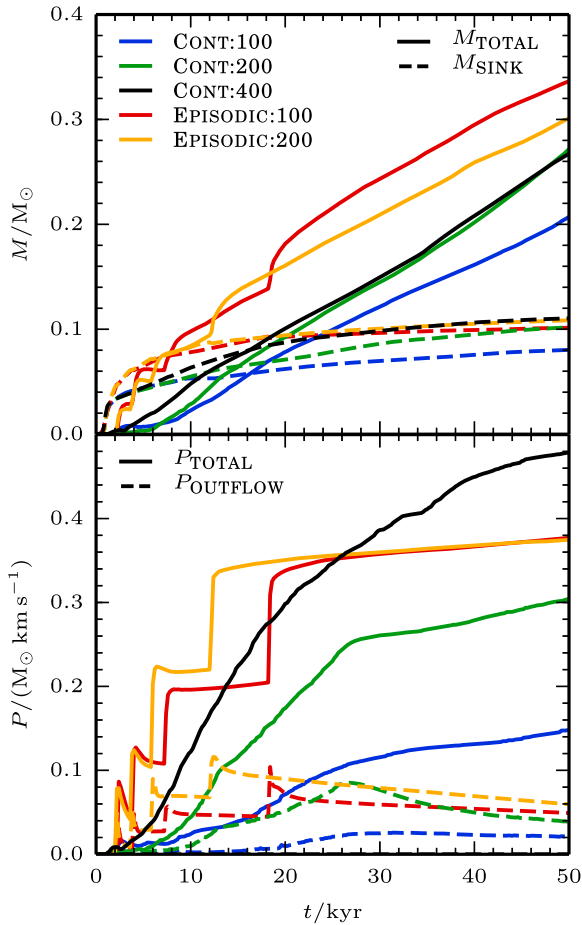


**Figure 5.** As Fig. 4, but for Run 1 (CONT:100; blue), Run 2 (CONT:200; green), Run 3 (CONT:400; black), Run 6 (EPISODIC:100; red), and Run 7 (EPISODIC:200; yellow), comparing and contrasting episodic and continuous outflow feedback.

at  $\sim 50$  kyr, Run 13 (with  $r_{\text{LAUNCH}} = 0.14$  AU) has experienced one more outburst than the other two runs, and the increases in  $M_{\text{TOTAL}}$  and  $P_{\text{TOTAL}}$  are reduced to 28 per cent and 23 per cent respectively; the decrease in  $M_{\text{SINK}}$  is still  $\sim 21$  per cent. We conclude that reducing  $r_{\text{LAUNCH}}$  by a factor of 3 reduces the rate at which  $M_{\text{SINK}}$  grows by 21 per cent, and increases the rate at which mass and momentum escape by  $42 \pm 14$  per cent and  $52 \pm 29$  per cent, respectively, with the uncertainty deriving from when the comparison is made and how many outbursts there have been.

### 3.3.3 The jet opening angle, $\theta_{\text{JET}}$

We consider three jet opening angles,  $\theta_{\text{JET}} = 0.05$  radian (Run 15; this is the maximum suggested by Matzner & McKee (1999)), 0.01 radian (fiducial Run 6) and 0.005 radian (Run 16). The evolution of  $M_{\text{SINK}}(t)$  and  $M_{\text{TOTAL}}(t)$  is shown in the middle left-hand panel of Fig. 6, and the evolution of  $P_{\text{OUTFLOW}}(t)$  and  $P_{\text{TOTAL}}(t)$  in the middle left-hand panel of Fig. 7. Smaller values of  $\theta_{\text{JET}}$  correspond to more tightly collimated, faster jets (see equations (13) and (16), and Fig. 1), which are slightly more effective in reducing the rate of growth of the sink (lower  $M_{\text{SINK}}$ ), and slightly more effective

in dispersing the core (larger  $M_{\text{TOTAL}}$  and  $P_{\text{TOTAL}}$ ). Specifically, if we make the comparison at the end of the simulations ( $\sim 50$  kyr), then, as  $\theta_{\text{JET}}$  is reduced from 0.05 radian to 0.005 radian (i.e. by a factor of 10),  $M_{\text{SINK}}$  decreases by  $\sim 7$  per cent,  $M_{\text{TOTAL}}$  increases by  $\sim 15$  per cent, and  $P_{\text{TOTAL}}$  increases by  $\sim 19$  per cent. The timing of outbursts is also not very sensitive to  $\theta_{\text{JET}}$ , and we conclude that  $\theta_{\text{JET}}$  is not a very critical parameter

### 3.3.4 The ejection fraction, $f_{\text{EJECT}}$

We consider three ejection fractions,  $f_{\text{EJECT}} = 0.2$  (Run 17), 0.1 (fiducial Run 6), and 0.05 (Run 18). The evolution of  $M_{\text{SINK}}(t)$  and  $M_{\text{TOTAL}}(t)$  is shown in the middle right-hand panel of Fig. 6, and the evolution of  $P_{\text{OUTFLOW}}(t)$  and  $P_{\text{TOTAL}}(t)$  in the middle right-hand panel of Fig. 7. If  $f_{\text{EJECT}}$  is reduced, the sink grows faster, the amount of mass and momentum escaping from the core goes down, and there are longer downtimes between outbursts. If we make the comparison at the end of the simulations ( $\sim 50$  kyr), then, as  $f_{\text{EJECT}}$  is reduced from 0.2 to 0.05 (i.e. by a factor of 4),  $M_{\text{SINK}}$  increases by  $\sim 38$  per cent,  $M_{\text{TOTAL}}$  decreases by  $\sim 23$  per cent, and  $P_{\text{TOTAL}}$  decreases by  $\sim 52$  per cent. We conclude that  $f_{\text{EJECT}}$  is a mildly critical parameter.

### 3.3.5 The minimum injection radius, $r_{\text{MIN}}$

We consider three minimum injection radii,  $r_{\text{MIN}} = 30$  AU (Run 19), 20 AU (fiducial Run 6), and 10 AU (Run 20). The evolution of  $M_{\text{SINK}}(t)$  and  $M_{\text{TOTAL}}(t)$  is shown in the bottom left-hand panel of Fig. 6, and the evolution of  $P_{\text{OUTFLOW}}(t)$  and  $P_{\text{TOTAL}}(t)$  in the bottom left-hand panel of Fig. 7. Reducing  $r_{\text{MIN}}$  from 30 AU to 10 AU (i.e. by a factor of 3) has very little effect, apart from increasing the downtime between outbursts; at the end of the simulations ( $\sim 50$  kyr)  $M_{\text{SINK}}$ ,  $M_{\text{TOTAL}}$  and  $P_{\text{TOTAL}}$  all differ by at most  $\sim 5$  per cent. We conclude that  $r_{\text{MIN}}$  is not a critical parameter.

### 3.3.6 The Shakura–Sunyayev viscosity parameter, $\alpha_{\text{MRI}}$

We consider three Shakura–Sunyayev viscosity parameters,  $\alpha_{\text{MRI}} = 0.2$  (Run 21), 0.1 (fiducial Run 6), and 0.05 (Run 22). The evolution of  $M_{\text{SINK}}(t)$  and  $M_{\text{TOTAL}}(t)$  is shown in the bottom right-hand panel of Fig. 6, and the evolution of  $P_{\text{OUTFLOW}}(t)$  and  $P_{\text{TOTAL}}(t)$  in the bottom right-hand panel of Fig. 7. In the Stamatellos et al. (2012) prescription for episodic accretion,  $\alpha_{\text{MRI}}$  controls the accretion rate from the IAD onto the protostar during an outburst. Reducing  $\alpha_{\text{MRI}}$  leads to longer, but less intense, outbursts, and the net effect is rather small. If we make the comparison at the end of the simulations ( $\sim 50$  kyr), then, as  $\alpha_{\text{MRI}}$  is reduced from 0.2 to 0.05 (i.e. by a factor of 4),  $M_{\text{SINK}}$  increases by  $< 2$  per cent,  $M_{\text{TOTAL}}$  by  $< 6$  per cent, and  $P_{\text{TOTAL}}$  by  $< 16$  per cent. We conclude that  $\alpha_{\text{MRI}}$  is not a critical parameter.

### 3.3.7 Self-regulated outflow feedback

The most critical physical parameters appear to be  $\theta_{\text{WIND}}$  (because it influences the extent to which the outflow is concentrated in the jet),  $r_{\text{LAUNCH}}$  (because it influences the velocity at which the outflow is launched) and  $f_{\text{EJECT}}$  (because it influences the amount of mass going into the outflow). Furthermore, the quantity that is most sensitive to these parameters is  $P_{\text{TOTAL}}$ , and  $M_{\text{SINK}}$  is least sensitive. However,

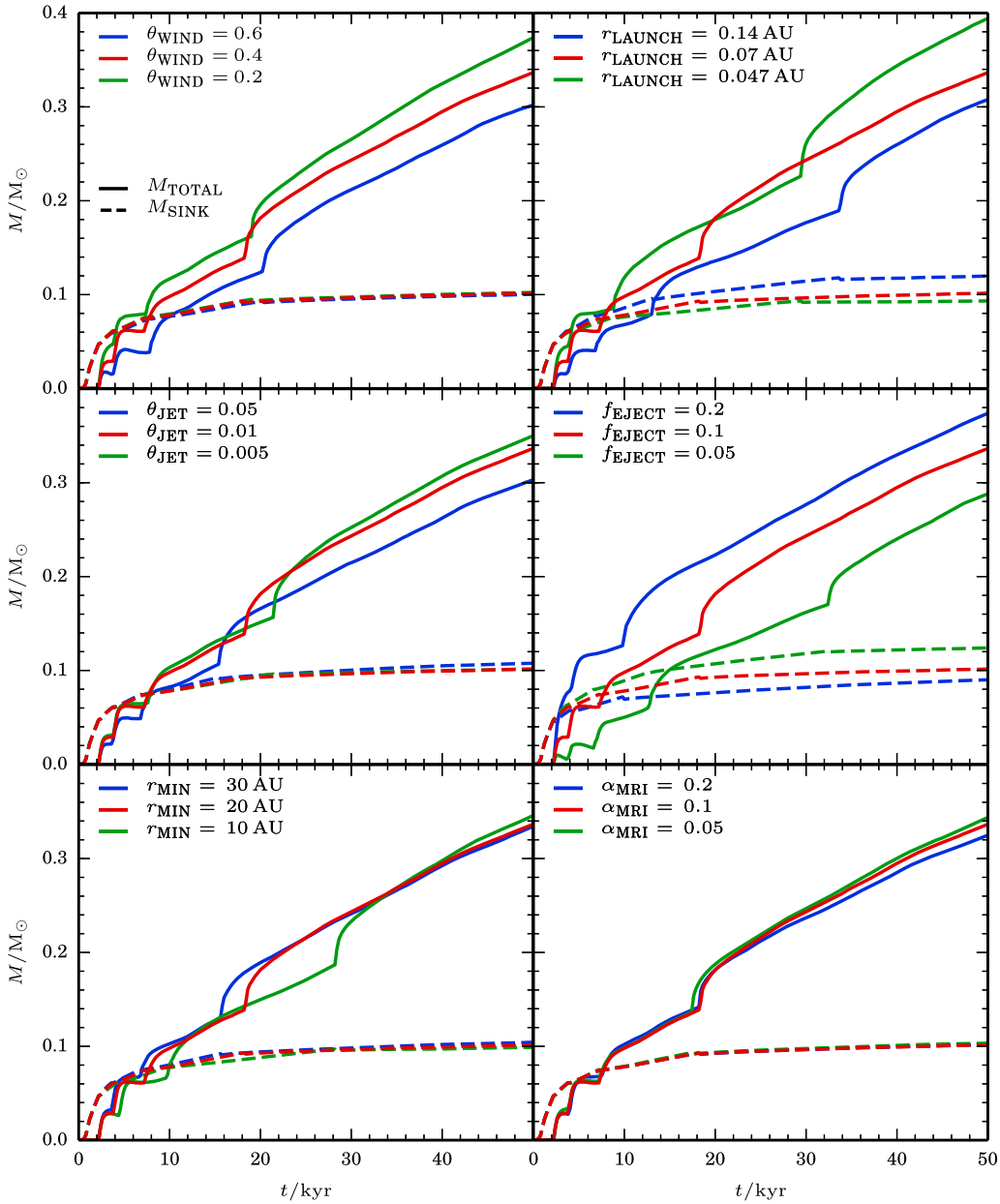


**Figure 6.** The evolution of the sink mass ( $M_{\text{SINK}}(t)$ , dashed lines) and the total mass carried away by all the escaping SPH particles ( $M_{\text{TOTAL}}(t)$ , solid lines), for different values of the model parameters. *Top left:* the wind opening angle,  $\theta_{\text{WIND}} = 0.2$  radian, 0.4 radian (default) and 0.6 radian. *Top right:* the launch radius,  $r_{\text{LAUNCH}} = 0.047$  AU, 0.07 AU (default), and 0.14 AU. *Middle left:* the jet opening angle,  $\theta_{\text{JET}} = 0.005$  radian, 0.01 radian (default), and 0.05 radian. *Middle right:* the ejected fraction,  $f_{\text{EJECT}} = 0.05, 0.1$  (default), and 0.2. *Bottom left:* the minimum injection radius,  $r_{\text{MIN}} = 10$  AU, 20 AU (default) and 30 AU. *Bottom right:* the Shakura–Sunayev viscosity parameter,  $\alpha_{\text{MRI}} = 0.05, 0.1$  (default), and 0.2.

all the dependences are ‘sub-linear’. For example, the three most extreme dependences are

$$\frac{d \ln(P_{\text{TOTAL}})}{d \ln(\theta_{\text{WIND}})} \sim -0.63, \quad (43)$$

$$-0.54 \lesssim \frac{d \ln(P_{\text{TOTAL}})}{d \ln(r_{\text{LAUNCH}})} \lesssim -0.19, \quad (44)$$

$$-0.40 \lesssim \frac{d \ln(M_{\text{TOTAL}})}{d \ln(r_{\text{LAUNCH}})} \lesssim -0.22. \quad (45)$$

The basic reason for these rather weak dependences is a self-regulation mechanism. In runs with parameters that reduce the impact of the outflow on the core, the sink is able to accrete faster, leading to more frequent outbursts, and shorter downtimes between

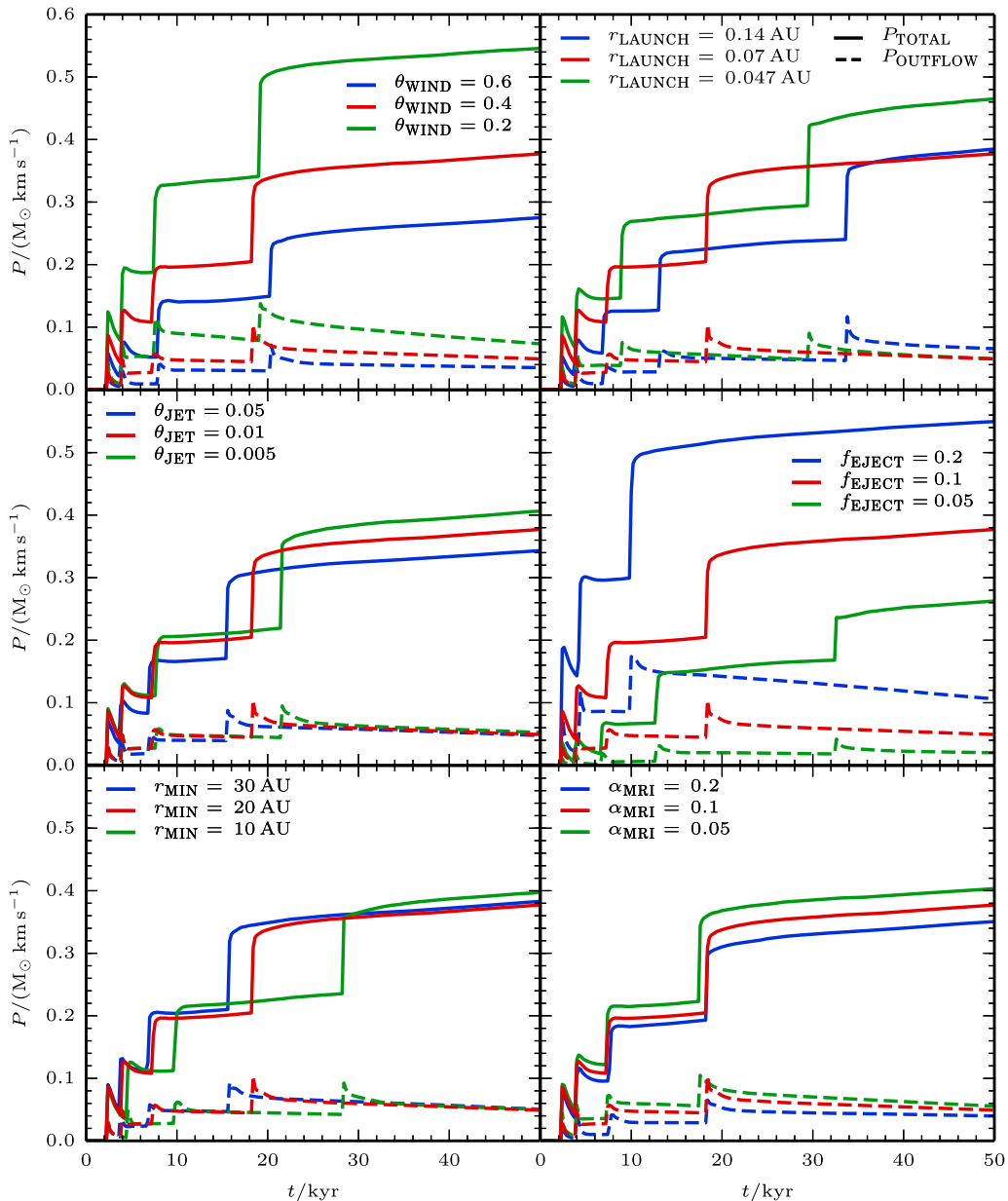


**Figure 7.** As Fig. 6 but for the evolution of the momentum carried away by the escaping outflow SPH particles alone ( $P_{\text{OUTFLOW}}(t)$ , dashed lines), and by all the escaping SPH particles (i.e. including ambient SPH particles entrained in the flow;  $P_{\text{TOTAL}}(t)$ , solid lines).

outbursts. We conclude that using the default parameter values will not significantly affect our main findings.

#### 4 THE TURBULENT SETUP

In order to illustrate a more realistic situation, Fig. 8 shows column-density images from a run with the Turbulent Setup (see Section 2.4). All parameters for the Episodic Accretion Model (Section 2.2) and the Outflow Feedback Model (Section 2.3) are the same as in the Rotating Setup fiducial Run 6 (see Table 2). A single protostar forms at  $\sim 90$  kyr with a final mass of  $M_* = 0.45 M_{\odot}$ . Its

accretion ceases at  $\sim 180$  kyr since by this stage most of the gas has either been accreted or dispersed. The simulation is finally stopped at  $\sim 230$  kyr.

The protostar launches outflow bullets labelled  $A_{L/R}$  through  $E_{L/R}$  corresponding to the left and right outflow lobe. In the remainder of the paper, we will only refer to the left lobe and therefore we drop the subscript L henceforth. The outflow bullets form an S-shaped chain of Herbig–Haro objects. The S-shape is due to the varying orientation of the angular momentum,  $L_{\text{IAD}}$ , caused by anisotropic accretion onto the IAD from core (Ybarra et al. 2006; Wu, Takakuwa & Lim 2009; Zhang et al. 2013; Frank et al. 2014).

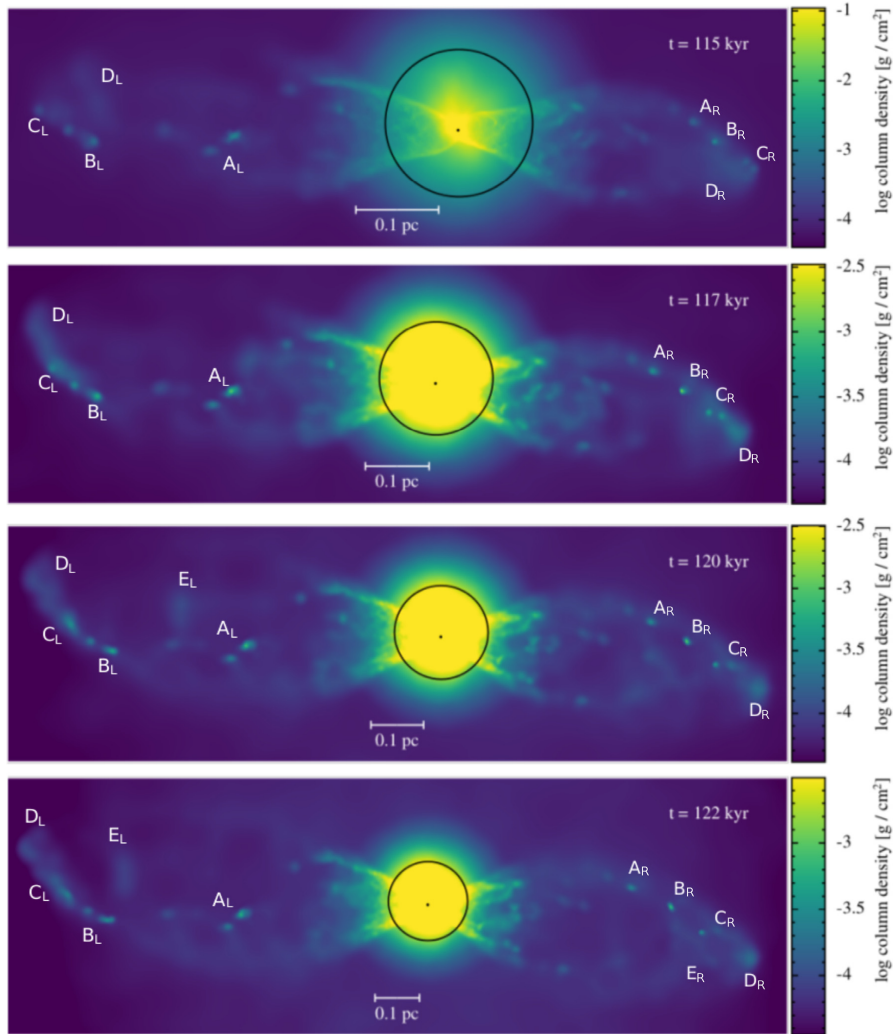


**Figure 8.** Column density images of the Turbulent Setup, at  $t = 115$ ,  $117$ ,  $120$  and  $122$  kyr. The circle indicates the initial radius of the core, and the viewing angle is chosen so that the outflow axis is approximately horizontal. The bullets are labelled  $A_{L/R}$  through  $E_{L/R}$  for the corresponding left and right lobe, in order of increasing age (see Fig. 9). The time series, from top to bottom, shows the end of a cycle of a bullet, here bullet  $D_L$ , when it hits the leading shock front. Bullet  $D_L$  hits the leading shock front with high velocity, overtakes the older bullets and decelerates. In the last panel, the newly ejected bullet  $E_L$  is in a comparable position as former bullet  $D_L$  in the first frame.

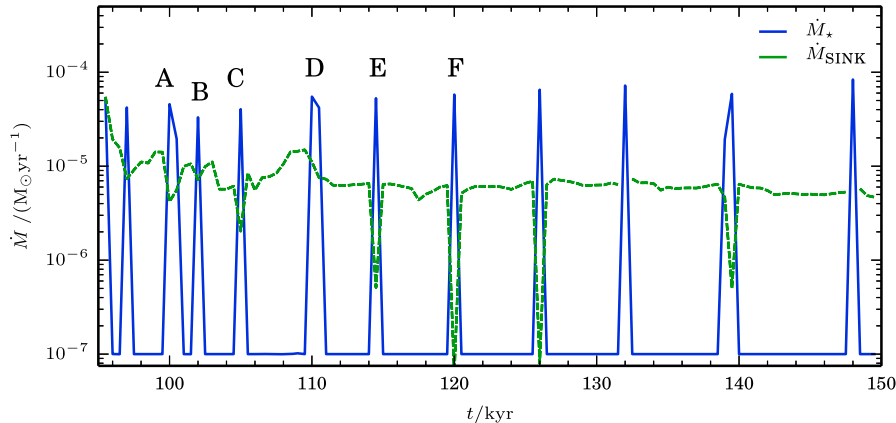
The first two bullets interact with the collapsing dense core material and are thus not visible in Fig. 8. The timespan from 115 kyr to 122 kyr is chosen to capture the end of a cycle of an outflow bullet, here bullet D, when it hits the leading shock front. This cycle happens in a similar fashion for all other bullets, except the first bullet A. This is the first bullet that breaks out of the core and survives as a coherent structure. Bullets B and C have higher velocity and have overtaken A. Bullet D starts off faster still, and by the final frame it has overtaken all the others and hit the leading shock, where it is slowed down. Bullet E is even faster, but by the final frame it has not yet caught up with D and is in a similar position as former bullet D in the first frame. A sixth bullet has been launched, but is still inside the core, and therefore can not be seen on Fig. 8.

Fig. 9 shows the accretion rates onto the sink,  $\dot{M}_{\text{SINK}}$  and onto the protostar,  $\dot{M}_*$ , between  $t = 90$  kyr (when the protostar forms) and

$t = 150$  kyr.  $\dot{M}_{\text{SINK}}$  is relatively constant, between  $\sim 2 \times 10^{-5}$  and  $\sim 5 \times 10^{-6} M_{\odot} \text{ yr}^{-1}$ . The accretion rate tends to decrease over time. It drops briefly, following an outburst, because the outburst heats the accretion disc (cf. Lomax et al. 2014, 2015). The accretion rate of the protostar is low in the quiescent phase,  $\dot{M}_* = 10^{-7} M_{\odot} \text{ yr}^{-1}$ , but approaches  $10^{-3} M_{\odot} \text{ yr}^{-1}$  during an outburst. Note that the time resolution in Fig. 9 is too coarse to resolve the very short outbursts. The downtime between outbursts is  $\sim 4000 \pm 2000$  yr and the duration of an outburst is  $\sim 40 \pm 20$  yr (Stamatellos et al. 2007, 2011b).

#### 4.1 Position–velocity diagrams

In order to determine whether the simulated outflow reproduces the ‘Hubble-Law’ relation, and individual ‘Hubble Wedges’, as observed, for example, by Bachiller et al. (1990); Arce & Goodman



**Figure 9.** Evolution of the accretion rates onto the sink particle,  $\dot{M}_{\text{SINK}}(t)$  (green), and the protostar,  $\dot{M}_*(t)$  (blue). The labels, A–F, correspond to the outflow bullets formed in the individual outbursts (see Figs. 8 and 10). Note that the time resolution in this figure is too coarse to fully resolve the very short outbursts.

(2001); Tafalla et al. (2004); Santiago-García et al. (2009); Wang et al. (2014), we construct PV-diagrams, i.e. false-colour plots of

$$\Delta M_{\text{PIXEL}} = \frac{d^2M}{dr dv_{\text{RAD}}} \Delta r \Delta v_{\text{RAD}} \quad (46)$$

on the  $(r, v_{\text{RAD}})$  plane. Here,  $r$  is radial distance, and  $v_{\text{RAD}}$  is radial velocity, both measured from the centre of mass. For the velocity axis we take 180 bins with a width of  $\Delta v_{\text{RAD}} = 0.56 \text{ km s}^{-1}$ . For the spatial axis, we take 180 spherically symmetric shells around the centre of mass with a width of  $\Delta r = 0.0056 \text{ pc}$  and consider only particles with radial outflow velocities larger than the escape velocity (equation (37)). Note that in this case  $M_{\text{TOTAL}} = 3.9 M_{\odot}$ , so the escape velocity at 0.1 pc is  $0.58 \text{ km s}^{-1}$ . This effectively constrains our analysis to the outflow cones. As a final step, we use a kernel density estimator to compute  $\Delta M_{\text{PIXEL}}$ , with a smoothing length obtained using “Scott’s Rule” (Scott 1992).

Fig. 10 (right-hand side) shows PV diagrams for the left lobe of the outflow at the same times as shown on Fig. 8. Features associated with the individual bullets are marked A, B, C, etc., in both figures.

The PV-diagram at 115 kyr is shown in the top right-hand panel of Fig. 10. At this stage, bullets A, B, and C define the Hubble Law. The oldest bullet, A, moves slowest, at  $\sim 25 \text{ km s}^{-1}$  and has only reached  $\sim 0.3 \text{ pc}$ . Bullets B and C appear merged, but are in fact kinematically separate. B moves outwards faster than A, at  $\sim 30 \text{ km s}^{-1}$ , and has reached  $\sim 0.46 \text{ pc}$ . C moves outwards faster than B, at  $\sim 40 \text{ km s}^{-1}$ , and has reached  $\sim 0.52 \text{ pc}$ . Bullet D moves outwards at  $\sim 80 \text{ km s}^{-1}$ , but has only been going for  $\sim 6 \text{ kyr}$ , so it has not yet hit the leading shock and been decelerated. Bullet E has only just been launched, within the last  $\sim 1 \text{ kyr}$ ; the outburst at  $\sim 114 \text{ kyr}$  that launches E can be seen on Fig. 9.

At subsequent times (reading down the right-hand column of Fig. 10: 117 kyr, 120 kyr, and 122 kyr) we see Bullet D decelerate and line up with the Hubble Law; Bullet E start to hit the leading shock and decelerate, and the launch of Bullet F; the outburst at  $\sim 120 \text{ kyr}$  that launches F can be seen on Fig. 9. These results are very similar to the 350 GHz continuum and CO  $J = 3 - 2$  observations of the outflow from IRAS 04166 + 2706 reported by Wang et al. (2014). They find numerous high-velocity outflow bullets, which slowly decelerate as they move outwards.

## 4.2 Mass–velocity Relation

The left-hand panels of Fig. 10 show MV-diagrams for the left lobe of the simulated outflow, i.e. plots of

$$\Delta M = \frac{dM}{dv_{\text{RAD}}} \Delta v_{\text{RAD}} \quad (47)$$

against  $v_{\text{RAD}}$ , at the same times as the PV-diagrams in the right-hand panels. Each point represents the mass in a radial velocity interval  $\Delta v_{\text{RAD}} = 2 \text{ km s}^{-1}$ , and only points that correspond to  $\geq 22$  SPH articles ( $\geq 10^{-4} M_{\odot}$ ) are considered. At low velocities,  $v_{\text{RAD}} \lesssim 80 \text{ km s}^{-1}$ , the plots can be fitted well with a single shallow power-law,

$$\frac{dM}{dv_{\text{RAD}}} \propto v_{\text{RAD}}^{-\gamma}, \quad (48)$$

with  $\gamma \simeq 1.5$ , in good agreement with observed and simulated values (Kuiper et al. 1981; Lada & Fich 1996; Bachiller & Tafalla 1999; Richer et al. 2000; Keegan & Downes 2005; Arce et al. 2007; Liu et al. 2017; Li et al. 2018).

Some observers have reported a knee, at high velocities, above which the slope abruptly becomes much steeper. We find no evidence for this, possibly because our simulation is unable to resolve the small amounts of mass involved.

On the MV diagram, the bullets are manifest as small local peaks. The oldest bullet, A, has the lowest velocity, and the youngest bullet, F, has the highest. There are two reasons for this. (a) The protostellar mass,  $M_*(t)$  increases, and so the later bullets are launched at higher velocity (see equation (16)). (b) The later bullets encounter less resistance because earlier bullets have cleared the way for them.

## 5 DISCUSSION

Using our new model, we are able to simulate the collapse of a core to form a protostar, and the role of episodic accretion and outflow in regulating the growth of the protostar and launching high-velocity bullets into the surroundings. This produces kinematic features that mimic the Hubble Law and Hubble Wedge features seen in real star-forming cores with outflows, and allows us to connect these features in an evolutionary sequence. The bullets launched later have higher velocities, up to  $\sim 120 \text{ km s}^{-1}$ ; this is basically because the mass of the protostar increases, and hence the escape speed from its locality

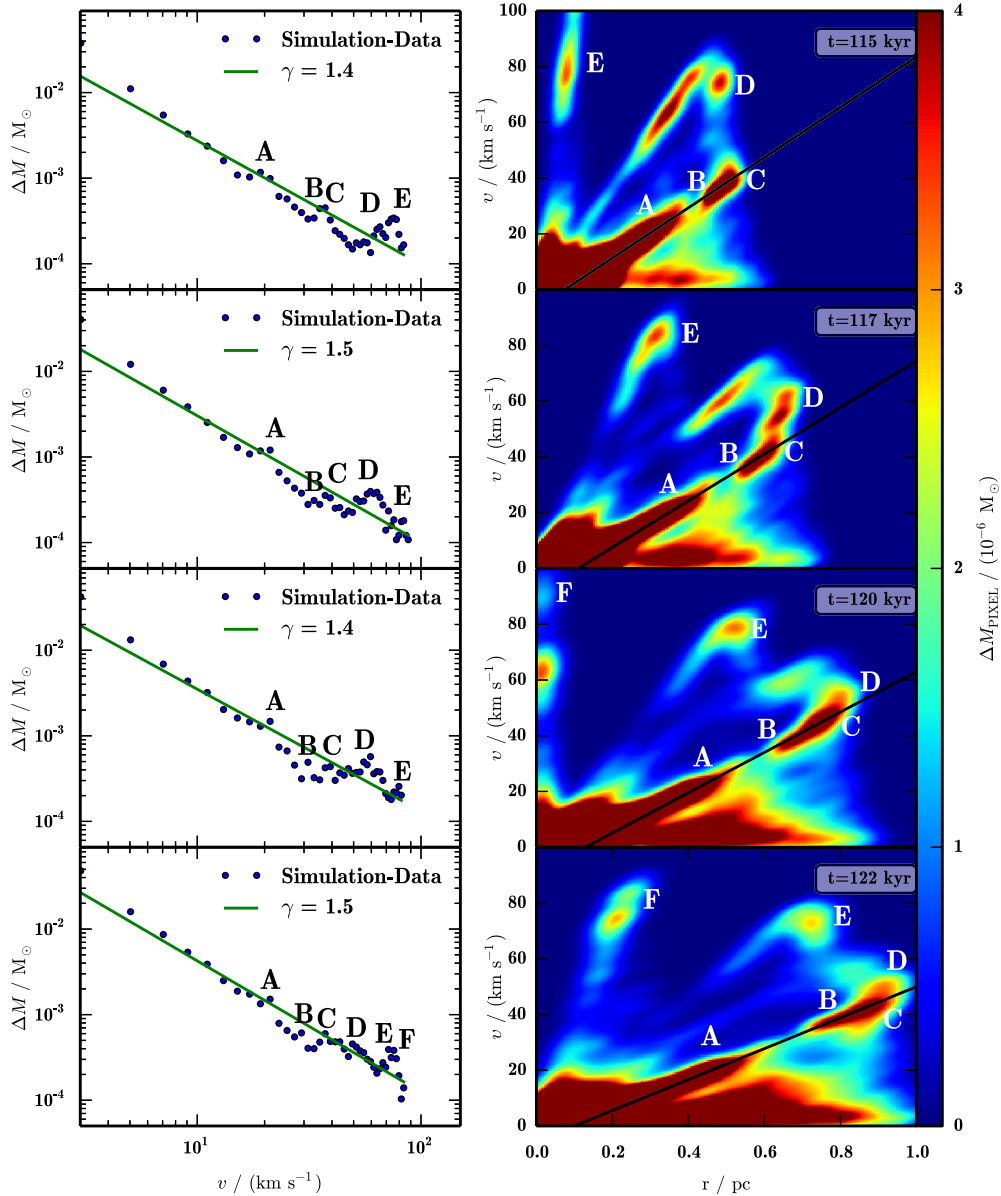


**Figure 10.** MV- and PV-diagrams for the lefthand outflow lobe, at the same four times illustrated in Fig. 8, and using the same labels (A through F) to identify features associated with the individual bullets. *Left Panels:* MV-diagrams showing power-law behaviour with slope  $\gamma \sim 1.5$ . The locations of individual bullets are marked by small jumps on this plot. *Right panels:* PV-diagram. The black line shows the best-fit Hubble law ( $v_{\text{RAD}} \sim v_0 + v'_0 r$ ), and marks the location of bullets that have already been decelerated at the leading shock; those bullets that have not yet been decelerated lie above this line.

increases. They are also launched into a cavity that has been cleared out by earlier bullets (Wang et al. 2014), and therefore they tend to travel further before they run into the ambient medium and are decelerated. As a result the later bullets leave wakes pointing back towards the star – these are the Hubble Wedges – and the earlier bullets define an approximately linear Hubble-like velocity field. In our simulations, the individual outflow events also produce bumps in the MV relation that are similar to those observed by Qiu & Zhang (2009)

The main difference between the prescriptions for ejection used by e.g. Federrath et al. 2014; Offner & Arce 2014; Offner & Chabran 2017 and our model is such that the ejection rate is not determined directly by the accretion rate onto the sink, but by the accretion rate onto the central protostar within the sink, and this rate is moderated by an episodic cycle. Nonetheless, like Federrath et al. (2014) we find that the feedback is self-regulated, in the sense that the outflow properties do not depend strongly on the ejection fraction  $f_{\text{EJECT}}$ .

By varying  $\theta_{\text{JET}}$  we find, like Offner & Arce (2014), that even highly collimated jets are able to entrain large fractions of gas. In contrast to their turbulent simulation, we find a significant precession of the outflow, leading to an S-shaped chain of Herbig–Haro objects. Compared with Federrath et al. (2014) and Offner & Chaban (2017) we find a much higher ratio of entrained to ejected gas,  $\sim 30$ , because we eject gas at higher velocities of up to  $120 \text{ km s}^{-1}$ . This also explains our lower star formation efficiency, of only  $\sim 10$  per cent.

We note the following shortcomings of our Outflow Feedback Model. Unlike Offner & Chaban (2017), we do not use a stellar evolution model, and therefore we have to invoke a somewhat more arbitrary prescription for the outflow velocity, and for the amount of angular momentum that is carried away by the outflow; specifically, we assume a constant fraction of the angular momentum is removed (Herbst et al. 2007; Bouvier et al. 2014). A stellar evolution model would also improve the treatment of radiative feedback from the protostar – in the sense that the current treatment probably underestimates the protostellar luminosity between outbursts – and we are planning to include the protostellar model of Offner & Chaban (2017) in a follow-up paper (Rohde, Walch & Seifried).

In addition, although the treatment of radiation transport (Stamatellos et al. 2007, 2011b) appears to work reasonably well in the context of collapsing cores, and even accretion disks, it is unlikely to work so well in the walls of the outflow cavity (Kuiper, Turner & Yorke 2016). However, since we are simulating the formation of low mass stars, the effects of radiation are expected to be small compared with the outflow feedback.

Finally, the role of the magnetic field is implicit in the model for accretion onto the protostar and the outflow launching prescription, but its effect on the dynamics of core collapse and the interaction between the core and the outflow is ignored here, and could be significant (Commerçon et al. 2010; Seifried et al. 2012; Wurster, Price & Bate 2016; Wurster, Bate & Price 2018).

In future work, we will use the model presented in this paper to study the influence of episodic outflow feedback on the star formation efficiency and the shape of the stellar initial mass function. With higher resolution, we will be able to study the high-velocity tail of the PV-diagram, which is not resolved in the simulations presented in this study. These high-resolution simulations will also enable us to examine the rotational properties of outflow bullets, and to compare them with the observations of e.g. Launhardt et al. (2009), Chen et al. (2016), Lee et al. (2017), and Tabone et al. (2017).

## 6 CONCLUSION

Recent studies of outflows from young, low-mass protostars suggest that their accretion and outflows are episodic. Our newly developed sub-grid outflow model for SPH takes this episodic behaviour into account. Besides the benefits of a more realistic outflow model, episodicity actually decreases the mass-resolution needed to properly model the outflow (because the gas is denser in an outflow burst than in a continuous outflow), and at the same time reduces the computation required (because the outflow particles are launched in short outbursts).

We explore the effect of episodic accretion and outflow from a protostar formed at the centre of an initially static, rigidly rotating, spherically symmetric core with  $\rho \propto r^{-2}$ . We show that key properties like the rate of growth of the protostar, and the net mass and momentum carried away by the outflow, are only weakly dependent on numerical parameters. In particular, reliable results can probably

be obtained with quite low mass-resolution ( $m_{\text{SPH}} \sim 2 \times 10^{-5} M_{\odot}$ ) and low sink creation density ( $\rho_{\text{SINK}} \sim 10^{-12} \text{ g cm}^{-3}$ ). The rate of growth of the protostar, and the net mass and momentum carried away by the outflow, are also rather weakly dependent on the physical parameters, because of self-regulation: if the physical parameters are changed so as to increase the outflow driven by a given rate of accretion onto the protostar, then the rate of accretion is reduced by the outflow, so the actual rate of outflow is little changed. We conclude that our model can be implemented in large-scale simulations of molecular clouds, where  $m_{\text{SPH}}$  has to be large, and  $\rho_{\text{SINK}}$  has to be small, in order to follow simultaneously the formation of many protostars, all potentially having outflows.

We follow the effect of episodic accretion and outflow from a protostar formed near the centre of an initially turbulent, spherically symmetric core with density profile proportional to that of a Bonnor–Ebert sphere. The episodic outflow produces a parsec-long S-shaped chain of bullets, which we identify with Herbig–Haro objects. The position–velocity diagram for these bullets shows two features. Bullets that were ejected early were ejected with lower radial velocities, and have by now been decelerated at the leading shock; these bullets have radial velocities that are linearly proportional to their radial distance, i.e. they subscribe to a Hubble Law. Bullets that were only ejected recently have higher radial velocities and have not yet been decelerated at the leading shock front; these bullets form Hubble wedges. The mass–velocity relation for the gas in the outflow can be fit approximately with  $dM/dv_{\text{RAD}} \propto v_{\text{RAD}}^{-1.5}$ , in good agreement with observation. Individual bullets are manifest as small bumps along this relation. If there is a steeper slope at higher velocities, we are unable to resolve it in this simulation.

## ACKNOWLEDGEMENTS

The authors like to thank the anonymous referee for the comments that helped to significantly improve the paper. PFR, SW, and SDC acknowledge support via the ERC starting grant No. 679852 ‘RAD-FEEDBACK’. PFR, SW, and SDC acknowledge the support of the Bonn-Cologne Graduate School, which is funded through the German Excellence Initiative. SDC and SW thank the DFG for funding via the SFB 956 ‘Conditions & impact of SF’. APW gratefully acknowledges the support of a consolidated grant (ST/K00926/1) from the UK Science and Technology Facilities Council. The authors gratefully acknowledge the Gauss Centre for Supercomputing e.V. ([www.gauss-centre.eu](http://www.gauss-centre.eu)) for funding this project by providing computing time on the GCS Supercomputer SuperMUC at Leibniz Supercomputing Centre (<http://www.lrz.de>). PFR acknowledges D. Price for providing the visualization tool SPLASH (Price 2011).

## REFERENCES

- André P., Di Francesco J., Ward-Thompson D., Inutsuka S.-I., Pudritz R. E., Pineda J. E., 2014, in Beuther H., Klessen R. S., Dullemond C. P., Henning T., eds, *Protostars and Planets VI*, University of Arizona Press, Tucson, p. 27
- Arce H. G., Goodman A. A., 2001, *ApJ*, 551, L171
- Arce H. G., Shepherd D., Gueth F., Lee C.-F., Bachiller R., Rosen A., Beuther H., 2007, in Reipurth B., Jewitt D., Keil K., eds, *Protostars and Planets V*, University of Arizona Press, Tucson, p. 245
- Audard M. et al., 2014, in Beuther H., Klessen R. S., Dullemond C. P., Henning T., eds, *Protostars and Planets*, University of Arizona Press, Tucson, p. 387.
- Bachiller R., Tafalla M., 1999, in Lada C. J., Kylafis N. D., eds, *NATO Advanced Science Institutes (ASI) Series C Vol. 540*, NATO Advanced Science Institutes (ASI) Series C, p. 227

- Bachiller R., Martin-Pintado J., Tafalla M., Cernicharo J., Lazareff B., 1990, *A&A*, 231, 174
- Balbus S. A., Hawley J. F., 1991, *ApJ*, 376, 214
- Bally J., 2016, *ARA&A*, 54, 491
- Bate M. R., Bonnell I. A., Price N. M., 1995, *MNRAS*, 277, 362
- Bate M. R., Tricco T. S., Price D. J., 2014, *MNRAS*, 437, 77
- Belloche A., André P., Despois D., Blinder S., 2002, *A&A*, 393, 927
- Birks J. R., Fuller G. A., Gibb A. G., 2006, *A&A*, 458, 181
- Blandford R. D., Payne D. G., 1982, *MNRAS*, 199, 883
- Bonnor W. B., 1956, *ZAp*, 39, 143
- Bouvier J., Matt S. P., Mohanty S., Scholz A., Stassun K. G., Zanni C., 2014, in Beuther H., Klessen R. S., Dullemond C. P., Henning T., eds, *Protostars and Planets VI*, University of Arizona Press, Tucson, p. 433.
- Cabrit S., Raga A., Gueth F., 1997, in Reipurth B., Bertout C., eds, *IAU Symposium Vol. 182, Herbig-Haro Flows and the Birth of Stars*. p. 163
- Calvet N., Hartmann L., Kenyon S. J., 1993, *ApJ*, 402, 623
- Cesaroni R. et al., 2018, *A&A*, 612, 103
- Chen X., Arce H. G., Zhang Q., Launhardt R., Henning T., 2016, *ApJ*, 824, 72
- Choi M. et al., 2017, *ApJS*, 232, 24
- Clarke S. D., Whitworth A. P., Duarte-Cabral A., Hubber D. A., 2017, *MNRAS*, 468, 2489
- Commerçon B., Hennebelle P., Audit E., Chabrier G., Teyssier R., 2010, *A&A*, 510, L3
- Croswell K., Hartmann L., Avrett E. H., 1987, *ApJ*, 312, 227
- Cullen L., Dehnen W., 2010, *MNRAS*, 408, 669
- Cunningham A. J., Klein R. I., Krumholz M. R., McKee C. F., 2011, *ApJ*, 740, 107
- Davis C. J., Moriarty-Schieven G., Eisloffel J., Hoare M. G., Ray T. P., 1998, *AJ*, 115, 1118
- Dunham M. M., Vorobyov E. I., 2012, *ApJ*, 747, 52
- Ebert R., 1957, *ZAp*, 42, 263
- Federrath C., Schrön M., Banerjee R., Klessen R. S., 2014, *ApJ*, 790, 128
- Fehér O., Kóspál Á., Ábrahám P., Hogerheijde M. R., Brinch C., 2017, *A&A*, 607, A39
- Frank A. et al., 2014, in Beuther H., Klessen R. S., Dullemond C. P., Henning T., eds, *Protostars and Planets VI*, University of Arizona Press, Tucson, p. 451
- Hartigan P., Edwards S., Ghandour L., 1995, *ApJ*, 452, 736
- Hartmann L., 1997, in Reipurth B., Bertout C., eds, *IAU Symposium Vol. 182, Herbig-Haro Flows and the Birth of Stars*. p. 391
- Hartmann L., Calvet N., 1995, *AJ*, 109, 1846
- Hartmann L., Kenyon S. J., 1985, *ApJ*, 299, 462
- Hartmann L., Kenyon S. J., Hewett R., Edwards S., Strom K. M., Strom S. E., Stauffer J. R., 1989, *ApJ*, 338, 1001
- Hennebelle P., Commerçon B., Joos M., Klessen R. S., Krumholz M., Tan J. C., Teyssier R., 2011, *A&A*, 528, A72
- Herbig G. H., 1966, *Vistas in Astronomy*, 8, 109
- Herbst W., Eisloffel J., Mundt R., Scholz A., 2007, in Reipurth B., Jewitt D., Keil K., eds, *Protostars and Planets V*, University of Arizona Press, Tucson, p. 297
- Hsieh T.-H., Murillo N. M., Belloche A., Hirano N., Walsh C., van Dishoeck E. F., Lai S.-P., 2018, *ApJ*, 854, 15
- Hubber D. A., Batty C. P., McLeod A., Whitworth A. P., 2011, *A&A*, 529, A27
- Hubber D. A., Walch S., Whitworth A. P., 2013, *MNRAS*, 430, 3261
- Hubber D. A., Rosotti G. P., Booth R. A., 2018, *MNRAS*, 473, 1603
- Ibryamov S. I., Semkov E. H., Peneva S. P., 2018, *PASA*, 35, e007
- Keegan R., Downes T. P., 2005, *A&A*, 437, 517
- Kenyon S. J., Hartmann L., 1995, *ApJS*, 101, 117
- Kenyon S. J., Hartmann L. W., Strom K. M., Strom S. E., 1990, *AJ*, 99, 869
- Kenyon S. J., Gomez M., Marzke R. O., Hartmann L., 1994, *AJ*, 108, 251
- King A. R., Pringle J. E., Livio M., 2007, *MNRAS*, 376, 1740
- Konigl A., Pudritz R. E., 2000, in Mannings V., Boss A. P., Russell S. S., eds, *Protostars and Planets IV*, University of Arizona Press, Tucson, p. 759
- Kuffmeier M., Frimann S., Jensen S. S., Haugbølle T., 2018, *MNRAS*, 475, 2642
- Kuiper R., Yorke H. W., Turner N. J., 2015, *ApJ*, 800, 86
- Kuiper R., Turner N. J., Yorke H. W., 2016, *ApJ*, 832, 40
- Kuiper T. B. H., Zuckerman B., Rodriguez Kuiper E. N., 1981, *ApJ*, 251, 88
- Lada C. J., Fich M., 1996, *ApJ*, 459, 638
- Launhardt R. et al., 2009, *A&A*, 494, 147
- Lee C.-F., Mundy L. G., Stone J. M., Ostriker E. C., 2002, *ApJ*, 576, 294
- Lee C.-F., Ho P. T. P., Li Z.-Y., Hirano N., Zhang Q., Shang H., 2017, *Nature Astron.*, 1, 0152
- Lewis B. T., Bate M. R., 2017, *MNRAS*, 467, 3324
- Liu T. et al., 2017, *ApJ*, 849, 25
- Liu J., Qiu K., Wyrowski F., Menten K., Guesten R., Cao Y., Wang Y., 2018, preprint (arXiv:1805.03990)
- Li P. S., Klein R. I., McKee C. F., 2018, *MNRAS*, 473, 4220
- Lomax O., Whitworth A. P., Hubber D. A., Stamatellos D., Walch S., 2014, *MNRAS*, 439, 3039
- Lomax O., Whitworth A. P., Hubber D. A., Stamatellos D., Walch S., 2015, *MNRAS*, 447, 1550
- Lomax O., Whitworth A. P., Hubber D. A., 2016a, *PASA*, 33, e004
- Lomax O., Whitworth A. P., Hubber D. A., 2016b, *MNRAS*, 458, 1242
- Lynden-Bell D., 2003, *MNRAS*, 341, 1360
- Machida M. N., 2014, *ApJ*, 796, L17
- Machida M. N., Hosokawa T., 2013, *MNRAS*, 431, 1719
- Machida M. N., Inutsuka S.-i., Matsumoto T., 2008, *ApJ*, 676, 1088
- Machida M. N., Inutsuka S.-i., Matsumoto T., 2009, *Astrophys. Space Sci. Proc.*, 13, 405
- Mao C.-h., Yang J., Lu D.-r., 2014, *Chinese Astron. Astrophys.*, 38, 19
- Matzner C. D., McKee C. F., 1999, *ApJ*, 526, L109
- Morris J. P., Monaghan J. J., 1997, *J. Comput. Phys.*, 136, 41
- Motte F., André P., Ward-Thompson D., Bontemps S., 2001, *A&A*, 372, L41
- Mundt R., Fried J. W., 1983, *ApJ*, 274, L83
- Myers A. T., Klein R. I., Krumholz M. R., McKee C. F., 2014, *MNRAS*, 439, 3420
- Nakamura F., Li Z.-Y., 2007, *ApJ*, 662, 395
- Offner S. S. R., Arce H. G., 2014, *ApJ*, 784, 61
- Offner S. S. R., Chaban J., 2017, *ApJ*, 847, 104
- Offner S. S. R., McKee C. F., 2011, *ApJ*, 736, 53
- Offner S. S. R., Klein R. I., McKee C. F., Krumholz M. R., 2009, *ApJ*, 703, 131
- Pelletier G., Pudritz R. E., 1992, *ApJ*, 394, 117
- Peters T., Klaassen P. D., Mac Low M.-M., Schrön M., Federrath C., Smith M. D., Klessen R. S., 2014, *ApJ*, 788, 14
- Plunkett A. L., Arce H. G., Corder S. A., Dunham M. M., Garay G., Mardones D., 2015, *ApJ*, 803, 22
- Price D. J., 2011, SPLASH: An Interactive Visualization Tool for Smoothed Particle Hydrodynamics Simulations, Astrophysics Source Code Library ascl:1103.004
- Price D. J., Tricco T. S., Bate M. R., 2012, *MNRAS*, 423, L45
- Pudritz R. E., Ouyed R., Fendt C., Brandenburg A., 2007, Reipurth B., , Jewitt D., Keil K., eds, *Protostars and Planets V*, University of Arizona Press, Tucson, p. 277
- Qiu K., Zhang Q., 2009, *ApJ*, 702, L66
- Qiu K., Wyrowski F., Menten K. M., Güsten R., Leurini S., Leinz C., 2011, *ApJ*, 743, L25
- Reipurth B., 1989, *Nature*, 340, 42
- Reipurth B., Bally J., Devine D., 1997, *AJ*, 114, 2708
- Reipurth B., Devine D., Bally J., 1998, *AJ*, 116, 1396
- Richer J. S., Shepherd D. S., Cabrit S., Bachiller R., Churchwell E., 2000, in Mannings V., Boss A. P., Russell S. S., eds, *Protostars and Planets IV*, University of Arizona Press, Tucson, p. 867
- Ridge N. A., Moore T. J. T., 2001, *A&A*, 378, 495
- Safron E. J. et al., 2015, *ApJ*, 800, L5
- Samal M. R., Chen W.-P., Takami M., Jose J., Froebrich D., 2018, preprint (arXiv:1803.11413)

2580 *P. F. Rohde et al.*

- Santiago-García J., Tafalla M., Johnstone D., Bachiller R., 2009, *A&A*, 495, 169
- Scott D. W., 1992, *Multivariate Density Estimation*
- Seifried D., Banerjee R., Klessen R. S., Duffin D., Pudritz R. E., 2012, in Capuzzo-Dolcetta R., Limongi M., Tornambè A., eds, *Astronomical Society of the Pacific Conference Series Vol. 453, Advances in Computational Astrophysics: Methods, Tools, and Outcome*. p. 391
- Shakura N. I., Sunyaev R. A., 1973, *A&A*, 24, 337
- Shu F. H., 1977, *ApJ*, 214, 488
- Shu F. H., Adams F. C., 1987, in Appenzeller I., Jordan C., eds, *IAU Symposium Vol. 122, Circumstellar Matter*. p. 7
- Shu F. H., Lizano S., Ruden S. P., Najita J., 1988, *ApJ*, 328, L19
- Stamatellos D., Whitworth A. P., Bisbas T., Goodwin S., 2007, *A&A*, 475, 37
- Stamatellos D., Hubber D., Whitworth A., 2011a, in Qain S., Leung K., Zhu L., Kwok S., eds, *Astronomical Society of the Pacific Conference Series Vol. 451, 9th Pacific Rim Conference on Stellar Astrophysics*. p. 213 preprint([arXiv:1109.2100](https://arxiv.org/abs/1109.2100))
- Stamatellos D., Whitworth A. P., Hubber D. A., 2011b, *ApJ*, 730, 32
- Stamatellos D., Whitworth A. P., Hubber D. A., 2012, *MNRAS*, 427, 1182
- Stojimirović I., Snell R. L., Narayanan G., 2008, *ApJ*, 679, 557
- Tabone B. et al., 2017, *A&A*, 607, L6
- Tafalla M., Santiago J., Johnstone D., Bachiller R., 2004, *A&A*, 423, L21
- Tan J. C., Beltrán M. T., Caselli P., Fontani F., Fuente A., Krumholz M. R., McKee C. F., Stolte A., 2014, in Beuther H., Klessen R. S., Dullemond C. P., Henning T., eds, *Protostars and Planets VI*, University of Arizona Press, Tucson, p. 149
- Tomida K., 2014, *ApJ*, 786, 98
- Tomida K., Okuzumi S., Machida M. N., 2015, *ApJ*, 801, 117
- Walch S., Naab T., Whitworth A., Burkert A., Gritschneider M., 2010, *MNRAS*, 402, 2253
- Walch S., Whitworth A. P., Girichidis P., 2012, *MNRAS*, 419, 760
- Wang L.-Y., Shang H., Su Y.-N., Santiago-García J., Tafalla M., Zhang Q., Hirano N., Lee C.-F., 2014, *ApJ*, 780, 49
- Whitworth A. P., Bhattal A. S., Francis N., Watkins S. J., 1996, *MNRAS*, 283, 1061
- Wu P.-F., Takakuwa S., Lim J., 2009, *ApJ*, 698, 184
- Wurster J., Price D. J., Bate M. R., 2016, *MNRAS*, 457, 1037
- Wurster J., Bate M. R., Price D. J., 2018, *MNRAS*, 475, 1859
- Ybarra J. E., Barsony M., Haisch K. E., Jr., Jarrett T. H., Sahai R., Weinberger A. J., 2006, *ApJ*, 647, L159
- Zhang M. et al., 2013, *A&A*, 553, A41
- Zhu Z., Hartmann L., Gammie C., 2009a, *ApJ*, 694, 1045
- Zhu Z., Hartmann L., Gammie C., McKinney J. C., 2009b, *ApJ*, 701, 620
- Zhu Z., Hartmann L., Gammie C. F., Book L. G., Simon J. B., Engelhard E., 2010a, *ApJ*, 713, 1134
- Zhu Z., Hartmann L., Gammie C., 2010b, *ApJ*, 713, 1143

This paper has been typeset from a  $\text{\TeX}/\text{\LaTeX}$  file prepared by the author.

5

PAPER II

---



# The impact of episodic outflow feedback on stellar multiplicity and the star formation efficiency

P. F. Rohde<sup>1</sup>,<sup>\*</sup> S. Walch,<sup>1</sup> S. D. Clarke<sup>1</sup>,<sup>\*</sup> D. Seifried<sup>1</sup>,<sup>\*</sup> A. P. Whitworth<sup>2</sup> and A. Klepikó<sup>1</sup>

<sup>1</sup>*Physikalisches Institut, Universität zu Köln, Zùlpicher Str. 77, D-50937 Köln, Germany*

<sup>2</sup>*School of Physics and Astronomy, Cardiff University, Cardiff CF24 3AA, UK*

Accepted 2020 September 21. Received 2020 September 2; in original form 2020 July 10

## ABSTRACT

The accretion of material on to young protostars is accompanied by the launching of outflows. Observations show that accretion, and therefore also outflows, are episodic. However, the effects of episodic outflow feedback on the core scale are not well understood. We have performed 88 smoothed particle hydrodynamic simulations of turbulent dense  $1 M_{\odot}$  cores to study the influence of episodic outflow feedback on the stellar multiplicity and the star formation efficiency (SFE). Protostars are represented by sink particles, which use a subgrid model to capture stellar evolution, inner-disc evolution, episodic accretion, and the launching of outflows. By comparing simulations with and without episodic outflow feedback, we show that simulations with outflow feedback reproduce the binary statistics of young stellar populations, including the relative proportions of singles, binaries, triples, etc. and the high incidence of twin binaries with  $q \geq 0.95$ ; simulations without outflow feedback do not. Entrainment factors (the ratio between total outflowing mass and initially ejected mass) are typically  $\sim 7 \pm 2$ , but can be much higher if the total mass of stars formed in a core is low and/or outflow episodes are infrequent. By decreasing both the mean mass of the stars formed and the number of stars formed, outflow feedback reduces the SFE by about a factor of 2 (as compared with simulations that do not include outflow feedback).

**Key words:** methods: numerical – binaries: general – stars: formation – stars: low-mass – stars: protostars – stars: winds, outflows.

## 1 INTRODUCTION

One of the fundamental open questions in modern astrophysics is why molecular gas is very inefficiently converted into stars. On molecular cloud scales, the star formation efficiency (SFE) is only a few per cent (Leroy et al. 2008; Utomo et al. 2018; Schrubba, Kruijssen & Leroy 2019), and stellar feedback is presumed to be the reason for this low efficiency (Murray 2011). Along with stellar winds, ionizing radiation and supernovae, protostellar outflows are one of the feedback mechanisms that might substantially reduce the overall SFE, particularly in regions where there are no massive stars (e.g. Nakamura & Li 2007; Hansen et al. 2012; Federrath et al. 2014; Krumholz et al. 2014; Cunningham et al. 2018; Li, Klein & McKee 2018).

Low-mass stars form preferentially in pre-stellar cores, which tend to be concentrated in dense filaments inside molecular clouds (Shu & Adams 1987; André et al. 2007; Myers 2009; André et al. 2014; Könyves et al. 2015; Marsh et al. 2016; Könyves et al. 2020). In contrast to the elongated shapes of filaments, pre-stellar cores are approximately spherical, and their density profiles are often described as Bonnor–Ebert spheres, with typical radii of  $R_{\text{CORE}} \sim 0.01$  pc to 0.1 pc (Bonnor 1956; Ebert 1957; Johnstone et al. 2000; Alves, Lada & Lada 2001; Tafalla et al. 2004; Könyves et al. 2020). The pre-stellar core mass function (CMF) approximates to a lognormal distribution

with a peak around  $\sim 0.5 M_{\odot}$  (Könyves et al. 2015, 2020; Marsh et al. 2016). Molecular line observations of pre-stellar cores show non-thermal velocity components indicating internal turbulence (André et al. 2007; Pineda et al. 2011; Friesen et al. 2017).

Protostellar outflows often accompany the star formation process (Bally 2016). Observations and numerical simulations suggest that outflows consist of two components: a collimated high-velocity jet (Mundt & Fried 1983; Reipurth & Bally 2001; Tafalla et al. 2010; Lee et al. 2017) and a slower wide-angle disc wind, launched further out in the accretion disc (Machida 2014; Tabone et al. 2017; Liu et al. 2018; Louvet et al. 2018; Zhang et al. 2019). Both components are known to be rotating (Hirota et al. 2017; Lee et al. 2017; Zhang et al. 2018, 2019). Therefore, outflows carry away angular momentum from the disc-star system, which in turn allows the central protostar to accrete while staying below its breakup speed (Pudritz et al. 2007; Bjerkeli et al. 2016).

Protostellar jets are launched from the innermost regions of protostellar accretion discs. Numerous authors have simulated protostellar outflows self-consistently using magnetohydrodynamic (MHD) simulations (e.g. Machida, Inutsuka & Matsumoto 2009; Hennebelle et al. 2011; Price, Tricco & Bate 2012; Seifried et al. 2012; Machida & Hosokawa 2013; Bate, Tricco & Price 2014; Machida 2014; Tomida 2014; Tomida, Okuzumi & Machida 2015; Lewis & Bate 2017; Machida & Basu 2019; Saiki & Machida 2020). However, such simulations must resolve the launching region down to  $r_{\text{LAUNCH}} \sim R_{\odot}$  to reproduce the extremely high-velocity jet component that originates in the innermost disc region. It is

\* E-mail: rohde@ph1.uni-koeln.de

presently not computationally feasible to follow the evolution of protostars through the whole protostellar phase using such a high resolution. Other authors therefore mitigate this problem by invoking almost resolution-independent subgrid models to launch outflows (Nakamura & Li 2007; Cunningham et al. 2011; Federrath et al. 2014; Myers et al. 2014; Offner & Arce 2014; Peters et al. 2014; Kuiper, Yorke & Turner 2015; Offner & Chaban 2017; Li et al. 2018; Rohde et al. 2019)

Exactly how the gas is launched is still not well understood (see, e.g. the reviews of Arce et al. 2007; Frank et al. 2014; Bally 2016). However, the consensus is that outflows are accretion powered: gravitational energy is converted into kinetic and magnetic energy, which then drives and collimates the outflow, either through magnetic pressure or magneto-centrifugal forces (Blandford & Payne 1982; Königl & Pudritz 2000; Lynden-Bell 2003; Pudritz et al. 2007; Machida, Inutsuka & Matsumoto 2008; Seifried et al. 2012). Since the accretion on to a protostar is episodic, outflows are also episodic (Reipurth 1989; Hartigan, Edwards & Ghandour 1995; Hartmann 1997; Königl & Pudritz 2000; Arce et al. 2007; Hennebelle et al. 2011; Kuiper et al. 2015; Bally 2016; Choi et al. 2017; Cesaroni et al. 2018; Samal et al. 2018; Zhang et al. 2019).

Protostellar outflows inject a significant amount of energy and momentum into the surroundings (Arce et al. 2010; Plunkett et al. 2013; Feddersen et al. 2020), and are likely to have a profound impact on their host cores. This is especially true in the context of low-mass star formation where other feedback mechanisms do not come into play. The ‘primary’ ejected gas from the immediate vicinity of the protostar entrains ‘secondary’ core material, thereby carving out a cavity which widens over time (Arce & Sargent 2006). Within the cavity, accretion flows on to the protostar are suppressed, lowering the amount of gas which can fall directly on to the protostar, and hence lowering the protostellar accretion rate. (Wang et al. 2010). The resulting feedback loop of accretion and outflow launching is not fully understood. Because outflows act to disperse a star’s birth core, they are presumed to play a role in terminating the accretion process (Zhang et al. 2016). Theoretical studies show that this may cause the SFE on core scales to be as low as 15–50 per cent (Machida & Hosokawa 2013; Offner & Arce 2014; Offner & Chaban 2017). However, more observations and theoretical studies are needed to fully understand the effects of outflow feedback on core scales.

The stellar initial mass function (IMF; Kroupa 2002; Chabrier 2003) and the initial statistics of multiple systems (e.g. Duchêne & Kraus 2013) are key constraints on theories of star formation. Raghavan et al. (2010) find that in the field roughly 50 per cent of systems are single stars like our Sun; all the rest are binaries or higher-order multiples (i.e. triples, quadruples, quintuples, etc., hereafter HOMs). Recent observations have started to reveal the multiplicity statistics of pre-main-sequence stars (Duchêne et al. 2007; Connelley, Reipurth & Tokunaga 2008; Chen et al. 2013; Pineda et al. 2015; Tobin et al. 2016; Shan et al. 2017; Duchêne et al. 2018; Tobin et al. 2018; Kounkel et al. 2019). Tobin et al. (2016) have observed the Perseus molecular cloud using the VLA and report an overall multiplicity fraction of  $mf = 0.4$  for Class 0/I protostars. Like Chen et al. (2013), they find that  $mf$  decreases for later evolutionary stages. Dynamical  $N$ -body interactions are probably the main reason for the decay of HOMs (e.g. Bate & Bonnell 2005; Goodwin et al. 2007). Another observed property of low-mass stellar multiples is the excess of almost equal-mass binary systems, referred to as ‘twin’ binaries (Lucy 2006; Simon & Obbie 2009; Kounkel et al. 2019).

Although multiplicity statistics are an important benchmark for simulations of star formation, such simulations should also reveal the detailed physical processes that deliver the observed multiplicity

statistics (see, e.g. Offner 2011; Bate 2012; Lomax et al. 2015; Li et al. 2018; Kuffmeier, Calcutt & Kristensen 2019; Wurster, Bate & Price 2019). Here we explore the effect of outflow feedback on the formation and evolution of multiple systems.

The paper is structured as follows. In Section 2, we describe the computational method, outline modifications to the subgrid outflow model developed earlier by Rohde et al. (2019), and define the initial and boundary conditions. In Section 3, we present the results of the simulations and discuss how the stellar properties depend on the initial conditions. In Section 4, we describe the multiplicity statistics and how they are influenced by outflow feedback. In Section 5, we analyse the properties of the outflows and their relation to the SFE. In Section 6 we summarize our results.

## 2 COMPUTATIONAL METHOD

### 2.1 SPH code GANDALF

For the hydrodynamical simulations, we use the highly object-orientated smoothed particle hydrodynamics (SPH) and mesh-less finite-volume (MFV) code GANDALF (Hubber, Rosotti & Booth 2018). GANDALF adopts the ‘grad-h’ SPH formulation (Springel & Hernquist 2002) with an M4 kernel (Monaghan & Lattanzio 1985) and  $\eta = 1.2$ , giving on average  $\sim 58$  neighbours. GANDALF uses hierarchical block time-stepping. In our simulations the number of allowed time-step levels is  $N_{\text{LVL}} = 9$ . Therefore an SPH particle on the highest level has  $2^{N_{\text{LVL}}} = 512$  times more time-steps than a particle on the lowest level. During a time-step, all particles are allowed to adapt to higher levels if this is necessary. GANDALF uses the artificial viscosity prescription proposed by Morris & Monaghan (1997), regulated by a time-dependent switch (Cullen & Dehnen 2010). GANDALF offers various integration schemes, and we choose the second-order Leapfrog KDK scheme.

As in Rohde et al. (2019), we use the approximate radiative heating and cooling algorithm of Stamatellos et al. (2007). This method uses local SPH particle quantities to estimate a mean optical depth, which is then used to compute heating and cooling rates. The method accounts for changes in specific heat due to dissociation and ionization of H and He. The opacity accounts for ice-mantle evaporation and dust sublimation, as well as the switch from dust opacity to molecular-line opacity. In contrast to Stamatellos et al. (2007), we do not use the local gravitational potential, but the local pressure gradient, to estimate the mean optical depth. This change to the original method has been proposed by Lombardi, McInally & Faber (2015), and improves the behaviour in non-spherical geometries, such as accretion discs and collision interfaces.

### 2.2 Sink particles

Sink particles, as originally proposed by Bate, Bonnell & Price (1995), are used in pre-stellar core-collapse simulations to limit the otherwise continuously decreasing time-steps. We use the improved sink particle description introduced by Hubber, Walch & Whitworth (2013). Sink particles have radius  $R_{\text{SINK}} \sim 1$  AU, and are introduced at densities exceeding  $\rho_{\text{SINK}} = 10^{-10}$  g cm $^{-3}$ . We use gravitational softening on scales of order  $R_{\text{SINK}}$  to make the  $N$ -body integration more robust. SPH particles in the vicinity of a sink particle are not accreted instantaneously, but smoothly over a few time-steps. Therefore the vicinity of a sink particle is not empty, and this leads to improved hydrodynamical behaviour. Besides limiting the time-steps, sink particles serve as active star particles, each hosting the four subgrid models detailed in the next four subsections.

### 2.3 Episodic accretion

Following Stamatellos, Whitworth & Hubber (2012) we divide sink particles into an unresolved inner accretion disc (IAD) and a central protostar. We keep track of the masses,  $M_{\text{IAD}}$  and  $M_{\star}$ , and the angular momenta,  $L_{\text{IAD}}$  and  $L_{\star}$ , of the inner accretion disc and the central protostar,

$$M_{\text{SINK}} = M_{\text{IAD}} + M_{\star}, \quad (1)$$

$$L_{\text{SINK}} = L_{\text{IAD}} + L_{\star}. \quad (2)$$

Gas accreted by the sink particle is initially stored in the IAD. This gas may then be accreted on to the central protostar via two accretion channels,

$$\frac{dM_{\star}}{dt} = \left. \frac{dM}{dt} \right|_{\text{BG}} + \left. \frac{dM}{dt} \right|_{\text{MRI}}. \quad (3)$$

The background accretion rate,  $\left. \frac{dM}{dt} \right|_{\text{BG}} = 10^{-7} M_{\odot} \text{yr}^{-1}$ , allows for low but continuous accretion of gas on to the central protostar. The additional episodic accretion rate is much higher, on average  $\left. \frac{dM}{dt} \right|_{\text{MRI}} \simeq 5 \times 10^{-4} M_{\odot} \text{yr}^{-1}$ , but only contributes during outburst events, which typically last a few tens of years. Stamatellos et al. (2012) assume that a combination of gravitational and magneto-rotational instabilities (MRI) acts as the main trigger for outbursts (Zhu, Hartmann & Gammie 2009; Zhu et al. 2010). In this way we obtain realistic accretion rates, similar to those observed in FU Orionis Type stars (Bell & Lin 1994). We use the episodic accretion rate for the following subgrid models. Varying  $\left. \frac{dM}{dt} \right|_{\text{MRI}}$  has little effect on the outcome of the simulations (Rohde et al. 2019).

### 2.4 Stellar evolution model

Improving upon Rohde et al. (2019) we implement the one-zone stellar evolution model described in Offner et al. (2009), originally introduced by Nakano, Hasegawa & Norman (1995), and subsequently improved by Nakano et al. (2000) and Tan & McKee (2004). This subgrid model describes the evolution of the stellar radius,  $R_{\star}$ , and luminosity,  $L_{\star}$ , due to the energy balance between accretion, gravitational contraction, nuclear burning, ionization and radiation. The change in protostellar radius,  $\dot{R}_{\star}$ , is given by

$$\dot{R}_{\star} = \frac{2}{M_{\star}} \frac{dM_{\star}}{dt} \left( 1 - \frac{1 - f_{\text{K}}}{a_{\text{G}}(n)\beta} + \frac{1}{2} \frac{d \log \beta}{d \log M_{\star}} \right) R_{\star} - \frac{2}{a_{\text{G}}(n)\beta} \left( \frac{R_{\star}}{GM_{\star}^2} \right) (L_{\text{INT}} + L_{\text{DI}} - L_{\text{DB}}) R_{\star}. \quad (4)$$

Here,  $G$  is the gravitational constant,  $f_{\text{K}} = 0.5$  is the fraction of kinetic energy that is radiated away in the inner accretion disc,  $a_{\text{G}}(n)$  is the gravitational energy coefficient for a sphere with polytropic index  $n < 5$  (Nakano et al. 2000, and references therein),  $\beta$  is the ratio of gas pressure to total pressure (gas plus radiation) in the protostar,  $L_{\text{INT}}$  is the internal luminosity,  $L_{\text{DI}}$  is the power required to dissociate and ionize the accreted gas, and  $L_{\text{DB}}$  is the power released by deuterium burning.

This model follows the protostellar evolution through six distinct phases: (i) the initial ‘pre-collapse’ phase; (ii) the ‘no burning’ phase; (iii) the ‘core deuterium burning at fixed  $T_{\text{c}}$ ’ phase; (iv) the ‘core deuterium burning at variable  $T_{\text{c}}$ ’ phase; (v) the ‘shell deuterium burning’ phase; and (vi) the ‘zero-age main-sequence’ phase (Tout et al. 1996).

We follow the implementation described by Offner et al. (2009) and also used by Murray, Goyal & Chang (2018) and Cunningham et al. (2018). However, we use the mass of the subgrid protostar,  $M_{\star}$

(rather than the mass of the sink particle,  $M_{\text{SINK}}$ ) and the episodic accretion rate from the IAD on to the protostar,  $\left. \frac{dM_{\star}}{dt} \right|_{\text{MRI}}$  (rather than the sink particle’s accretion rate,  $\left. \frac{dM_{\text{SINK}}}{dt} \right|_{\text{MRI}}$ ; Section 2.3). The accretion luminosity depends linearly on the accretion rate and is therefore highly variable due to the episodic nature of accretion on to the protostar.

### 2.5 Radiative feedback

Radiative feedback from young protostars can heat and stabilize their surrounding accretion discs, thus suppressing further disc fragmentation (Jones & Bate 2018). Theoretical studies have shown that this reduces the number of brown dwarfs and low-mass protostars formed (Chabrier 2003; Offner et al. 2009; Rice et al. 2011; Guszejnov, Krumholz & Hopkins 2016; Guszejnov, Hopkins & Krumholz 2017). However, continuous radiative feedback (i.e. neglecting episodic accretion effects) tends to suppress the formation of brown dwarfs and low-mass protostars too efficiently, resulting in a lower stellar multiplicity than observed (Stamatellos et al. 2012; Lomax et al. 2014, 2015; Mercer & Stamatellos 2017).

We make use of the episodic accretion model in Stamatellos et al. (2012; Section 2.3), in combination with the stellar evolution model in Offner et al. (2009; Section 2.4) to compute the highly variable protostellar luminosities. These luminosities are taken into account by invoking a pseudo background radiation field with temperature,  $T_{\text{BG}}$ . At general position  $\mathbf{r}$ ,  $T_{\text{BG}}$  is given by

$$T_{\text{BG}}^4(\mathbf{r}) = (10 \text{ K})^4 + \sum_n \left( \frac{L_{\star,n}}{16\pi\sigma_{\text{SB}}|\mathbf{r} - \mathbf{r}_{\star,n}|^2} \right) \quad (5)$$

(Stamatellos et al. 2007). Here,  $\mathbf{r}_{\star,n}$  and  $L_{\star,n}$  are the position and luminosity of the  $n$ th protostar. In the vicinity of a protostar  $T_{\text{BG}}$  decreases with distance  $d$  from the protostar approximately as  $d^{-1/2}$ . This method will not capture accurately the radiative feedback from massive stars. However, we are interested here in the formation of low-mass stars (our initial core mass is just  $1 M_{\odot}$ ) and the model has been extensively tested in this regime (Stamatellos et al. 2012; Lomax et al. 2014, 2015; Mercer & Stamatellos 2017; Rohde et al. 2019).

### 2.6 Outflow feedback

We use the subgrid episodic outflow model presented in Rohde et al. (2019) with a few modifications. Here, we briefly outline the model and focus on the modifications. A more detailed description, including a parameter and resolution study, can be found in Rohde et al. (2019).

As in most subgrid outflow models we assume that the mass ejection rate is a fixed fraction of the accretion rate,

$$\left. \frac{dM}{dt} \right|_{\text{EJECT}} = f_{\text{EJECT}} \frac{dM_{\star}}{dt}. \quad (6)$$

Here we adopt the default value  $f_{\text{EJECT}} = 0.1$ , based on observations and theoretical studies (see Crowell, Hartmann & Avrett 1987; Shu et al. 1988; Pelletier & Pudritz 1992; Calvet, Hartmann & Kenyon 1993; Hartmann & Calvet 1995; Nisini et al. 2018, or the review by Bally 2016). In contrast to most other subgrid outflow models, we do not use the accretion rate on to the sink particle,  $\left. \frac{dM_{\text{SINK}}}{dt} \right|_{\text{MRI}}$ , but the episodic accretion rate on to the central star,  $\left. \frac{dM_{\star}}{dt} \right|_{\text{MRI}}$  (Section 2.3). This leads to the intermittent ejection of individual outflow bullets (Rohde et al. 2019). To model the density and velocity distribution of the outflowing gas, we use the prescription for hydrodynamical

outflows derived by Matzner & McKee (1999). In this way we obtain a two-component outflow, with a collimated high-velocity jet, and a low-velocity wide-angle disc wind.

For the outflow velocity we assume

$$v_{\text{OUT}} = \left( \frac{GM_{\star}}{r_{\text{LAUNCH}}} \right)^{1/2} P(\theta), \quad (7)$$

which is the Keplerian velocity at radius  $r_{\text{LAUNCH}}$ , modulated with the angular distribution,  $P(\theta)$ , derived by Matzner & McKee (1999). Here,  $\theta$  is the angle at which the SPH particle is ejected relative to the spin axis of the accretion disc. In contrast to Rohde et al. (2019) we do not adopt a fixed value for the launching radius,  $r_{\text{LAUNCH}}$ . Instead we use a time-dependent radius depending on the stellar radius,  $R_{\star}$ , provided by the stellar evolution model,

$$r_{\text{LAUNCH}} = 2 R_{\star}. \quad (8)$$

This gives us a more physically motivated outflow velocity, and avoids the need to invoke an arbitrary launching radius.

Outflows play a crucial role in removing angular momentum from the gas that is about to be accreted (Hartmann & Stauffer 1989; Matt & Pudritz 2005). Recent observations show that outflows are rotating and thus carry away angular momentum (Launhardt et al. 2009; Chen et al. 2016; Lee et al. 2017; Tabone et al. 2017). We incorporate rotating outflows by adding to the outward velocity,  $\mathbf{v}_{\text{OUT}}$ , a rotational velocity component,

$$\mathbf{v}_{\text{ROT}} = \mathbf{r} \times \boldsymbol{\omega} \quad (9)$$

with

$$\boldsymbol{\omega} = \frac{\ell_{\text{SPH}}}{m_{\text{SPH}} \sin^2(\theta) r^2} \hat{\mathbf{e}}_{\text{IAD}}. \quad (10)$$

Here,  $m_{\text{SPH}}$  is the mass of an SPH particle and  $\hat{\mathbf{e}}_{\text{IAD}} = \mathbf{L}_{\text{IAD}}/|\mathbf{L}_{\text{IAD}}|$  is the spin axis of the IAD. In contrast to Rohde et al. (2019), we calculate the angular momentum each ejected particle carries away,  $\ell_{\text{PART}}$ , from the breakup angular momentum of the protostar,

$$L_{\text{BREAKUP}} = M_{\star} \sqrt{GM_{\star} R_{\star}}; \quad (11)$$

this assumes that the protostar rotates at its breakup angular speed. Whenever angular momentum is accreted from the IAD on to the central protostar, we compute the excess angular momentum,

$$\ell_{\text{SPH}} = \frac{|\mathbf{L}_{\star}| - L_{\text{BREAKUP}}}{N_{\text{EJECT}}}, \quad (12)$$

allocate it to the ejected particles, and reduce  $|\mathbf{L}_{\star}|$  to  $L_{\text{BREAKUP}}$ ;  $N_{\text{EJECT}}$  is the number of ejected particles during this time-step.

## 2.7 Simulation setup

We have performed 88 simulations with different initial conditions or physical processes. All simulations start from a spherically symmetric, dense core with  $M_{\text{CORE}} = 1 M_{\odot}$  embedded in a low-density envelope at  $T = 10$  K. The density profile follows the radial distribution of a Bonnor–Ebert sphere (BES; Bonnor 1956; Ebert 1957). To obtain cores with  $M_{\text{CORE}} = 1 M_{\odot}$ , we first construct a critical BES, truncated at the critical dimensionless radius  $\xi_0 = 6.5$ . The central densities are chosen in such a way, that the masses of the BESs are  $M_{\odot}/3$ ,  $M_{\odot}/4$ , and  $M_{\odot}/5$ , corresponding to physical core radii of  $r_{\text{CORE}} = 0.017$ ,  $0.013$ , and  $0.010$  pc, respectively. Then we increase the central densities by factors of  $f_{\text{BES}} = 3$ ,  $4$ , or  $5$ , respectively, to  $\rho_{\text{CENTRAL}} = 2.0 \times 10^{-17}$ ,  $4.8 \times 10^{-17}$ , or  $9.4 \times 10^{-17}$  g cm $^{-3}$  so that all the cores have  $M_{\text{CORE}} = 1 M_{\odot}$ . This makes the cores more and more supercritical with increasing  $f_{\text{BES}}$ . Thus, cores with higher

$f_{\text{BES}}$  are smaller, denser and have shorter free-fall times, respectively,  $t_{\text{FF}} = 36.8$  kyr,  $24.6$  kyr and  $16.6$  kyr.

At  $r_{\text{CORE}}$ , the radial density profile decreases smoothly but quickly (power law with index  $\gamma = -4$ ) to  $\rho_{\text{ENV}} = 10^{-23}$  g cm $^{-3}$ . The envelope then extends to  $r_{\text{ENV}} = 0.75$  pc, which allows us to study the interaction of outflows with a low-density ambient medium. The total mass of the core plus envelope is  $M_{\text{TOTAL}} \sim 1.86 M_{\odot}$ ; this mass varies by at most 0.2 per cent due to varying  $r_{\text{CORE}}$ .

As in Walch et al. (2010), we add an isotropic random Gaussian velocity field to the dense cores, in order to study the influence of turbulence on core collapse. The amplitudes follow a power spectrum of the form

$$P_k \propto k^{-4} \quad \text{with } k \in [k_{\text{MIN}}, 64]. \quad (13)$$

Due to the steep power spectrum, most of the turbulent energy is associated with the smallest wavenumber,  $k_{\text{MIN}}$ . We stipulate  $k_{\text{MIN}} = 1, 2$  or  $3$ , with  $\frac{2\pi}{k_{\text{MIN}}} = 1$  corresponding to the core diameter. In this way we change the velocity field from large-scale motions ( $k_{\text{MIN}} = 1$ ) with high net angular momentum, to small-scale turbulence ( $k_{\text{MIN}} = 3$ ) with low net angular momentum (Walch, Whitworth & Girichidis 2012). We vary the strength of the turbulence by adjusting the virial ratio

$$\alpha_{\text{VIR}} = \frac{2(E_{\text{TURB}} + E_{\text{THERM}})}{|E_{\text{GRAV}}|}. \quad (14)$$

We perform simulations for all combinations of  $\alpha_{\text{VIR}} = 0.5, 1.0, 2.0$ , and  $3.0$ ,  $k_{\text{MIN}} = 1, 2$ , and  $3$ , and  $r_{\text{CORE}} = 0.010, 0.013$ , and  $0.017$  pc. In addition, we perform runs with  $\alpha_{\text{VIR}} = 1.0$ ,  $k_{\text{MIN}} = 1$ , and  $r_{\text{CORE}} = 0.013$  pc for eight different turbulent seeds. To study the influence of outflow feedback on the SFE we produce a comparison run without outflow feedback for each setup. This adds up to 88 simulations in total (see Table 1). The mass resolution is 400 000 SPH particles per  $M_{\odot}$ , resulting in a total number of  $N_{\text{TOTAL}} \sim 740$  000 SPH particles.

## 3 RESULTS

Due to their different initial conditions, some simulations form stars faster than others. To carry out objective comparisons between the simulations, we make them at times  $t_{\tau}$  where  $t_{\tau} = t_0 + \tau t_{\text{FF}}$ ; here  $t_0$  is the time at which the first sink forms,  $t_{\text{FF}} = \pi (r_{\text{CORE}}^3 / (8GM_{\text{CORE}}))^{1/2}$  is the core's free-fall time, and we use  $\tau = 0.5, 1.5$ , and  $5.0$ . All simulations are terminated at  $t_5 \sim 200 \pm 50$  kyr. The ensemble of simulations is divided into those with outflow feedback (the OF-sample, with odd IDs and run names ending in 'O-1') and those without outflow feedback (RF-sample, with even IDs and run names ending in 'O-0'). Both samples contain 44 simulations (Table 1). The OF-sample forms  $N_{\star O-1} = 132$  stars in total, whereas the RF-sample forms  $N_{\star O-0} = 163$ . All statistical tests use a significance threshold of  $p < 1$  per cent.

### 3.1 Stellar diversity

The ensemble of simulations produces a wide variety of stellar configurations: single stars and multiple systems; circumstellar and/or circumbinary discs; aligned and misaligned outflows. Fig. 1 illustrates four representative runs with outflow feedback, all at  $t_{0.5}$ . The green markers represent sink particles. The left-hand column shows the central regions around the sink particles and their accretion discs. The right-hand column shows the outflows on larger scales.

The simulation on the top row of Fig. 1 (S-5\_V-2.0\_K-3-R-0.017\_O-1) forms a wide binary system with a circumbinary

**Table 1.** Parameter summary for all the simulations performed. Reading from left to right the columns give the run number, the run name, the turbulent random seed ( $\chi$ ), the virial ratio ( $\alpha_{\text{VIR}}$ ), the smallest turbulent wavenumber ( $k_{\text{MIN}}$ ), and the core radius ( $r_{\text{CORE}}/\text{pc}$ ). Each combination of parameters is simulated once with, and once without, outflow feedback. The simulations with outflow feedback have odd IDs and their run names end with  $x = 1$ . The simulations without outflow feedback have even IDs and their run names end with  $x = 0$ .

#	Run	$\chi$	$\alpha_{\text{VIR}}$	$k_{\text{MIN}}$	$r_{\text{CORE}}$
1/2	S-1_V-0.5_K-1_R-0.017_O-x	5	0.5	1	0.017
3/4	S-1_V-1.0_K-1_R-0.017_O-x	5	1.0	1	0.017
5/6	S-1_V-2.0_K-1_R-0.017_O-x	5	2.0	1	0.017
7/8	S-1_V-3.0_K-1_R-0.017_O-x	5	3.0	1	0.017
9/10	S-1_V-0.5_K-2_R-0.017_O-x	5	0.5	2	0.017
11/12	S-1_V-1.0_K-2_R-0.017_O-x	5	1.0	2	0.017
13/14	S-1_V-2.0_K-2_R-0.017_O-x	5	2.0	2	0.017
15/16	S-1_V-3.0_K-2_R-0.017_O-x	5	3.0	2	0.017
17/18	S-1_V-0.5_K-3_R-0.017_O-x	5	0.5	3	0.017
19/20	S-1_V-1.0_K-3_R-0.017_O-x	5	1.0	3	0.017
21/22	S-1_V-2.0_K-3_R-0.017_O-x	5	2.0	3	0.017
23/24	S-1_V-3.0_K-3_R-0.017_O-x	5	3.0	3	0.017
25/26	S-1_V-0.5_K-1_R-0.013_O-x	5	0.5	1	0.013
27/28	S-1_V-1.0_K-1_R-0.013_O-x	5	1.0	1	0.013
29/30	S-1_V-2.0_K-1_R-0.013_O-x	5	2.0	1	0.013
31/32	S-1_V-3.0_K-1_R-0.013_O-x	5	3.0	1	0.013
33/34	S-1_V-0.5_K-2_R-0.013_O-x	5	0.5	2	0.013
35/36	S-1_V-1.0_K-2_R-0.013_O-x	5	1.0	2	0.013
37/38	S-1_V-2.0_K-2_R-0.013_O-x	5	2.0	2	0.013
39/40	S-1_V-3.0_K-2_R-0.013_O-x	5	3.0	2	0.013
41/42	S-1_V-0.5_K-3_R-0.013_O-x	5	0.5	3	0.013
43/44	S-1_V-1.0_K-3_R-0.013_O-x	5	1.0	3	0.013
45/46	S-1_V-2.0_K-3_R-0.013_O-x	5	2.0	3	0.013
47/48	S-1_V-3.0_K-3_R-0.013_O-x	5	3.0	3	0.013
49/50	S-1_V-0.5_K-1_R-0.010_O-x	5	0.5	1	0.010
51/52	S-1_V-1.0_K-1_R-0.010_O-x	5	1.0	1	0.010
53/54	S-1_V-2.0_K-1_R-0.010_O-x	5	2.0	1	0.010
55/56	S-1_V-3.0_K-1_R-0.010_O-x	5	3.0	1	0.010
57/58	S-1_V-0.5_K-2_R-0.010_O-x	5	0.5	2	0.010
59/60	S-1_V-1.0_K-2_R-0.010_O-x	5	1.0	2	0.010
61/62	S-1_V-2.0_K-2_R-0.010_O-x	5	2.0	2	0.010
63/64	S-1_V-3.0_K-2_R-0.010_O-x	5	3.0	2	0.010
65/66	S-1_V-0.5_K-3_R-0.010_O-x	5	0.5	3	0.010
67/68	S-1_V-1.0_K-3_R-0.010_O-x	5	1.0	3	0.010
69/70	S-1_V-2.0_K-3_R-0.010_O-x	5	2.0	3	0.010
71/72	S-1_V-3.0_K-3_R-0.010_O-x	5	3.0	3	0.010
73/74	S-2_V-1.0_K-1_R-0.013_O-x	0	1.0	1	0.013
75/76	S-3_V-1.0_K-1_R-0.013_O-x	1	1.0	1	0.013
77/78	S-4_V-1.0_K-1_R-0.013_O-x	2	1.0	1	0.013
79/80	S-5_V-1.0_K-1_R-0.013_O-x	3	1.0	1	0.013
81/82	S-6_V-1.0_K-1_R-0.013_O-x	4	1.0	1	0.013
83/84	S-7_V-1.0_K-1_R-0.013_O-x	6	1.0	1	0.013
85/86	S-8_V-1.0_K-1_R-0.013_O-x	7	1.0	1	0.013
87/88	S-9_V-1.0_K-1_R-0.013_O-x	8	1.0	1	0.013

disc. A third star forms in the circumbinary disc via disc-fragmentation. The binary system becomes an hierarchical triple system when the third star spirals inwards. The outflows from all three stars are well aligned and produce a broad outflow cavity.

The simulation on the second row of Fig. 1 (S-5\_V-0.5\_K-1\_R-0.010\_O-1) also forms three stars that end up in a stable triple system. Two of these stars belong to a close binary system with a circumbinary disc, while the third star has its own circumstellar disc. These two systems are surrounded by a larger accretion disc,

and material from this larger disc streams inwards along a spiral structure and on to the two smaller discs.

The simulation on the third row of Fig. 1 (S-5\_V-3.0\_K-1\_R-0.013\_O-1) forms four stars in total. Initially these stars are in an hierarchical quadruple system (a close binary, a third star orbiting further out, and a fourth star orbiting even further out). This fourth star has the largest accretion disc, and there are spiral accretion flows feeding material inwards from larger scales and on to the accretion discs. Later on only the close binary remains bound.

The simulation on the bottom row of Fig. 1 (S-5\_V-1.0\_K-3\_R-0.017\_O-1) forms two stars in a binary system. Both stars have their own circumstellar accretion discs, with a bridge in between. At this stage the outflows from the stars point in slightly different directions, but later on they align.

### 3.2 Overview of stellar masses and multiplicities

Fig. 2 shows, as a function of the total mass in stars,  $M_{\text{TOTAL}}$  at  $t_5$ , the number of stars formed in a core,  $N_*$  (top row), the mass of the most massive star,  $M_{\text{MM}}$  (second row), the order of the highest order system,  $O_{\text{SYS-MAX}}$  (third row), and the total stellar mass of this highest-order system,  $M_{\text{SYS-MAX}}$  (bottom row). The left-hand column shows the results for the OF-sample, and the right-hand column shows them for the RF-sample. The SFE is  $\text{SFE} = M_{\text{TOTAL}}/M_{\text{CORE}}$  at  $t_5$ . Since the core can accrete matter from its surroundings and convert this matter into stars, SFE can exceed unity.

The top row of Fig. 2 indicates that there is no significant correlation between  $N_*$  and  $M_{\text{TOTAL}}$ , for either sample. A Kendall Rank Correlation (KRC) test confirms this, with  $p \sim 30$  per cent for both samples. On average, the RF-sample forms more stars per core,  $\bar{N}_*(\text{O-0}) = 3.88 \pm 2.12$  than the OF-sample,  $\bar{N}_*(\text{O-1}) = 3.14 \pm 1.95$ . The theoretical model of Holman et al. (2013) predicts a slightly higher number,  $N_* = 4.1 \pm 0.4$ . The core that forms the highest number of stars,  $N_* = 9$ , is S-5\_V-1.0\_K-3\_R-0.010\_O-0 in the RF-sample. The OF-sample contains 13 simulations which form only a single star, as compared with only 5 in the RF-sample.

The second row of Fig. 2 shows that the ratio of the mass of the most massive star to the total stellar mass,  $M_{\text{MM}}/M_{\text{TOTAL}}$ , is between  $\sim 0.2$  and  $\sim 0.6$ . For the OF-sample, this ratio shows no correlation with the total stellar mass,  $M_{\text{TOTAL}}$ . For the RF-sample, the ratio shows a slight tendency to increase with increasing  $M_{\text{TOTAL}}$ , but with a large scatter.

The third row of Fig. 2 shows that the order of the highest-order system formed in each core,  $O_{\text{SYS-MAX}}$ , is not significantly correlated with  $M_{\text{TOTAL}}$ .<sup>1</sup> Multiple systems are identified and characterized using the method proposed by Lomax et al. (2015), which iteratively pairs up stars and multiples in an hierarchical order, taking into account their mutual gravitational and kinetic energies, their eccentricity, and whether the pair is tidally bound. Many single stars are ejected by dynamical interactions with multiples. We discuss these ejected stars in Section 4.

Strictly speaking, only binary systems are truly stable, in the sense that they can survive indefinitely, in isolation. However, HOMs can survive for a very long time if they are arranged hierarchically. Consequently, some of them will survive long after the dispersal of the birth core, but many will end up as binaries, and some will dissolve completely into singles (e.g. run S-5\_V-1.0\_K-3\_R-0.010\_O-1). In general, the larger the number of stars, the larger the number of

<sup>1</sup>The highest-order system formed in a core is not necessarily a higher-order multiple (HOM), it could be a single or a binary.

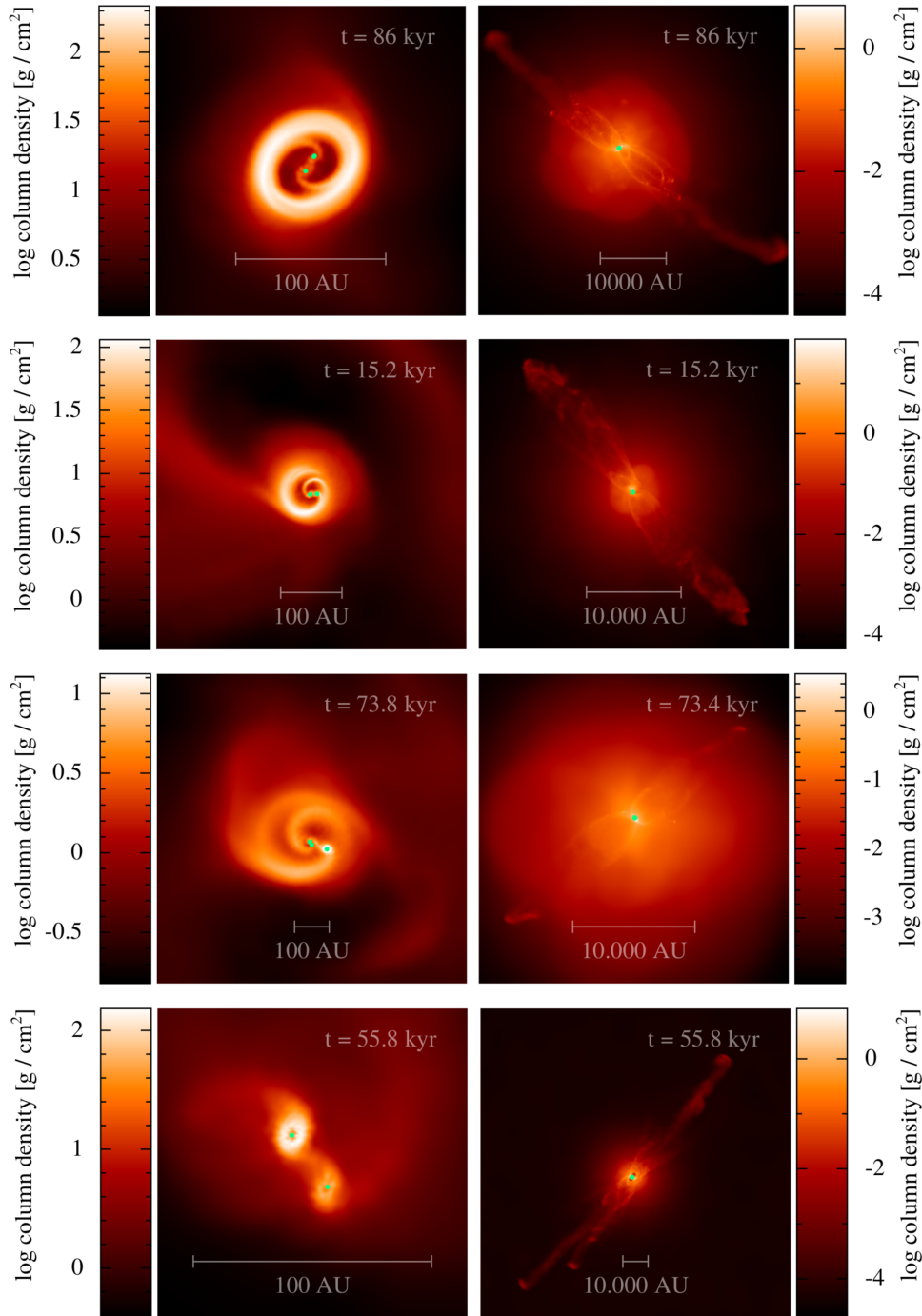


**Figure 1.** Column density plots of four representative simulations with outflow feedback at  $t_{0.5} \equiv t_0 + 0.5 t_{\text{ff}}$ . The left-hand column shows the multiple systems and accretion discs in the central regions. The right-hand column shows the same simulations, but zoomed out to reveal their outflows. The green dots represent sink particles. The simulations are from top to bottom S-5\_V-2.0\_K-3\_R-0.017\_O-1, S-5\_V-0.5\_K-1\_R-0.010\_O-1, S-5\_V-3.0\_K-1\_R-0.013\_O-1, and S-5\_V-1.0\_K-3\_R-0.017\_O-1. Note that the scale, the colour bar, and the viewing-angle are different for each panel.

ejected singles. For example, run S-5\_V-1.0\_K-3\_R-0.010\_O-0 forms nine stars, but ejects six of them and ends up as an hierarchical triple system. In all simulations that form only two stars, these two always end up in a binary.

One very striking difference between the OF- and RF-samples is the fractions of single ( $S_1$ ), binary ( $B_2$ ), triple ( $T_3$ ), and quadruple ( $Q_4$ ) systems formed. For the OF-sample, there is a monotonic decrease with increasing order, viz. ( $S_1 : B_2 : T_3 : Q_4$ ) = (0.38 : 0.29 : 0.24 : 0.10).

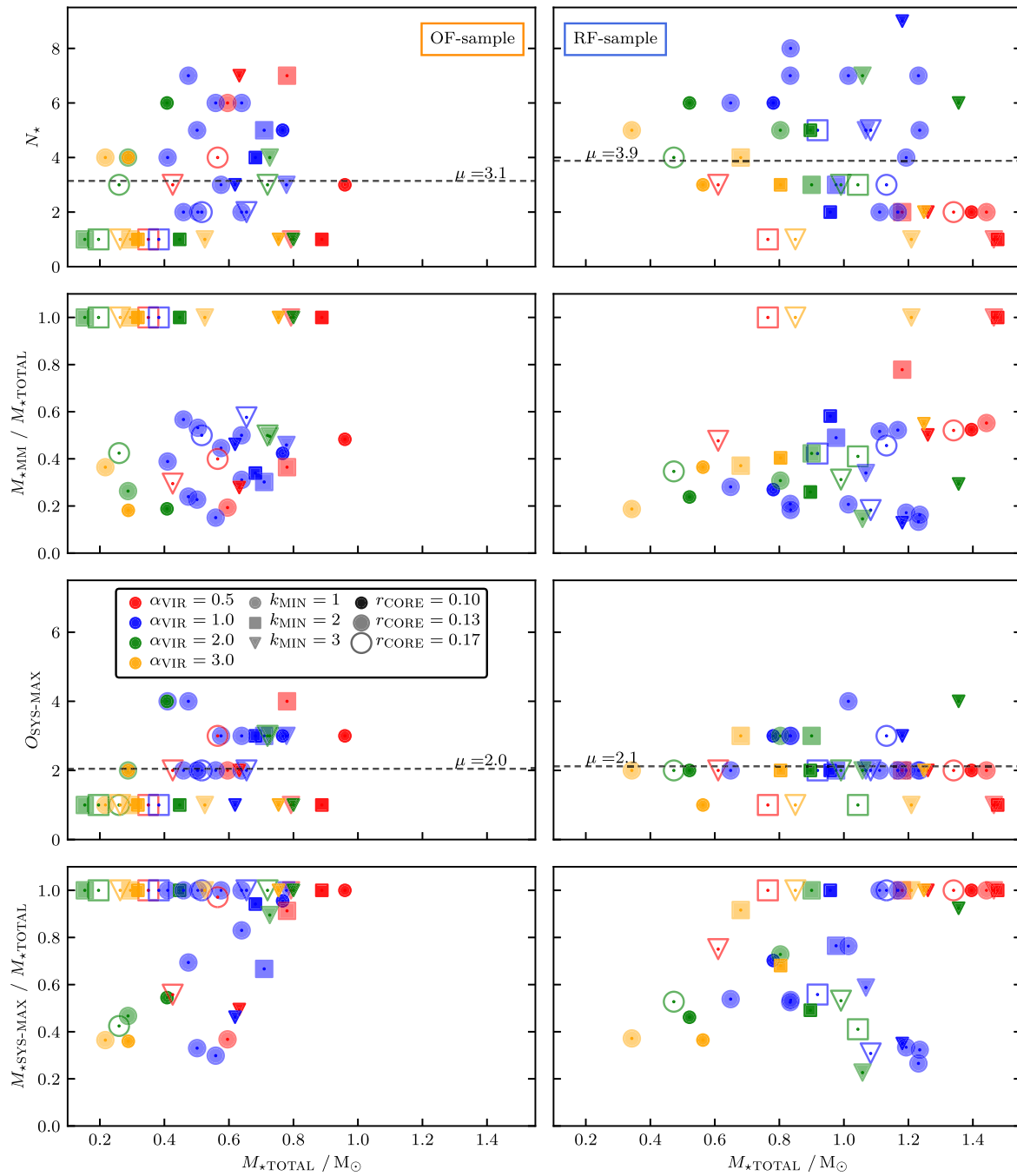


**Figure 2.** Scatter plots showing the properties of the stars formed in a core against total mass of stars, for all the simulations, at  $t_5 \equiv t_0 + 5 t_{\text{ff}}$ . The left-hand column shows the OF sample, and the right-hand column shows the RF-sample. The size of the symbol encodes the core's initial radius,  $r_{\text{CORE}}$ ; the colour of the symbol encodes the core's initial virial parameter,  $\alpha_{\text{VIR}}$ ; and the shape of the symbol encodes the wavenumber of the largest initial turbulent mode in the core (see key on third panel down, left-hand side). The top row shows the total number of stars,  $N_*$ , and the dashed lines indicate the mean values,  $\bar{N}_*(O-1) = 3.14 \pm 1.95$  and  $\bar{N}_*(O-0) = 3.88 \pm 2.12$ . The second row shows the mass of the most massive star, as a fraction of the total mass of stars,  $M_{*MM}/M_{*TOTAL}$ . The third row shows the order of the highest-order system, and the dashed lines indicate the mean values,  $\bar{O}_{\text{SYS}}(O-1) = 2.05 \pm 1.00$  and  $\bar{O}_{\text{SYS}}(O-0) = 2.12 \pm 0.73$ . The bottom row shows the mass of the highest-order system, as a fraction of the total mass of stars,  $M_{*SYS-MAX}/M_{*TOTAL}$ .

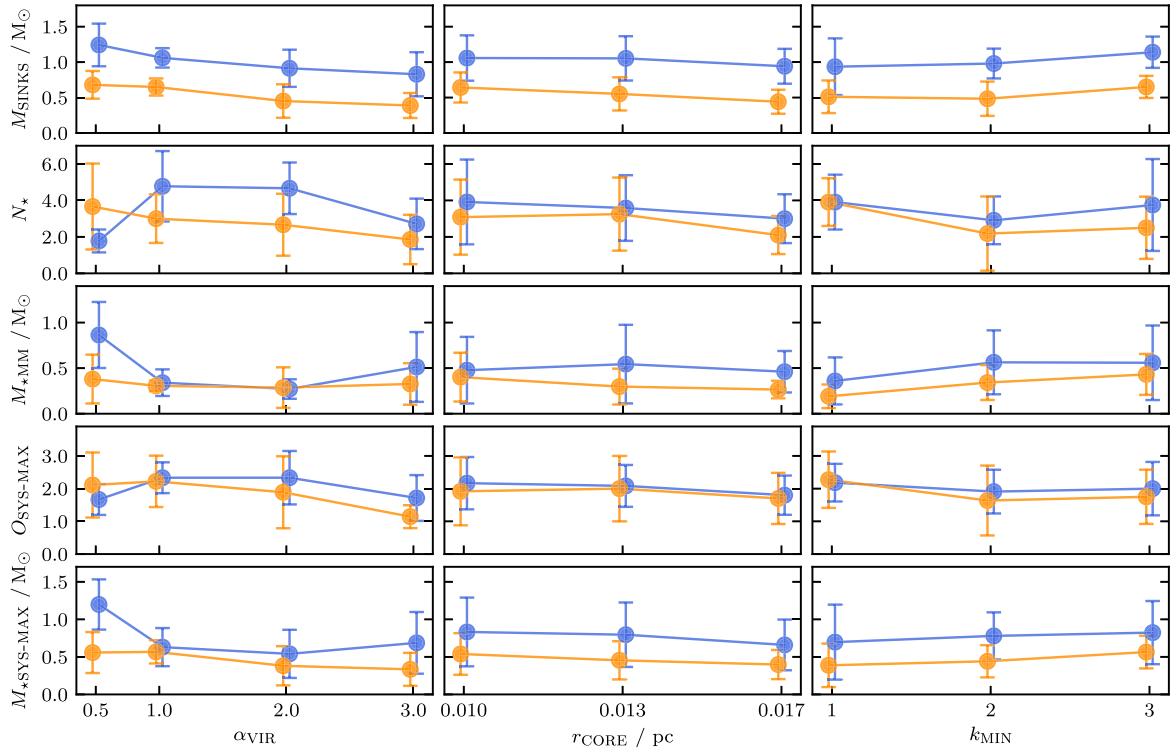


**Figure 3.** Mean values for the stellar parameters plotted in Fig. 2, as a function of the parameters defining the initial conditions of the birth core. Simulations from the OF-sample are plotted in orange, and those from the RF-sample are plotted in blue. The left-hand column shows the means for subsets with the same  $\alpha_{\text{VIR}} = 0.5, 1.0, 2.0$  or  $3.0$  (i.e. averaged over all values of  $r_{\text{CORE}}$  and  $k_{\text{MIN}}$ ). The middle column shows the means for subsets with the same  $r_{\text{CORE}} = 0.010$  pc,  $0.013$  pc or  $0.017$  pc (i.e. averaged over all values of  $\alpha_{\text{VIR}}$  and  $k_{\text{MIN}}$ ). The right-hand column shows the means for subsets with the same  $k_{\text{MIN}} = 1, 2$  or  $3$  (i.e. averaged over all values of  $\alpha_{\text{VIR}}$  and  $r_{\text{CORE}}$ ). The top row shows the mean total stellar mass,  $\bar{M}_{\text{TOTAL}}$ ; the second row shows the mean number of stars,  $\bar{N}_{\text{*}}$ ; the third row shows the mean mass of the most massive star,  $\bar{M}_{\text{*MM}}$ ; the fourth and fifth rows show the mean order,  $\bar{O}_{\text{SYS}}$ , and the mean mass,  $\bar{M}_{\text{*SYS-MAX}}$ , of the highest-order system. The initial conditions of the birth core appear to have very limited influence on the properties of the stars formed.

In contrast, the RF-sample mainly forms binary systems,  $(S_1 : B_2 : T_3 : Q_4) = (0.17 : 0.60 : 0.19 : 0.05)$ . The fraction of triple and quadruple systems is slightly higher for the OF-sample. However, due to the high fraction of binaries in the RF-sample, the mean orders of the largest systems are very similar:  $O_{\text{SYS-MAX}} = 2.0$  for the OF-sample, and  $O_{\text{SYS-MAX}} = 2.1$  for the RF-sample.

The bottom row of Fig. 2 shows the ratio of the mass in the highest-order system to the total stellar mass,  $M_{\text{*SYS-MAX}}/M_{\text{*TOTAL}}$ . The OF-sample has significantly more simulations with  $M_{\text{*SYS-MAX}}/M_{\text{*TOTAL}} = 1.0$ , because many more simulations form just a single star. Setting aside the systems with a ratio close to one,  $M_{\text{*SYS-MAX}}/M_{\text{*TOTAL}}$  tends to increase with increasing  $M_{\text{*TOTAL}}$ , up to  $M_{\text{*TOTAL}} \sim 0.8 M_{\odot}$ , for both samples, albeit with large scatter. Above  $M_{\text{*TOTAL}} \sim 0.8 M_{\odot}$ , there are no multiple systems in the OF-sample, but for the RF-sample  $M_{\text{*SYS-MAX}}/M_{\text{*TOTAL}}$  then tends to decrease with increasing  $M_{\text{*TOTAL}}$ ; this is because these simulations produce large numbers of stars and only a few of them end up in the highest-order system.

### 3.3 Influence of initial core properties

The initial conditions for the simulated cores are characterized by four parameters: the core radius, which takes values  $r_{\text{CORE}} = 0.010$  pc,  $0.013$  pc and  $0.017$  pc; the virial ratio, which takes values  $\alpha_{\text{VIR}} = 0.5, 1.0, 2.0$  and  $3.0$ ; the minimum wavenumber for the

imposed turbulent modes, which takes values  $k_{\text{MIN}} = 1, 2$  and  $3$ ; and the seed for the random turbulent modes excited, which takes the same value  $\chi = 1$  for all combinations of  $(r_{\text{CORE}}, \alpha_{\text{VIR}}, k_{\text{MIN}})$  except for  $(r_{\text{CORE}}, \alpha_{\text{VIR}}, k_{\text{MIN}}) = (0.013 \text{ pc}, 1.0, 1)$ , for which we perform runs with  $\chi = 1, 2, 3, 4, 5, 6, 7$ , and  $8$ .

In order to explore how these parameters influence the masses and multiplicities of the stars formed in a core, we compute average values at  $t_5 \equiv t_0 + 5t_{\text{FF}}$  for (i) the total stellar mass,  $\bar{M}_{\text{*TOTAL}}$ , (ii) the number of stars,  $\bar{N}_{\text{*}}$ , (iii) the mass of the most massive star,  $\bar{M}_{\text{*MM}}$ , (iv) the order of the highest-order system,  $\bar{O}_{\text{SYS}}$ , and (v) the mass of the highest order system,  $\bar{M}_{\text{*SYS-MAX}}$ , for all the simulations with a given radius  $r_{\text{CORE}}$  but different values of  $\alpha_{\text{VIR}}$  and  $k_{\text{MIN}}$  – and similarly for all the simulations with a given virial parameter  $\alpha_{\text{VIR}}$  but different  $r_{\text{CORE}}$  and  $k_{\text{MIN}}$ , and all the simulations with a given minimum turbulent wavenumber  $k_{\text{MIN}}$  but different  $r_{\text{CORE}}$  and  $\alpha_{\text{VIR}}$ . The results are presented on Fig. 3, where the results for simulations from the OF-sample are in orange, and those from the RF-sample are in blue.

To quantify the results presented in Fig. 3 we evaluate the dependence of these mean stellar parameters ( $\bar{M}_{\text{*TOTAL}}, \bar{N}_{\text{*}}, \bar{M}_{\text{*MM}}, \bar{O}_{\text{SYS}}, \bar{M}_{\text{*SYS-MAX}}$ ) on the initial condition parameters ( $\alpha_{\text{VIR}}, r_{\text{CORE}}, k_{\text{MIN}}$ ) by computing the Kendall Rank Correlation statistics,  $\tau$  and  $p$  (see Table 2);  $\tau$  gives the degree of correlation (or anticorrelation, if negative). In addition, we evaluate whether the OF- and RF-samples are drawn from the same underlying distribution, by computing the non-parametric Kolmogorov–Smirnov

**Table 2.** Non-parametric measures of the correlations, and their statistical significances, for the data presented in Fig. 3. The left double-column gives the stellar parameters considered, in the same order as in Fig. 3, and the sample used (outflow OF or reference RF). The second double-column gives the Kolmogorov–Smirnov statistics,  $d$  and  $p$ , which reflect the likelihood that the two samples are drawn from the same distribution. The last three double-columns give the Kendall Rank Correlation (KRC) statistics,  $\tau$  and  $p$ , which reflect the likelihood that the stellar parameters are correlated with, respectively,  $\alpha_{\text{VIR}}$ ,  $r_{\text{CORE}}$ , and  $k_{\text{MIN}}$ ; the KRC statistics are evaluated separately for the OF- and RF-samples. Correlations that satisfy our significance threshold of  $p < 1\%$  are highlighted.

Subset		KS-test		$\tau$	$\alpha_{\text{VIR}}$	$\tau$	$r_{\text{CORE}}$	$\tau$	$k_{\text{MIN}}$
		$d$	$p$ (per cent)		$p$ (per cent)		$p$ (per cent)		$p$ (per cent)
$M_{\star\text{TOTAL}}$	OF	<b>0.68</b>	<b>&lt; 0.01</b>	<b>-0.40</b>	<b>0.06</b>	<b>-0.34</b>	<b>0.45</b>	0.20	9.94
	RF			<b>-0.42</b>	<b>0.03</b>	-0.21	7.71	0.18	12.39
$N_{\star}$	OF	0.18	42.25	<b>-0.33</b>	<b>0.73</b>	-0.20	12.21	-0.29	2.01
	RF			0.04	71.56	-0.17	17.47	-0.16	20.45
$M_{\star\text{MM}}$	OF	0.31	1.76	-0.15	18.89	-0.17	14.37	<b>0.39</b>	<b>0.11</b>
	RF			<b>-0.36</b>	<b>0.16</b>	-0.04	69.44	0.19	10.40
$O_{\text{SYS-MAX}}$	OF	0.18	42.25	-0.30	1.69	-0.13	31.62	-0.30	2.27
	RF			-0.07	55.24	-0.25	5.63	-0.19	14.98
$M_{\text{SYS-MAX}}$	OF	<b>0.36</b>	<b>0.41</b>	<b>-0.30</b>	<b>0.10</b>	-0.23	4.95	0.22	7.18
	RF			<b>-0.41</b>	<b>0.01</b>	-0.19	11.61	0.12	30.00

(KS) statistics,  $d$  and  $p$ ;  $d$  measures the difference between the two distributions. In both cases,  $p$  gives the probability of obtaining the evaluated correlation ( $\tau$ ) or difference ( $d$ ) assuming the null hypothesis (i.e. that both samples are drawn from the same underlying distribution).

Fig. 3 and Table 2 demonstrate clearly that varying the initial conditions – at least in the range we have studied – has little influence on the properties of the stars formed. The correlations between stellar parameters and initial condition parameters are at best weak ( $|\tau| \leq 40$ ), and in most cases they are not significant, so we only discuss those for which  $p < 1$  per cent. For both samples (OF and RF),  $\bar{M}_{\star\text{TOTAL}}$  decreases with increasing  $\alpha_{\text{VIR}}$  (because the cores have more support and collapse more slowly); for the OF-sample,  $\bar{M}_{\star\text{TOTAL}}$  also decreases with increasing  $r_{\text{CORE}}$  (first because the cores collapse more slowly, and secondly because the outflow feedback acts on more rarefied gas and is therefore more effective). For the OF-sample,  $\bar{N}_{\star}$  decreases with increasing  $\alpha_{\text{VIR}}$  (because the cores have more support and are therefore more easily dispersed by outflow feedback).  $\bar{M}_{\star\text{MM}}$  increases with increasing  $k_{\text{MIN}}$  for the OF-sample (because the turbulence is concentrated on small scales which dissipate more rapidly), and with decreasing  $\alpha_{\text{VIR}}$  for the RF-sample (because the cores have less turbulent support and therefore their collapse is more focused).  $\bar{M}_{\star\text{SYS-MAX}}$  increases with decreasing  $\alpha_{\text{VIR}}$  for both samples (again, because the cores have less turbulent support and therefore their collapse is more focused).

The one exception to these correlations, anticorrelations and insignificant correlations is the  $\alpha_{\text{VIR}} = 0.5$  RF subset, which bucks most of the trends seen in the other subsets. The very low level of core support ( $\alpha_{\text{VIR}} = 0.5$ ) and the lack of outflow feedback (RF) result in a rather focused infall on to the centre of the core, and consequently the formation of either a massive single star, or a massive binary (usually with approximately equal-mass components).

The second double column of Table 2 demonstrates that the OF- and RF-samples are statistically distinct. In particular,  $\bar{M}_{\star\text{TOTAL}}$  is almost twice as large for the RF-sample as for the OF-sample (see Fig. 3, top panel).  $\bar{M}_{\star\text{MM}}$  and  $\bar{M}_{\star\text{SYS-MAX}}$  are also larger for the RF-sample than the OF-sample, by  $\sim 50$  per cent (see Fig. 3, third and bottom panels). These differences are mainly due to the fact that in the OF simulations the outflow feedback disperses the gas surrounding

the core, but in the RF simulations the surrounding gas falls on to the core and replenishes its mass.  $\bar{N}_{\star}$  and  $\bar{O}_{\text{SYS}}$  are indistinguishable between the two samples.

### 3.4 Influence of turbulent seeds

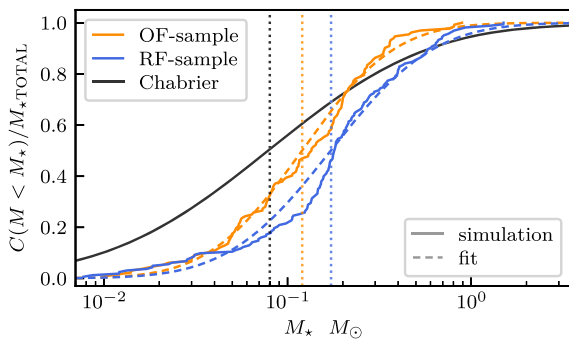
To make sure our results are not dominated by the particular choice of the turbulent velocity field for the fiducial runs, we perform eight additional runs with different random turbulent seeds (Table 1, runs with number 73–88), with and without outflow feedback. These runs have otherwise the same initial condition values as our fiducial runs S-5\_V-1\_K-1\_R-4\_O-x. In Fig. 2 the subset of these runs ( $\chi$ -subset) are represented by the middle-sized, blue shaded circles. The spread of the ( $\chi$ -subset) is comparable to the spread of the runs with varying initial conditions (IC-subset). Remarkable is that the  $\chi$ -subset contains no run that forms only a single star.

Table 3 gives the mean and standard deviation of the full sample (OF and RF), the  $\chi$ -subset and the IC-subset for all quantities presented in Figs 2 and 3. The mean values and their spread are comparable for both samples. Two differences, however not statistically significant, are that the  $\chi$ -subset (a) forms on average slightly more stars and (b) has slightly lower masses of the most massive star due to the absence of runs forming a single star. The last two columns of Table 3 give the Kolmogorov–Smirnov statistics,  $d$  and  $p$ , reflecting the difference between the  $\chi$ - and IC-subset and the probability of finding these results assuming the null hypothesis is true. We do not find a statistical difference between the two subsets, and we are unable to reject the null hypothesis that both subsets have the same underlying distribution. However, we caution that this is not a proof that the distributions are the same.

The similarity between the  $\chi$ -subset and the IC-subset makes us confident that our results are not dominated by the choice of the random seeds. On the other hand, this finding supports our result from Section 3.3. Since the influence of the varying initial conditions on the outcome of the simulation is not higher than the influence due to different turbulent seeds, the core properties play at most a limited role in the outcome of the simulation.

**Table 3.** Mean and standard deviation for the quantities presented in Fig. 2 for the subsets with varying turbulent seeds and initial conditions (IC). The first column gives the quantities presented in Fig. 2, the second column the feedback mechanism. The third, fourth, and fifth column give the mean and standard deviation for the full OF- and RF-samples (full-sample), the reduced subset with varying turbulent seeds ( $\chi$ -subset) and the reduced subset with varying initial condition parameters (IC-subset). The sixth and seventh column give the Kolmogorov–Smirnov statistics,  $d$  and  $p$ , which reflect the likelihood that the  $\chi$ - and IC-sample are drawn from the same distribution.

Quantity	Feedback	Full-sample	$\chi$ -subset	IC-subset	$d$	$p$ (per cent)
$\bar{M}_{\star\text{TOTAL}}$	OF	$0.54 \pm 0.20$	$0.53 \pm 0.08$	$0.54 \pm 0.22$	0.38	19.04
	RF	$1.00 \pm 0.28$	$1.03 \pm 0.20$	$1.00 \pm 0.30$	0.24	74.01
$\bar{N}_{\star}$	OF	$3.14 \pm 1.95$	$4.11 \pm 1.85$	$2.85 \pm 1.87$	0.38	19.04
	RF	$3.88 \pm 2.12$	$5.33 \pm 2.11$	$3.53 \pm 1.93$	0.41	14.00
$\bar{M}_{\star\text{MM}}$	OF	$0.30 \pm 0.20$	$0.20 \pm 0.08$	$0.32 \pm 0.21$	0.45	8.22
	RF	$0.46 \pm 0.34$	$0.27 \pm 0.17$	$0.50 \pm 0.36$	0.54	2.82
$\bar{O}_{\text{SYS-MAX}}$	OF	$2.05 \pm 1.00$	$2.67 \pm 0.82$	$1.88 \pm 0.96$	0.47	6.81
	RF	$2.12 \pm 0.73$	$2.44 \pm 0.68$	$2.03 \pm 0.71$	0.21	86.28
$\bar{M}_{\text{SYS-MAX}}$	OF	$0.45 \pm 0.24$	$0.42 \pm 0.16$	$0.47 \pm 0.25$	0.35	27.61
	RF	$0.74 \pm 0.41$	$0.60 \pm 0.31$	$0.77 \pm 0.42$	0.37	21.49



**Figure 4.** Cumulative mass functions for the OF-sample (132 stars, solid orange line) and the RF-sample (163 stars, solid blue line) at  $t_5 = t_0 + 5 t_{\text{FF}}$ . The dashed lines show lognormal fits to these distributions, and the dotted lines indicate the mean values,  $\bar{M}_{\text{OF}} = 0.13 M_{\odot}$  and  $\bar{M}_{\text{RF}} = 0.18 M_{\odot}$ . The black line shows the Chabrier IMF for comparison ( $\bar{M}_{\text{CHAB}} = 0.08 M_{\odot}$ ).

### 3.5 Initial mass function

The stellar IMF gives the probability that a newly formed star has a certain mass (Chabrier 2003). The IMFs observed in different local star-forming regions appear to be very similar, implying that the star formation process is independent of environment (Kroupa 2001, 2002). Numerical simulations reproduce this universal IMF well for a large variety of initial conditions (Bate 2005, 2009a,b).

We cannot attempt to reproduce the observed IMF here because we have only treated a single core mass ( $1 M_{\odot}$ ). Observed cores are known to have a distribution of masses, given by the core mass function (CMF), and the CMF appears to be similar in shape to the IMF but shifted to higher masses (e.g. André et al. 2010; Könyves et al. 2015, 2020). However we can evaluate the mean stellar mass function (MF) produced by a  $1 M_{\odot}$  core, with and without outflow feedback. Fig. 4 shows the Chabrier IMF (solid black line), the cumulative MF for the OF-sample (solid orange line), the cumulative MF for the RF-sample (solid blue line), a lognormal fit to the OF-sample (dashed orange line) and a lognormal fit to the RF-sample (dashed blue line). The fits are obtained using data-likelihood maximization Markov-Chain Monte Carlo sampling. The mean masses,  $\bar{M}_{\text{CHAB}} = 0.08 M_{\odot}$ ,  $\bar{M}_{\text{OF}} = 0.13 M_{\odot}$  and  $\bar{M}_{\text{RF}} =$

$0.18 M_{\odot}$  are shown as vertical dotted lines. The corresponding standard deviations are  $\sigma_{\text{CHAB}} = 0.69 \pm 0.05$ ,  $\sigma_{\text{OF}} = 0.40 \pm 0.06$  and  $\sigma_{\text{RF}} = 0.44 \pm 0.06$ . Thus, outflow feedback reduces the mean stellar mass produced by a  $1 M_{\odot}$  core by  $\sim 28$  per cent (cf. Krumholz, Klein & McKee 2012; Hansen et al. 2012). If we compare the cumulative MFs using the KS test, it returns statistics  $s = 0.24$  and  $p < 0.1$  per cent. We conclude that the OF- and the RF-samples are not drawn from the same underlying distribution. This conclusion is confirmed by an Anderson–Darling test (Stephens 1974).

If the fragmentation of a core into stars is a statistically self-similar process – in the sense that the probability that a core of mass  $M_{\text{CORE}}$  spawns a star of mass  $M_{\star}$  is the same as the probability that a core of mass  $\beta M_{\text{CORE}}$  spawns a star of mass  $\beta M_{\star}$  – the width of the observed IMF is

$$\sigma_{\text{CHAB}} \simeq \sqrt{\sigma_{\text{CORE}}^2 + \sigma_{\text{FRAG}}^2}. \quad (15)$$

Here,  $\sigma_{\text{CORE}}$  is the logarithmic standard deviation of the CMF, and  $\sigma_{\text{FRAG}}$  is the logarithmic standard deviation of the stellar MF from a single core. Equation (15) implicitly assumes that both the CMF, and the stellar MF from a single core, are approximately lognormal. Substituting  $\sigma_{\text{FRAG}} = \sigma_{\text{OF}}$ , we obtain

$$\sigma_{\text{CORE}} \simeq \sqrt{\sigma_{\text{CHAB}}^2 - \sigma_{\text{OF}}^2} \simeq 0.57 \pm 0.07. \quad (16)$$

In other words – if the assumption of statistically self-similar core fragmentation is correct – the CMF makes a larger contribution to the standard deviation of the IMF than the process of core fragmentation. However, we should be mindful that the fragmentation of more massive cores might be very different from those we have simulated here.

## 4 MULTIPLICITY

Most field stars with  $M_{\star} \gtrsim M_{\odot}$ , and a high fraction of those with lower mass, are in multiple systems (e.g. Raghavan et al. 2010; Whitworth & Lomax 2015). The fraction of newly formed stars in multiple systems is even higher, and the presumption is that some of these multiples are subsequently ionized by  $N$ -body interactions or tidal stresses to produce the distribution in the field. It follows that numerical simulations of star formation should (a) reproduce the multiplicity statistics observed, and (b) demonstrate how multiple systems actually form.

We use three multiplicity descriptors (e.g. Reipurth & Zinnecker 1993). The multiplicity frequency,

$$mf = \frac{B_2 + T_3 + Q_4 + Q_5 + \dots}{S_1 + B_2 + T_3 + Q_4 + Q_5 + \dots}, \quad (17)$$

gives the number of systems with more than one member (i.e. order higher than one). The higher-order frequency,

$$hf = \frac{T_3 + Q_4 + Q_5 + \dots}{S_1 + B_2 + T_3 + Q_4 + Q_5 + \dots}. \quad (18)$$

gives the number of systems with more than two members (i.e. order higher than two). The pairing factor,

$$pf = \frac{B_2 + 2T_3 + 3Q_4 + 4Q_5 + \dots}{S_1 + B_2 + T_3 + Q_4 + Q_5 + \dots}, \quad (19)$$

gives the average number of companions to a randomly picked primary star.

#### 4.1 VANDAM survey

We compare the multiplicity statistics from our simulations with those from the VANDAM survey (Tobin et al. 2016), which used the VLA to measure the multiplicity statistics of 64 Class 0/I multiple protostars with separations between 15 AU and 10,000 AU, in the Perseus molecular cloud. A proper comparison would require the generation of synthetic observations, taking account of sensitivity, beam size, UV-coverage, confusion and projection; for example, some of the close binary systems in our simulations have very small separations and might not be detectable as binaries. However, generating synthetic observations is outside the scope of this paper, and therefore we simply make direct comparisons between our simulations and the observations.

The protostars observed within the VANDAM survey are slightly more massive than the stars in our OF-sample. Tobin et al. (2016) do not provide masses for individual observed stars or multiple systems. However, using the protostellar luminosity function of McKee & Offner (2010), McKee & Offner (2011) they compute a protostellar mass function and expect their stars to be progenitors of K- and M-dwarfs ( $0.08\text{--}0.8 M_\odot$ ) with a mean protostellar mass of  $\sim 0.2 M_\odot$  of which  $\sim 14$  per cent have masses between  $0.7 M_\odot$  and  $2.5 M_\odot$ . In our simulations the mean protostellar mass at  $t_5$  is  $0.17 \pm 0.15 M_\odot$  (OF-sample) and  $0.26 \pm 0.25 M_\odot$  (RF-sample), respectively. Only 3 per cent (OF-sample) and 5 per cent (RF-sample) of the stars are more massive than  $0.7 M_\odot$ . Fig. 5 shows the stellar bolometric luminosity distribution of the multiple systems in our simulations at  $t_5$ . The luminosities are computed using the stellar evolution model by Offner et al. (2009; Sections 2.4 and 2.5). Since, at this point, most of the gas is either bound in stars or entrained by the outflows, we expect the stellar bolometric luminosity to be comparable with those observed by Tobin et al. (2016). Comparing the luminosities of multiple systems in our simulations to the VANDAM survey (Fig. 5) indicates that we are not probing exactly the same mass range. Despite this difference, the VANDAM survey is still the best survey of protostellar multiple systems and the only one we can compare our simulation with.

#### 4.2 Multiplicity statistics

Fig. 6 shows the fractions of systems that are single, binary, triple, etc., for the OF-sample (orange) and the RF-sample (blue), at  $t_{0.5}$  (top panel) and  $t_5$  (middle and bottom panels), compared with the VANDAM survey (grey). The top and middle panels show the fractions

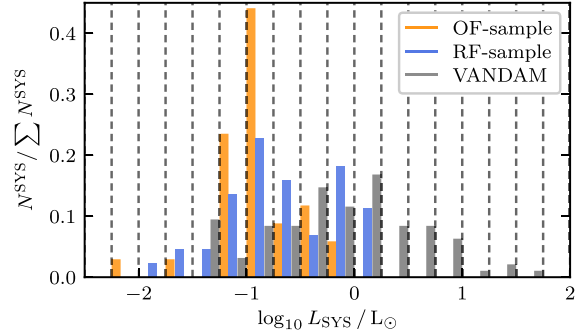


**Figure 5.** Stellar bolometric luminosities of all multiple systems in the OF-sample (orange) and RF-sample (blue) at  $t_5$  compared to the observed bolometric luminosities of multiples in the VANDAM survey (grey; Tobin et al. 2016). The luminosities of the VANDAM survey multiples are higher, suggesting that somewhat more massive stars are present.

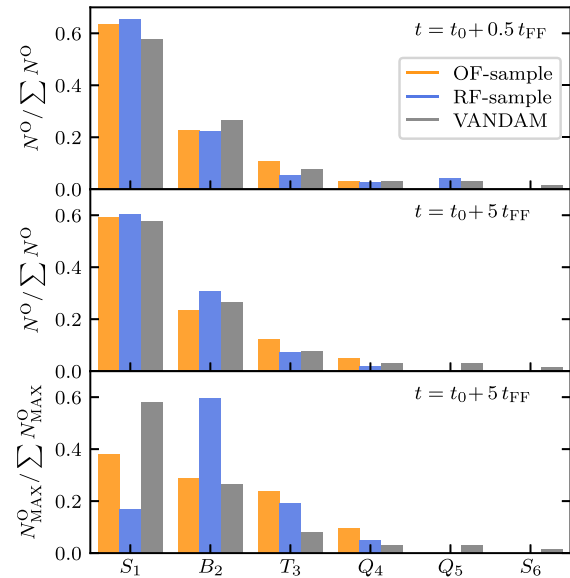


**Figure 6.** The fractions of systems that are single, binary, triple, etc., for the OF-sample (orange) and the RF-sample (blue), at  $t_{0.5}$  (top panel) and  $t_5$  (middle and bottom panels), compared with the VANDAM survey (grey). The top and middle panels include all systems, whereas the bottom panel includes only the highest-order system from each simulation. The OF-sample distribution changes little between the top and middle panels. In contrast, many of the quadruple and quintuple systems that form early in the RF-sample (top panel) quickly decay into binaries (middle panel); this is even clearer in the bottom panel where binaries dominate the distribution of highest-order systems for the RF-sample.

of all systems,  $N^O / \sum^O \{N^O\}$ , with  $N^O$  the number of systems of order  $O (= S_1, B_2, T_3, Q_4, Q_5, \text{etc.})$ . The bottom panel instead shows the distribution of  $N^O_{\text{MAX}} / \sum^O \{N^O_{\text{MAX}}\}$ , where  $N^O_{\text{MAX}}$  only takes account of the highest-order system from each simulation (Section 3.2).

Already by  $t_{0.5}$  (Fig. 6, top panel) the RF-sample includes many HOMS, including quintuples. However, these systems are very unstable, and by  $t_5$  (Fig. 6, middle panel) they have decayed to binaries. When taking into account only the highest-order systems, binaries dominate the distribution (Fig. 6, bottom panel).

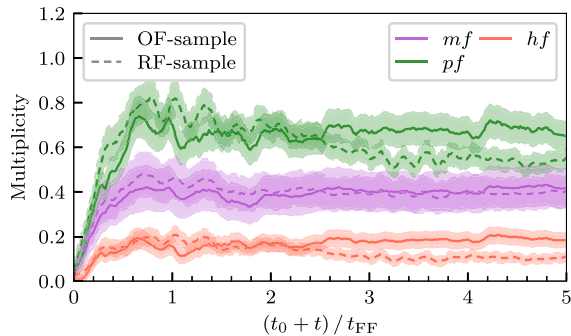


**Figure 7.** Time evolution of the multiplicity frequency, mf (purple), pairing factor, pf (green), and higher-order frequency, hf (red), for the OF-sample (solid lines) and RF-sample (dashed lines). The areas, surrounding the lines in corresponding colours, indicate the time-dependent propagated upper-limit on the Poisson uncertainty. The x-axis shows the time after the formation of the first sink, in units of the free-fall time. While the multiplicity frequency is comparable for the two samples, the pairing factor and higher-order frequency are significantly higher for the OF-sample after  $2.5t_{\text{FF}}$ .

In contrast, the multiplicity distribution of the OF-sample remains rather constant between  $t_{0.5}$  and  $t_5$ . It is a monotonically decreasing function of the order, and matches the VANDAM survey well; the highest-order systems are not dominated by binaries.

The fraction of singles that are the highest-order system is low (Fig. 6, bottom panel) because many singles are low-mass stars that are ejected during the dynamical interactions that reduce HOMs to binary systems. This is particularly true for the RF-sample, where 89 per cent of singles are ejecta; for the OF-sample only 67 per cent of singles are ejecta.

### 4.3 Time evolution of the stellar multiplicity

Fig. 7 shows the time evolution of the multiplicity descriptors defined in equations (17) through (19), for all the simulations in the OF- and RF-samples. Here, time is measured from when the first sink forms ( $t_0$ ), in units of the free-fall time of the birth core ( $t_{\text{FF}}$ ). Once star formation starts, the multiplicity rises rapidly up to  $\sim 0.6t_{\text{FF}}$ . Thereafter the multiplicity frequency is approximately constant and comparable for both samples,  $m_{\text{f,OF}} \sim m_{\text{f,RF}} \sim 0.40$ . For the OF-sample, most of the multiple systems are quite stable, and therefore the higher-order frequency and pairing factor are also approximately constant, at  $h_{\text{f,OF}} \sim 0.15$  and  $p_{\text{f,OF}} \sim 0.65$  respectively. However, for the RF-sample, the HOMs immediately start to eject lower-mass members and decay to binaries; this has no effect on the multiplicity frequency,  $m_{\text{f,RF}}$ , but the higher-order frequency and pairing factor both decrease steadily, and by  $t \sim 5t_{\text{FF}}$ , they are  $h_{\text{f,RF}} \sim 0.10$  and  $p_{\text{f,RF}} \sim 0.50$ .

The multiplicities of the OF- and RF-samples are very similar in the early phase of star formation. The RF-sample forms somewhat more multiples and forms them somewhat faster, but these differences are small, and most of the HOMs formed in the RF-sample quickly reduce to binaries. HOMs are more stable against disruption when outflows are present.

Table 4 compares mf, pf, and hf for both samples at  $t_5$  with the VANDAM survey. All the statistics for the OF-sample agrees with the VANDAM survey within the uncertainties;  $m_{\text{f,OF}}$  and  $h_{\text{f,OF}}$  agree very well, but  $p_{\text{f,OF}}$  only just agrees. For the RF-sample, only  $m_{\text{f,RF}}$  agrees with VANDAM, both  $p_{\text{f,RF}}$  and  $h_{\text{f,RF}}$  are much too low. This is largely due to the decay of HOMs in the RF-sample.

**Table 4.** Multiplicity statistics for the OF- and RF-samples at  $t_5$ , compared with the VANDAM survey (Tobin et al. 2016). The first column gives the sample, followed by the multiplicity frequency (equation 17), the pairing factor (equation 19), and the high-order frequency (equation 18).

Sample	mf	pf	hf
RF-sample	$0.40 \pm 0.07$	$0.51 \pm 0.05$	$0.09 \pm 0.02$
OF-sample	$0.40 \pm 0.09$	$0.63 \pm 0.06$	$0.17 \pm 0.03$
VANDAM	$0.40 \pm 0.06$	$0.71 \pm 0.06$	$0.16 \pm 0.04$

Note that a direct comparison with the VANDAM survey is biased since they observe slightly more massive stars than we produce in our simulations (Section 4.1). Observations show that the multiplicity fraction is strongly dependent on the primary mass (see, e.g. Fig. 1 in Whitworth & Lomax 2015). However, this relation is valid for main-sequence stars and it is not clear whether it holds for the pre-main-sequence regime. Taking this relation into account, it seems that our simulations produce a too high multiplicity, given the low protostellar masses. However, our simulations do not include magnetic fields. With magnetic fields, we would expect less fragmentation and hence a somewhat lower multiplicity (see the discussion in Section 4.6). The missing magnetic fields could possibly explain why we are matching the VANDAM survey so well, even though we are probing a lower mass regime.

### 4.4 Stability of triple systems

Fig. 7 shows that the fraction of HOMs in the RF-sample decreases after  $t_1$ , while the fraction is almost constant for the OF-sample. To confirm objectively that this is because the hierarchical triple systems in the OF-sample are more stable, we compute the two different criteria for the stability of hierarchical triple systems which Zhuchkov, Kiyaveva & Orlov (2010) has shown to be most reliable.

An hierarchical triple system is one in which a pair of stars (labelled individually ‘1’ and ‘2’, and together ‘1+2’) are on a tight orbit around one another, and this pair and a third star (labelled ‘3’) are then on a much wider orbit around one another. The masses of the stars are  $m_1$ ,  $m_2$ , and  $m_3$ , and the total mass of the tight pair is  $m_{\text{IN}} = m_1 + m_2$ . The semimajor axis and eccentricity of the tight orbit (involving stars 1 and 2) are  $a_{\text{IN}}$  and  $e_{\text{IN}}$ . The semimajor axis and eccentricity of the wide orbit (involving star 3 and the pair 1+2) are  $a_{\text{OUT}}$  and  $e_{\text{OUT}}$ . The system is hierarchical in the sense that  $a_{\text{OUT}} \gg a_{\text{IN}}$ . With these definitions, the criterion for stability developed by Aarseth (2003) is

$$f_{\text{A}} = 0.36 \frac{a_{\text{OUT}}(1 - e_{\text{OUT}})}{a_{\text{IN}}} \left[ \left( 1 + \frac{m_3}{m_{\text{IN}}} \right) \frac{1 + e_{\text{OUT}}}{\sqrt{1 - e_{\text{OUT}}}} \right]^{-2/5} > 1; \quad (20)$$

and the criterion developed by Valtonen, Karttunen & Gutzwiller (2007) is

$$f_{\text{V}} = 3 \frac{a_{\text{OUT}}(1 - e_{\text{OUT}})^{7/6}}{a_{\text{IN}}} \times \left[ \left( 1 + \frac{m_3}{m_{\text{IN}}} \right) \left( \frac{7}{4} + \frac{\cos(i)}{2} - \cos^2(i) \right) \right]^{-1/3} > 1, \quad (21)$$

where  $i$  is the angle between the angular momentum vectors of the tight and wide orbits.

Fig. 8 shows the time evolution of  $\bar{f}_{\text{A,OF}}$  (orange dashed line) and  $\bar{f}_{\text{V,OF}}$  (orange full line), i.e.  $f_{\text{A}}$  and  $f_{\text{V}}$  averaged over all the triple systems in the O-sample; and the time evolution of  $\bar{f}_{\text{A,RF}}$  (blue dashed line) and  $\bar{f}_{\text{V,RF}}$  (blue full line), i.e.  $f_{\text{A}}$  and  $f_{\text{V}}$  averaged over all the triple systems in the R-sample.  $\bar{f}_{\text{A,OF}}$  is almost indistinguishable from

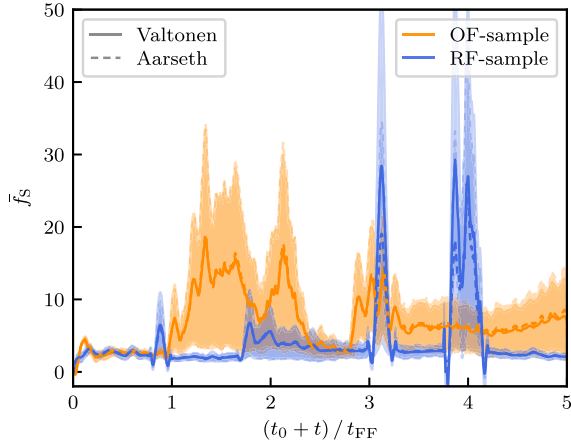


**Figure 8.** Time evolution of the Aarseth and Valtonen stability parameters (equations 20 and 21), averaged over all the triple systems in the OF-sample (orange), and over all the triple systems in the RF-sample (blue). The dashed lines show the results obtained for the Aarseth parameter ( $f_A$ ), and the solid lines show the results obtained for the Valtonen parameter ( $f_V$ ). At most times the dashed lines cannot be discerned because they sit on top of the solid lines. The coloured shading represents the standard deviation about the mean. Triple systems in the OF-sample are markedly more stable than triple systems in the RF-sample.

$\bar{f}_{V,OF}$ , and likewise  $\bar{f}_{A,RF}$  from  $\bar{f}_{V,RF}$ , indicating that they are mutually consistent. After  $t_{FF}$ ,  $\bar{f}_{A,OF}$ , and  $\bar{f}_{V,OF}$  are almost always well above  $\bar{f}_{A,RF}$  and  $\bar{f}_{V,RF}$ , on average by a factor  $2.53 \pm 0.05$ .  $\bar{f}_{A,OF}$  and  $\bar{f}_{V,OF}$  are also well above unity most of the time, and end up at  $\sim 7$ , so most of the triples are stable. In contrast,  $\bar{f}_{A,RF}$  and  $\bar{f}_{V,RF}$  are almost always  $\sim 2$ , so outliers with lower than average values tend to be unstable and decay.

#### 4.5 Twin binaries

Observations of low-mass binary systems reveal a high fraction of systems in which the ratio of the secondary mass to the primary mass,  $q = M_{*-S}/M_{*-P}$ , is close to unity (see Lucy 2006; Simon & Obbie 2009; Fernandez et al. 2017; Kounkel et al. 2019; El-Badry et al. 2019, or the review by Duchêne & Kraus (2013)); these systems are referred to as ‘twin binaries’. Fig. 9 shows the distribution of  $q$  for the 35 binary systems in the OF-sample, and the 44 binaries in the RF-sample. Both samples are peaked at high  $q$  with a tail towards low  $q$ , similar to the observations reported by Fernandez et al. (2017) and Kounkel et al. (2019). The convention (e.g. Kounkel et al. 2019; El-Badry et al. 2019) is to class binary systems with  $q \geq q_{\text{CRIT}} = 0.95$  as twins. Using this definition,  $f_{\text{TWIN-OF}} = 43$  per cent for the OF-sample, compared with  $f_{\text{TWIN-RF}} = 9$  per cent for the RF-sample. Since, with the small number of binaries in our sample, the ratio  $f_{\text{TWIN-OF}}/f_{\text{TWIN-RF}}$  is particularly high for  $q_{\text{CRIT}} = 0.95$ , we have varied  $q_{\text{CRIT}}$  between 0.90 and 0.99, but for all  $q$ -values in this range, there are always more twins in the OF-sample,  $f_{\text{TWIN-OF}}/f_{\text{TWIN-RF}} \geq 2.1 \pm 0.6$ .

The excess of almost equal mass binaries is thought to be the result of competitive accretion (Tokovinin 2000). For a low- $q$  binary, the secondary is on a larger orbit and therefore accretes matter with high specific angular momentum faster than the primary, thereby driving the mass ratio towards unity (Whitworth et al. 1995; Young & Clarke 2015; Matsumoto, Saigo & Takakuwa 2019). In the present context this happens because the binary is accreting from a circumbinary disc (see Fig. 1 and El-Badry et al. 2019).

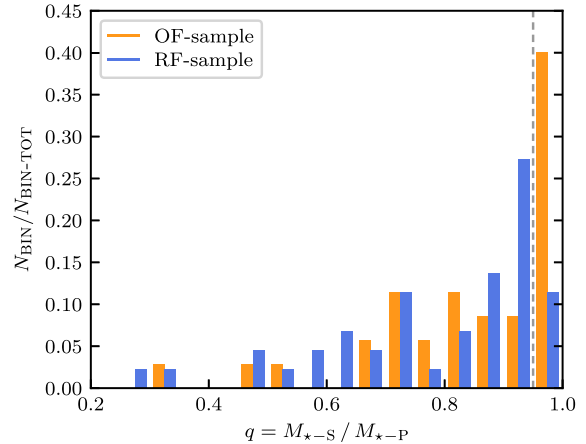


**Figure 9.** The normalized distribution of the mass ratio between the secondary and primary components,  $q = M_{*-S}/M_{*-P}$ , for all binary systems in the OF-sample (orange) and all binary systems in the RF-sample (blue), at  $t_5 \equiv t_0 + 5t_{FF}$ . At this stage there are 35 binaries in the OF sample, and 44 in the RF-sample. Both distributions are peaked at high  $q$ , with a tail towards low  $q$ . Outflow feedback appears to enhance the formation of twin binaries with  $q \geq 0.95$  (bin to the right of the dashed grey line).

Fig. 10 shows the two-dimensional probability density function (PDF) for the stellar mass  $M_*$  at  $t_5$  and the fraction of this mass acquired by disc accretion as opposed to direct infall,  $f_{\text{DISC}} = M_{\text{DISC}}/(M_{\text{DISC}} + M_{\text{DIRECT}})$ . The corresponding one-dimensional PDFs are shown in the top and right-hand panels.

To compute  $f_{\text{DISC}}$  we evaluate the mass flow through a sphere around each star, with the radius of the sphere equal to half the radius of the corresponding accretion disc. SPH particles are assigned to an accretion disc if (a) their density is  $> 10^{-14} \text{ g cm}^{-3}$ , (b) their rotational velocity component is greater than their radial velocity component with respect to the corresponding sink, and (c) they are gravitationally bound to the star. The mean disc radius for the OF-sample at  $t_2$  is  $\bar{r}_{\text{DISC}} = 103 \pm 55 \text{ AU}$ , which is in good agreement with recent observations of Class 0/I stars (Maury et al. 2019). Only stars in multiple systems that have both an accretion disc and a velocity lower than the escape speed contribute to the evaluation of  $f_{\text{DISC}}$ . The mass flow contributes to  $M_{\text{DISC}}$  if  $\frac{\pi - \theta_{\text{OPEN}}}{2} < \theta < \frac{\pi + \theta_{\text{OPEN}}}{2}$ , where  $\theta$  is the angle between the position vector (relative to the star) and the angular momentum axis of the disc. We set  $\theta_{\text{OPEN}} = 1/3 \pi$ ; varying  $\theta_{\text{OPEN}}$  between  $1/2 \pi$  and  $1/6 \pi$  shows no qualitative difference.

The peak of the OF-sample PDF is shifted to higher  $f_{\text{DISC}}$  compared with the peak of the RF-sample. A one-sided Mann–Whitney–U test confirms that this difference is significant with  $p \ll 1$  per cent. Outflow cavities stop stars from accreting so rapidly via direct infall, thereby enhancing the contribution from disc accretion and hence increasing the fraction of twin binaries in the OF-sample.

#### 4.6 Magnetic fields and disc fragmentation

Observations show that dense cores are threaded by magnetic fields (Troland & Crutcher 2008; Kandori et al. 2018). Recent numerical simulations suggest that magnetic fields have a profound impact on the star formation process (see, e.g. the review of Wurster & Li 2018). In the ideal MHD case, magnetic braking almost entirely prohibits the formation of accretion discs (Commerçon et al. 2012; Bate et al. 2014). However, the introduction of non-ideal MHD

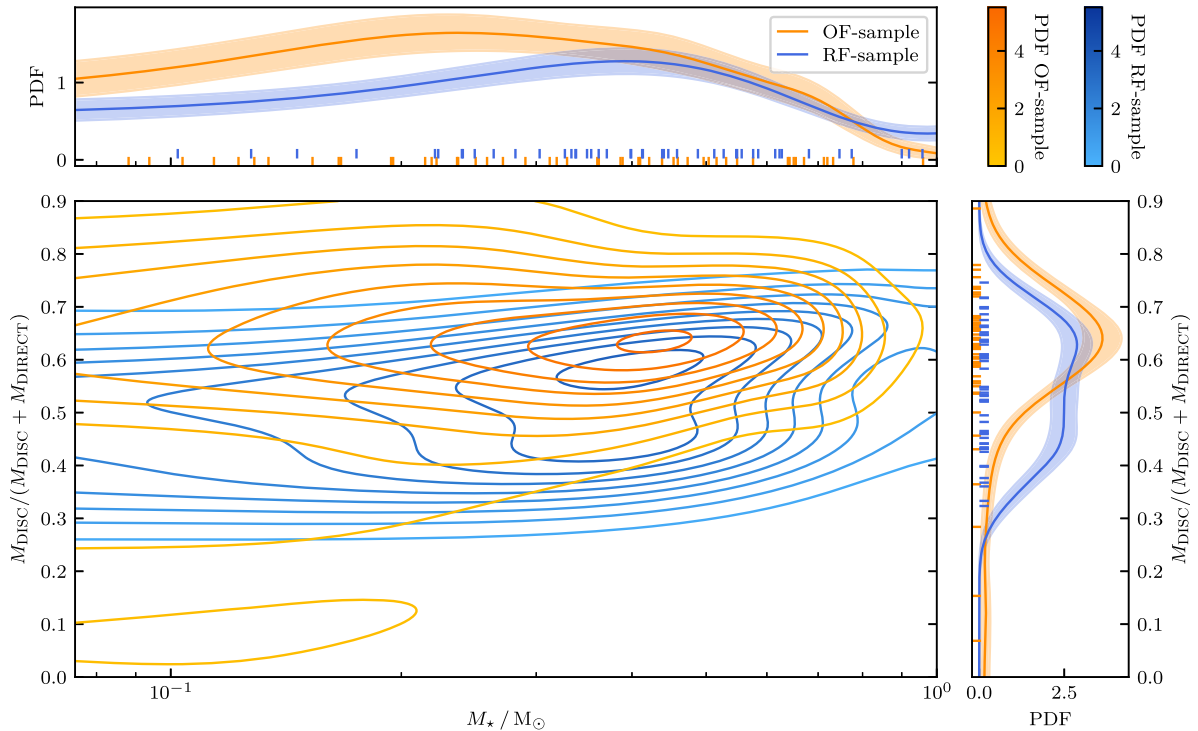


**Figure 10.** The two-dimensional probability density function (PDF) for the ‘final’ stellar mass,  $M_*$ , against the fraction of that mass that has been acquired by disc accretion (as opposed to by direct infall),  $M_{\text{disc}}/(M_{\text{disc}} + M_{\text{infall}})$ ; here ‘final’ means at  $t_S \equiv t_0 + 5t_{\text{ff}}$ . Contours at 10 per cent, 20 per cent, . . . . 90 per cent of the maximum probability are in shades of orange for the OF sample, and in shades of blue for the RF sample. The top panel shows the one-dimensional PDF for  $M_*$ . The right-hand panel shows the one-dimensional PDF for  $M_{\text{disc}}/(M_{\text{disc}} + M_{\text{infall}})$ . On the top and right-hand panels, the shaded regions indicate uncertainties estimated using bootstrapping, and the small tick marks represent individual systems. Evidently simulations with outflow feedback lead to stars accreting more gas by disc accretion.

effects mitigates the efficiency of magnetic braking to some extent (Hennebelle et al. 2016; Wurster, Price & Bate 2016; Zhao et al. 2018). Moreover, turbulence can cause a misalignment of the angular momentum and the magnetic field vector, which may significantly reduce the magnetic braking efficiency and enable the formation of massive discs (Seifried et al. 2013, 2015; Wurster et al. 2016; Gray, McKee & Klein 2018; Wurster & Li 2018; Wurster et al. 2019). Including the Hall-effect in non-ideal MHD simulations, Wurster & Li (2018) show that for the case of anti-aligned magnetic field and angular momentum vectors, they obtain results which are most similar to a pure hydrodynamical calculation. The magnetic Toomre- $Q$  parameter implies that these magnetized discs are generally more stable against fragmentation than pure hydrodynamical discs (Toomre 1964; Kim & Ostriker 2001; Wurster & Bate 2019).

Our code, GANDALF, does not currently include magnetic fields. With magnetic fields, we would expect to have slightly smaller discs that fragment less readily (Hennebelle & Inutsuka 2019; Wurster & Bate 2019). Therefore, the number of simulations forming a single star would increase resulting in fewer ejected stars and somewhat lower multiplicities.

Compared to the RF-sample, our OF-sample contains significantly more cores which form only a single star (Section 3.2). With episodic accretion feedback, the accretion discs are frequently severely disturbed and the amount of fragmentation is damped to a realistic level (Stamatellos et al. 2012; Lomax et al. 2014, 2015; Mercer & Stamatellos 2017). We therefore speculate that magnetic fields would

have a limited additional effect on disc fragmentation if episodic accretion feedback were taken into account.

## 5 SELF-REGULATION OF OUTFLOW FEEDBACK

### 5.1 Entrainment factor

Molecular outflows from protostars consist mainly of secondary entrained material (Tabone et al. 2017; Zhang et al. 2019), i.e. core gas that is swept up by the primary ejected gas. For low-mass star formation the entrained gas mass is estimated to range from  $0.1 M_\odot$  to  $1.0 M_\odot$  (Arce et al. 2007). The entrainment factor  $\epsilon_{\text{OF}}$  is defined as the ratio of total outflowing mass,  $M_{\text{OUT}}$ , to primary ejected mass,  $M_{\text{EJECT}}$ . An SPH particle contributes to  $M_{\text{OUT}}$  if its radial velocity is higher than the local escape velocity and at least  $0.1 \text{ km s}^{-1}$ . Using numerical MHD simulations, Offner & Chaban (2017) conclude that  $\epsilon_{\text{OF}} \sim 4$ .

Fig. 11 shows the entrainment factors at  $t_{0.5}$  (top row),  $t_{1.5}$  (middle row), and  $t_5$  (bottom row), plotted against the total stellar mass,  $M_{\text{TOTAL}}$  (left-hand column) and against outburst frequency,  $f_{\text{OB}}$  (right-hand column). Most simulations have  $\epsilon_{\text{OF}} \sim 7$ , but some have much higher values, up to  $\epsilon_{\text{OF}} \sim 33$ , particularly at low  $M_{\text{TOTAL}}$  and/or low  $f_{\text{OB}}$ . By  $t_5$  there is a well-defined anticorrelation between  $\epsilon_{\text{OF}}$  and  $M_{\text{TOTAL}}$ , with  $5 \lesssim \epsilon_{\text{OF}} \lesssim 26$  and Spearman Rank Correlation coefficient  $r_s = -0.94$  and  $p \ll 0.01$  per cent.

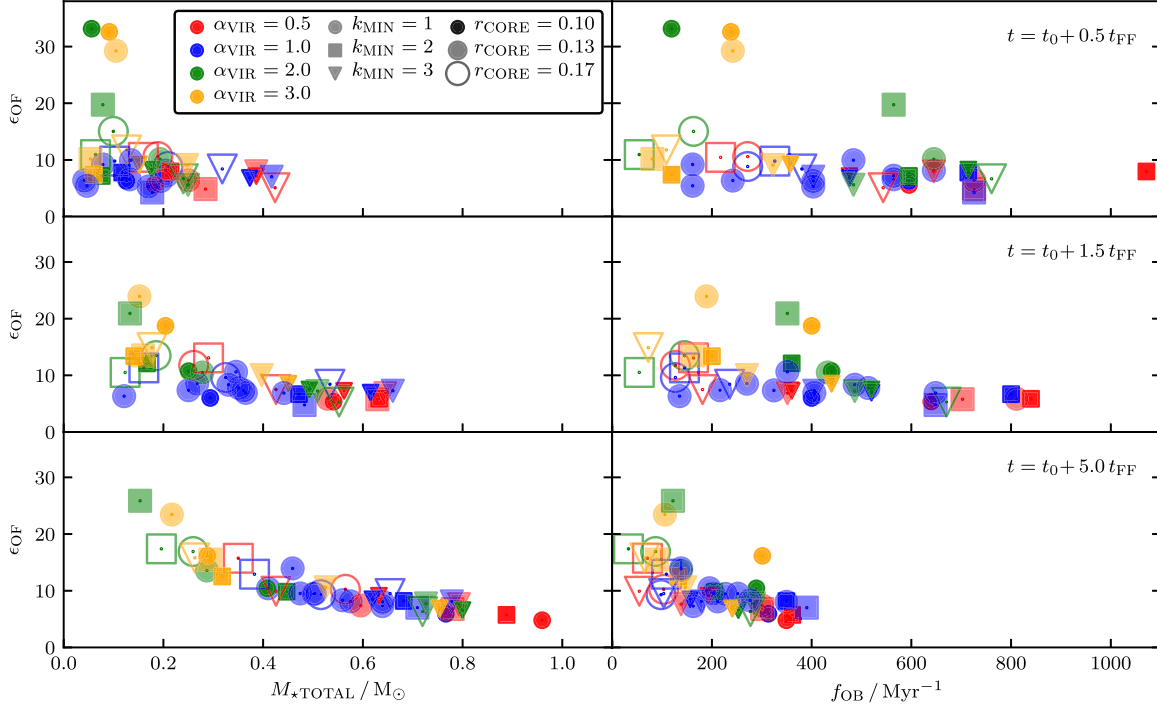


**Figure 11.** Entrainment factors,  $\epsilon_{\text{OF}} = M_{\text{OUT}}/M_{\text{EJECT}}$ , for all the simulations in the OF sample, plotted against total stellar mass,  $M_{\star\text{TOTAL}}$  (left-hand column), and against outburst frequency,  $f_{\text{OB}}$  (right-hand column), at  $t_{0.5}$  (top row),  $t_{1.5}$  (middle row), and  $t_5$  (bottom row), where  $t_t = t_0 + \tau t_{\text{FF}}$ . At  $t_5$ , the entrainment factors range from  $\epsilon_{\text{OF}} \simeq 5$  to  $\epsilon_{\text{OF}} \simeq 26$ . With increasing time,  $\epsilon_{\text{OF}}$  becomes strongly anticorrelated with  $M_{\star\text{TOTAL}}$ , and weakly anticorrelated with  $f_{\text{OB}}$ .

There are several possible reasons for this anticorrelation. The higher the total mass in stars, the less mass there is left in the core envelope, and therefore the less mass there is left to entrain. Moreover, as time advances the outflows are increasingly likely to be launched into cavities blown by previous outflows, in which case there is even less material for them to entrain; this is especially true when a core has formed a multiple system with aligned outflows.

The right-hand column of Fig. 11, shows the entrainment factor,  $\epsilon_{\text{OF}}$ , against the outburst frequency,  $f_{\text{OB}}$ , averaged between the time when the first star forms,  $t_0$ , and – respectively –  $t_{0.5}$ ,  $t_{1.5}$ , and  $t_5$ . There is an anticorrelation between  $\epsilon_{\text{OF}}$  and  $f_{\text{OB}}$  which gets stronger with time. By  $t_5$ , the Spearman rank correlation coefficient is  $r = -0.70$  with  $p \ll 0.01$  per cent. Simulations with lower  $f_{\text{OB}}$  (i.e. episodic accretion and outflow concentrated in a few massive outbursts) have higher  $\epsilon_{\text{OF}}$ . The asymptotic limit of high  $f_{\text{OB}}$  is continuous outflow, and this might explain the lower  $\epsilon_{\text{OF}} \sim 4$  found by Offner & Chaban (2017), since the protostars in their simulations generate continuous outflows.

## 5.2 Outflowing gas mass

Fig. 12 (right-hand column) shows the outflowing gas mass,  $M_{\text{OUT}}$ , for each simulation in the OF-sample, plotted against its total stellar mass,  $M_{\star\text{TOTAL}}$ , at  $t_{0.5}$ ,  $t_{1.5}$ , and  $t_5$ . At  $t_{0.5}$ ,  $M_{\text{OUT}}$  and  $M_{\star\text{TOTAL}}$  are tightly correlated,  $M_{\text{OUT}} \simeq 0.01 M_{\odot} + 0.58 M_{\star\text{TOTAL}}$ , with Spearman Rank Correlation coefficient  $r = 0.76$  and  $p \ll 0.01$  per cent. Since 10 per cent of the matter entering a sink is ejected, this corresponds to an average entrainment factor of  $\epsilon_{\text{OF}} \sim 0.58/0.1 \sim 6.4$ , in good agreement with Fig. 11.

At later times, the correlation remains strong but flattens, because cores with low  $M_{\star\text{TOTAL}}$  have more gas left, and therefore higher entrainment factors and more massive outflows (see Fig. 11). By  $t_5$ , the correlation has become  $M_{\text{OUT}} \simeq 0.29 M_{\odot} + 0.29 M_{\star\text{TOTAL}}$  with a non-zero intercept.

## 5.3 Relative star formation efficiency

Fig. 12 (left-hand column) shows the total stellar mass of each simulation in the OF-sample,  $M_{\star\text{TOTAL-OF}}$ , plotted against the total stellar mass in the corresponding simulation in the RF-sample,  $M_{\star\text{TOTAL-RF}}$ , at  $t_{0.5}$ ,  $t_{1.5}$ , and  $t_5$ . At  $t_{0.5}$ , the masses are strongly correlated,  $M_{\star\text{TOTAL-OF}} \sim 0.60 M_{\star\text{TOTAL-RF}}$ , with Spearman Rank Correlation coefficient  $r = 0.90$  and  $p \ll 0.01$  per cent. Thus, the early star formation rate (SFR) is  $\sim 40$  per cent lower if outflows are present.

This strong correlation arises because (a)  $f_{\text{EJECT}} = 0.1$ , i.e. exactly 10 per cent of the matter entering a sink is ejected and the remaining 90 per cent is accreted, so  $dM_{\star}/dt|_{\text{OF}} = 9dM/dt|_{\text{EJECT}}$ ; and (b) in the early stages the entrainment factor is approximately universal,  $\epsilon_{\text{OF}} \simeq 7$ , so  $dM/dt|_{\text{OUT}} \sim 7dM/dt|_{\text{EJECT}}$ . It follows that

$$\frac{dM_{\star}/dt|_{\text{OF}}}{dM_{\star}/dt|_{\text{OF}} + dM/dt|_{\text{OUT}}} \sim \frac{9}{9+7} = 56 \text{ per cent.} \quad (22)$$

If one assumes that, in the absence of outflow feedback, the outflowing matter would have ended up in the stars, the mass of stars in the OF-sample should be of order 56 per cent of the mass of stars in the RF-sample.

At later times the correlation persists, but with greater scatter. For example, at  $t_5$ ,  $M_{\star\text{TOTAL-OF}} \simeq 0.53 M_{\star\text{TOTAL-RF}}$  with Spearman Rank Correlation coefficient  $r = 0.65$  and  $p < 0.01$  per cent.

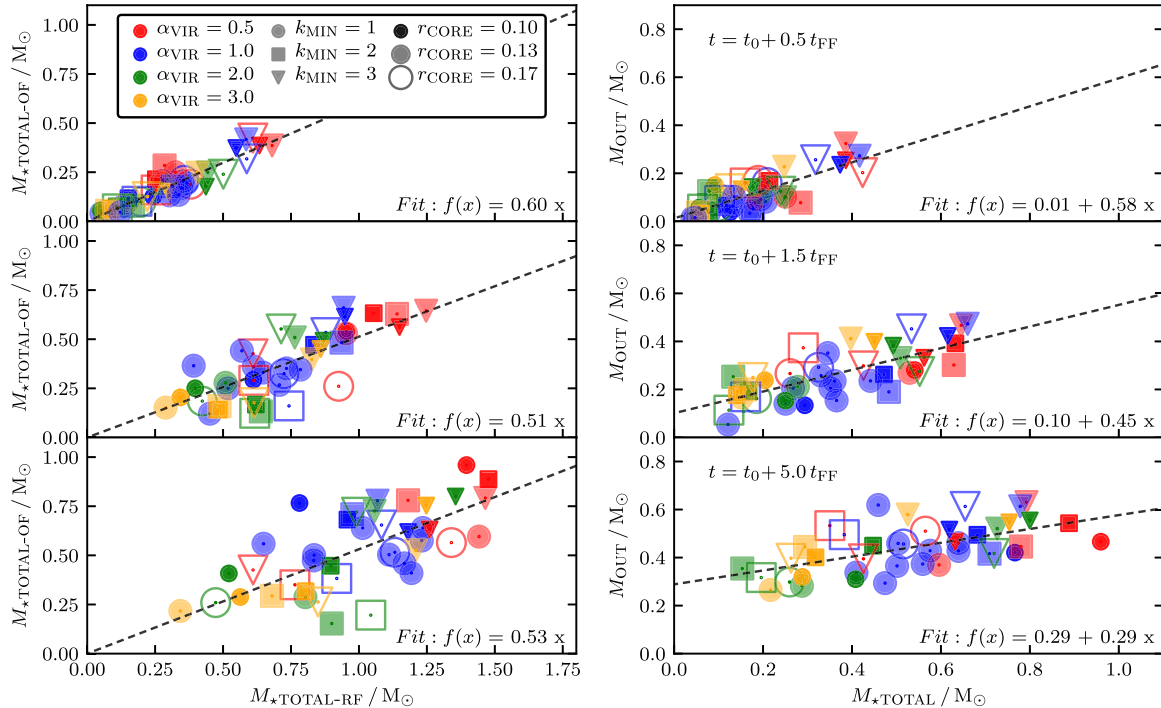


**Figure 12.** Left: The total stellar mass for each simulation in the OF-sample against the total stellar mass for the corresponding simulation in the RF sample, at  $t_{0.5}$  (top),  $t_{1.5}$  (middle), and  $t_5$  (bottom), where  $t_t = t_0 + \tau t_{\text{FF}}$ . The dashed lines are linear fits to the data, with  $0.5 \lesssim M_{\star\text{TOTAL-OF}}/M_{\star\text{TOTAL-RF}} \lesssim 0.6$ . At  $t_{0.5}$  the fit is very tight, but the scatter around the fit increases at later times, due to changes in the entrainment factor and hence changes in the effectiveness of outflow feedback (see Fig. 11). Right: The outflowing gas mass,  $M_{\text{OUT}}$ , for all the simulations in the OF sample, against the total stellar mass,  $M_{\star\text{TOTAL}}$ , at  $t_{0.5}$  (top),  $t_{1.5}$  (middle), and  $t_5$  (bottom). At  $t_{0.5}$ , there is a strong correlation,  $M_{\text{OUT}} \simeq 0.01 M_{\odot} + 0.58 M_{\star\text{TOTAL}}$ . At later times, the correlation remains strong, but flattens, becoming  $M_{\text{OUT}} \simeq 0.29 M_{\odot} + 0.29 M_{\star\text{TOTAL}}$  at  $t_5$ ; this is because by this stage cores with relatively low  $M_{\star\text{TOTAL}}$  have more gas left, and therefore higher entrainment factors and –relatively speaking– more massive outflows (see Fig. 11).

#### 5.4 Possible effects of magnetic fields on the outflow structure

Magnetic fields are obviously very important for protostellar outflows since magnetic fields are necessary to launch outflows in the first place (Bally 2016). This regime is covered by our episodic outflow subgrid model, which is based on the episodic MRI instability of the inner disc. Computing the outflow launching self-consistently is not expected to alter the outflow properties significantly with respect to our subgrid model (see, e.g. Federrath et al. 2014).

The influence of magnetic fields on the already launched or entrained gas is not well understood. Outflows are highly connected to the stellar accretion rate. Therefore, it is complicated to disentangle (i) the lower accretion rate due to magnetic fields (Offner & Chaban 2017) from (ii) the direct effects of magnetic fields on the outflowing gas. We argue that (i) episodic outflows are highly self-regulated (Rohde et al. 2019) and that therefore a slower collapse would not alter the outflow properties notably. Offner & Chaban (2017) show that magnetic fields do not affect the entrainment factor (Section 5.1) and therefore (ii) the influence on already launched gas is limited. Moreover, the typical velocity of outflowing gas, up to  $\sim 100 \text{ km s}^{-1}$ , is much higher than the characteristic Alfvén speed,  $v_A = B/\sqrt{\rho} = 1 \text{ km s}^{-1}$  for typical values of  $B = 10 \mu\text{G}$  and  $\rho = 10^{-20} \text{ g cm}^{-3}$  for the low-density gas in the outflow cavity. Therefore, we argue that including magnetic fields would not alter the properties of the outflows in this work significantly.

However, in simulations of star cluster formation with initial gas masses of  $100\text{--}1000 M_{\odot}$ , it has been shown that the combination of outflows and magnetic fields is important. The momentum delivered by the outflows coupled to the magnetic fields maintains turbulence such that the parental molecular clouds stay close to virial equilibrium (see the review by Krumholz & Federrath 2019). Therefore, we might not be able to expand our simulations to larger scales without taking into account the potentially significantly higher impact of magnetic fields.

## 6 CONCLUSIONS

Outflows are the dominant feedback mechanism in the early phase of low-mass star formation. However, the consequences of outflow feedback for the evolution of a pre-stellar core are not well understood. Three questions are especially important. (1) Does outflow feedback affect the properties of the individual stars formed? (2) Does outflow feedback affect the stellar multiplicity statistics? (3) How much does outflow feedback reduce the SFE?

To answer these questions, we have performed a large ensemble of smoothed particle hydrodynamics simulations of dense pre-stellar cores. All the cores have the dimensionless density profile of a Bonnor–Ebert sphere, but we vary the initial core radius ( $r_{\text{CORE}} = 0.017, 0.013, 0.01 \text{ pc}$ ), the initial virial ratio ( $\alpha_{\text{VIR}} = 0.5, 1.0, 2.0, 3.0$ ), the wavenumber of the dominant mode in the initial turbulent velocity field ( $k_{\text{MIN}} = 1, 2, 3$ ). For each combination

of ( $r_{\text{CORE}}, \alpha_{\text{VIR}}, k_{\text{MIN}}$ ) and eight additional runs with different turbulent seeds, we perform one simulation with outflow feedback, and one without. The resulting ensemble of 88 simulations reveals the following features.

(i) The stellar statistics (total mass in stars, number of stars, mass of most massive star, total mass and order of the highest-order system) depend only weakly on the initial conditions of the birth core, i.e. ( $r_{\text{CORE}}, \alpha_{\text{VIR}}, k_{\text{MIN}}$ ).

(ii) The total mass in stars, the mass of the most massive star and the total mass of the highest-order system all tend to decrease markedly when outflow feedback is included. The total number of stars and the order of the highest-order system tend to decrease very slightly when outflow feedback is included – except for the cores with low  $\alpha_{\text{VIR}}$  where these trends are reversed.

(iii) The distribution of stellar masses can be represented by a lognormal. Without outflow feedback the mean and standard deviation of  $\log_{10}(M_*/M_{\odot})$  are  $-0.74$  and  $0.44$ . When outflow feedback is included, they become  $-0.89$  and  $0.40$ , i.e. the mean mass is reduced by  $\sim 30$  per cent.

(iv) The simulations without outflow feedback produce a large number of HOMs, but many of them are unstable and quickly decay to binaries. As a result, these simulations deliver an higher-order frequency (hf) and a pairing factor (pf) that are inconsistent with the values observed in the VANDAM survey by Tobin et al. (2016).

(v) The simulations with outflow feedback produce slightly fewer HOMs, but most of them are stable. As a result, these simulations deliver an hf and a pf which, within the uncertainties, agree with the distribution observed in the VANDAM survey by Tobin et al. (2016).

(vi) The inclusion of outflow feedback increases considerably the fraction of twin binaries with almost equal-mass components. This is because outflow feedback reduces the role of direct infall on to a growing protostar, so the components of a binary system have to acquire their mass by accretion from a circumbinary disc.

(vii) The mean entrainment factor (the ratio between outflowing mass at large radius and the mass ejected from the protostar and its disc) is  $\bar{\epsilon}_{\text{OF}} \sim 7$ , significantly larger than the value of 4 obtained by Offner & Chaban (2017) in simulations with *continuous* outflow. Above average  $\epsilon_{\text{OF}}$  values are confined to cores with low total stellar mass (especially those with high  $\alpha_{\text{VIR}}$  and low  $r_{\text{CORE}}$ ), because there is then more gas left to entrain (and it is more easily unbound).

(viii) In the early stages, the outflowing mass,  $M_{\text{OUT}}$ , is approximately proportional to the total stellar mass,  $M_{\text{OUT}} \sim 0.7M_{\text{TOTAL}}$ . At later times this is still true in cores where  $M_{\text{TOTAL}}$  is low, but in cores where  $M_{\text{TOTAL}}$  is high, and there is less gas left to push out,  $M_{\text{OUT}} < 0.7M_{\text{TOTAL}}$ .

(ix) Since we have assumed that the rate of mass ejection from a protostar is exactly proportional to the rate of mass accretion on to the protostar, and since there is not a huge variation in entrainment factors, the mass converted into stars when outflow feedback is included is an approximately constant fraction of the mass converted into stars when there is no outflow feedback; after five free-fall times this fraction is  $\sim 53$  per cent. This is partly because on average the stars have lower masses, and partly because there are fewer of them.

## ACKNOWLEDGEMENTS

The authors like to thank the anonymous referee for the comments that helped to significantly improve the paper. PFR, SW, SDC, and AK acknowledge support via the European Research Council (ERC) starting grant No. 679852 ‘RADFEEDBACK’. DS and SW thank the Deutsche Forschungsgemeinschaft (DFG) for funding

via the SFB 956 ‘Conditions & impact of star formation’, via the subprojects C5 and C6. APW gratefully acknowledges the support of a consolidated grant (ST/K00926/1) from the UK Science and Technology Facilities Council. The authors gratefully acknowledge the Gauss Centre for Supercomputing e.V. ([www.gauss-centre.eu](http://www.gauss-centre.eu)) for funding this project (ID: pr47pi) by providing computing time on the GCS Supercomputer SuperMUC at Leibniz Supercomputing Centre (<http://www.lrz.de>). PFR acknowledges D. Price for providing the visualization tool SPLASH (Price 2011).

## DATA AVAILABILITY

The data underlying this article will be shared on reasonable request to the corresponding author.

## REFERENCES

- Aarseth S. J., 2003, *Gravitational N-Body Simulations*. Cambridge Univ. Press, Cambridge
- Alves J., Lada C., Lada E., 2001, *The Messenger*, 103, 1
- André P., Belloche A., Motte F., Peretto N., 2007, *A&A*, 472, 519
- André P., Di Francesco J., Ward-Thompson D., Inutsuka S. I., Pudritz R. E., Pineda J. E., 2014, in Beuther H., Klessen R. S., Dullemond C. P., Henning T., eds, *Protostars and Planets VI*, Univ. Arizona Press, Tucson, AZ, p. 27
- André P. et al., 2010, *A&A*, 518, L102
- Arce H. G., Borkin M. A., Goodman A. A., Pineda J. E., Halle M. W., 2010, *ApJ*, 715, 1170
- Arce H. G., Sargent A. I., 2006, *ApJ*, 646, 1070
- Arce H. G., Shepherd D., Gueth F., Lee C.-F., Bachiller R., Rosen A., Beuther H., 2007, in Reipurth B., Jewitt D., Keil K., eds, *Protostars and Planets V*, Univ. Arizona Press, Tucson, AZ, 245
- Bally J., 2016, *ARA&A*, 54, 491
- Bate M. R., 2005, *MNRAS*, 363, 363
- Bate M. R., 2009a, *MNRAS*, 392, 1363
- Bate M. R., 2009b, *MNRAS*, 397, 232
- Bate M. R., 2012, *MNRAS*, 419, 3115
- Bate M. R., Bonnell I. A., 2005, *MNRAS*, 356, 1201
- Bate M. R., Bonnell I. A., Price N. M., 1995, *MNRAS*, 277, 362
- Bate M. R., Tricco T. S., Price D. J., 2014, *MNRAS*, 437, 77
- Bell K. R., Lin D. N. C., 1994, *ApJ*, 427, 987
- Bjerkeli P., van der Wiel M. H. D., Harsono D., Ramsey J. P., Jørgensen J. K., 2016, *Nature*, 540, 406
- Blandford R. D., Payne D. G., 1982, *MNRAS*, 199, 883
- Bonnor W. B., 1956, *Z. Astrophys.*, 39, 143
- Calvet N., Hartmann L., Kenyon S. J., 1993, *ApJ*, 402, 623
- Cesaroni R. et al., 2018, *A&A*, 612, A103
- Chabrier G., 2003, *PASP*, 115, 763
- Chen X., Arce H. G., Zhang Q., Launhardt R., Henning T., 2016, *ApJ*, 824, 72
- Chen X. et al., 2013, *ApJ*, 768, 110
- Choi M. et al., 2017, *ApJS*, 232, 24
- Commerçon B., Hennebelle P., Audit E., Chabrier G., Teyssier R., Henning T., 2012, in Capuzzo-Dolcetta R., Limongi M., Tornambè A., eds, *ASP Conf. Ser. Vol. 453, Advances in Computational Astrophysics: Methods, Tools, and Outcome*, Astron. Soc. Pac., San Francisco, p. 13
- Connelley M. S., Reipurth B., Tokunaga A. T., 2008, *AJ*, 135, 2496
- Croswell K., Hartmann L., Avrett E. H., 1987, *ApJ*, 312, 227
- Cullen L., Dehnen W., 2010, *MNRAS*, 408, 669
- Cunningham A. J., Klein R. I., Krumholz M. R., McKee C. F., 2011, *ApJ*, 740, 107
- Cunningham A. J., Krumholz M. R., McKee C. F., Klein R. I., 2018, *MNRAS*, 476, 771
- Duchêne G., Bontemps S., Bouvier J., André P., Djujvik A. A., Ghez A. M., 2007, *A&A*, 476, 229
- Duchêne G., Kraus A., 2013, *ARA&A*, 51, 269

- Duchêne G., Lacour S., Moraux E., Goodwin S., Bouvier J., 2018, *MNRAS*, 478, 1825
- Ebert R., 1957, *ZA*, 42, 263
- El-Badry K., Rix H.-W., Tian H., Duchêne G., Moe M., 2019, *MNRAS*, 489, 5822
- Feddersen J. R. et al., 2020, *ApJ*, 896, 11
- Federrath C., Schrön M., Banerjee R., Klessen R. S., 2014, *ApJ*, 790, 128
- Fernandez M. A. et al., 2017, *PASP*, 129, 084201
- Frank A. et al., 2014, in Beuther H., Klessen R. S., Dullemond C. P., Henning T., eds, *Protostars and Planets VI*. Univ. Arizona Press, Tucson, AZ, p. 451
- Friesen R. K. et al., 2017, *ApJ*, 843, 63
- Goodwin S. P., Kroupa P., Goodman A., Burkert A., 2007, in Reipurth B., Jewitt D., Keil K., eds, *Protostars and Planets V*. Univ. Arizona Press, Tucson, AZ, p. 133
- Gray W. J., McKee C. F., Klein R. I., 2018, *MNRAS*, 473, 2124
- Guszejnov D., Hopkins P. F., Krumholz M. R., 2017, *MNRAS*, 468, 4093
- Guszejnov D., Krumholz M. R., Hopkins P. F., 2016, *MNRAS*, 458, 673
- Hansen C. E., Klein R. I., McKee C. F., Fisher R. T., 2012, *ApJ*, 747, 22
- Hartigan P., Edwards S., Ghandour L., 1995, *ApJ*, 452, 736
- Hartmann L., 1997, in Reipurth B., Bertout C., eds, *IAU Symp. Vol. 182, Herbig-Haro Flows and the Birth of Stars*, Kluwer, Dordrecht, p. 391
- Hartmann L., Calvet N., 1995, *AJ*, 109, 1846
- Hartmann L., Stauffer J. R., 1989, *AJ*, 97, 873
- Hennebelle P., Commerçon B., Chabrier G., Marchand P., 2016, *ApJ*, 830, L8
- Hennebelle P., Commerçon B., Joos M., Klessen R. S., Krumholz M., Tan J. C., Teyssier R., 2011, *A&A*, 528, A72
- Hennebelle P., Inutsuka S.-I., 2019, *Front. Astron. Space Sci.*, 6, 5
- Hirota T., Machida M. N., Matsushita Y., Motogi K., Matsumoto N., Kim M. K., Burns R. A., Honma M., 2017, *Nat. Astron.*, 1, 0146
- Holman K., Walch S. K., Goodwin S. P., Whitworth A. P., 2013, *MNRAS*, 432, 3534
- Hubber D. A., Rosotti G. P., Booth R. A., 2018, *MNRAS*, 473, 1603
- Hubber D. A., Walch S., Whitworth A. P., 2013, *MNRAS*, 430, 3261
- Johnstone D., Wilson C. D., Moriarty-Schieven G., Joncas G., Smith G., Gregersen E., Fich M., 2000, *ApJ*, 545, 327
- Jones M. O., Bate M. R., 2018, *MNRAS*, 480, 2562
- Kandori R. et al., 2018, *ApJ*, 865, 121
- Kim W.-T., Ostriker E. C., 2001, *ApJ*, 559, 70
- Kounkel M. et al., 2019, *AJ*, 157, 196
- Königl A., Pudritz R. E., 2000, in Mannings V., Boss A. P., Russell S. S., eds, *Protostars and Planets IV*, Univ. Arizona Press, Tucson, AZ, p. 759
- Könyves V. et al., 2015, *A&A*, 584, A91
- Könyves V. et al., 2020, *A&A*, 635, A34
- Kroupa P., 2001, *MNRAS*, 322, 231
- Kroupa P., 2002, *Science*, 295, 82
- Krumholz M. R., Federrath C., 2019, *Front. Astron. Space Sci.*, 6, 7
- Krumholz M. R., Klein R. I., McKee C. F., 2012, *ApJ*, 754, 71
- Krumholz M. R. et al., 2014, in Beuther H., Klessen R. S., Dullemond C. P., Henning T., eds, *Protostars and Planets VI*, Univ. Arizona Press, Tucson, AZ, p. 243
- Kuffmeier M., Calcutt H., Kristensen L. E., 2019, *A&A*, 628, A112
- Kuiper R., Yorke H. W., Turner N. J., 2015, *ApJ*, 800, 86
- Launhardt R. et al., 2009, *A&A*, 494, 147
- Lee C.-F., Ho P. T. P., Li Z.-Y., Hirano N., Zhang Q., Shang H., 2017, *Nat. Astron.*, 1, 0152
- Leroy A. K., Walter F., Brinks E., Bigiel F., de Blok W. J. G., Madore B., Thornley M. D., 2008, *AJ*, 136, 2782
- Lewis B. T., Bate M. R., 2017, *MNRAS*, 467, 3324
- Li P. S., Klein R. I., McKee C. F., 2018, *MNRAS*, 473, 4220
- Liu J., Qiu K., Wyrowski F., Menten K., Guesten R., Cao Y., Wang Y., 2018, *ApJ*, 860, 106
- Lomax O., Whitworth A. P., Hubber D. A., Stamatellos D., Walch S., 2014, *MNRAS*, 439, 3039
- Lomax O., Whitworth A. P., Hubber D. A., Stamatellos D., Walch S., 2015, *MNRAS*, 447, 1550
- Lombardi J. C., McNally W. G., Faber J. A., 2015, *MNRAS*, 447, 25
- Louvet F., Dougados C., Cabrit S., Mardones D., Ménard F., Tabone B., Pinte C., Dent W. R. F., 2018, *A&A*, 618, A120
- Lucy L. B., 2006, *A&A*, 457, 629
- Lynden-Bell D., 2003, *MNRAS*, 341, 1360
- Machida M. N., 2014, *ApJ*, 796, L17
- Machida M. N., Basu S., 2019, *ApJ*, 876, 149
- Machida M. N., Hosokawa T., 2013, *MNRAS*, 431, 1719
- Machida M. N., Inutsuka S.-I., Matsumoto T., 2008, *ApJ*, 676, 1088
- Machida M. N., Inutsuka S.-I., Matsumoto T., 2009, *Astrophys. Space Sci. Proc.*, 13, 405
- Marsh K. A. et al., 2016, *MNRAS*, 459, 342
- Matsumoto T., Saigo K., Takakuwa S., 2019, *ApJ*, 871, 36
- Matt S., Pudritz R. E., 2005, *ApJ*, 632, L135
- Matzner C. D., McKee C. F., 1999, *ApJ*, 526, L109
- Maury A. J. et al., 2019, *A&A*, 621, A76
- McKee C. F., Offner S. R. R., 2011, in Alves J., Elmegreen B. G., Girart J. M., Trimble V., eds, *IAU Symposium, Vol. 270, Computational Star Formation*. Kluwer, Dordrecht, p. 73
- McKee C. F., Offner S. R. R., 2010, *ApJ*, 716, 167
- Mercer A., Stamatellos D., 2017, *MNRAS*, 465, 2
- Monaghan J. J., Lattanzio J. C., 1985, *A&A*, 149, 135
- Morris J. P., Monaghan J. J., 1997, *J. Comput. Phys.*, 136, 41
- Mundt R., Fried J. W., 1983, *ApJ*, 274, L83
- Murray D., Goyal S., Chang P., 2018, *MNRAS*, 475, 1023
- Murray N., 2011, *ApJ*, 729, 133
- Myers A. T., Klein R. I., Krumholz M. R., McKee C. F., 2014, *MNRAS*, 439, 3420
- Myers P. C., 2009, *ApJ*, 700, 1609
- Nakamura F., Li Z.-Y., 2007, *ApJ*, 662, 395
- Nakano T., Hasegawa T., Morino J.-I., Yamashita T., 2000, *ApJ*, 534, 976
- Nakano T., Hasegawa T., Norman C., 1995, *ApJ*, 450, 183
- Nisini B., Antonucci S., Alcalá J. M., Giannini T., Manara C. F., Natta A., Fedele D., Biazzo K., 2018, *A&A*, 609, A87
- Offner S. R. R., 2011, in Alves J., Elmegreen B. G., Girart J. M., Trimble V., eds, *IAU Symp. Vol. 270, Computational Star Formation*. Kluwer, Dordrecht, p. 231
- Offner S. R. R., Arce H. G., 2014, *ApJ*, 784, 61
- Offner S. R. R., Chaban J., 2017, *ApJ*, 847, 104
- Offner S. R. R., Klein R. I., McKee C. F., Krumholz M. R., 2009, *ApJ*, 703, 131
- Pelletier G., Pudritz R. E., 1992, *ApJ*, 394, 117
- Peters T., Klaassen P. D., Mac Low M.-M., Schrön M., Federrath C., Smith M. D., Klessen R. S., 2014, *ApJ*, 788, 14
- Pineda J. E., Goodman A. A., Arce H. G., Caselli P., Longmore S., Corder S., 2011, *ApJ*, 739, L2
- Pineda J. E. et al., 2015, *Nature*, 518, 213
- Plunkett A. L., Arce H. G., Corder S. A., Mardones D., Sargent A. I., Schnee S. L., 2013, *ApJ*, 774, 22
- Price D. J., 2011, *SPLASH: An Interactive Visualization Tool for Smoothed Particle Hydrodynamics Simulations*, Astrophysics Source Code Library, record ascl:1103.004
- Price D. J., Tricco T. S., Bate M. R., 2012, *MNRAS*, 423, L45
- Pudritz R. E., Ouyed R., Fendt C., Brandenburg A., 2007, in Reipurth B., Jewitt D., Keil K., eds, *Protostars and Planets V*. Univ. Arizona Press, Tucson, AZ, p.277
- Raghavan D. et al., 2010, *ApJS*, 190, 1
- Reipurth B., 1989, *Nature*, 340, 42
- Reipurth B., Bally J., 2001, *ARA&A*, 39, 403
- Reipurth B., Zinnecker H., 1993, *A&A*, 278, 81
- Rice W. K. M., Armitage P. J., Mamatsashvili G. R., Lodato G., Clarke C. J., 2011, *MNRAS*, 418, 1356
- Rohde P. F., Walch S., Seifried D., Whitworth A. P., Clarke S. D., Hubber D. A., 2019, *MNRAS*, 483, 2563
- Saiki Y., Machida M. N., 2020, *ApJ*, 897, L22
- Samal M. R., Chen W. P., Takami M., Jose J., Froebrich D., 2018, *MNRAS*, 477, 4577
- Schruba A., Kruijssen J. M. D., Leroy A. K., 2019, *ApJ*, 883, 2

3612 *P. F. Rohde et al.*

- Seifried D., Banerjee R., Pudritz R. E., Klessen R. S., 2013, *MNRAS*, 432, 3320
- Seifried D., Banerjee R., Pudritz R. E., Klessen R. S., 2015, *MNRAS*, 446, 2776
- Seifried D., Pudritz R. E., Banerjee R., Duffin D., Klessen R. S., 2012 *MNRAS*, 422, 347
- Shan Y. et al., 2017, *ApJ*, 846, 93
- Shu F. H., Adams F. C., 1987, in Appenzeller I., Jordan C., eds, IAU Symp. Vol. 122, Circumstellar Matter. Kluwer, Dordrecht, p. 7
- Shu F. H., Lizano S., Ruden S. P., Najita J., 1988, *ApJ*, 328, L19
- Simon M., Obbie R. C., 2009, *AJ*, 137, 3442
- Springel V., Hernquist L., 2002, *MNRAS*, 333, 649
- Stamatellos D., Whitworth A. P., Bisbas T., Goodwin S., 2007, *A&A*, 475, 37
- Stamatellos D., Whitworth A. P., Hubber D. A., 2012, *MNRAS*, 427, 1182
- Stephens M. A., 1974, *J. Am. Stat. Assoc.*, 69, 730
- Tabone B. et al., 2017, *A&A*, 607, L6
- Tafalla M., Myers P. C., Caselli P., Walmsley C. M., 2004, *A&A*, 416, 191
- Tafalla M., Santiago-García J., Hacar A., Bachiller R., 2010, *A&A*, 522, A91
- Tan J. C., McKee C. F., 2004, *ApJ*, 603, 383
- Tobin J. J. et al., 2016, *ApJ*, 818, 73
- Tobin J. J. et al., 2018, *ApJ*, 867, 43
- Tokovinin A. A., 2000, *A&A*, 360, 997
- Tomida K., 2014, *ApJ*, 786, 98
- Tomida K., Okuzumi S., Machida M. N., 2015, *ApJ*, 801, 117
- Toomre A., 1964, *ApJ*, 139, 1217
- Tout C. A., Pols O. R., Eggleton P. P., Han Z., 1996, *MNRAS*, 281, 257
- Troland T. H., Crutcher R. M., 2008, *ApJ*, 680, 457
- Utomo D. et al., 2018, *ApJ*, 861, L18
- Valtonen M., Karttunen H., Gutzwiller M. C., 2007, *Phys. Today*, 60, 59
- Walch S., Naab T., Whitworth A., Burkert A., Gritschneider M., 2010, *MNRAS*, 402, 2253
- Walch S., Whitworth A. P., Girichidis P., 2012, *MNRAS*, 419, 760
- Wang P., Li Z.-Y., Abel T., Nakamura F., 2010, *ApJ*, 709, 27
- Whitworth A. P., Chapman S. J., Bhattal A. S., Disney M. J., Pongracic H., Turner J. A., 1995, *MNRAS*, 277, 727
- Whitworth A. P., Lomax O., 2015, *MNRAS*, 448, 1761
- Wurster J., Bate M. R., 2019, *MNRAS*, 486, 2587
- Wurster J., Bate M. R., Price D. J., 2019, *MNRAS*, 489, 1719
- Wurster J., Li Z.-Y., 2018, *Front. Astron. Space Sci.*, 5, 39
- Wurster J., Price D. J., Bate M. R., 2016, *MNRAS*, 457, 1037
- Young M. D., Clarke C. J., 2015, *MNRAS*, 452, 3085
- Zhang Y. et al., 2016, *ApJ*, 832, 158
- Zhang Y. et al., 2018, *ApJ*, 864, 76
- Zhang Y. et al., 2019, *ApJ*, 883, 1
- Zhao B., Caselli P., Li Z.-Y., Krasnopolsky R., 2018, *MNRAS*, 473, 4868
- Zhuchkov R. Y., Kiyayeva O. V., Orlov V. V., 2010, *Astron. Rep.*, 54, 38
- Zhu Z., Hartmann L., Gammie C., 2009, *ApJ*, 694, 1045
- Zhu Z., Hartmann L., Gammie C. F., Book L. G., Simon J. B., Engelhard E., 2010, *ApJ*, 713, 1134

This paper has been typeset from a  $\text{\TeX}/\text{\LaTeX}$  file prepared by the author.

6

PAPER III

---



# Protostellar outflows: a window to the past

P. F. Rohde<sup>1</sup>,<sup>\*</sup> S. Walch,<sup>1</sup> D. Seifried<sup>1</sup>,<sup>\*</sup> A. P. Whitworth<sup>2</sup> and S. D. Clarke<sup>1</sup>

<sup>1</sup>*Physikalisches Institut, Universität zu Köln, Zùlpicher Str. 77, D-50937 Köln, Germany*

<sup>2</sup>*School of Physics and Astronomy, Cardiff University, Cardiff CF24 3AA, UK*

Accepted 2021 December 1. Received 2021 November 26; in original form 2021 August 4

## ABSTRACT

During the early phases of low-mass star formation, episodic accretion causes the ejection of high-velocity outflow bullets, which carry a fossil record of the driving protostar’s accretion history. We present 44 SPH simulations of  $1 M_{\odot}$  cores, covering a wide range of initial conditions, and follow the cores for five free-fall times. Individual protostars are represented by sink particles, and the sink particles launch episodic outflows using a sub-grid model. The OPTICS algorithm is used to identify individual episodic bullets within the outflows. The parameters of the overall outflow and the individual bullets are then used to estimate the age and energetics of the outflow, and the accretion events that triggered it, and to evaluate how reliable these estimates are, if observational uncertainties and selection effects (like inclination) are neglected. Of the commonly used methods for estimating outflow ages, it appears that those based on the length and speed of advance of the lobe are the most reliable in the early phases of evolution, and those based on the width of the outflow cavity and the speed of advance are most reliable during the later phases. We describe a new method that is almost as accurate as these methods, and reliable throughout the evolution. In addition, we show how the accretion history of the protostar can be accurately reconstructed from the dynamics of the bullets if each lobe contains at least two bullets. The outflows entrain about 10 times more mass than originally ejected by the protostar.

**Key words:** methods: numerical – stars: formation – stars: low-mass – stars: protostars – stars: winds, outflows.

## 1 INTRODUCTION

There is growing evidence that accretion on to protostars occurs in episodic bursts rather than being continuous. Accretion events can be observed directly (e.g. Lee et al. 2020; Rigliaco et al. 2020; Stock et al. 2020) or indirectly using chemical modelling (e.g. Hsieh et al. 2019; Rab et al. 2019; Anderl et al. 2020; Sharma et al. 2020). So-called FU Orionis (FUor) stars are observed to undergo short outbursts lasting 10 of years during which the accretion rate rises to  $\sim 10^{-4} M_{\odot} \text{ yr}^{-1}$ , followed by long quiescent phases of  $\sim 10^3 - 10^4$  yr with low-accretion rates of  $\sim 10^{-7} M_{\odot} \text{ yr}^{-1}$  (Audard et al. 2014; Safron et al. 2015; Fehér et al. 2017; Pérez et al. 2020; Takagi et al. 2020). These short outbursts of high accretion naturally mitigate the long-standing ‘luminosity problem’ (Kenyon et al. 1990; Cesaroni et al. 2018; Hsieh et al. 2018; Ibryamov, Semkov & Peneva 2018; Kuffmeier et al. 2018). Possible causes of episodic accretion are manifold. They include thermal, gravitational, or magneto-rotational instabilities in the accretion disc (Kuffmeier et al. 2018; Kadam et al. 2020; Sharma et al. 2020) and close encounters in multiple systems (Kuruwita, Federrath & Haugbølle 2020).

Protostellar outflows accompany the early phases of star formation (Bally 2016), and it is widely believed that the launching of protostellar outflows is directly related to accretion on to protostars (Sicilia-Aguilar et al. 2020). The mechanisms underlying the launching are still debated (see e.g. the reviews of Arce et al. 2007; Frank et al. 2014; Lee 2020), but most proposed mechanisms entail the magneto-centrifugal force converting the gravitational energy of the accreted

gas into kinetic energy (Blandford & Payne 1982; Königl & Pudritz 2000; Lynden-Bell 2003; Pudritz et al. 2007; Machida, Inutsuka & Matsumoto 2008; Seifried et al. 2012). Jets originating from the accretion disc’s innermost part are highly collimated and have high velocities (Reipurth & Bally 2001; Tafalla et al. 2010; Bjerkeli et al. 2016; Lee et al. 2017; Gómez-Ruiz et al. 2019), whereas winds launched further out in the accretion disc are less collimated and slower (Hirota et al. 2017; Lee et al. 2017; Zhang et al. 2018, 2019). Simulating numerically the inner ejection regions that produce the high-velocity jet component is still a challenging task (e.g. Machida, Inutsuka & Matsumoto 2009; Hennebelle et al. 2011; Price, Tricco & Bate 2012; Seifried et al. 2012; Machida & Hosokawa 2013; Bate, Tricco & Price 2014; Machida 2014; Tomida 2014; Tomida, Okuzumi & Machida 2015; Lewis & Bate 2017; Machida & Basu 2019; Saiki & Machida 2020). The high spatial and temporal resolution required by such simulations is not easily combined with following the outflows on larger time and spatial scales. When focusing on the interaction of outflows with the stellar environment, this problem can be mitigated by introducing an almost resolution independent sub-grid model to launch the outflows (Nakamura & Li 2007; Cunningham et al. 2011; Federrath et al. 2014; Myers et al. 2014; Offner & Arce 2014; Peters et al. 2014; Kuiper, Yorke & Turner 2015; Offner & Chaban 2017; Li, Klein & McKee 2018; Rohde et al. 2019). Once the ejecta are launched, they carve out a cavity by entraining envelope material. Ejecta and entrained material together form a molecular outflow. Sideways motions of bow-shocks (Tafalla et al. 2017; Jhan & Lee 2021), together with the wide-angle wind, cause the cavity wall to widen over time (Arce & Sargent 2006; Seale & Looney 2008; Velusamy, Langer & Thompson 2014).

\* E-mail: [rohde@ph1.uni-koeln.de](mailto:rohde@ph1.uni-koeln.de)

If the accretion and ejection of gas are strongly coupled, episodic accretion events can be indirectly detected by the episodic outflows they trigger (Arce et al. 2007; Vorobyov et al. 2018; Sicilia-Aguilar et al. 2020). In particular, where the rapidly ejected high-velocity gas shocks against the slower gas inside the cavity, it produces high-velocity outflow bullets, a frequently observed characteristic of protostellar outflows (Chen et al. 2016; Cheng et al. 2019; Tychoniec et al. 2019). In position–velocity diagrams, these outflow bullets – in this context often called ‘Hubble Wedges’ – stand out from the otherwise linear position–velocity relation (Bachiller et al. 1990; Lada & Fich 1996; Arce & Goodman 2001; Tafalla et al. 2004; Santiago-García et al. 2009; Wang et al. 2014; Rohde et al. 2019; Nony et al. 2020). Once an outflow bullet leaves the dense core and appears at optical wavelengths, it is referred to as an Herbig–Haro object. Herbig–Haro objects often form parsec-scale long chains (Reipurth, Bally & Devine 1997; Reipurth, Devine & Bally 1998; Cortes-Rangel et al. 2020; Ferrero et al. 2020; Movsessian, Magakian & Dodonov 2021). The spacing and kinematics of outflow bullets in such a chain should carry a fossil record of the underlying episodic protostellar accretion history (Bally 2016; Lee 2020).

There are several methods for estimating the age of a young protostellar object. The most common ones involve the spectral energy distribution (SED) of a protostar (Lada 1987). As a protostar evolves and grows, the ratio of the mass of the protostar plus disc to the mass of the envelope is expected to increase, altering the SED. This ratio,  $(M_{\text{DISK}} + M_*) / M_{\text{ENV}}$ , can be used to estimate the stellar age (Young & Evans 2005; Vazzano et al. 2021). The age can also be estimated by calculating the slope of the SED between two fixed wavelengths (e.g. 2  $\mu\text{m}$  and 25  $\mu\text{m}$ ; Lada & Wilking 1984); by calculating the bolometric temperature,  $T_{\text{BOL}}$ , i.e. the temperature for which a blackbody spectrum has the same flux-weighted mean frequency as the SED (Myers & Ladd 1993; Enoch et al. 2009); or by calculating the ratio of bolometric to sub-millimeter luminosity,  $L_{\text{BOL}} / L_{\text{SUBMM}}$ , (Andre, Ward-Thompson & Barsony 1993; Young & Evans 2005). A different approach is to estimate ages from chemical abundances in the stellar envelope (e.g. Tobin et al. 2013; Busquet et al. 2017).

Alternatively, one may study protostellar outflows. (i) Dynamical ages of outflows and their embedded bullets can be used to estimate protostellar ages indirectly (Zhang et al. 2005; Downes & Cabrit 2007; Li et al. 2020; Nony et al. 2020). (ii) The outflow activity is expected to diminish over time, which can be used to estimate the driving protostar’s evolutionary stage (Curtis et al. 2010; Yıldız et al. 2015; Lee 2020; Podio et al. 2021). (iii) As the opening angles of the outflow cavities widen over time, there exists a relation between opening angle and age (Arce & Sargent 2006; Seale & Looney 2008; Velusamy et al. 2014; Hsieh, Lai & Belloche 2017). However, studying a sample of seven objects in Lupus, Vazzano et al. (2021) show that these different methods do not always agree on an evolutionary sequence.

In this paper, we analyse an ensemble of 44 hydrodynamic simulations of low-mass star formation which include episodic protostellar outflow feedback. The outflows consist of ejected gas and core material. The core material is entrained as the outflow carves a bipolar cavity through the core. These simulations enable us to test whether protostellar outflows are a window on the past, i.e. whether they can be used to determine the evolutionary stage, the age, and the accretion history of the underlying protostar.

The paper is structured as follows. In Section 2, we describe the computational method, the sub-grid outflow model developed earlier by Rohde et al. (2019, 2021), and how we define outflow lobes and extract outflow bullets from these lobes. In Section 3, we

present outflow properties, estimate entrainment factors, and study different velocity components of the simulated outflows. In Section 4, we estimate stellar ages and evolutionary stages from dynamical time-scales, outflow rates, and cavity opening angles. In addition, we estimate the mean accretion rates and the episodic accretion rates associated with individual outflow bullets. Limitations of the underlying simulations are discussed in Section 5. In Section 6, we summarize our results.

## 2 METHOD

### 2.1 The GANDALF SPH code

We perform simulations using the smoothed particle hydrodynamics (SPH) and mesh-less finite volume code GANDALF (Hubber, Rosotti & Booth 2018). We use the ‘grad-h’ SPH formulation (Springel & Hernquist 2002) with an M4 smoothing kernel, which with  $\eta_{\text{SPH}} = 1.2$  overlaps  $\sim 58$  neighbours. We invoke hierarchical block time-stepping (Hernquist & Katz 1989). The maximum number of allowed time-step levels is  $N_{\text{LVL}} = 9$ ; hence an SPH particle on the highest level receives  $2^{N_{\text{LVL}}} = 512$  times more updates than a particle on the lowest level. For the time-integration, we adopt the second-order Leapfrog KDK integration scheme. GANDALF uses the artificial viscosity prescription of Morris & Monaghan (1997) and the time-dependent viscosity switch of Cullen & Dehnen (2010).

We compute heating and cooling rates using the approximate radiative heating and cooling method of Stamatellos et al. (2007) with the modifications developed by Lombardi, McInally & Faber (2015). The method uses local SPH particle quantities such as density, temperature and pressure gradient to estimate a mean optical depth. It accounts for changes in the specific heat due to the ionization of hydrogen and helium, and the dissociation of molecular hydrogen. It also accounts for changes in the opacity, for example due to ice mantle sublimation.

### 2.2 Feedback models

In the simulations, protostars are represented by sink particles (Hubber, Walch & Whitworth 2013), which use a combination of four different sub-grid models, labelled (i)–(iv). Below we give a brief description of these sub-grid models and how they are combined. For further details see Rohde et al. (2019, 2021) and references therein.

(i) Episodic accretion is modelled following Stamatellos, Whitworth & Hubber (2012). Protostars spend most of the time in a quiescent phase with a low accretion rate,  $\dot{M}_{\text{BG}} = 10^{-7} M_{\odot} \text{yr}^{-1}$ . These quiescent phases lasting  $10^3$ – $10^4$  yr are interrupted by short ( $\sim 50$  yr) outbursts. Stamatellos et al. (2012) assume that a combination of gravitational and magneto-rotational instabilities acts as the trigger for these outbursts (Zhu, Hartmann & Gammie 2009; Zhu et al. 2010). During an outburst the accretion rate quickly increases to  $\dot{M}_{\text{OB}} \simeq 5 \times 10^{-4} M_{\odot} \text{yr}^{-1}$  and afterwards decays back to the quiescent value.

(ii) We adopt the stellar evolution model of Offner et al. (2009), which uses the energy balance between accretion, gravitational contraction, nuclear burning, ionization, and radiation to predict the radius and luminosity of a protostar. Instead of using the accretion rate on to the sink particle, we make use of the accretion rate predicted by the episodic accretion model (i). As a result, the protostar delivers bursts of high luminosity emulating those of FUor type stars.

(iii) We capture radiative heating due to protostars by invoking a pseudo-background radiation field using the luminosities computed

from the stellar evolution model (ii). The temperature is assumed to drop with distance,  $d$ , from a protostar approximately as  $d^{-1/2}$ . Due to the episodic nature of accretion bursts from protostars, radiative heating temporarily stabilizes protostellar accretion discs (Forgan & Rice 2013) while at the same time allowing for some level of disc fragmentation to occur between bursts (Stamatellos, Whitworth & Hubber 2012; Lomax et al. 2014, 2015; Mercer & Stamatellos 2017).

(iv) To simulate episodic outflow feedback, we eject  $f_{\text{EJECT}} = 10$  per cent of the accreted mass in bidirectional lobes (Nisini et al. 2018). In contrast to most outflow sub-grid models, we do not use the direct mass accretion rate on to the sink particle, but rather the accretion rate from the episodic accretion sub-grid model (i). Consequently, the outflow occurs in bursts, leading to the formation of outflow bullets, as frequently observed (e.g. Li et al. 2020). The base velocity of the ejected particles corresponds to the Keplerian velocity at twice the stellar radius (ii). To produce a two-component outflow, combining a low-velocity wide-angle wind (Louvvet et al. 2018; Zhang et al. 2019; Pascucci et al. 2020; Lee et al. 2021) and a high-velocity jet, we modulate the base velocity with the angular distribution function derived by Matzner & McKee (1999; see Appendix B for more details). Additionally, we add a rotational velocity component (equation 9 in Rohde et al. 2021) to capture the angular momentum carried away by the outflow (de Valon et al. 2020; López-Vázquez et al. 2020; Tabone et al. 2020), and thereby keep the angular momentum of the protostar below breakup. SPH particles are ejected in symmetric groups of four to ensure linear and angular momentum conservation.

### 2.3 Simulation setup

We present an ensemble of 44 simulations with different initial conditions. The simulations are identical to the OF-sample, the subset of simulations with outflow feedback in Rohde et al. (2021). Each run starts from a dense core with mass  $M_{\text{CORE}} = 1 M_{\odot}$ , temperature  $T = 10$  K, and a Bonnor–Ebert density profile. We vary three core parameters (i–iii) between the simulations.

(i) The core radius is set to  $r_{\text{CORE}} = 0.017$  pc, 0.013 pc, or 0.010 pc. The runs with smaller  $r_{\text{CORE}}$  are more overcritical, accordingly 3, 4, and 5 times compared to a Bonnor–Ebert sphere in equilibrium. Smaller  $r_{\text{CORE}}$  leads to denser cores and correspondingly to shorter free-fall times, respectively,  $t_{\text{FF}} = 36.8$  kyr, 24.6 kyr, and 16.6 kyr. We choose these small core radii to be able to apply a high level of turbulence such that the turbulence is not mostly dissipated before the actual star formation sets in. The dense cores are embedded in a low-density envelope with radius  $r_{\text{ENV}} = 0.75$  pc. Outside the core boundary,  $r_{\text{CORE}}$ , the density decreases as  $\rho \propto r^{-4}$  until it falls to  $\rho_{\text{ENV}} = 10^{-23}$  g cm $^{-3}$ . Outside this, the density is uniform. We choose the  $r^{-4}$  as a trade-off between a computationally more expensive shallower profile and a discontinuity. The total envelope mass is  $M_{\text{ENV}} = 0.86 M_{\odot}$ . A fraction of this envelope mass contributes to the final stellar mass as the envelope falls in.

(ii) The dense cores start out with an initial turbulent velocity field (Walch et al. 2010), with power spectrum

$$P_k \propto k^{-4}, \quad k \in [k_{\text{MIN}}, 64]. \quad (1)$$

We vary the turbulent velocity field by adjusting the smallest (most energetic) wavenumber between  $k_{\text{MIN}} = 1, 2,$  and  $3$ , with  $k_{\text{MIN}} = 1$  corresponding to the core radius. This changes the turbulent velocity field from small-scale turbulence with low net angular momentum ( $k_{\text{MIN}} = 3$ ) to core-scale motions with – potentially – high-angular momentum ( $k_{\text{MIN}} = 1$ ) (Walch, Whitworth & Girichidis 2012).

(iii) We adjust the virial ratio,

$$\alpha_{\text{VIR}} = \frac{2(E_{\text{TURB}} + E_{\text{THERM}})}{|E_{\text{GRAV}}|}, \quad (2)$$

between  $\alpha_{\text{VIR}} = 0.5, 1.0, 2.0,$  and  $3.0$ ;  $\alpha_{\text{VIR}}$  regulates the strength of the turbulence.

Using the crossing time-scale  $\tau_{\text{CROSS}} = 2 r_{\text{CORE}} / v_{\text{TURB}}$  as an indicator of the dissipation time-scale of the turbulence (Mac Low et al. 1998; Stone, Ostriker & Gammie 1998), we find that the dissipation time-scales range between  $\tau_{\text{DISS}} = 14.0$  kyr and 83.4 kyr. These dissipation time-scales correspond to free-fall times between  $0.8 t_{\text{FF}}$  and  $2.3 t_{\text{FF}}$ . The first stars in our simulations form between 6.8 and 129.2 kyr with a mean of  $27.2 \pm 22.7$  kyr, which indicates that the dissipation time-scale is comparable to the time-scale of the first protostar formation.

We perform one run for each combination of the three core parameters ( $r_{\text{CORE}}, k_{\text{MIN}}, \alpha_{\text{VIR}}$ ). For the run with  $\alpha_{\text{VIR}} = 1.0, k_{\text{MIN}} = 1, r_{\text{CORE}} = 0.013$  pc, we perform eight additional runs with different turbulent random seeds,  $\chi$ . In total we perform 44 simulations with a mass resolution of 400 000 SPH particles per  $M_{\odot}$  (hence, mass resolution  $\sim 3 \times 10^{-4} M_{\odot}$ ). The sink creation threshold is  $\rho_{\text{CRIT}} = 10^{-10}$  g cm $^{-3}$ . A conservative estimate of the spatial resolution is  $4h_{\text{MIN}} \sim 1.2$  au. The parameters of the individual runs are listed in Table 1. For a more detailed description of the simulation setup, and a discussion of the influence of the initial conditions on the simulation outcomes, see Rohde et al. (2021).

#### 2.3.1 Outflow directions

The direction in which outflows are launched depends strongly on the local environment in which the protostar forms, such as the angular momentum axis of the accretion disc and the local magnetic field (Machida, Hirano & Kitta 2020). Angular momentum of the gas falling on to the accretion disc can significantly alter the orientation of the stellar accretion disc (Matsumoto, Machida & Inutsuka 2017). Therefore, the outflow direction might change significantly over time, possibly causing a quadrupolar outflow as e.g. in Machida et al. (2020). Protostellar companions can cause a precessing jet with a fixed period, as e.g. in Murphy et al. (2021). If multiple protostars form, e.g. via turbulent fragmentation, their outflow directions are random (Lee et al. 2016), which can lead to misaligned outflows (Hara et al. 2021) that may even collide (as described in Zapata et al. 2018).

These processes cause a rather chaotic outflow behaviour. However, numerous observations report very ordered outflows, where the outflow axis is straight on parsec scales (e.g. Bally & Chia 2019). For theoretical astrophysics, it would be of great interest to have some observationally informed statistics of complex versus straight outflows as a benchmark for the simulations. Additionally, such an analysis might allow observers to estimate the level of initial turbulence inside a core by observing the outflows.

Fig. 1 shows column density plots of all simulations with  $k_{\text{MIN}} = 1$  at  $t_{\text{EVAL}} = 4 t_{\text{FF}}$ . Some outflows forming in these simulations show a rather complicated behaviour, as e.g. the quadrupolar outflow in the top left panel. From looking by eye there is no clear trend that simulations with stronger turbulence (higher  $\alpha_{\text{VIR}}$ ) have a more complicated structure. There is no simulation showing a very straight outflow as e.g. in Bally & Chia (2019), which suggests that the general level of turbulence in our simulations could be somewhat too high. Alternatively, the largest mode of the turbulence with respect to the size of the core (here:  $k_{\text{MIN}} = 1$ ) could be smaller for real cores, which would lead to a more ordered collapse (Walch et al.

**Table 1.** Parameter summary for all the simulations performed. Reading from left to right, the columns give the run number, the run name, the turbulent random seed ( $\chi$ ), the virial ratio ( $\alpha_{\text{VIR}}$ ), the smallest turbulent wavenumber ( $k_{\text{MIN}}$ ), and the core radius ( $r_{\text{CORE}}$ /pc).

#	Run	$\chi$	$\alpha_{\text{VIR}}$	$k_{\text{MIN}}$	$r_{\text{CORE}}$ pc	$U_{\text{TURB}}$ km s <sup>-1</sup>
1	S:1-V:0.5-K:1-R:17	5	0.5	1	0.017	0.4
2	S:1-V:1.0-K:1-R:17	5	1.0	1	0.017	0.6
3	S:1-V:2.0-K:1-R:17	5	2.0	1	0.017	0.9
4	S:1-V:3.0-K:1-R:17	5	3.0	1	0.017	1.1
5	S:1-V:0.5-K:2-R:17	5	0.5	2	0.017	0.4
6	S:1-V:1.0-K:2-R:17	5	1.0	2	0.017	0.6
7	S:1-V:2.0-K:2-R:17	5	2.0	2	0.017	0.9
8	S:1-V:3.0-K:2-R:17	5	3.0	2	0.017	1.1
9	S:1-V:0.5-K:3-R:17	5	0.5	3	0.017	0.4
10	S:1-V:1.0-K:3-R:17	5	1.0	3	0.017	0.6
11	S:1-V:2.0-K:3-R:17	5	2.0	3	0.017	0.9
12	S:1-V:3.0-K:3-R:17	5	3.0	3	0.017	1.1
13	S:1-V:0.5-K:1-R:13	5	0.5	1	0.013	0.5
14	S:1-V:1.0-K:1-R:13	5	1.0	1	0.013	0.7
15	S:1-V:2.0-K:1-R:13	5	2.0	1	0.013	1.0
16	S:1-V:3.0-K:1-R:13	5	3.0	1	0.013	1.3
17	S:1-V:0.5-K:2-R:13	5	0.5	2	0.013	0.5
18	S:1-V:1.0-K:2-R:13	5	1.0	2	0.013	0.7
19	S:1-V:2.0-K:2-R:13	5	2.0	2	0.013	1.0
20	S:1-V:3.0-K:2-R:13	5	3.0	2	0.013	1.3
21	S:1-V:0.5-K:3-R:13	5	0.5	3	0.013	0.5
22	S:1-V:1.0-K:3-R:13	5	1.0	3	0.013	0.7
23	S:1-V:2.0-K:3-R:13	5	2.0	3	0.013	1.0
24	S:1-V:3.0-K:3-R:13	5	3.0	3	0.013	1.3
25	S:1-V:0.5-K:1-R:10	5	0.5	1	0.010	0.6
26	S:1-V:1.0-K:1-R:10	5	1.0	1	0.010	0.8
27	S:1-V:2.0-K:1-R:10	5	2.0	1	0.010	1.2
28	S:1-V:3.0-K:1-R:10	5	3.0	1	0.010	1.4
29	S:1-V:0.5-K:2-R:10	5	0.5	2	0.010	0.6
30	S:1-V:1.0-K:2-R:10	5	1.0	2	0.010	0.8
31	S:1-V:2.0-K:2-R:10	5	2.0	2	0.010	1.2
32	S:1-V:3.0-K:2-R:10	5	3.0	2	0.010	1.4
33	S:1-V:0.5-K:3-R:10	5	0.5	3	0.010	0.6
34	S:1-V:1.0-K:3-R:10	5	1.0	3	0.010	0.8
35	S:1-V:2.0-K:3-R:10	5	2.0	3	0.010	1.2
36	S:1-V:3.0-K:3-R:10	5	3.0	3	0.010	1.4
37	S:2-V:1.0-K:1-R:13	0	1.0	1	0.013	0.7
38	S:3-V:1.0-K:1-R:13	1	1.0	1	0.013	0.7
39	S:4-V:1.0-K:1-R:13	2	1.0	1	0.013	0.7
40	S:5-V:1.0-K:1-R:13	3	1.0	1	0.013	0.7
41	S:6-V:1.0-K:1-R:13	4	1.0	1	0.013	0.7
42	S:7-V:1.0-K:1-R:13	6	1.0	1	0.013	0.7
43	S:8-V:1.0-K:1-R:13	7	1.0	1	0.013	0.7
44	S:9-V:1.0-K:1-R:13	8	1.0	1	0.013	0.7

2012). Alternatively, including magnetic fields could also stabilize the outflow direction.

## 2.4 Outflow-lobe cavity analysis

### 2.4.1 Outflow lobe identification

In order to analyse the evolution of the outflow kinematics, we need to identify and characterize outflow lobes in SPH simulations. This is not a trivial task. Because of the turbulence in the core, the directions in which outflows are launched change with time, in unpredictable ways. To identify outflows lobes, we use a k-means clustering algorithm (KMCA; Lloyd 1982).

First, we identify all outflowing SPH particles. SPH particle  $p$  is tagged as ‘outflowing’ if its speed is higher than the local escape speed,  $v_p > v_{\text{ESC}}(\mathbf{r}_p)$ , and  $v_p > 1 \text{ km s}^{-1}$ . Here  $\mathbf{r}_p$  is the position

## Protostellar outflows: a window to the past 2555

vector of particle  $p$  with respect to the core’s centre of mass (COM), and the escape velocity is given by

$$v_{\text{ESC}}(\mathbf{r}_p) = \sqrt{\frac{2GM_{\text{ENC}}(|\mathbf{r}_p|)}{|\mathbf{r}_p|}}, \quad (3)$$

where  $M_{\text{ENC}}(|\mathbf{r}_p|)$  is the mass enclosed by a sphere around the COM with radius  $|\mathbf{r}_p|$ . The threshold of  $1 \text{ km s}^{-1}$  is chosen to exclude the weakly bound envelope gas.

Next, we determine  $n_{\text{LOBE,SIM}}$  k-means clusters, here called lobes, and referenced with the index  $l$ . Initially, the lobes point in random directions  $\mathbf{e}_l$ , away from the core’s COM. For a specified  $n_{\text{LOBE,SIM}}$ , we iteratively repeat the following two steps:

(i) For each SPH particle, we find the lobe with the smallest angle between the particle position  $\mathbf{r}_p$  and the lobe direction  $\mathbf{e}_l$ .

(ii) For each lobe, we compute a new lobe direction,  $\mathbf{e}_l$ , parallel to the mean position vector of all the SPH particles associated with that lobe.

Iteration ceases as soon as no SPH particle is reassigned to a different lobe in step (i). The number of SPH particles associated with lobe  $l$  is  $n_{\text{ASS},l}$ .

To evaluate whether the resulting lobes represent the structure of the outflow accurately, we use the Silhouette method (Rousseeuw 1987), which gives a measure of how well each outflowing particle is represented by the lobe to which it has been assigned, as compared with the neighbouring lobe. The Silhouette for particle  $p_l$ , assigned to lobe  $l$ , is given by

$$s(p_l) = \frac{b(p_l) - a(p_l)}{\max(b(p_l), a(p_l))}. \quad (4)$$

Here  $a(p_l)$  is the mean ‘distance’ between particle  $p_l$  and all the other particles,  $q_l$ , in lobe  $l$ , i.e.

$$a(p_l) = \frac{1}{n_{\text{ASS},l} - 1} \sum_{q_l=0, q_l \neq p_l}^{n_{\text{ASS},l}} \text{dist}_{\text{K-MEANS}}(p_l, q_l). \quad (5)$$

Similarly,  $b(p_l)$  is the mean ‘distance’ between particle  $p_l$  and all the other particles,  $q_m$ , in the closest neighbouring lobe,  $m$ , i.e.

$$b(p_l) = \frac{1}{n_{\text{ASS},m}} \sum_{q_m=0}^{n_{\text{ASS},m}} \text{dist}_{\text{K-MEANS}}(p_l, q_m). \quad (6)$$

The closest neighbouring lobe is the one that minimizes  $b(p_l)$  but does not contain particle  $p_l$ . As a distance measure,  $\text{dist}_{\text{K-MEANS}}(p, q)$ , we use the angle between the two particles  $p$  and  $q$  with respect to the COM. The Silhouette of a lobe is defined as the mean of all the associated particles’ Silhouettes,

$$S(l) = \frac{1}{n_{\text{ASS},l}} \sum_{p_l=0}^{n_{\text{ASS},l}} s(p_l). \quad (7)$$

The resulting  $S(l) \in [-1, 1]$ , and the highest value of  $S(l)$  corresponds to the best-fitting lobe structure. A set containing  $n_{\text{LOBE,SIM}}$  lobes is characterized by its mean Silhouette,

$$\bar{S} = \frac{1}{n_{\text{LOBE,SIM}}} \sum_l^{n_{\text{LOBE,SIM}}} S(l). \quad (8)$$

The results of the KMCA depend on the randomly initialized lobe directions  $\mathbf{e}_l$ . To find the best-fitting set of lobes, i.e. the one with the highest  $\bar{S}$ , we perform the KMCA for 10 different sets of initial  $\mathbf{e}_l$ . One of the 10 initial sets is the best-fitting one from the previous snapshot.

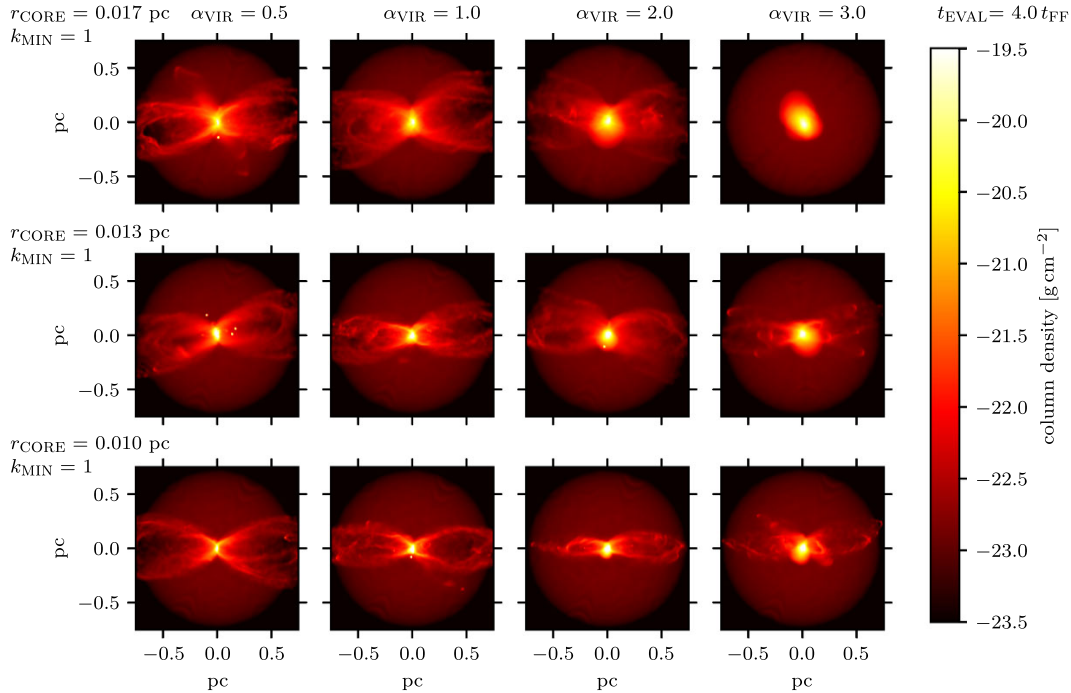


**Figure 1.** Column density plots of the simulations with  $k_{\text{MIN}} = 1$  (see Table 1) at  $t_{\text{EVAL}} = 4 t_{\text{FF}}$ . The rows show simulations with different  $r_{\text{CORE}}$ , whereas the columns show simulations with different  $\alpha_{\text{VIR}}$ . The simulations are rotated such that the prominent outflow lobe preferentially lies along the  $x$ -axis. The simulation in the top right panel does not collapse, due to the high level of turbulence in combination with the relatively large core radius.

It is a priori not clear how many lobes are present in a simulation at a given time. Therefore, for each  $n_{\text{LOBE,SIM}} \in [2, 4, 6, 8]$  we compute 10 KMCA runs; we only consider even numbers of lobes because the sub-grid sink module always launches bipolar outflows. Out of the resulting 40 different realizations, the lobe configuration with the highest mean Silhouette  $\bar{S}$  is chosen to represent the outflow cavities. We denote the final lobe vectors as

$$\mathbf{r}_l = r_{\text{FRONT},l} \mathbf{e}_l, \quad (9)$$

where  $r_{\text{FRONT},l}$  is the distance from the COM to the most distant SPH particle allocated to lobe  $l$ . We repeat this process for each snapshot.

#### 2.4.2 Locating the outflow-lobe cavity wall

To characterize an outflow cavity, we generate an array of evaluation points within each outflow lobe (see Fig. 2). Along the lobe axis, defined by  $\mathbf{r}_l$  (Section 2.4.1, equation 9), we place  $n_s = 64$  perpendicular slices. These slices are logarithmically spaced between  $10^{-5}$  and 0.75 pc (white dashed lines on Fig. 2), with an additional slice at 10 pc. We use the index  $s$  for slices, with  $s = 0$  referring to the slice nearest the centre of mass. Each of these slices contains  $n_R = 90$  rays,  $\mathbf{r}_{l,s,r}$ , which are evenly spaced azimuthally around the outflow axis. We use the index  $r$  for rays. Each ray consists of  $n_e = 500$  evaluation points, logarithmically spaced between  $10^{-5}$  and 0.5 pc radially outward from the lobe axis (blue dots on Fig. 2). We use the index  $e$  for evaluation points. The outer radius of 0.5 pc is chosen so that we do not miss any part of a lobe. We use the SPH gather method to evaluate the physical properties of the gas at each evaluation point (see e.g. Monaghan 1992).

To define the cavity volume, we walk each ray outwards from the lobe axis. The last evaluation point,  $p_i$ , for which (a) the gas is outflowing ( $v_e > v_{\text{ESC}}(\mathbf{r}_e)$  and  $v_e > 1 \text{ km s}^{-1}$ ), and (b) there is at least one neighbouring particle that is an initially ejected particle, is considered to mark the cavity wall at radius  $r_{\text{WALL},l,s,r}$ , provided it is closer to  $\mathbf{r}_l$  than to any another outflow axis. With this definition of the cavity wall we find all SPH particles within each lobe,  $n_{\text{PART},l}$ . Fig. 3 shows an example of an outflow cavity delineated this way.

## 2.5 Tracking outflow bullets

To locate and track outflow bullets we use the OPTICS clustering algorithm (Ankerst et al. 1999). This algorithm has the advantage that it is density-based and therefore well suited to the Lagrangian nature of SPH simulations. Compared to the frequently used DBSCAN algorithm (Ester et al. 1996), OPTICS allows for steeper density gradients, which in our simulations will occur naturally as bullets propagate supersonically through an outflow lobe.

### 2.5.1 Optics algorithm

Here, we give a brief description of the OPTICS algorithm, and focus on the modifications needed to apply the algorithm to our simulation data. For a more detailed description, see Ankerst et al. (1999).

The OPTICS algorithm orders SPH particles in a one-dimensional ‘reachability list’, based on their distance from each other,  $\text{dist}_{\text{OPTICS}}$ . In order to extract high-velocity bullets, we use a distance measure that combines the spatial separation and velocity difference between

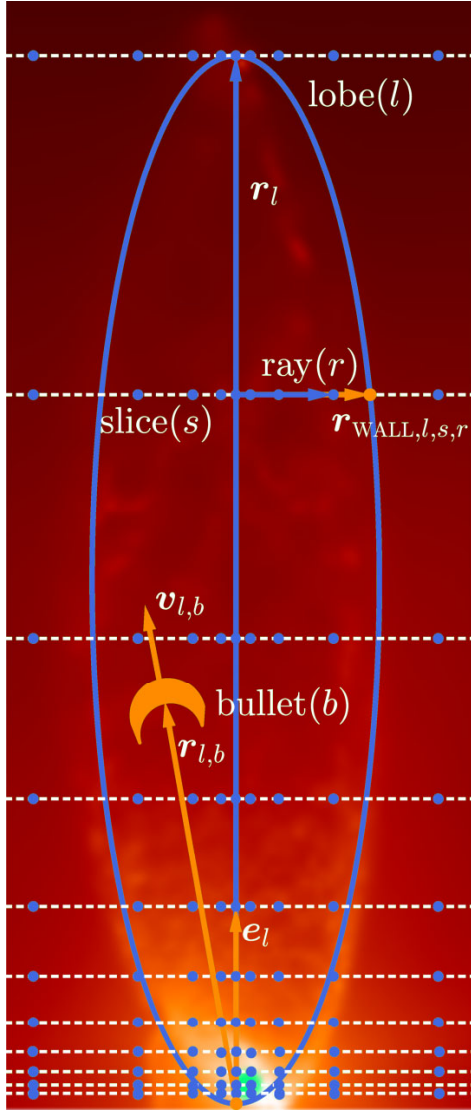


**Figure 2.** Sketch showing the most important properties of the cavity analysis. The outflow direction,  $e_l$ , of lobe  $l$ , is divided into logarithmically spaced slices (index  $s$ , dashed white lines) made up of individual rays (index  $r$ ) radiating orthogonally from the lobe axis. Along each ray the simulation is evaluated at logarithmically spaced evaluation points (index  $e$ , blue dots). Bullets are denoted with the index  $b$ . The background shows a column density plot from the simulation S:5-V:3-K:3-R:13 at  $t = 60.6$  kyr.

two particles,  $p$  and  $q$ , viz

$$\text{dist}_{\text{OPTICS}}(p, q) = \sqrt{\left(\frac{|r_p - r_q|}{r_{\text{FRONT}}}\right)^2 + \left(\frac{|v_p - v_q|}{v_{\text{MAX}}}\right)^2}. \quad (10)$$

Here,  $r_{\text{FRONT}}$  is the extent of the lobe and  $v_{\text{MAX}}$  is the highest velocity amongst the particles in the lobe. In order to reduce the computational overhead, we limit application of the OPTICS algorithm to particles with  $v_p > v_{\text{MIN}} = 10 \text{ km s}^{-1}$ .

The algorithm involves the following four steps.

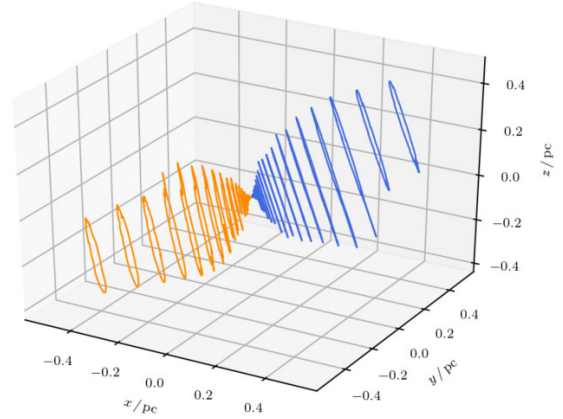


**Figure 3.** Extracted cavity wall from run S:5-V:3.0-K:3-R:13 at  $t = 51$  kyr. The orange and blue lines lie within evaluation slices perpendicular to the outflow axis and show the extracted cavity wall for both lobes.

(i) Starting from a random particle,  $p$ , we find  $p$ 's 'neighbour list', i.e. the 150 closest particles to  $p$  (see equation 10) that are also within the same outflow lobe (Section 2.4).

(ii) Using this neighbour list we compute the core distance of particle  $p$ , i.e. the distance from particle  $p$  to the  $\eta$ th closest particle on  $p$ 's neighbour list,

$$d_{\text{CORE}}(p) = \text{dist}_{\text{OPTICS}}(p, \eta). \quad (11)$$

The number of particles required to form a cluster,  $\eta$ , is a free parameter, which in the results presented here we have set to  $\eta = 15$ .

(iii) For each particle,  $q$ , on the neighbour list we compute the reachability distance

$$d_{\text{RD}}(p, q) = \max(\text{dist}_{\text{OPTICS}}(p, q), d_{\text{CORE}}(p)), \quad (12)$$

and add this quantity to particle  $q$  as a new attribute.

(iv) We add particle  $p$  to the 'reachability list', and the  $q$  neighbouring particles, sorted by their reachability distance  $d_{\text{RD}}$ , are added to the 'seed list'.

We then take the first particle from the seed list and repeat steps (i) through (iv). In step (iv), if a particle  $q$  is already on the seed list and the new  $d_{\text{RD}}$  is smaller than its former value on the seed list,  $q$  is moved forward in the list and  $d_{\text{RD}}$  is updated. These steps are repeated until all particles in the outflow lobe have been added to the reachability list. Fig. 4 illustrates a reachability list.

### 2.5.2 Extracting bullets

The OPTICS algorithm provides us with an ordered list of the particles' reachability. Ankerst et al. (1999) provide an automated method that extracts clusters from the reachability list. Low  $d_{\text{RD}}(p, q)$  indicates that particles  $p$  and  $q$  are close, in terms of the chosen distance measure (equation 10). In Fig. 4 we plot the reachability distance against the position of the particles on the reachability list. Following Ankerst et al. (1999), we identify (sub-)clusters of particles according to 'steep-down' (blue) and 'steep-up' (orange) regions (plus some other more arcane criteria detailed in Ankerst et al. 1999). We sort these (sub-)clusters into an hierarchical structure of clusters and sub-clusters. From top to bottom, the horizontal black lines in Fig. 4 show the extracted hierarchical structure of clusters (on the top level) and sub-clusters below.

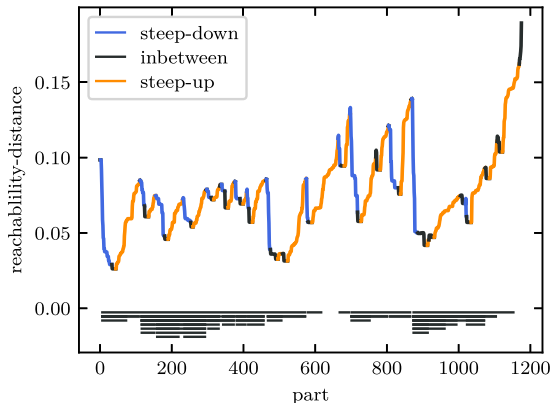


**Figure 4.** Reachability distance (equation 12) against position in the reachability list for particles from simulation S:5-V:3.0-K:3-R:13 at  $t = 104$  kyr. Following (Ankerst et al. 1999), clustered particles are found in dips of the reachability distance. The colour indicates whether a particle is part of a steep-down (blue) or steep-up region (orange). The horizontal black lines on the bottom show the clusters (on the top level) and their sub-clusters.

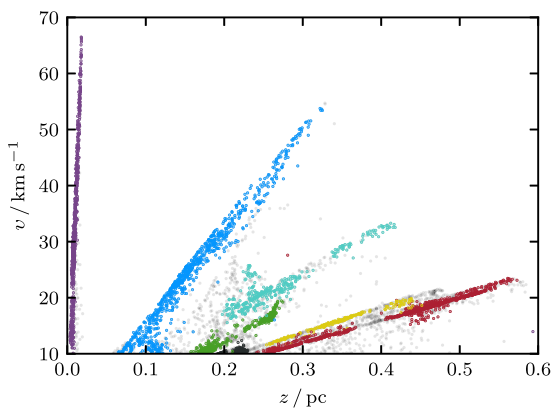


**Figure 5.** Position–velocity diagram for one of the outflow lobes from simulation S:5-V:3.0-K:3-R:13 at  $t = 70$  kyr. Dots represent individual SPH particles. Different colours represent six different outflow bullets identified by the OPTICS algorithm. Linear features represent individual outflow bullets, called Hubble wedges (Rohde et al. 2019).

To link a (sub-)cluster to an outburst event, we make use of the sub-set of particles in that (sub-)cluster that were initially ejected by the protostar. If, from this sub-set of initially ejected particles, more than 80 per cent belong to the same outburst event, we link the (sub-)cluster to that outburst event. We go through the hierarchical structure from top (clusters) to bottom (smallest sub-clusters) until this criterion is fulfilled. Fig. 5 shows the position–velocity diagram of the particles in an outflow lobe, where the colours represent the individual bullets. Since bullets that have decelerated too much are challenging to track, we only consider bullets which contain particles with velocities exceeding  $20 \text{ km s}^{-1}$ . The OPTICS algorithm is very effective in tracing the particles,  $n_{\text{PART},l,b}$ , corresponding to a specific outflow bullet,  $b$ , over the course of a simulation.

### 3 OUTFLOW PROPERTIES

We extract all the outflow cavities and bullets from the simulations with episodic outflow feedback in Rohde et al. (2021), using the methodology of Section 2. Based on this information we then compute various outflow properties which can be constrained by observation (e.g. Dunham et al. 2014b; Mottram et al. 2017; Li et al. 2020). We note that the observations cover a wide range of core masses from  $\sim 0.1 M_{\odot}$  to  $\sim 80 M_{\odot}$ , whereas our simulations only treat cores with a mass of  $1 M_{\odot}$ . Due to the different initial conditions for the simulations, and their corresponding free-fall times, some cores form protostars faster than others. We evaluate each simulation at time  $t_{\text{EVOL}} = t - t_0$ , where,  $t$  is the simulation time and  $t_0$  is the time when the first protostar in a given simulation reaches the threshold mass for protostellar feedback,  $M_0 = 0.02 M_{\odot}$ .

The ages of observed protostars cannot be measured directly, but there are several ways in which protostars can be arranged in an approximate evolutionary sequence, as discussed in Section 1. The most commonly used scheme is the one proposed by Lada (1987), based on the observed infrared spectral index and the predictions of theoretical models by Adams & Shu (1986). This scheme involves three Classes, labelled I, II, and III, corresponding to an embedded main accretion phase (Class I), a disc accretion phase where the envelope has faded (Class II), to an isolated pre-main-sequence phase (Class III; Adams, Lada & Shu 1987). Andre et al. (1993) suggest an additional Class 0 for deeply embedded sources, which show no emission between  $2 \mu\text{m}$  and  $20 \mu\text{m}$  but have powerful outflows and are defined observationally by their large sub-millimetre excess,  $L_{\text{SUBMM}}/L_{\text{BOL}} > 0.005$ . However, this classification scheme can be misleading as an evolutionary sequence, because the same object might be classified differently depending on the viewing angle (Calvet et al. 1994; Crapsi et al. 2008). Consequently, Robitaille et al. (2006) have proposed a different scheme, involving stages, and based on the physical properties of the protostar.

As we are interested in evaluating evolutionary stages without explicitly using SEDs, we follow the classification scheme of Robitaille et al. (2006), in which Stage 0 ends, and Stage I begins, when the protostellar mass exceeds the bound core mass (Dunham et al. 2014a). Averaged over all the simulations the mean Stage 0 lifetime as  $t_{\text{S1}} = 34 (\pm 25)$  kyr, which is close to the mean simulated Stage 0 lifetime of  $\sim 27$  kyr reported by Dunham & Vorobyov (2012), but significantly lower than observed Class 0 lifetimes of  $\sim 130$ – $\sim 260$  kyr estimated by Dunham et al. (2015). Reasons why the simulated Stage 0 lifetimes are rather short might be

- (i) the small radii of the dense cores, which lead to a rapid collapse,
- (ii) missing magnetic fields, which would slow down collapse,
- (iii) a missing larger scale envelope compared to cores embedded in molecular clouds.

Since we frequently wish to discuss mean values of some quantity,  $q_l$ , averaged over all the identified lobes from all the simulations,  $l = 1$  to  $l = n_{\text{LOBE}}$ , we define

$$\langle q_l \rangle = \frac{1}{n_{\text{LOBE}}} \sum_{l=1}^{n_{\text{LOBE}}} q_l. \quad (13)$$

To evaluate the quality of an estimated quantity,  $q_{\text{EST}}$ , we compare it with the ground truth,  $q_{\text{TRUE}}$ , for the underlying simulation, over a specified time interval,  $t_0$ – $t_1$ . If during this time interval we have  $n_s$  snapshots in the range  $[n_0, n_1]$ , the mean absolute error is

$$\bar{\Delta}_{\text{ABS},[t_0,t_1]} q_{\text{EST}} = \frac{1}{n_s} \sum_{i=n_0}^{n_1} |q_{\text{EST}}(i) - q_{\text{TRUE}}(i)|, \quad (14)$$

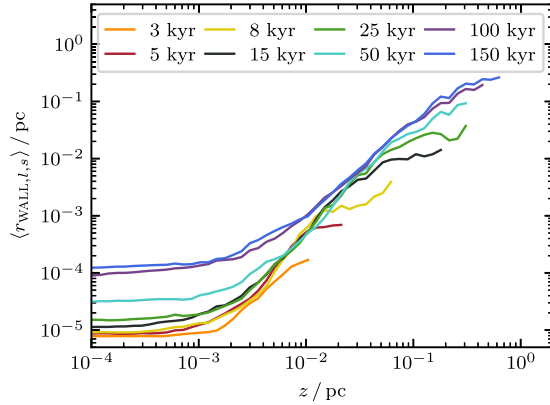


**Figure 6.** Mean outflow width,  $\langle r_{\text{WALL},l,s} \rangle$  (equation 16), against the length along the outflow lobe,  $z$ , at various times  $t_{\text{EVOL}} = 3\text{--}150$  kyr (orange to blue). Outflow lobes grow in length and width.

and the mean fractional error is

$$\overline{\Delta}_{\text{REL},[t_0,t_1]} q_{\text{EST}} = \frac{1}{n_s} \sum_{i=0}^{n_l} \frac{|q_{\text{EST}}(i) - q_{\text{TRUE}}(i)|}{|q_{\text{TRUE}}(i)|}. \quad (15)$$

The important time intervals are Stage 0 ( $t_0=0$  kyr to  $t_1=34$  kyr), Stage I ( $t_0=34$  kyr to  $t_1=150$  kyr), and the total simulation time ( $t_0=0$  kyr to  $t_1=150$  kyr). These time intervals are denoted with indices [s0], [sI], or [s0 + I].

### 3.1 Radius

Given the location of the outflow cavity wall (see Section 2.4.2), we can compute the mean cavity radius (Fig. 2) for slice  $s$  in lobe  $l$ ,

$$r_{\text{WALL},l,s} = \frac{1}{n_R} \sum_{i=0}^{n_R} r_{\text{WALL},l,s,i}. \quad (16)$$

Here,  $r_{\text{WALL},l,s,i}$  is the distance from the outflow axis to the cavity wall along ray  $i$  in slice  $s$  of lobe  $l$  (Section 2.4.2). We use the largest mean cavity radius,  $\max(r_{\text{WALL},l,s})$ , for all the slices along the outflow axis as the characteristic half-width of the whole outflow lobe,  $r_{\text{WALL},l}$ .

Fig. 6 shows the mean cavity width for all the outflow lobes from all the simulations,  $\langle r_{\text{WALL},l,s} \rangle$ , plotted against the length of the outflow lobe,  $z$ , for eight different times between  $t_{\text{EVOL}} = 3$  kyr and 150 kyr. Similar to what is observed (Frank et al. 2014), the outflow cavity steadily expands with increasing  $z$ , reaching a maximum width of 0.3 pc.

### 3.2 Outflow properties

The mean outflow velocity of each lobe  $l$  is

$$v_l = \frac{1}{n_{\text{PART},l}} \left| \sum_{p=0}^{n_{\text{PART},l}} \mathbf{v}_{l,p} \right|, \quad (17)$$

where  $\mathbf{v}_{l,p}$  is the velocity of particle  $p$  and the summation is over all the particles in the lobe. Similarly, the total momentum of each lobe is

$$p_l = M_{\text{PART}} \left| \sum_{p=0}^{n_{\text{PART},l}} \mathbf{v}_{l,p} \right|, \quad (18)$$

## Protostellar outflows: a window to the past 2559

where  $M_{\text{PART}}$  is the mass of a single SPH particle, and the mass of each lobe is

$$M_l = n_{\text{PART},l} M_{\text{PART}}. \quad (19)$$

We can then compute means over all the lobes from all the simulations (equation 13). Fig. 7 shows the mean outflow length,  $\langle r_{\text{FRONT},l} \rangle$  (left-hand panel; equation 9), mean outflow mass,  $\langle M_l \rangle$  (middle panel; equation 19), and mean outflow momentum,  $\langle p_l \rangle$  (right-hand panel; equation 18), against the evolutionary time (orange lines). The blue line shows these outflow properties for a single simulation (S:7-V:1.0-K:1-R:13). Observational data from Dunham et al. (2014b), Mottram et al. (2017), and Li et al. (2020) are shown with, respectively, red, green, and black markers. The time-scales on the  $x$ -axis for these observations are dynamical ages (see Section 4.1.1) which depend on the outflow length and should therefore be interpreted as lower limits.

The mean outflow length is almost constant at  $\sim 0.02$  pc for the first  $\sim 3$  kyr, and thereafter grows continuously with a power-law slope,  $\langle r_{\text{FRONT},l} \rangle \propto t_{\text{EVOL}}^{1.4}$ . Our simulations are in good agreement with the observations of Mottram et al. (2017), but somewhat lower than those of Li et al. (2020). The mean outflow mass increases asymptotically towards  $\sim 0.13 M_{\odot}$ , and is in the same range as in the aforementioned observations during Stage 0. The mean outflow momentum behaves similarly to the mean outflow mass during Stage 0. However, the mean outflow momentum has a peak at  $\sim 60$  kyr, and then decreases during Stage I. Dividing the mean outflow momentum by the mean outflow mass gives a mean outflow velocity of only a few  $\text{km s}^{-1}$ . While the mean outflow mass and momentum are continuous, the single simulation (blue lines) shows strong evidence for episodic outbursts. The extremely low mass and momentum values for some of the lobes (orange shaded region) originate in a few cases where the K-means algorithm finds a lobe, but no corresponding volume, e.g. for inactive ancient lobes. However, this does not mean that the other lobes in such a simulation also have such low outflow masses and momenta.

### 3.3 Outflow velocity

When observing protostellar outflows, the initial ejection velocity is hard to measure, because the ejected gas almost immediately interacts with the cavity or envelope material, and consequently is slowed down. However, to estimate accretion rates or entrainment factors from outflow properties, the ejection velocity is crucial.

Fig. 8 shows kernel density estimates (KDEs) for three different characteristic velocities, from all the simulated outflows over the period  $t_{\text{EVOL}} = 0$  to 150 kyr. The purple line shows the mean lobe velocity,  $v_l$  (equation 17), peaking at  $v = 2.4 \text{ km s}^{-1}$ . The red line shows the mean velocity for all the outflow bullets (Section 2.5). Outflow bullets have higher mean velocities with a peak at  $19.6 \text{ km s}^{-1}$ , and maximum values up to  $90 \text{ km s}^{-1}$ . Averaging over all outburst events from all simulations gives a mean Keplerian velocity of  $15 \text{ km s}^{-1}$  at the launching radius (i.e. two times the stellar radius). Since we eject particles with this Keplerian velocity modulated by the distribution derived by Matzner & McKee (1999), which in our case has a mean value of 2.2 (see Appendix B), the mean ejection velocity is  $33 \text{ km s}^{-1}$ . We can estimate the true ejection velocity from the simulations at a given time by computing the mean velocity of all particles ejected during the current time-step (blue line). The mean ejection velocities range from  $\sim 10 \text{ km s}^{-1}$  to  $\sim 50 \text{ km s}^{-1}$  with a peak at  $\sim 30 \text{ km s}^{-1}$ , in good agreement with the expected ejection velocity. For all further estimates we use ejection velocities between

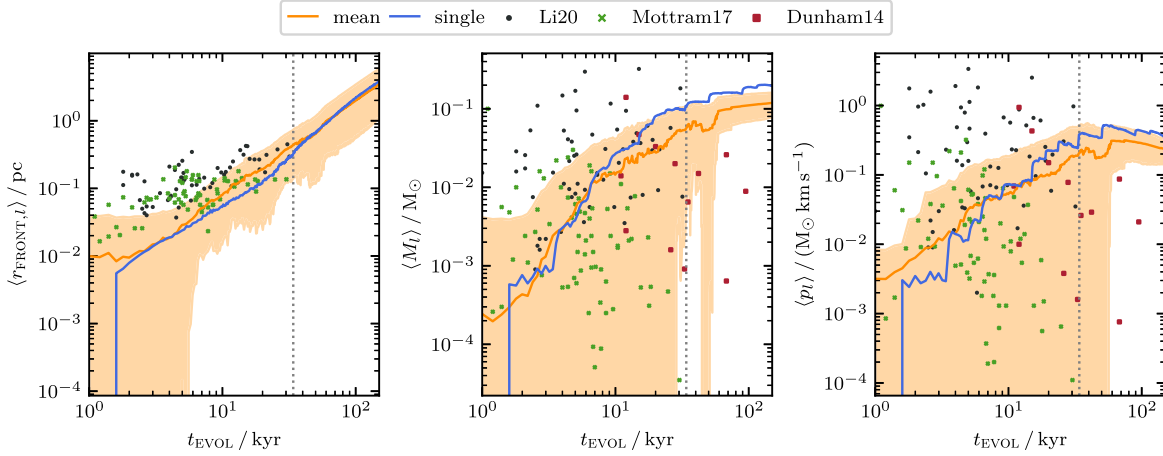


**Figure 7.** The mean outflow length,  $\langle r_{\text{FRONT},l} \rangle$  (left-hand panel), mass,  $\langle M_l \rangle$  (middle panel), and momentum,  $\langle p_l \rangle$  (right-hand panel), averaged over all the lobes from all the simulations (orange), plotted against the evolutionary time. The orange shaded region shows the standard deviation. For comparison, the blue line shows the results from a single simulation (S:7-V:1.0-K:1-R:13). Observational data from Dunham et al. (2014b), Mottram et al. (2017), and Li et al. (2020) are shown with, respectively, red, green, and black markers. Dunham et al. (2014b) do not provide data for the outflow length. The grey dotted lines indicate the transition from Stage 0 to Stage I averaged over all simulations. The mean outflow length (left) is continuously growing. The mean outflow mass (middle, equation 19) grows asymptotically towards  $0.13 M_{\odot}$ . The mean outflow momentum (right, equation 18) grows during Stage 0 and decreases during Stage I. While the mean mass and mean outflow momentum change quite smoothly, the single simulation shows highly episodic variations.

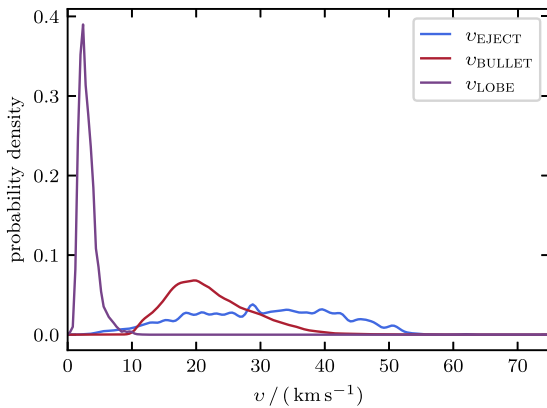


**Figure 8.** Probability density of the mean outflow- (purple), mean bullet- (red), and mean ejection-velocity (blue) for all lobes from all simulations averaged over  $t_{\text{EVOL}} = 0$  to 150 kyr. The mean outflow velocity peaks at a few  $\text{km s}^{-1}$ , and the mean bullet velocity peaks at  $\sim 20 \text{ km s}^{-1}$ ; the mean ejection velocity is more broadly distributed between  $\sim 10$  and  $\sim 50 \text{ km s}^{-1}$ .

$v_{\text{EJECT}} = 20 \text{ km s}^{-1}$  and  $40 \text{ km s}^{-1}$ , with  $v_{\text{EJECT}} = 30 \text{ km s}^{-1}$  being the default value.

### 3.4 Entrainment factor

Ejected outflow gas entrains secondary envelope gas, and together they form a molecular outflow (Tabone et al. 2017; Zhang et al. 2019). The entrainment factor, i.e. the ratio of total outflow mass to ejected mass, is generally not known, but can be estimated if we know the initial ejection velocity.

Assuming that the momentum of the initially ejected gas is conserved, we have

$$M_l v_l = M_{\text{EJECT},l} v_{\text{EJECT},l}, \quad (20)$$

and hence an estimate of the entrainment factor is given by

$$\epsilon_{\text{OF},l} \equiv \frac{M_l}{M_{\text{EJECT},l}} = \frac{v_{\text{EJECT},l}}{v_l}. \quad (21)$$

Here,  $M_{\text{EJECT}}$  is the ejected gas mass,  $v_{\text{EJECT},l}$  is the ejection velocity (Section 3.3),  $v_l$  and  $M_l$  are given by equations (17) and (19). Note that the ejected momentum will actually be somewhat higher than the outflow momentum, since the envelope is still collapsing and therefore contributes momentum opposing the ejected momentum.

Fig. 9 compares the time evolution of the true mean entrainment factor (blue line and blue shading for the standard deviation) and the time evolution of the mean entrainment factor estimated using equation (21) with (a)  $v_{\text{EJECT}} = 30 \text{ km s}^{-1}$  (orange line) and (b)  $20 \text{ km s}^{-1} \leq v_{\text{EJECT}} \leq 40 \text{ km s}^{-1}$  (orange shading). For the first  $\sim 7$  kyr, the entrainment factor has a very large spread, but thereafter it settles down to  $\langle \epsilon_{\text{OF}, \text{TRUE},l} \rangle \sim 10 (\pm 5)$ .

For the first  $\sim 80$  kyr, the entrainment factor estimated using equation (21) with  $v_{\text{EJECT}} = 30 \text{ km s}^{-1}$  resembles the true one very well; the mean absolute error is  $\overline{\Delta}_{\text{ABS}, [0 \text{ kyr}, 80 \text{ kyr}]} (\epsilon_{\text{OF},l}) = 0.4$ . At later times, the mean outflow velocity drops (Fig. 7), causing equation (21) to give an overestimate of the entrainment factor. Over the full time evolution the mean absolute error is  $\overline{\Delta}_{\text{ABS}, \text{S0+I}} (\epsilon_{\text{OF},l}) = 1.5$ . The orange shaded region on Fig. 9 shows the entrainment factor estimated using equation (21) with  $20 \text{ km s}^{-1} \leq v_{\text{EJECT}} \leq 40 \text{ km s}^{-1}$ . This range of ejection velocities translates into a change in the entrainment factor of  $\sim \pm 4$ , which is comparable to the standard deviation of the true entrainment factor.

We have used equation (21) to estimate entrainment factors from the observations of Dunham et al. (2014b), Mottram et al. (2017), and Li et al. (2020), assuming an ejection velocity of  $v_{\text{EJECT}} = 30 \text{ km s}^{-1}$ , and compared them with our simulations. The entrainment factors estimated from the Li et al. (2020) data (black markers) are about a factor of two smaller, probably because their mean outflow velocity,  $\bar{v}_{\text{LI}} = 11.2 \pm 9.2$ , is significantly higher than for our simulated outflows. The entrainment factors computed from the Dunham et al. (2014b) data (green markers) and the Mottram et al. (2017) data

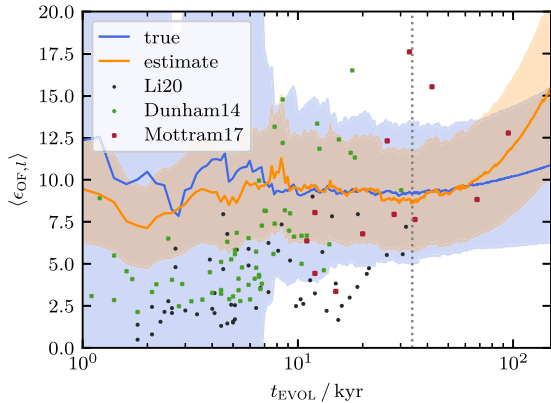


**Figure 9.** The time evolution of the mean entrainment factors, averaged over all simulations. The blue line shows the mean true entrainment factor, and the blue shading represents the standard deviation. The orange line shows the mean entrainment factor estimated using equation 21 with a fixed ejection velocity of  $v_{EJECT} = 30 \text{ km s}^{-1}$ , and orange shading shows the range that is obtained if  $v_{EJECT}$  is varied between  $20 \text{ km s}^{-1}$  and  $40 \text{ km s}^{-1}$ . Observational data from Dunham et al. (2014b), Mottram et al. (2017), and Li et al. (2020) are shown with – respectively – green, red, and black markers. The grey dotted line indicates the transition from Stage 0 to Stage I. The mean estimated entrainment factor is close to the mean true entrainment factor during Stage 0, but at late times tends to give an overestimate.

(red markers) are correlated with dynamical age. A Kendall Rank Correlation test gives the correlation statistic  $\tau_{KR} = 0.51$ , with the probability that the null hypothesis is true  $p \ll 0.01$ . This follows directly from their similarly anticorrelated outflow velocities. Our simulated entrainment factors do not follow this trend.

#### 4 INFERRING STELLAR AGES AND ACCRETION RATES FROM OUTFLOWS

Observers infer stellar ages and accretion rates from outflow properties (e.g. Li et al. 2020; Nony et al. 2020). Using similar methods, we estimate stellar ages and accretion histories from the outflow properties computed in the preceding section (Section 3). These estimates are then compared with the underlying simulations to evaluate the different methods. We assume that observational uncertainties and selection effects (like inclination) can be neglected.

##### 4.1 Age estimation

Especially when studying young embedded protostars, it is crucial to have a reliable estimate of the protostellar age. The most common methods for estimating protostellar ages rely on analysing the SED, which provides, for example the bolometric temperature (Myers & Ladd 1993; Enoch et al. 2009) and the ratio of bolometric to submillimeter luminosity (Andre et al. 1993; Young & Evans 2005), and hence a constraint on the protostar’s evolutionary stage. Using the spectral index between  $2 \mu\text{m}$  and  $20 \mu\text{m}$ , sources can be divided into Classes 0 through III (Lada 1987), roughly corresponding to evolutionary Stages 0 through III. The drawbacks with these methods are that high-angular resolution observations are needed that the classification depends on the viewing angle (Calvet et al. 1994; Crapsi et al. 2008), and that the distinction between classes constrains the evolutionary stage but not the actual stellar age (Vazzano et al. 2021). Frimann, Jørgensen & Haugbølle (2016) perform comprehensive

#### Protostellar outflows: a window to the past 2561

numerical simulations, including radiative transfer modelling, and find that the bolometric temperature and ratio of bolometric to submillimeter luminosity trace the evolutionary stage well but are poor measures of the protostellar age.

##### 4.1.1 Dynamical ages

An alternative to SED-based methods is to determine dynamical time-scales on the basis of the observed properties of outflows. Since outflows occur during the earliest phases of star formation, dynamical ages constrain protostellar ages. Here we compute dynamical ages using five different methods, and evaluate how accurately they reflect true outflow ages, and hence protostellar ages.

The most common method for estimating dynamical ages is to compute the ratio of the lobe extent to the maximum velocity found in the lobe (e.g. Mottram et al. 2017)

$$\tau_{\text{MAX-VEL},l} = \frac{r_{\text{FRONT},l}}{v_{\text{MAX},l}}. \quad (22)$$

For this method,  $v_{\text{MAX},l}$  is defined as the mean velocity of the 50 fastest SPH particles in lobe  $l$ .

Another common method is to use the terminal speed at the front of the lobe instead of the highest velocity (e.g. Zhang et al. 2005)

$$\tau_{\text{FRONT},l} = \frac{r_{\text{FRONT},l}}{v_{\text{FRONT},l}}. \quad (23)$$

For this method,  $v_{\text{FRONT},l}$  is defined as the mean velocity of the 50 most distant SPH particles in the lobe  $l$ .

Li et al. (2020) estimate the dynamical age using the ‘perpendicular’ method proposed by Downes & Cabrit (2007),

$$\tau_{\text{PERP},l} = \frac{r_{\text{WALL},l}}{v_l}, \quad (24)$$

where  $v_l$  the mean lobe velocity (equation 17). Downes & Cabrit (2007) include an additional factor  $1/3$  on the right-hand side of equation (24), to account for inclination uncertainty, but since we neglect inclination, we omit this factor.

In addition to dynamical ages based on the properties of the whole lobe, we can also estimate dynamical ages based on individual outflow bullets. The dynamical age for an individual bullet (Section 2.5) is

$$\tau_{l,b} = \frac{r_{\text{MAX},l,b}}{v_{\text{MAX},l,b}}, \quad (25)$$

where  $r_{\text{MAX},l,b}$  and  $v_{\text{MAX},l,b}$  are the mean distance and velocity of the bullet’s head.  $r_{\text{MAX},l,b}$  and  $v_{\text{MAX},l,b}$  are computed by identifying the largest distance and largest velocity among particles in the given bullet and then averaging over all particles in the bullet exceeding 90 per cent of these largest values. Following Nony et al. (2020), we use the greatest dynamical age among all the bullets in a lobe as an estimate of the lobe’s dynamical age,  $\tau_{\text{BULLET},l}$ .

Finally, we propose a new method for estimating the dynamical age, which we call the  $\Delta$ -method. Given two distinct successive outflow bullets in a lobe, we can compute the time-scale between the two corresponding outbursts (cf. Li et al. 2020),

$$\Delta t_{l,b} = \tau_{l,b+1} - \tau_{l,b}, \quad (26)$$

where  $\tau_{l,b}$  is given by equation (25). If the number of SPH particles in bullet  $b$  of lobe  $l$  is  $n_{\text{PART},l,b}$ , the momentum of bullet  $b$  is

$$p_{l,b} = M_{\text{PART}} \sum_{p=1}^{n_{\text{PART},l,b}} v_{l,b,p}, \quad (27)$$

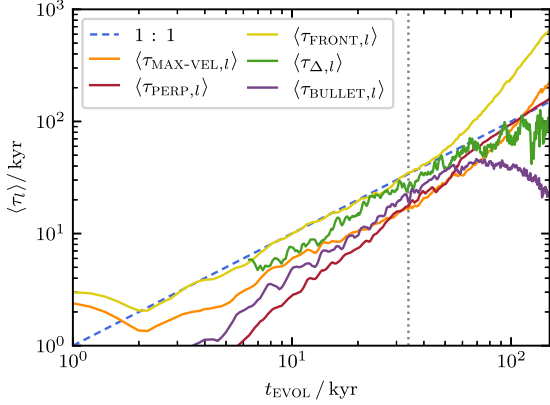


**Figure 10.** Mean dynamical age estimates,  $\langle \tau_l \rangle$ , obtained with the five different methods detailed in Section 4.1.1, plotted against the true protostellar age, for all lobes from all simulations. The blue dashed line shows the one-to-one correlation, and the grey dotted line indicates the transition from Stage 0 to Stage I. The  $\tau_{\text{FRONT}}$  method gives a good estimate of the protostellar age during Stage 0, and the  $\tau_{\text{PERP}}$  method gives a good estimate during Stage I. The  $\Delta$ -method gives a good estimate during both Stages, but suffers from being inapplicable at very early times.

**Table 2.** The mean absolute error (equation 14) in kyr, and the mean fractional error (in brackets, equation 15), for the different dynamical age estimates, averaged over Stage 0, Stage I, and both Stages combined.

Method	$\bar{\Delta}_{\text{S0}} \langle \tau \rangle / \text{kyr}$		$\bar{\Delta}_{\text{SI}} \langle \tau \rangle / \text{kyr}$		$\bar{\Delta}_{\text{S0+I}} \langle \tau \rangle / \text{kyr}$	
$\tau_{\text{MAX-VEL}}$	8.4	(0.47)	25.5	(0.30)	21.7	(0.34)
$\tau_{\text{FRONT}}$	0.8	(0.08)	159.7	(1.36)	125.5	(1.07)
$\tau_{\text{PERP}}$	10.3	(0.66)	9.2	(0.15)	9.4	(0.26)
$\tau_{\text{BULLET}}$	8.0	(0.52)	57.0	(0.55)	46.2	(0.55)
$\tau_{\Delta}$	4.4	(0.22)	25.3	(0.24)	20.5	(0.24)

and the number of bullets needed to account for the total lobe momentum, multiplied by the time between the two youngest bullets ( $b = 0$  and  $b = 1$ ), then gives the dynamical age

$$\tau_{\Delta,l} = \frac{2 p_l}{p_{l,b=0} + p_{l,b=1}} \Delta t_{l,b=0}. \quad (28)$$

We only consider bullets that have  $\tau_{\Delta,l,b} > 1$  kyr since they would otherwise overlap too much.

Fig. 10 shows the mean dynamical age estimates,  $\langle \tau_l \rangle$ , obtained with the five different methods detailed above, plotted against the true protostellar age,  $t_{\text{EVOL}}$ ; the dashed blue line indicates one to one correspondence between  $\langle \tau_l \rangle$  and  $t_{\text{EVOL}}$ . Table 2 gives the mean absolute error,  $\bar{\Delta}_{\text{ABS},x}$  (equation 14), between  $\langle \tau_l \rangle$  and  $t_{\text{EVOL}}$  averaged over Stage 0, Stage I, and both Stages together; the values in brackets give the mean fractional errors,  $\bar{\Delta}_{\text{REL},x}$  (equation 15).

On average, the most commonly used,  $\tau_{\text{MAX-VEL}}$  method (equation 22) underestimates the true protostellar age during Stage 0 (by 8.4 kyr;  $\bar{\Delta}_{\text{REL,S0}} \langle \tau_{\text{MAX-VEL}} \rangle = 0.47$ ), and overestimates it during Stage I ( $\bar{\Delta}_{\text{REL,SI}} \langle \tau_{\text{MAX-VEL}} \rangle = 0.30$ ).

Using the  $\tau_{\text{FRONT}}$  method (equation 23) yields a dynamical age,  $\tau_{\text{FRONT}}$ , which is very accurate during Stage 0, with a mean fractional error of  $\bar{\Delta}_{\text{REL,S0}} \langle \tau_{\text{FRONT}} \rangle = 0.08$ . However, this method significantly overestimates the protostellar age during Stage I, with a mean absolute error of  $\sim 160$  kyr.

The  $\tau_{\text{PERP}}$  method (equation 24) underestimates the true protostellar age during Stage 0 ( $\bar{\Delta}_{\text{REL,S0}} \langle \tau_{\text{PERP}} \rangle = 0.66$ ) but is significantly more accurate during Stage I ( $\bar{\Delta}_{\text{REL,SI}} \langle \tau_{\text{PERP}} \rangle = 0.15$ ).

Using the  $\tau_{\text{BULLET}}$  method (equation 25), generally underestimates the protostellar age ( $\bar{\Delta}_{\text{REL,S0+I}} \langle \tau_{\text{BULLET}} \rangle = 0.55$ ). This may be because we cannot distinguish bullets that have interacted strongly with the envelope from the rest of the outflow. Observers probably face a similar problem identifying these bullets.

If there are two distinct bullets in the outflow cavity, the  $\Delta$ -method works well: the estimated dynamical ages,  $\tau_{\Delta}$ , have the lowest fractional error overall  $\bar{\Delta}_{\text{REL,S0+I}} \langle \tau_{\Delta} \rangle = 0.24$  and the  $\Delta$ -method performs second best for both Stage 0 and Stage I individually. The high scatter is caused by the reduced sample size of lobes with at least two distinct bullets.

This study ignores observational uncertainties, in particular inclination and selection effects. For an outflow inclined at angle  $\theta$  to the line of sight, the outflow velocity is reduced by  $\cos(\theta)$ , and the length (but not the width) is reduced by  $\sin(\theta)$ . Therefore, dynamical ages are affected by inclination. For randomly oriented outflows, the mean inclination is  $\bar{\theta} = 57.3^\circ$  (Bontemps et al. 1996), and for this inclination the estimates  $\tau_{\text{MAX-VEL},l}$  (equation 22),  $\tau_{\text{FRONT},l}$  (equation 23),  $\tau_{l,b}$  (equation 24), and  $\tau_{\Delta,l}$  (equation 25) will be too high by  $\tan(\bar{\theta}) = 1.56$ , whilst the estimate  $\tau_{\text{PERP},l}$  (equation 24) will be too high by  $\sec(\bar{\theta}) = 1.85$ . We cannot compute mean correction factors for a random distribution of inclinations, because the integrals involved diverge. In Appendix A we give correction factors for extreme inclinations. However, we note that for low inclinations lengths are very inaccurate, and for high inclinations velocities are very inaccurate.

Curtis et al. (2010) and Vazzano et al. (2021) argue that dynamical ages are an imprecise measure of protostellar age and may only represent lower limits. Our simulations show that dynamical ages have an average intrinsic error of at least 15 per cent during Stage I in the ideal case of nearly perfect information. Dynamical ages computed from observations might come with significantly larger errors, e.g. due to undetected bullets further out. If there are two young and distinct bullets in the outflow, the  $\Delta$ -method seems to be a good alternative to other commonly used methods. Otherwise, we recommend using the perpendicular method since this is the most accurate method during Stage I. If it is known from other indicators that the system is still in Stage 0, the  $\tau_{\text{FRONT}}$  method is probably the best method, but it is very inaccurate for more evolved systems. The  $\tau_{\text{MAX-VEL}}$  method gives reasonable estimates overall, whilst the  $\tau_{\text{BULLET}}$  method is the most inaccurate.

#### 4.1.2 Outflow rates

Another indicator of the protostellar evolutionary Stage is the outflow activity. Outflow activity is expected to be high during Stage 0 and to decay thereafter (Sperling et al. 2021). Curtis et al. (2010) and Yıldız et al. (2015) find that the outflow rates for momentum and energy are higher in Class 0 sources than in Class I sources. Observers estimate the outflow rates for mass, momentum, and energy outflow rates from the outflow properties (Section 3.2) and the dynamical age (Section 4.1.1). In the sequel we compute outflow rates for our simulated outflows using the same methodology as Li et al. (2020) and compare the results obtained when adopting different dynamical age estimates, as well as the true protostellar age.

The mass outflow rate is given by

$$\dot{M}_{\text{OUT},l} = \frac{M_l}{\tau_l}, \quad (29)$$

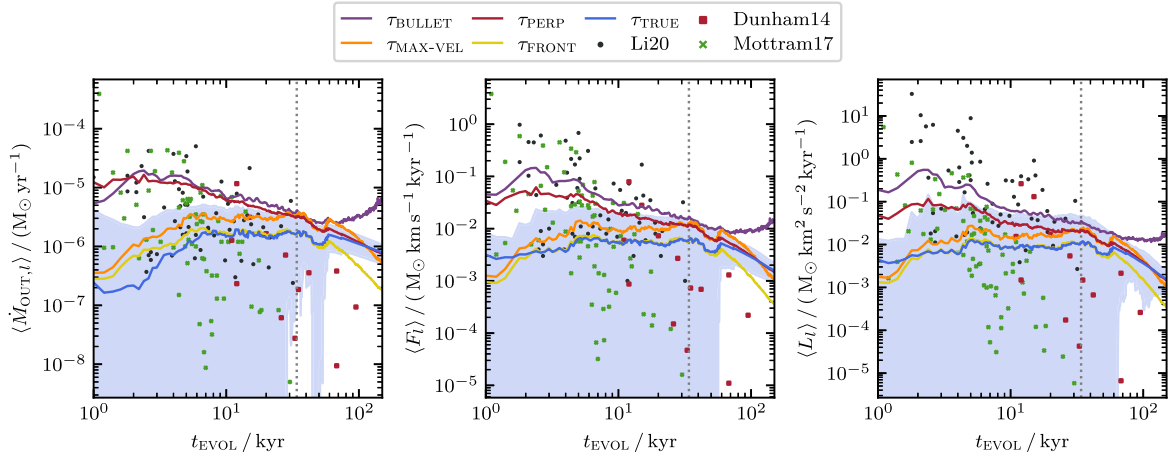


**Figure 11.** The mean outflow rates for mass (left panel, equation 29), momentum (middle panel, equation 30), and energy (right panel, equation 31) computed using different estimated dynamical ages and the true protostellar age, as per the colour code shown in the key; for the true protostellar age, the blue shading shows the standard deviation. The grey dotted vertical lines indicates the transition from Stage 0 to Stage I. Observational data from Dunham et al. (2014b), Mottram et al. (2017), and Li et al. (2020) are shown with – respectively – red, green, and black marker; the outflow rates for mass and energy from the Dunham et al. (2014b) observational data are computed using equations (29) and (31). The outflow rates for momentum and energy are rather constant in Stage 0, and slowly decay in Stage I.

**Table 3.** Mean absolute error (equation 14) between mean outflow rates for mass, momentum, and energy, estimated using the five different dynamical age estimates detailed in Section 4.1.1, and the corresponding rates obtained using the true protostellar age. The mean absolute errors are given separately for Stage 0, Stage I, and for the whole simulation. The values in brackets are the corresponding mean fractional errors (equation 15).

Method	$\overline{\Delta_x} \langle \dot{M}_{out,t} \rangle / (10^{-6} M_{\odot} \text{ yr}^{-1})$			$\overline{\Delta_x} \langle F_l \rangle / (10^{-3} M_{\odot} \text{ km s}^{-1} \text{ kyr}^{-1})$			$\overline{\Delta_x} \langle L_l \rangle / (10^{-3} M_{\odot} \text{ km}^2 \text{ s}^{-2} \text{ kyr}^{-1})$		
	Stage 0	Stage I	Stage 0 + I	Stage 0	Stage I	Stage 0 + I	Stage 0	Stage I	Stage 0 + I
$\tau_{\text{MAX-VEL}}$	1.5 (1.15)	0.6 (0.43)	0.8 (0.59)	4.8 (0.88)	1.8 (0.43)	2.4 (0.53)	8.1 (0.88)	2.8 (0.43)	3.9 (0.53)
$\tau_{\text{FRONT}}$	0.2 (0.21)	0.5 (0.47)	0.4 (0.41)	0.3 (0.06)	1.3 (0.47)	1.1 (0.38)	0.5 (0.06)	1.7 (0.47)	1.4 (0.38)
$\tau_{\text{PERP}}$	4.4 (6.48)	0.3 (0.22)	1.2 (1.61)	14.3 (3.00)	1.0 (0.22)	3.9 (0.84)	24.1 (3.00)	1.6 (0.22)	6.6 (0.84)
$\tau_{\text{BULLET}}$	5.5 (7.14)	2.4 (2.38)	3.1 (3.44)	27.9 (5.96)	7.2 (2.80)	11.8 (3.51)	75.1 (9.94)	11.2 (3.28)	25.4 (4.77)
$\tau_{\Delta}$	1.6 (0.32)	0.5 (0.38)	0.8 (0.37)	8.0 (0.32)	1.7 (0.38)	3.1 (0.37)	19.9 (0.32)	2.9 (0.38)	6.8 (0.37)

the outflow force by

$$F_l = \frac{p_l}{\tau_l}, \quad (30)$$

and the outflow mechanical luminosity by

$$L_l = \frac{1}{2} \frac{M_l v_l^2}{\tau_l}. \quad (31)$$

Fig. 11 shows the time evolution of the mean outflow rates computed using the different dynamical age estimates derived in Section 4.1.1, and using the true protostellar age (blue line). The outflow rates for mass (left-hand panel), momentum (middle panel), and energy (right-hand panel) show similar trends, increasing for the first  $\sim 5$  kyr, thereafter staying relatively constant during Stage 0, and then starting to decrease during Stage I.

The different dynamical age estimates lead to significantly different estimates of the outflow rates. Some methods work better for young outflows, and others work better for more evolved outflows. Table 3 gives the mean absolute errors and mean fractional errors for Stage 0, Stage I, and the two Stages together.

If dynamical age estimates based on the  $\tau_{\text{MAX-VEL}}$  method are used (orange line) the outflow rates are overestimated for most of the evolution, and particularly during Stage 0.

Dynamical age estimates based on the  $\tau_{\text{FRONT}}$  method (yellow line) yield the most accurate outflow rates during Stage 0, but thereafter underestimate the outflow rates.

Dynamical age estimates based on  $\tau_{\text{PERP}}$  method (red line) give significantly overestimated outflow rates during Stage 0, but return the most accurate outflow rates for more evolved outflows.

Dynamical age estimates based on the  $\tau_{\text{BULLET}}$  method (purple line) give significantly overestimated outflow rates for both young and evolved outflows; overall these are the least accurate outflow rates.

Fig. 11 does not show outflow rates computed using dynamical age estimates based on the  $\tau_{\Delta}$  method (equation 28), because not all lobes feature two distinct outflow bullets at the same time, and therefore the blue line is not a valid reference for this method. However, we can compute a valid reference using the true dynamical age for those cases where the  $\Delta$ -method is applicable and compute the corresponding mean absolute error (see Table 3). During Stage 0, the  $\tau_{\Delta}$  method yields the second best results after the  $\tau_{\text{FRONT}}$  method. For more evolved objects the  $\tau_{\Delta}$  method provides the second best estimate after the  $\tau_{\text{PERP}}$  method.

The estimated outflow rates from the simulations lie roughly in the middle of the range of observed outflow rates reported by Dunham et al. (2014b), Mottram et al. (2017), and Li et al. (2020). However, the observed outflow rates decline steeply with time, whereas the rates from the simulations are (a) approximately

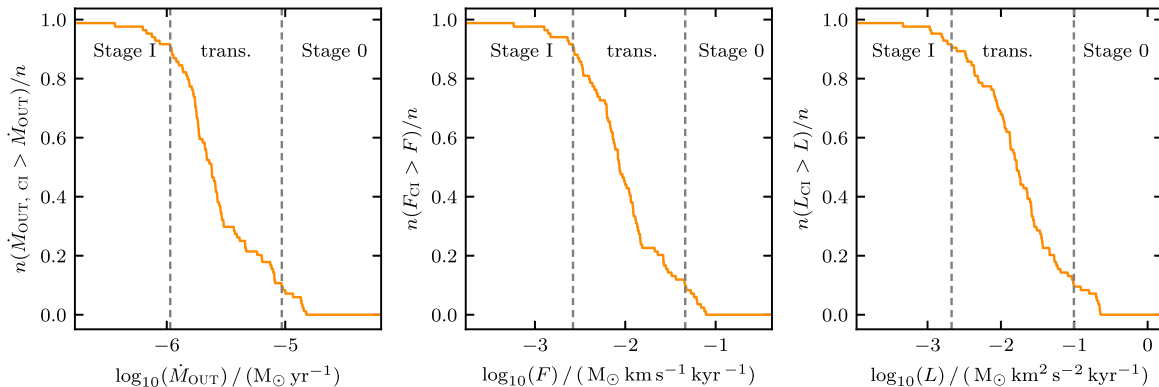


**Figure 12.** The fraction of lobes that have higher outflow rates for mass (left-hand panel), momentum (middle panel), and energy (right-hand panel) when entering Stage I, than the value on the  $x$ -axis. The vertical grey lines indicate where only 10 per cent of the lobes have a higher outflow rate (left line) and where only 90 per cent of the lobes have a lower outflow rate (right line) when entering Stage I. Using these thresholds we can define a transition region separating Stage 0 and Stage I sources.

constant and lower than the observed ones during Stage 0, and (b) higher than the observed ones and only slowly declining during Stage I.

Since the core still contains a significant amount of unaccreted mass at the transition between Stage 0 and Stage I, we expect the accretion rate and therefore the outflow activity to diminish slowly across the transition. This slow-down in activity might serve as an indicator of whether the protostar is in Stage 0 or Stage I. In order to quantify the outflow rates for mass ( $\dot{M}_{\text{OUT}, \text{CI}}$ ; left-hand panel of Fig. 12), momentum ( $F_{\text{CI}}$ ; middle panel), and energy ( $L_{\text{CI}}$ ; right-hand panel) that mark the transition from Stage 0 or Stage I, we compute these rates for each simulation at the time when the protostar enters Stage I. In Fig. 12 we count all objects with a transition value larger than the value on the  $x$ -axis, i.e. we show the fraction of objects that have already transitioned to Stage I at a given value of  $\dot{M}_{\text{OUT}, \text{CI}}$ ,  $F$  or  $L$ . The objects have a mean gradient of  $\langle \nabla \dot{M}_{\text{OUT}, \text{CI}} \rangle = -1.4 \times 10^{-7} \text{ M}_{\odot} \text{ yr}^{-1} \text{ kyr}^{-1}$ ,  $\langle \nabla F_{\text{CI}} \rangle = -7 \times 10^{-4} \text{ M}_{\odot} \text{ km s}^{-1} \text{ kyr}^{-2}$ , and  $\langle \nabla L_{\text{CI}} \rangle = -2 \times 10^{-3} \text{ M}_{\odot} \text{ km}^2 \text{ s}^{-2} \text{ kyr}^{-2}$  at the transition to Stage I and are therefore mostly decreasing. Hence we interpret the outflow rates on the  $x$ -axis as an evolutionary sequence, and classify objects as mainly Stage 0 or Stage I on the basis of their respective mass, momentum, and energy outflow rates. The vertical grey lines on Fig. 12 indicate the 10<sup>th</sup> and 90<sup>th</sup> percentile where most objects are still in Stage 0 or have already transitioned to Stage I, respectively.

The transition region between the 10<sup>th</sup> and 90<sup>th</sup> percentile is rather narrow for  $\dot{M}_{\text{OUT}}$  and this might facilitate a reliable test of whether the object is in Stage 0 or Stage I. However, our simulation sample is limited to  $1 \text{ M}_{\odot}$  cores, and the thresholds might vary significantly with core mass. Distinguishing evolutionary stages becomes even more challenging when account is taken of the fact that outflow rates, especially the energy rate (mechanical luminosity), depend strongly on the inclination angle (see Table A1).

#### 4.1.3 Opening angle

Protostellar outflows do not only expand along the outflow direction; they also widen over time (Frank et al. 2014; Hsieh et al. 2017). We compute the time evolution of the opening angles of the simulated outflows, and compare them to the observational data from Arce & Sargent (2006), Seale & Looney (2008), and Velusamy et al.

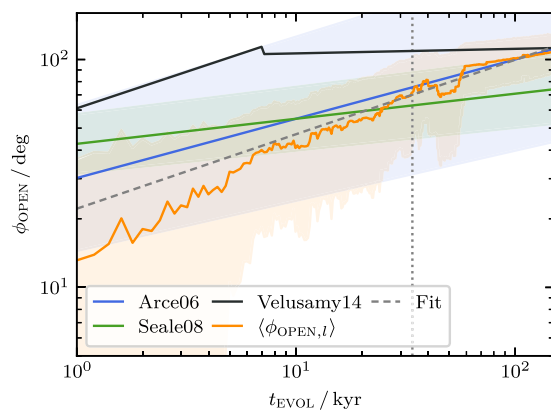


**Figure 13.** Mean opening angle against protostellar age. The orange line shows the mean opening angle,  $\langle \phi_{\text{OPEN}, I} \rangle$ , with its standard deviation (shaded region) for all outflow lobes from all simulations. The grey dotted vertical line indicates the transition from Stage 0 to Stage I, and the grey dashed line shows the best power-law fit to the simulation results (as per equation 33). The blue and green lines show the relations derived by – respectively – Arce & Sargent (2006) and Seale & Looney (2008) from observations, with the corresponding shaded regions representing the uncertainties. The black line shows the relation derived by Velusamy et al. (2014) from observations. Our results match the results of Arce & Sargent (2006) well, and confirm that the opening angles of outflow cavities widen over time.

(2014), to assess whether opening angles might be used to estimate protostellar ages.

We first compute the opening angle of each slice along the outflow axis (see Section 2.4.2 and Fig. 2),

$$\phi_{\text{OPEN}, I, s} = 2 \arctan \left( \frac{r_{\text{PERP}, I, s}}{z_{I, s}} \right). \quad (32)$$

Then we define the opening angle of the lobe,  $\phi_{\text{OPEN}, I, s}$ , as the largest  $\phi_{\text{OPEN}, I, s}$  along the outflow axis, with the constraint that  $z_{I, s} > 0.002 \text{ pc}$ . We use this threshold to exclude extremely large opening angles close to the source.

Fig. 13 shows how the opening angle varies with protostellar age according to Arce & Sargent (2006; blue line), Seale & Looney (2008; green line), and Velusamy et al. (2014; black line). The orange

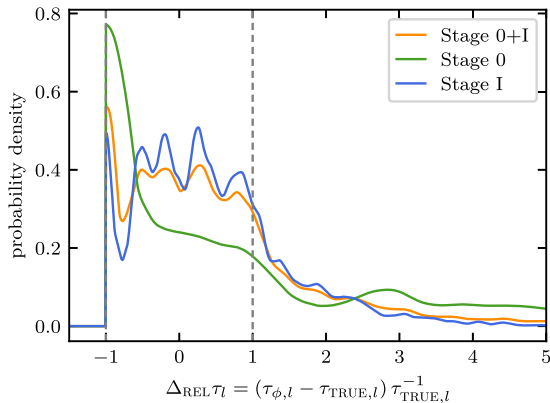


**Figure 14.** Probability density of the fractional error (i.e.  $\Delta_{\text{REL}}\tau_\phi = (\tau_\phi - \tau_{\text{TRUE}})/\tau_{\text{TRUE}}$ ) for all dynamical age estimates,  $\tau_\phi$ , made using the opening angle–age relation (equation 33). The green line shows the probability density of the error for Stage 0, the blue line for Stage I, and the orange line for both Stages together. The high chance of seriously over or underestimating the true protostellar age demonstrates that the opening angle–age relation is not a reliable method for estimating protostellar ages.

line shows the mean opening angle for all lobes from all simulations,  $\langle\phi_{\text{OPEN},l}\rangle$ , together with the corresponding standard deviation (orange shaded region). The grey dashed line shows a least-squares fit to the time evolution of  $\langle\phi_{\text{OPEN},l}\rangle$ , of the form

$$\phi_{\text{OPEN}}(t) = b [t/\text{kyr}]^\alpha, \quad (33)$$

with parameters  $b = 22.2(\pm 0.3)^\circ$  and  $\alpha = 0.327(\pm 0.003)$ . The mean opening angles range from  $\langle\phi_{\text{OPEN},l}\rangle \sim 13^\circ$  to  $\sim 110^\circ$ , with the trend that more evolved outflows have higher opening angles. A Kendall Rank Correlation test yields a correlation statistic  $\tau_{\text{KR}} = 0.39$ , with a probability that the null hypothesis is true  $p \ll 0.01$ .

Comparing our simulated outflows with observations, we find significantly lower opening angles during the first  $\sim 7$  kyr. Thereafter, the simulations are in good agreement with the observations of Arce & Sargent (2006). The power-law relation obtained by Arce & Sargent (2006) has an exponent  $\alpha_{\text{ARCE}} = 0.26$ , which is close to our fit with  $\alpha = 0.327$  and within the standard deviation (orange shaded region). Our relation is significantly steeper than the one found by Seale & Looney (2008). The broken power-law relation of Velusamy et al. (2014) predicts much larger opening angles during the early evolution, and only matches our results at late times,  $\sim 150$  kyr. Offner et al. (2011) use a completely different method to compute the opening angles in their simulations, but their opening angles are in good agreement with ours.

Even though we find a correlation between opening angle and age, the opening angle–age relation gives very imprecise estimates of the protostellar age. Due to turbulence, we find a large scatter in the opening angles at a given age (orange shaded region on Fig. 13), which in combination with the shallow slope of  $\alpha = 0.327$ , translates into large errors in the estimated age; even a small change in  $\phi_{\text{OPEN}}$  produces a large change in the estimated age. In Fig. 14 we plot the distribution of fractional errors when using the opening angle–age relation to estimate the age of a simulated outflow. Especially during Stage 0, we underestimate the protostellar age significantly. There is a prominent peak in the distribution of errors at  $\Delta_{\text{REL}}\tau_\phi \sim -1$ , which corresponds to an underestimate of the true age by almost 100 per cent. During Stage I, the distribution of errors is somewhat better, but there is still a high chance of an error of  $\sim 100$  per cent.

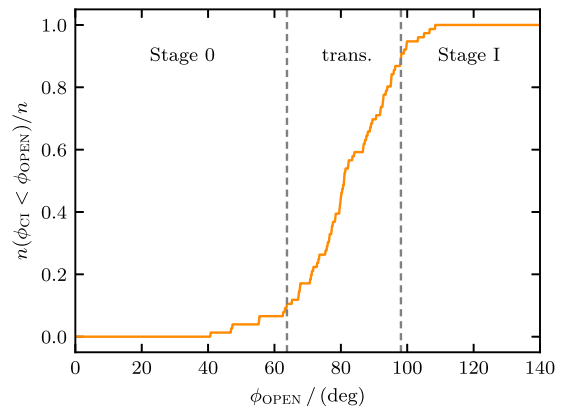


**Figure 15.** The cumulative distribution of opening angles when the simulated lobes transition to Stage I. The dashed grey lines indicate the opening angles below which only 10 per cent of the lobes have a smaller opening angle (left line), and above which only 10 per cent have a larger opening angle (right line), when entering Stage I. The opening angles can be divided into three regimes: sources with  $\phi_{\text{OPEN},l} < 64^\circ$  (left line) are very likely to be in Stage 0, and those with opening angles  $\phi_{\text{OPEN},l} > 98^\circ$  (right line) are very likely to be in Stage I; those with intermediate  $\phi_{\text{OPEN},l}$  might be in either Stage.

Another reason for the inaccuracy of the estimates is that a power-law fit does not fully describe the time evolution of the opening angles. In the first  $\sim 10$  kyr, the actual slope is steeper than  $\alpha = 0.327$ , and, since the opening angles must have a maximum, it starts to flatten at  $\sim 60$  kyr.

Even though the opening angle does not give an accurate estimate of the protostellar age, it still helps us to distinguish between Stage 0 and Stage I. Fig. 15 shows the cumulative distribution of opening angles when the simulated lobes transition to Stage I. Only 10 per cent of simulations have  $\phi_{\text{OPEN}} < 64^\circ$  when transitioning to Stage I, and only 10 per cent of simulations have  $\phi_{\text{OPEN}} > 98^\circ$ . Thus we conclude that outflows with opening angles  $\phi_{\text{OPEN}} \lesssim 65^\circ$  are very likely to be in Stage 0, and those with  $\phi_{\text{OPEN}} \gtrsim 100^\circ$  are very likely to be in Stage I. In between there is a transition region where both Stages are possible. Arce & Sargent (2006) find a similar division, with most YSOs with  $\phi_{\text{OPEN}} < 55^\circ$  being Class 0, and most YSOs with  $\phi_{\text{OPEN}} > 75^\circ$  being Class I.

## 4.2 Accretion history

### 4.2.1 Outflow bullet age

Outflow bullets carry valuable information about the accretion history of the launching protostar. Knowing when a bullet was ejected allows us to reconstruct this accretion history. Here, we estimate the ejection times of outflow bullets using their dynamical ages,  $\tau_{l,b}$  (equation 25), and compare them to the true ages,  $\tau_{\text{TRUE},l,b}$ . The error is

$$\Delta\tau_{l,b} = \tau_{l,b} - \tau_{\text{TRUE},l,b}. \quad (34)$$

Fig. 16 shows the KDEs of  $\Delta\tau_{l,b}$  for all bullets with  $v_{\text{MAX},l,b} > 20 \text{ km s}^{-1}$  (blue line), and for high-velocity bullets only with  $v_{\text{MAX},l,b} > 60 \text{ km s}^{-1}$  (orange line). High-velocity bullets tend to be recently ejected and have not yet been decelerated much by their environment, so they give an accurate record of the accretion history. Their error distribution (orange line in Fig. 16) is highly peaked. A Gaussian fit to KDE shows that the distribution is peaked at

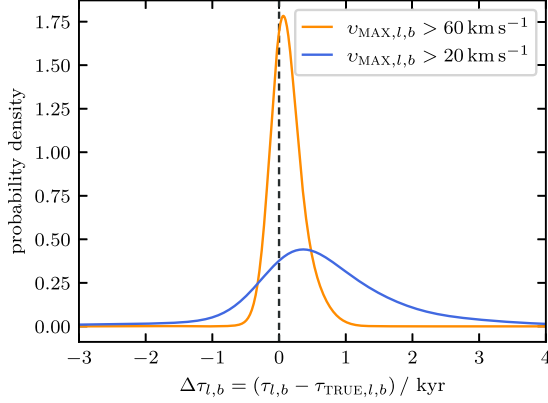


**Figure 16.** Probability density of the difference between the estimated bullet dynamical age,  $\tau_{l,b}$  (equation 25), and the true dynamical age,  $\tau_{TRUE,l,b}$ . The orange line represents only bullets with  $v_{MAX,l,b} > 60 \text{ km s}^{-1}$ . The blue line represents all bullets with  $v_{MAX,l,b} > 20 \text{ km s}^{-1}$ . Dynamical ages inferred from high-velocity outflow bullets are very reliable.

$\Delta\tau = 0.07 \text{ kyr}$  and has a width of  $\sigma = 0.12 \text{ kyr}$ . The bullets' ejection times can therefore be estimated very precisely; on average, we overestimate the ejection time by  $\lesssim 0.1 \text{ kyr}$ . A Gaussian fit to the error distribution for all bullets with  $v_{MAX,l,b} > 20 \text{ km s}^{-1}$  (blue line on Fig. 16) is much broader ( $\sigma = 0.5 \text{ kyr}$ ) and the peak is shifted to a higher  $\Delta\tau = 0.44 \text{ kyr}$ .

Hence the dynamical age of an outflow bullet gives a good estimate of the ejection time, especially if the bullet is young and has not been significantly decelerated by its environment. However, one should keep in mind that the dynamical age is always affected by inclination (see Table A1).

#### 4.2.2 Time-averaged accretion rate

The kinematic information carried by the outflow allows us to estimate the time-averaged accretion rate on to the underlying protostar. The mass ejection rate is given by

$$\dot{M}_{EJECT,l} = \frac{\dot{M}_{OUT,l}}{\epsilon_{OF,l}} = \frac{M_l v_l}{v_{EJECT} \tau_l}, \quad (35)$$

where the second expression on the right-hand side is obtained by substituting for  $\dot{M}_{OUT,l}$  from equation (29), and for  $\epsilon_{OF,l}$  from equation (21). The time-averaged mass accretion rate is then given by

$$\begin{aligned} \dot{M}_{ACC,l} &= \frac{2 \dot{M}_{EJECT,l}}{f_{EJECT}} = \frac{2 M_l v_l}{f_{EJECT} v_{EJECT} \tau_l} \\ &= 2 \times 10^{-5} M_{\odot} \text{ yr}^{-1} \left( \frac{M_l}{0.01 M_{\odot}} \right) \left( \frac{v_l}{3 \text{ km s}^{-1}} \right) \\ &\quad \times \left( \frac{f_{EJECT}}{0.1} \right)^{-1} \left( \frac{v_{EJECT}}{30 \text{ km s}^{-1}} \right)^{-1} \left( \frac{\tau_l}{\text{kyr}} \right)^{-1}, \end{aligned} \quad (37)$$

where the factor 2 on the right-hand side of equation (36) derives from the fact that there are two outflow lobes.

Fig. 17 shows the time evolution of the mean estimated accretion rate averaged over all lobes from all simulations,  $\langle \dot{M}_{ACC,l} \rangle$ , assuming  $v_{EJECT} = 30 \text{ km s}^{-1}$  (orange line); the shaded orange region shows the mean rates obtained if  $v_{EJECT}$  is varied between  $20 \text{ km s}^{-1}$  and  $40 \text{ km s}^{-1}$ . The blue line shows the evolution of the mean *true* accretion rate, defined as the total protostellar mass divided by the

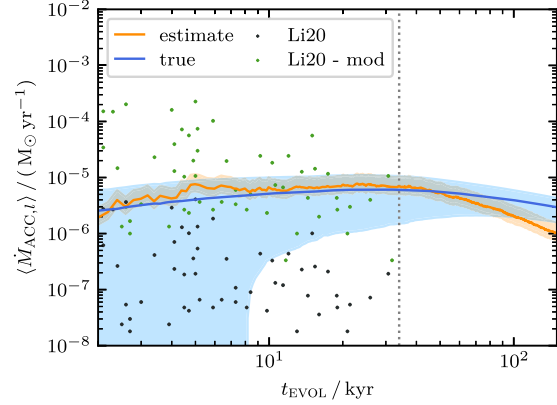


**Figure 17.** Mean accretion rate,  $\langle \dot{M}_{ACC,l} \rangle$ , against time,  $t_{EVOL}$ . The blue line shows the mean *true* accretion rate for all lobes from all simulations, with the standard deviation delineated by the blue shaded region. The orange line shows the mean accretion rate estimated using equation (36) with  $v_{EJECT} = 30 \text{ km s}^{-1}$ ; and the orange shaded region shows the range of accretion rates if  $v_{EJECT}$  is varied between  $20 \text{ km s}^{-1}$  and  $40 \text{ km s}^{-1}$ . The observational rates reported by Li et al. (2020; black markers) are much smaller than our estimated rates. However, if we recompute these observational rates using our default values for  $v_{EJECT}$  and  $f_{EJECT}$ , they are in better agreement with our results (green markers).

time since the protostar was born. We use this definition for *true* accretion rate as it is the definition used by Li et al. (2020). However, the actual accretion rate on to a protostar is highly episodic, as can be seen in fig. 9 of Rohde et al. (2019). We attempt to estimate the episodic accretion rates in Section 4.2.3.

During Stage 0, the estimated accretion rates fit the *true* accretion rates well, with a mean absolute error of  $\overline{\Delta}_{ABS,s0} \langle \dot{M}_{ACC,l} \rangle = 1.2 \times 10^{-6} M_{\odot} \text{ yr}^{-1}$ , corresponding to a mean fractional error of  $\overline{\Delta}_{REL,s0} \langle \dot{M}_{ACC,l} \rangle = 0.23$ . The estimated accretion rate becomes slightly less accurate during Stage I; there the mean absolute and fractional errors are  $\overline{\Delta}_{ABS,sI} \langle \dot{M}_{ACC,l} \rangle = 1.5 \times 10^{-6} M_{\odot} \text{ yr}^{-1}$  and  $\overline{\Delta}_{REL,sI} \langle \dot{M}_{ACC,l} \rangle = 0.39$ . Overall the estimated accretion rates are accurate to a mean fractional error of  $\overline{\Delta}_{REL,s0+I} \langle \dot{M}_{ACC,l} \rangle = 0.36$ .

The black markers represent the accretion rates estimated by Li et al. (2020). Their accretion rates are significantly lower than ours, but this is because they assume an ejection velocity of  $v_{EJECT} = 500 \text{ km s}^{-1}$  and an ejection fraction of  $f_{EJECT} = 0.3$ . If we instead adopt our default values ( $v_{EJECT} = 30 \text{ km s}^{-1}$  and  $f_{EJECT} = 0.1$ ), the observational estimates (green markers) match ours much better.

#### 4.2.3 Outburst accretion rate

Accretion on to young protostars is observed to be episodic rather than continuous. Outflow bullets are a consequence of these episodic accretion events. In the sequel we estimate the accretion rates during outbursts from the dynamics of the resulting outflow bullets, and compare these estimates with the actual accretion rates.

We compute the accretion rate required to trigger the simultaneous ejection of two oppositely directed bullets using an equation similar to equation (36), viz.

$$\dot{M}_{OB,l,b} = \frac{2 M_{l,b} v_{l,b}}{f_{EJECT} v_{EJECT} dt_{OB}} \quad (38)$$

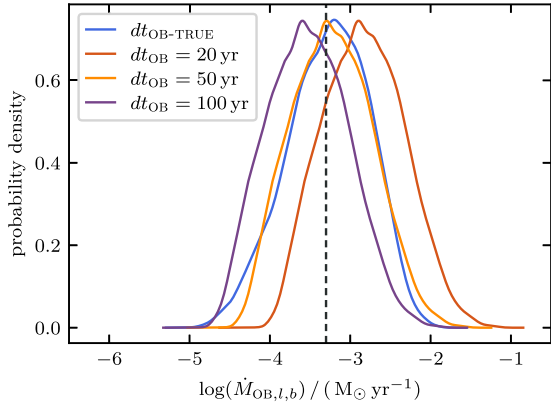


**Figure 18.** Probability density of the estimated accretion rate during an outburst event inferred from the properties of the corresponding outflow bullet (see equation 38). The vertical grey dashed line shows the true accretion rate, which is fixed at  $\dot{M}_{\text{OB}} = 5 \times 10^{-4} M_{\odot} \text{ yr}^{-1}$  (see Section 2.2). The blue line shows the accretion rate estimated using the true outburst duration,  $dt_{\text{OB-TRUE}}$ , whilst the red, orange, and purple lines show the accretion rates estimated using – respectively –  $dt_{\text{OB}} = 20$  yr, 50 yr, and 100 yr. Accretion rates estimated using  $dt_{\text{OB-TRUE}}$  and  $dt_{\text{OB}} = 50$  yr yield distributions peaked very close to the true rate,  $\dot{M}_{\text{OB}}$ . Using  $dt_{\text{OB}} = 20$  yr or 100 yr, respectively, over or underestimates the accretion rate.

$$= 8 \times 10^{-4} M_{\odot} \text{ yr}^{-1} \left( \frac{M_{l,b}}{0.003 M_{\odot}} \right) \left( \frac{v_{l,b}}{20 \text{ km s}^{-1}} \right) \times \left( \frac{f_{\text{EJECT}}}{0.1} \right)^{-1} \left( \frac{v_{\text{EJECT}}}{30 \text{ km s}^{-1}} \right)^{-1} \left( \frac{dt_{\text{OB}}}{50 \text{ yr}} \right)^{-1}; \quad (39)$$

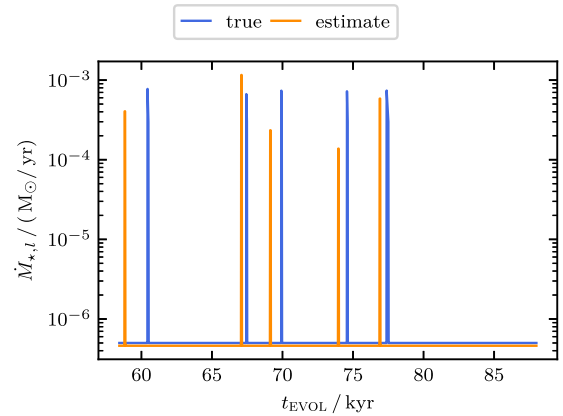
the only differences from equation (36) are that we have replaced the mass of the lobe,  $M_l$ , with the mass of the bullet,  $M_{l,b}$ ; the velocity of the lobe,  $v_l$ , with the velocity of the bullet,  $v_{l,b}$ ; and the lifetime of the lobe,  $\tau_l$ , with the duration of the outburst  $dt_{\text{OB}}$ .

Fig. 18 compares the KDEs of the estimated and actual accretion rates during the outburst events. The true accretion rate of the sub-grid model during an outburst is always  $\dot{M}_{\text{OB, TRUE}} = 5.0 \times 10^{-4} M_{\odot} \text{ yr}^{-1}$  (vertical black dashed line; see Section 2.2 and Stamatellos et al. 2012). We estimate outburst accretion rates assuming  $dt_{\text{OB}} = 20$  yr, 50 yr, and 100 yr, as shown by the red, orange, and purple lines on Fig. 18; and also using the true outburst duration, as shown by the blue line on Fig. 18. In all cases we assume an ejection velocity of  $v_{\text{EJECT}} = 30 \text{ km s}^{-1}$ .

The distribution of accretion rates obtained assuming the true outburst duration (blue line in Fig. 18) has a mean value  $\dot{M}_{\text{OB}} = 5.3 \times 10^{-4} M_{\odot} \text{ yr}^{-1}$ , very close to the true accretion rate of  $\dot{M}_{\text{OB}} = 5.0 \times 10^{-4} M_{\odot} \text{ yr}^{-1}$ . Similarly, the distribution of accretion rates obtained with  $dt_{\text{OB}} = 50$  yr (orange line on Fig. 18) has a mean value  $\dot{M}_{\text{OB}} = 5.9 \times 10^{-4} M_{\odot} \text{ yr}^{-1}$ , again very close to the true accretion rate. The distributions obtained with  $dt_{\text{OB}} = 20$  yr and 100 yr have mean values of  $\dot{M}_{\text{OB}} = 1.4 \times 10^{-3} M_{\odot} \text{ yr}^{-1}$  and  $\dot{M}_{\text{OB}} = 3 \times 10^{-4} M_{\odot} \text{ yr}^{-1}$ , which are still reasonable estimates. We conclude that the dynamical information carried by the outflow bullets allows us to estimate the accretion rate during the corresponding accretion event.

#### 4.2.4 Time-dependent accretion history

We can combine the estimated outflow-bullet ages from Section 4.2.1, with the estimated outburst accretion rates from Sec-



**Figure 19.** The accretion history for simulation S:5-V:0.5-K:2-R:10. The blue line shows the true accretion rate, and the orange line shows the accretion rate reconstructed using estimated outflow-bullet ages from Section 4.2.1, and estimated outburst accretion rates from Section 4.2.3.

tion 4.2.3, to reconstruct the accretion history of the underlying protostar between the current time  $t_0$  and a time in the past  $t_p = t_0 - \tau_{\text{MAX, BULLET},l}$ . Here,  $\tau_{\text{MAX, BULLET},l}$  (equation 25) is the longest dynamical age among the bullets in the lobe with  $v_{\text{MAX},l,b} > 20 \text{ km s}^{-1}$ ; typically it is  $\lesssim 100$  kyr.

The total estimated accretion rate is the sum of the estimated episodic accretion rate,  $\dot{M}_{\text{OB},l,b}$ , which is only active during an outburst event, and a much lower estimated background accretion rate,  $\dot{M}_{\text{BG},l}$ , i.e.

$$\dot{M}_{*,l} = \dot{M}_{\text{BG},l} + \dot{M}_{\text{OB},l,b}. \quad (40)$$

The background accretion rate is given by

$$\dot{M}_{\text{BG},l} = \max \left( \frac{M_{\text{CONT},l} - M_{\text{EPISODIC},l}}{t_0 - t_p}, 0 \right). \quad (41)$$

In equation (41),  $M_{\text{CONT},l}$  is an estimate of all the mass accreted between  $t_p$  and  $t_0$ , i.e.

$$M_{\text{CONT},l} = (t_0 - t_p) \dot{M}_{\text{ACC},l}, \quad (42)$$

with  $\dot{M}_{\text{ACC},l}$  given by equation (36); and  $M_{\text{EPISODIC},l}$  is an estimate of the mass accreted during all the episodic accretion or outburst events during the same period,

$$M_{\text{EPISODIC},l} = \sum_{b=0}^{n_{\text{BULLET},l}} dt_{\text{OB}} \dot{M}_{\text{OB},l,b}, \quad (43)$$

with  $n_{\text{BULLET},l}$  the number of distinct bullets,  $dt_{\text{OB}} = 50$  yr, and  $\dot{M}_{\text{OB},l,b}$  from equation (38).

The orange line in Fig. 19 shows the accretion history of simulation S:5-V:0.5-K:2-R:10 reconstructed in this way, and the blue line shows the true accretion history, demonstrating that the dynamical properties of outflow bullets allow us to reconstruct the accretion history well. The background accretion rate and the number of outburst events are reproduced almost exactly. The timings of the outburst events are accurate to  $\lesssim 1$  kyr, and the accretion rates during outburst to within a factor  $\lesssim 2$ .

## 5 CAVEATS

In this work, we have used simulations to evaluate the accuracy of some methods frequently used to estimate protostellar ages, accretion

histories, and outflow rates. Here, we discuss the most important limitations of this study.

Cores have a range of masses, described by the core mass function (Könyves et al. 2020), whereas our simulations only treat  $1 M_{\odot}$  cores, which limits the generality of our results. However, the final protostellar mass function of the simulations is compatible with the observed protostellar mass function (Rohde et al. 2021). Therefore, our results should approximately represent what happens in a low-mass star-forming region.

We perform hydrodynamic simulations and do not include magnetic fields. The importance of magnetic fields in launching outflows is implicit in our sub-grid outflow model. Magnetic fields are also expected to enhance the stability of accretion discs (e.g. Wurster & Bate 2019), but our episodic accretion model regulates the stability of the inner disc and therefore limits the influence of magnetic fields there (Lomax, Whitworth & Hubber 2016a, b). However, magnetic fields might slow down the collapse of our cores, and might also influence the propagation of the outflows.

Protostellar jets are observed to be embedded in low-velocity wide-angle winds. Since these wide-angle winds are launched from radii far out in the accretion disc, between  $\sim 10$  au and  $\sim 50$  au (Louvet et al. 2018; Pascucci et al. 2020; Lee et al. 2021; Podio et al. 2021), they might play an essential role in removing angular momentum from these regions, thus allowing gas to spiral inwards faster (Lee 2020). Our sub-grid outflow model episodically injects wide-angle winds but does not account for the associated removal of angular momentum. A single episodic wide-angle wind, similar to that in our outflow model, has been observed by Zhang et al. (2019), and further observations are needed to establish how common such winds are. However, self-consistently treated wide-angle winds are probably dynamically not very important due to their low velocities of about  $10 \text{ km s}^{-1}$ .

Although the radiative feedback model treats the star's close surrounding, including the inner accretion disc, it does not account for the effect of radiation on the outflow cavity (Stamatellos et al. 2007; Stamatellos, Whitworth & Hubber 2011). Since we are simulating low-mass star formation, we expect the effect of full radiative transfer to be rather limited. For example, the additional momentum due to radiation pressure

$$p_{\text{RAD}} = \sum_i^{n_*} \sum_t^{n_{\text{STEP}}} \left\{ \frac{L_{*,i}}{c} dt \right\}, \quad (44)$$

(where  $n_{\text{STEP}}$  is the number of simulation time-steps,  $dt$ , and  $c$  is the speed of light), would add  $\sim 1$  per cent to the total outflow momentum. Thus with radiative feedback the outflow cavities would widen somewhat faster than in our simulations (Kuiper, Turner & Yorke 2016).

The actual mechanism underlying outflow launching is not well understood. Many different aspects could alter how the gas is ejected. Our simulations are limited to one specific model of outflow launching with well-defined parameters, for example the ejection fraction. This parametrization is motivated by the study of Matzner & McKee (1999), who show that at sufficiently large distances from the driving source, all hydro-magnetic winds behave similarly. Moreover, as shown by Rohde et al. (2019), protostellar outflows are self-regulated, in the sense that varying the sub-grid model parameters has a limited impact on the outflow properties. Therefore, we believe that our simulated outflows should be evolving similarly to those of FU-or-like stars.

## 6 CONCLUSIONS

The early phases of stellar evolution and gas accretion are closely linked to, and regulated by, the launching of protostellar outflows. Therefore, these outflows carry fossil information about the stellar age and accretion history. Outflows extend far into the protostellar environment and are relatively easy to observe and resolve. We compute outflow properties from a set of 44 SPH simulations with episodic outflow feedback, estimate stellar ages and accretion histories from the outflows, and compare these estimates with the underlying simulations. In this way, we compute the uncertainties inherent in different observational methods for estimating ages and outflow properties – but ignoring intrinsic observational uncertainties and selection effects.

To compute the outflow properties, we extract the outflow lobes from our simulations and use the OPTICS clustering algorithm to trace individual outflow bullets. Here, we summarize our results, demonstrating that protostellar outflows are indeed a useful ‘window on the past’.

(i) Assuming momentum conservation, we estimate the gas entrainment factor  $\epsilon$ , i.e. the ratio of outflowing mass to ejected mass. The outflowing mass is much larger than the ejected mass, because gas in the parental core is swept up by the outflow. During Stage 0 we find good agreement with the true entrainment factor of  $\epsilon \sim 10$ . During Stage I, the estimated entrainment factor is larger than the true entrainment factor.

(ii) We compute dynamical ages for the outflows using five different methods and compare them. Estimating the dynamical age from the outflow front is very accurate during Stage 0, but becomes increasingly inaccurate during Stage I. Conversely, the perpendicular method is not very reliable during Stage 0, but very accurate during Stage I, with a fractional error of  $\sim 15$  per cent. The most commonly used method for deriving the dynamical age is based on taking the ratio of the outflow length to the highest outflow velocity, but it has a fractional error of  $\sim 34$  per cent. We propose a new method to estimate the dynamical age from two successive outflow bullets: if two distinct bullets are present in an outflow cavity, this method provides good age estimates for both Stage 0 and Stage I, with a fractional error of  $\sim 24$  per cent. These errors are for the case of nearly perfect information, observed dynamical ages probably come with significantly larger errors.

(iii) We find that dynamical ages of individual outflow bullets accurately describe their true age, especially if the bullets are young and have not yet swept up a significant amount of extra mass. On average, we overpredict the ages of bullets by  $\sim 0.44$  kyr, but for recently ejected bullets by only  $\sim 0.07$  kyr.

(iv) We find that outflow cavities widen over time, as observed. We fit an opening angle–age relation, similar to the one derived by Arce & Sargent (2006), but conclude that estimating the stellar age using this relation is not advisable, due to the large uncertainties caused by both the large variation in opening angles, and the shallow slope of the relation. However, we find that the opening angle can be used to differentiate between Stage 0 and Stage I sources. From our simulations, only 10 per cent of all lobes have opening angles smaller than  $\sim 65^\circ$ , and only 10 per cent have opening angles larger than  $\sim 100^\circ$ , when entering Stage I.

(v) Using these dynamical ages, as well as the true protostellar ages, we estimate the outflow rates of mass, momentum, and energy and compare them. We find that these rates are rather constant during Stage 0, and diminish slightly once the protostars enter Stage I. This reduction in outflow activity can help to distinguish between Stage 0 and Stage I sources.

(vi) The estimated outflow rates and entrainment factors allow us to reconstruct the protostellar accretion rates. During Stage 0 these estimates are on average accurate to  $\sim 23$  per cent; during Stage I the estimate is less accurate.

(vii) Using the derived dynamical properties of a bullet, we can estimate the accretion rate during the outburst event associated with the ejection of that bullet. The distribution of the estimated accretion rates peaks around the true accretion rate. These accretion rates, together with the bullet age, allow us to reconstruct rather accurately the protostellar accretion history.

Overall, protostellar outflows carry useful information which can be used to estimate the protostellar age and evolutionary Stage. Focusing on individual outflow bullets reveals the episodic accretion behaviour and allows the reconstruction of the accretion history.

## ACKNOWLEDGEMENTS

The authors like to thank the anonymous referee for comments that helped to significantly improve the paper. PFR, SW, and SDC acknowledge support via the ERC starting grant No. 679852 ‘RADFEEDBACK’. DS and SW thank the DFG for funding via the SFB 956 ‘Conditions & impact of star formation’, via the sub-projects C5 and C6. APW gratefully acknowledges the support of a consolidated grant (ST/K00926/1) from the UK Science and Technology Facilities Council. The authors gratefully acknowledge the Gauss Centre for Supercomputing e.V. ([www.gauss-centre.eu](http://www.gauss-centre.eu)) for funding this project (ID: pr47pi) by providing computing time on the GCS Supercomputer SuperMUC at Leibniz Supercomputing Centre (<http://www.lrz.de>). PR acknowledges D. Price for providing the visualisation tool SPLASH (Price 2011).

## DATA AVAILABILITY

The data underlying this article will be shared on reasonable request to the corresponding author.

## REFERENCES

Adams F. C., Shu F. H., 1986, *ApJ*, 308, 836  
 Adams F. C., Lada C. J., Shu F. H., 1987, *ApJ*, 312, 788  
 Anderl S. et al., 2020, *A&A*, 643, A123  
 Andre P., Ward-Thompson D., Barsony M., 1993, *ApJ*, 406, 122  
 Ankerst M., Breunig M. M., Peter Kriegl H., Sander J., 1999, ACM Press, p. 49  
 Arce H. G., Goodman A. A., 2001, *ApJ*, 551, L171  
 Arce H. G., Sargent A. I., 2006, *ApJ*, 646, 1070  
 Arce H. G., Shepherd D., Gueth F., Lee C.-F., Bachiller R., Rosen A., Beuther H., 2007, in Reipurth B., Jewitt D., Keil K., eds, *Protostars and Planets V*. Univ. Arizona Press, Tucson, p. 245  
 Audard M. et al., 2014, in Beuther H., Klessen R. S., Dullemond C. P., Henning T., eds, *Protostars and Planets VI*. Univ. Arizona Press, Tucson, p. 387  
 Bachiller R., Martín-Pintado J., Tafalla M., Cernicharo J., Lazareff B., 1990, *A&A*, 231, 174  
 Bally J., 2016, *ARA&A*, 54, 491  
 Bally J., Chia Z. H., 2019, *MNRAS*, 484, 4529  
 Bate M. R., Tricco T. S., Price D. J., 2014, *MNRAS*, 437, 77  
 Bjerkeli P., van der Wiel M. H. D., Harsono D., Ramsey J. P., Jørgensen J. K., 2016, *Nature*, 540, 406  
 Blandford R. D., Payne D. G., 1982, *MNRAS*, 199, 883  
 Bontemps S., Andre P., Terebey S., Cabrit S., 1996, *A&A*, 311, 858

Busquet G., Fontani F., Viti S., Codella C., Lefloch B., Benedettini M., Ceccarelli C., 2017, *A&A*, 604, A20  
 Calvet N., Hartmann L., Kenyon S. J., Whitney B. A., 1994, *ApJ*, 434, 330  
 Cesaroni R. et al., 2018, *A&A*, 612, A103  
 Chen X., Arce H. G., Zhang Q., Launhardt R., Henning T., 2016, *ApJ*, 824, 72  
 Cheng Y., Qiu K., Zhang Q., Wyrowski F., Menten K., Guesten R., 2019, *Molecular Bullets in A High-mass Protostar*, preprint ([arXiv:1904.01429](https://arxiv.org/abs/1904.01429))  
 Cortes-Rangel G., Zapata L. A., Toalá J. A., Ho P. T. P., Takahashi S., Mesa-Delgado A., Masqué J. M., 2020, *AJ*, 159, 62  
 Crapsi A., van Dishoeck E. F., Hogerheijde M. R., Pontoppidan K. M., Dullemond C. P., 2008, *A&A*, 486, 245  
 Cullen L., Dehnen W., 2010, *MNRAS*, 408, 669  
 Cunningham A. J., Klein R. I., Krumholz M. R., McKee C. F., 2011, *ApJ*, 740, 107  
 Curtis E. I., Richer J. S., Swift J. J., Williams J. P., 2010, *MNRAS*, 408, 1516  
 de Valon A., Dougados C., Cabrit S., Louvet F., Zapata L. A., Mardones D., 2020, *A&A*, 634, L12  
 Downes T. P., Cabrit S., 2007, *A&A*, 471, 873  
 Dunham M. M., Vorobyov E. I., 2012, *ApJ*, 747, 52  
 Dunham M. M. et al., 2014a, in Beuther H., Klessen R. S., Dullemond C. P., Henning T., eds, *Protostars and Planets VI*. Univ. Arizona Press, Tucson, p. 195  
 Dunham M. M., Arce H. G., Mardones D., Lee J.-E., Matthews B. C., Stutz A. M., Williams J. P., 2014b, *ApJ*, 783, 29  
 Dunham M. M. et al., 2015, *ApJS*, 220, 11  
 Enoch M. L., Evans N. J. I., Sargent A. I., Glenn J., 2009, *ApJ*, 692, 973  
 Ester M., Kriegl H.-P., Sander J., Xu X., 1996, in Proc. of 2nd International Conference on Knowledge Discovery and. p. 226  
 Federrath C., Schrön M., Banerjee R., Klessen R. S., 2014, *ApJ*, 790, 128  
 Fehér O., Kóspál Á., Abraham P., Hogerheijde M. R., Brinch C., 2017, *A&A*, 607, A39  
 Ferrero L. V., Cappa C. E., Saldaña H. P., Gómez M., Rubio M., Günthardt G., 2020, *MNRAS*, 496, 4239  
 Forgan D., Rice K., 2013, *MNRAS*, 430, 2082  
 Frank A. et al., 2014, in Beuther H., Klessen R. S., Dullemond C. P., Henning T., eds, *Protostars and Planets VI*. Univ. Arizona Press, Tucson, p. 451  
 Frimann S., Jørgensen J. K., Haugbølle T., 2016, *A&A*, 587, A59  
 Gómez-Ruiz A. I., Gusdorf A., Leurini S., Menten K. M., Takahashi S., Wyrowski F., Güsten R., 2019, *A&A*, 629, A77  
 Grudić M. Y., Guszejnov D., Hopkins P. F., Offner S. S. R., Faucher-Giguère C.-A., 2020, *MNRAS*, 506, 2199  
 Hara C. et al., 2021, *ApJ*, 912, 34  
 Hennebelle P., Commerçon B., Joos M., Klessen R. S., Krumholz M., Tan J. C., Teyssier R., 2011, *A&A*, 528, A72  
 Hernquist L., Katz N., 1989, *ApJS*, 70, 419  
 Hirota T., Machida M. N., Matsushita Y., Motogi K., Matsumoto N., Kim M. K., Burns R. A., Honma M., 2017, *Nature Astron.*, 1, 0146  
 Hsieh T.-H., Lai S.-P., Belloche A., 2017, *AJ*, 153, 173  
 Hsieh T.-H., Murillo N. M., Belloche A., Hirano N., Walsh C., van Dishoeck E. F., Lai S.-P., 2018, *ApJ*, 854, 15  
 Hsieh T.-H., Murillo N. M., Belloche A., Hirano N., Walsh C., van Dishoeck E. F., Jørgensen J. K., Lai S.-P., 2019, *ApJ*, 884, 149  
 Hubber D. A., Walch S., Whitworth A. P., 2013, *MNRAS*, 430, 3261  
 Hubber D. A., Rosotti G. P., Booth R. A., 2018, *MNRAS*, 473, 1603  
 Ibryamov S. I., Semkov E. H., Peneva S. P., 2018, *PASA*, 35, e007  
 Jhan K.-S., Lee C.-F., 2021, *ApJ*, 909, 11  
 Kadam K., Vorobyov E., Regály Z., Kóspál Á., Abraham P., 2020, *ApJ*, 895, 41  
 Kenyon S. J., Hartmann L. W., Strom K. M., Strom S. E., 1990, *AJ*, 99, 869  
 Königl A., Pudritz R. E., 2000, in Mannings V., Boss A. P., Russell S. S., eds, *Protostars and Planets IV*. Univ. Arizona Press, Tucson, p. 759

- Könyves V. et al., 2020, *A&A*, 635, A34
- Kuffmeier M., Frimann S., Jensen S. S., Haugbølle T., 2018, *MNRAS*, 475, 2642
- Kuiper R., Yorke H. W., Turner N. J., 2015, *ApJ*, 800, 86
- Kuiper R., Turner N. J., Yorke H. W., 2016, *ApJ*, 832, 40
- Kuruwita R. L., Federrath C., Haugbølle T., 2020, *A&A*, 641, A59
- Lada C. J., 1987, *Star formation - From OB associations to protostars*. Univ. Arizona Press, Tucson, p. 1
- Lada C. J., Fich M., 1996, *ApJ*, 459, 638
- Lada C. J., Wilking B. A., 1984, *ApJ*, 287, 610
- Lee Y.-H. et al., 2020, *ApJ*, 903, 5
- Lee C.-F., 2020, *A&AR*, 28, 1
- Lee C.-F., Ho P. T. P., Li Z.-Y., Hirano N., Zhang Q., Shang H., 2017, *Nature Astron.*, 1, 0152
- Lee C.-F., Tabone B., Cabrit S., Codella C., Podio L., Ferreira J., Jacquemin-Idé J., 2021, *ApJ*, 907, L41
- Lee K. I. et al., 2016, *ApJ*, 820, L2
- Lewis B. T., Bate M. R., 2017, *MNRAS*, 467, 3324
- Li S., Zhang Q., Pillai T., Stephens I. W., Wang J., Li F., 2019, *ApJ*, 886, 130
- Li S. et al., 2020, *ApJ*, 903, 119
- Li P. S., Klein R. I., McKee C. F., 2018, *MNRAS*, 473, 4220
- Lloyd S., 1982, *Proc. IEEE*, 903, 129
- Lomax O., Whitworth A. P., Hubber D. A., Stamatellos D., Walch S., 2014, *MNRAS*, 439, 3039
- Lomax O., Whitworth A. P., Hubber D. A., Stamatellos D., Walch S., 2015, *MNRAS*, 447, 1550
- Lomax O., Whitworth A. P., Hubber D. A., 2016a, *PASA*, 33, e004
- Lomax O., Whitworth A. P., Hubber D. A., 2016b, *MNRAS*, 458, 1242
- Lombardi J. C., McInally W. G., Faber J. A., 2015, *MNRAS*, 447, 25
- López-Vázquez J. A., Zapata L. A., Lizano S., Cantó J., 2020, *ApJ*, 904, 158
- Louvet F., Dougados C., Cabrit S., Mardones D., Ménard F., Tabone B., Pinte C., Dent W. R. F., 2018, *A&A*, 618, A120
- Lynden-Bell D., 2003, *MNRAS*, 341, 1360
- Mac Low M.-M., Klessen R. S., Burkert A., Smith M. D., 1998, *Phys. Rev. Lett.*, 80, 2754
- Machida M. N., 2014, *ApJ*, 796, L17
- Machida M. N., Basu S., 2019, *ApJ*, 876, 149
- Machida M. N., Hosokawa T., 2013, *MNRAS*, 431, 1719
- Machida M. N., Inutsuka S.-I., Matsumoto T., 2008, *ApJ*, 676, 1088
- Machida M. N., Inutsuka S.-I., Matsumoto T., 2009, *Astrophys. Space Sci. Proc.*, 13, 405
- Machida M. N., Hirano S., Kitta H., 2020, *MNRAS*, 491, 2180
- Matsumoto T., Machida M. N., Inutsuka S.-I., 2017, *ApJ*, 839, 69
- Matzner C. D., McKee C. F., 1999, *ApJ*, 526, L109
- Mercer A., Stamatellos D., 2017, *MNRAS*, 465, 2
- Monaghan J. J., 1992, *ARA&A*, 30, 543
- Morris J. P., Monaghan J. J., 1997, *J. Comput. Phys.*, 136, 41
- Mottram J. C. et al., 2017, *A&A*, 600, A99
- Movsessian T. A., Magakian T. Y., Dodonov S. N., 2021, *MNRAS*, 500, 2440
- Murphy A., Dougados C., Whelan E. T., Bacciotti F., Coffey D., Comerón F., Eisloffel J., Ray T. P., 2021, *A&A*, 652, A119
- Myers P. C., Ladd E. F., 1993, *ApJ*, 413, L47
- Myers A. T., Klein R. I., Krumholz M. R., McKee C. F., 2014, *MNRAS*, 439, 3420
- Nakamura F., Li Z.-Y., 2007, *ApJ*, 662, 395
- Nisini B., Antonucci S., Alcalá J. M., Giannini T., Manara C. F., Natta A., Fedele D., Biazzo K., 2018, *A&A*, 609, A87
- Nony T. et al., 2020, *A&A*, 636, A38
- Offner S. S. R., Arce H. G., 2014, *ApJ*, 784, 61
- Offner S. S. R., Chaban J., 2017, *ApJ*, 847, 104
- Offner S. S. R., Klein R. I., McKee C. F., Krumholz M. R., 2009, *ApJ*, 703, 131
- Offner S. S. R., Lee E. J., Goodman A. A., Arce H., 2011, *ApJ*, 743, 91
- Pascucci I. et al., 2020, *ApJ*, 903, 78
- Pérez S. et al., 2020, *ApJ*, 889, 59
- Peters T., Klaassen P. D., Mac Low M.-M., Schrön M., Federrath C., Smith M. D., Klessen R. S., 2014, *ApJ*, 788, 14
- Podio L. et al., 2021, *A&A*, 648, A45
- Price D. J., 2011, *Astrophysics Source Code Library*, record ascl:1103.004
- Price D. J., Tricco T. S., Bate M. R., 2012, *MNRAS*, 423, L45
- Pudritz R. E., Ouyed R., Fendt C., Brandenburg A., 2007, in Reipurth B., Jewitt D., Keil K., eds, *Protostars and Planets V*. Univ. Arizona Press, Tucson, p. 277
- Rab C. et al., 2019, *Proc. IAU Symp. 15, The Chemistry of Episodic Accretion*. Cambridge Univ. Press, Cambridge, p. 440
- Reipurth B., Bally J., 2001, *ARA&A*, 39, 403
- Reipurth B., Bally J., Devine D., 1997, *AJ*, 114, 2708
- Reipurth B., Devine D., Bally J., 1998, *AJ*, 116, 1396
- Rigliaco E. et al., 2020, *A&A*, 641, A33
- Robitaille T. P., Whitney B. A., Indebetouw R., Wood K., Denzmore P., 2006, *ApJS*, 167, 256
- Rohde P. F., Walch S., Seifried D., Whitworth A. P., Clarke S. D., Hubber D. A., 2019, *MNRAS*, 483, 2563
- Rohde P. F., Walch S., Clarke S. D., Seifried D., Whitworth A. P., Klepitko A., 2021, *MNRAS*, 500, 3594
- Rousseuw P., 1987, *J. Comput. Appl. Math.*, 20, 53
- Safron E. J. et al., 2015, *ApJ*, 800, L5
- Saiki Y., Machida M. N., 2020, *ApJ*, 897, L22
- Santiago-García J., Tafalla M., Johnstone D., Bachiller R., 2009, *A&A*, 495, 169
- Seale J. P., Looney L. W., 2008, *ApJ*, 675, 427
- Seifried D., Banerjee R., Klessen R. S., Duffin D., Pudritz R. E., 2012, in Capuzzo-Dolcetta R., Limongi M., Tornambè A., eds, *ASP Conf. Ser. Vol. 453, Advances in Computational Astrophysics: Methods, Tools, and Outcome*. Astron. Soc. Pac., San Francisco, p. 391
- Sharma R., Tobin J. J., Sheehan P. D., Megeath S. T., Fischer W. J., Jørgensen J. K., Safron E. J., Nagy Z., 2020, *ApJ*, 904, 78
- Shu F., Najita J., Ostriker E., Wilkin F., Ruden S., Lizano S., 1994, *ApJ*, 429, 781
- Shu F. H., Najita J., Ostriker E. C., Shang H., 1995, *ApJ*, 455, L155
- Sicilia-Aguilar A., Bouvier J., Dougados C., Grankin K., Donati J. F., 2020, *A&A*, 643, A29
- Sperling T., Eisloffel J., Nisini B., Giannini T., Fischer C., Krabbe A., 2021, *A&A*, 650, A173
- Springel V., Hernquist L., 2002, *MNRAS*, 333, 649
- Stamatellos D., Whitworth A. P., Bisbas T., Goodwin S., 2007, *A&A*, 475, 37
- Stamatellos D., Whitworth A. P., Hubber D. A., 2011, *ApJ*, 730, 32
- Stamatellos D., Whitworth A. P., Hubber D. A., 2012, *MNRAS*, 427, 1182
- Stock C., Caratti o Garatti A., McGinnis P., Garcia Lopez R., Antonucci S., Fedriani R., Ray T. P., 2020, *A&A*, 643, A181
- Stone J. M., Ostriker E. C., Gammie C. F., 1998, *ApJ*, 508, L99
- Tabone B. et al., 2017, *A&A*, 607, L6
- Tabone B. et al., 2020, *A&A*, 640, A82
- Tafalla M., Santiago J., Johnstone D., Bachiller R., 2004, *A&A*, 423, L21
- Tafalla M., Santiago-García J., Hacar A., Bachiller R., 2010, *A&A*, 522, A91
- Tafalla M. et al., 2017, *A&A*, 597, A119
- Takagi Y., Honda S., Arai A., Takahashi J., Oasa Y., Itoh Y., 2020, *ApJ*, 904, 53
- Tanaka K. E. I., Tan J. C., Zhang Y., Hosokawa T., 2018, *ApJ*, 861, 68
- Tobin J. J. et al., 2013, *ApJ*, 765, 18
- Tomida K., 2014, *ApJ*, 786, 98
- Tomida K., Okuzumi S., Machida M. N., 2015, *ApJ*, 801, 117
- Tychoniec Ł., Hull C. L. H., Kristensen L. E., Tobin J. J., Le Gouellec V. J. M., van Dishoeck E. F., 2019, *A&A*, 632, A101

- Vazzano M. M., Fernández-López M., Plunkett A., de Gregorio-Monsalvo I., Santamaría-Miranda A., Takahashi S., Lopez C., 2021, *A&A*, 648, A41
- Velusamy T., Langer W. D., Thompson T., 2014, *ApJ*, 783, 6
- Vorobyov E. I., Elbakyan V. G., Plunkett A. L., Dunham M. M., Audard M., Guedel M., Dionatos O., 2018, *A&A*, 613, A18
- Walch S., Naab T., Whitworth A., Burkert A., Gritschneider M., 2010, *MNRAS*, 402, 2253
- Walch S., Whitworth A. P., Girichidis P., 2012, *MNRAS*, 419, 760
- Wang L.-Y., Shang H., Su Y.-N., Santiago-García J., Tafalla M., Zhang Q., Hirano N., Lee C.-F., 2014, *ApJ*, 780, 49
- Wurster J., Bate M. R., 2019, *MNRAS*, 486, 2587
- Yildiz U. A. et al., 2015, *A&A*, 576, A109
- Young C. H., Evans N. J., II, 2005, *ApJ*, 627, 293
- Zapata L. A., Fernández-López M., Rodríguez L. F., Garay G., Takahashi S., Lee C.-F., Hernández-Gómez A., 2018, *AJ*, 156, 239
- Zhang Y. et al., 2018, *ApJ*, 864, 76
- Zhang Y. et al., 2019, *ApJ*, 883, 1
- Zhang Q., Hunter T. R., Brand J., Sridharan T. K., Cesaroni R., Molinari S., Wang J., Kramer M., 2005, *ApJ*, 625, 864
- Zhu Z., Hartmann L., Gammie C., 2009, *ApJ*, 694, 1045
- Zhu Z., Hartmann L., Gammie C. F., Book L. G., Simon J. B., Engelhard E., 2010, *ApJ*, 713, 1134

## APPENDIX A: INCLINATION

**Table A1.** Correction factors for various outflow properties depending on the inclination angle  $\theta$  (i.e. the angle between the outflow direction and the line of sight). Assuming that all orientations have an equal probability, the mean inclination is  $\theta = 57.3^\circ$  (Bontemps et al. 1996). This table is based on that in Li et al. (2019).

Outflow parameter	Inclination dependence	Correction angle		
		$\theta = 57.3^\circ$	$\theta = 5^\circ$	$\theta = 85^\circ$
$\tau_l$	$\cos(\theta)/\sin(\theta)$	0.6	11.4	0.09
$l_l$	$1/\sin(\theta)$	1.2	11.5	1.0
$v_l$	$1/\cos(\theta)$	1.9	1.0	11.5
$p_l$	$1/\cos(\theta)$	1.9	1.0	11.5
$\dot{M}_{\text{out},l}$	$\sin(\theta)/\cos(\theta)$	1.7	0.09	11.4
$F_l$	$\sin(\theta)/\cos^2(\theta)$	2.9	0.09	131.2
$L_l$	$\sin(\theta)/\cos^3(\theta)$	5.3	0.09	1505

## Protostellar outflows: a window to the past 2571

### APPENDIX B: OUTFLOW LAUNCHING

Assuming protostellar outflows are launched magneto-centrifugally as described by the x-wind model (Shu et al. 1994), Shu et al. (1995) show that the almost radially ejected winds become collimated to a cylindrical configuration

$$\rho_w \propto 1 / (r \sin(\theta))^2. \quad (\text{B1})$$

Here,  $\rho_w$  is the density of the wind and  $\theta$  the angle of the flow with respect to the outflow axis. Matzner & McKee (1999) generalize this finding to any momentum conserving MHD wind in an environment with a power-law density distribution. For radially ejected winds, it follows from equation (B1) that

$$\rho_w v_w^2 \propto 1 / (r \sin(\theta))^2, \quad (\text{B2})$$

where  $v_w$  is the wind velocity. Matzner & McKee (1999) argue that an angular force distribution,  $P(\mu)$ , must be flat for  $\mu \rightarrow 0$  and therefore approximate the distribution with

$$P(\theta) \propto r^2 \rho_w v_w^2 \simeq \left[ \ln \left( \frac{2}{\theta_{\text{JET}}} \right) (\sin^2(\theta) + \theta_{\text{JET}}^2) \right]^{-1}. \quad (\text{B3})$$

where  $\theta_{\text{JET}}$  is the angular scale over which the distribution is flattened. This force distribution for MHD winds at large distances from the launching point is often called the ‘wind-driven shell’ model and is used by numerous authors to approximate outflows in sub-grid outflow implementations (e.g. Cunningham et al. 2011; Offner & Arce 2014; Kuiper et al. 2015; Tanaka et al. 2018; Rohde et al. 2019; Grudić et al. 2020). Similarly, Rohde et al. (2019) assume this force distribution (equation B3) and separate it into distinct density and velocity distributions that satisfy the force distribution

$$\rho_{\text{INJECT}}(\theta) \propto P^{1/2}(\theta), \quad (\text{B4})$$

$$|v_{\text{INJECT}}(\theta)| \propto P^{1/4}(\theta). \quad (\text{B5})$$

The free parameter  $\theta_{\text{JET}}$ , regulating the collimation of the outflow, and  $\theta_{\text{OPEN}}$ , the opening angle where we cut-off the force distribution, have a rather limited influence on the outcome of the simulations (Rohde et al. 2019). Here, we use the default parameters from Rohde et al. (2019),  $\theta_{\text{JET}} = 0.01$  and  $\theta_{\text{OPEN}} = 0.4$ . Due to the cut-off at  $\theta_{\text{OPEN}} = 0.4$  the mean value of the velocity distribution (equation B5) is  $\sim 2.2$ .

This paper has been typeset from a  $\text{\TeX}/\text{\LaTeX}$  file prepared by the author.

## SUMMARY AND CONCLUSION

## 7.1

## SUMMARY

In *Paper I* the newly developed sub-grid, episodic outflow model is presented and tested. A resolution study shows that the new model consumes less computational resources than a typical continuous outflow model. Injected particles cause the simulation timestep to drop due to high ejection velocities (Eq. 2.43). The continuous outflow model suffers from constantly low timesteps, which is not the case for the short outbursts in the episodic outflow model. Another benefit of the new model over a continuous one is that lower mass resolution is required to resolve outflows since the particle density is naturally higher during a burst.

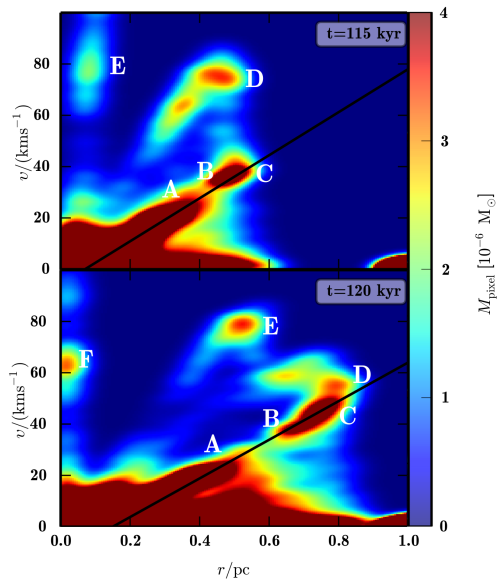


Figure 4: Two panels from Fig. 10 in *Paper I* showing the position-velocity relation's time evolution of an outflow lobe from the turbulent setup simulation. Letters A to F mark the position of individual outflow bullets. The black line corresponds to the Hubble law relation. Bullets that have decelerated at the leading shock front lie on the linear relation, whereas those that have not lie above the line.

Similar to observations, the individual outflow bullets manifest as high-velocity

A parameter study demonstrates how the model reacts to variation of the model parameters. It turns out that episodic protostellar outflows are highly self-regulating in the sense that varying the model parameter has only limited influence on the outflow properties such as outflow mass and momentum. Varying model parameter such that the outflow, assuming constant accretion rate, would be stronger, actually leads to a reduction in accretion rate such that the outflow properties are similar over a wide range of model parameters.

Position-velocity and mass-velocity diagrams are frequently used to study outflows. For the simulated outflow in the simulation with turbulent initial conditions, both relations are compared to observations. The mass-velocity relation can be fitted a power-law function with an exponent  $\gamma \sim 1.5$  in good agreement with observation. Individual bullets manifest as little peaks in the power-law relation.

Fig. 4 shows the position-velocity diagram for this simulation at  $t = 115$  kyr and  $t = 120$  kyr. The velocity increases linearly, like a Hubble-law, with distance from the source (Fig. 4 black lines).

Hubble wedges above the otherwise linear position-velocity relation (Fig. 4 A to F). The time evolution of these bullets reveals how they relate to the linear relation. The outflow bullets are ejected with high velocities and decelerate only marginally while moving through the already evacuated outflow cavity. The bullets decelerate at the leading shock front and align with the former bullets at the top of the linear position-velocity relation (Fig. 4).

*Paper II* focuses on the impact of episodic outflow feedback on the star formation process. Instead of varying model parameter, like in *Paper I*, the simulations in *Paper II* consist of an ensemble of cores with varying initial conditions. The simulations are divided into two identical samples, except one includes outflow feedback and the other not.

The influence of the initial conditions on the outcome of the star formation process, such as the number of stars, the order of the highest order multiple systems and their masses, is rather limited. One exception is the virial ratio of the initially turbulent velocity field. Simulations without outflow feedback and low virial ratio collapse monolithically into relative massive single or binary systems due to the lack of support against gravity. Outflow feedback aids this support against gravity and balances the effects of the low virial ratio.

Episodic outflow feedback influences the evolution of multiple systems. Simulations without outflow feedback form more stars and consequently more higher-order multiple systems during the early evolutionary phase. However, many of these systems are unstable and break apart. On the other hand, simulations with outflow feedback form fewer higher-order multiple systems, but these systems are more stable. A comparison to a large survey of multiplicity among Class 0 and I systems by [Tobin et al. \(2016\)](#) shows that outflow feedback is necessary to match the observed multiplicity statistics.

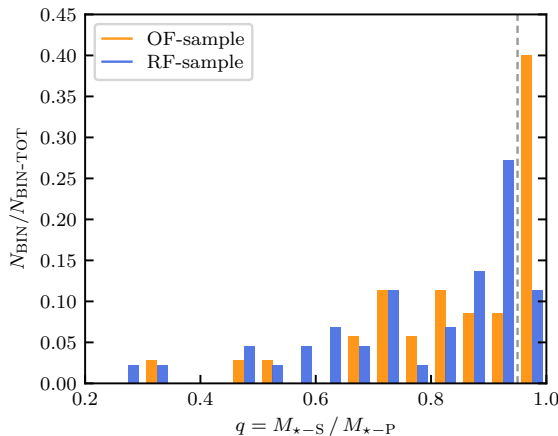


Figure 5: Normalised distribution of mass ratios,  $q$ , between the secondary,  $M_{*S}$ , and primary component,  $M_{*P}$ , of binary systems for the simulations with (orange) and without outflow feedback (blue). Simulations with outflow feedback have a significantly higher fraction of equal mass,  $q > 0.95$ , twin binaries. The original figure is found in *Paper II*.

Observations find an excess of almost equal mass twin binary systems ([Kounkel et al., 2019](#)). The simulated binary systems show a similar excess, as shown in Fig. 5, but only when including outflow feedback. The fraction of twin binaries in the sample with outflow feedback is 43% compared to only 9% in the sample without outflow feedback. A reason for the increased fraction of twin binaries when including outflow feedback is enhanced accretion via a circum-binary disc over direct infall accretion. Accretion via a circum-binary disc naturally balances the masses of the binary components.

Comparing simulations with and without outflow feedback reveals that episodic outflow

feedback has a tremendous impact on the stellar mass distribution. The simulated outflows entrain about seven and up to 32 times the initially ejected mass. These high entrainment factors are due to the episodic launching and are anti-correlated with the outburst frequency.

The entrained gas makes up about 70 % of the stellar mass. Since this entrained gas would otherwise be accreted onto the protostars, outflow feedback approximately halves the star formation efficiency. This reduction in star formation efficiency manifests in the stellar IMF by shifting the peak to lower masses. Therefore, outflow feedback plays an important role in resembling the observed stellar IMF, as well as the observed multiplicity statistics.

The goal of *Paper III* is to test the accuracy of methods that estimate protostellar ages, evolutionary stages and accretion rates from outflow properties. Outflows are often parsecs long and, therefore, relatively easy to observe. For the simulations including outflow feedback from *Paper II*, outflow cavities and bullets therein are extracted using a k-means and a OPTICS algorithm, respectively. Kinematic information of these outflows and bullets are then used to reconstruct the accretion history of the launching protostar (as can be seen in Fig. 6).

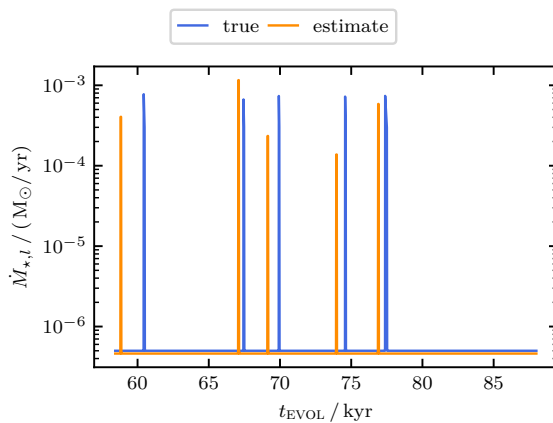


Figure 6: Estimated (orange) and true accretion history (blue) of a simulation presented in *Paper III*. Estimating the current accretion rate, the dynamical age of outflow bullets, and their corresponding accretion rate allows it to reconstruct the accretion history. The spacing of the outburst events and the episodic and background accretion rate resembles the underlying simulation. For the estimates, an ejection velocity of  $30 \text{ km s}^{-1}$  and an outburst duration of 50 yr is assumed.

Since the accretion of protostars ceases during the Stage I phase, the outflow activity decreases during this stage (Yildiz et al., 2015). Therefore, low outflow activity might be a sign of more evolved outflows. Outflow activity indicators, such as outflow mass, momentum and energy rate, are computed using the five dynamical age estimates and are compared to the underlying simulations. These outflow rates can be used to differentiate between Stage 0 and Stage I sources. For example, the transition region between Stage 0 and Stage I in outflow mass rates is

*Paper III* presents dynamical ages for these extracted outflows computed using five different methods. One of these methods is a new one, taking into account the momentum of two subsequent outflow bullets. Comparing the estimated dynamical ages against protostellar ages from the underlying simulations reveals that the new method predicts the stellar age with a mean relative error of 24%. Taking the ratio between outflow extend and the highest outflowing gas velocity to compute the dynamical age, a widely used method, comes with a mean relative error of 34%. The perpendicular method, proposed by Downes & Cabrit (2007), is especially accurate during the Stage I phase with a mean relative error of only 15%.

only about an order of magnitude.

The outflow lobes extracted from the simulations widen over time. Fitting the simulated opening angle age relation with a power-law function yields an exponent of  $\alpha = 0.33$ , in good agreement with observational data by [Arce & Sargent \(2006\)](#). However, directly estimating stellar ages from the opening angle age relation comes with large errors. Instead, opening angles can be used to differentiate between the Stage 0 and Stage I phase. Only 10 % of lobes have opening angles smaller than  $\sim 65^\circ$  or larger than  $\sim 100^\circ$  respectively when entering the Stage I phase.

Estimating continuous accretion rates similar to [Li et al. \(2020\)](#) results in a mean relative error of about 23 % during the Stage 0 phase. For more evolved stars, this method over predicts the actual accretion rates and the estimate becomes slightly worse. When assuming a characteristic outburst timescale, it is possible to estimate the accretion rate during an outburst event from the corresponding outflow bullet. Combining these episodic accretion rates with the bullets' dynamical ages allows for a reconstruction of the launching protostars accretion history. Fig. 6 shows such an accretion history for one of the simulations as an example.

## 7.2

### CONCLUSION

Protostellar outflows are considered the first rung of an increasingly disruptive feedback ladder. Even if protostellar outflows are not the most impactful feedback mechanism, they significantly shape the star formation process on core scales from the earliest moment of birth throughout the whole accretion phase. Outflows are the most important feedback mechanism in low-mass star formation since other feedback mechanisms, e.g. stellar winds, ionising radiation and supernovae, do not apply there. The three publications presented in this thesis shed light on the impact of outflow feedback on the star formation process and what we can learn from episodic outflows about the accretion history.

The numerical simulations presented in this work feature a newly developed episodic outflow feedback model. These simulations show that episodic outflow feedback influences many aspects of the star formation process. Protostellar outflows, launched in a narrow cone, widen over time and entrain many times the initially ejected gas mass from the environment that otherwise would be accreted onto the star. Therefore, protostellar outflows regulate the star formation process by approximately halving the star formation efficiency. This reduction in protostellar masses is reflected in a shift of the resulting stellar initial mass function.

Protostellar outflows cut off the accretion along their outflow directions, therefore altering how the protostars accrete by suppressing radial accretion. The instead promoted accretion via discs results in an enhanced fraction of twin binaries. The number of formed stars is lower when including episodic outflow feedback. However, the stability of higher-order multiple systems is enhanced if outflows are present. Simulations without outflow feedback show a high fraction of binary systems, such that the corresponding multiplicity statistics are not in agreement with observations. Instead, the simulations with outflow feedback are in good agreement with observations.

It is challenging to study the accretion onto protostars observationally due to the corresponding small AU scales of the inner accretion disc. However, the launching of protostellar outflows is directly coupled to the accretion at these scales and outflows are observable at parsec scales. Therefore, protostellar outflows and especially

individual outflow bullets carry the information of the accretion history. Dynamical ages of outflows and bullets allow for reliable age estimation, whereas the outflow opening angle and activity help to distinguish between evolutionary stages of the launching source. When combining these techniques, it is possible to reconstruct the accretion histories of launching protostars.

This work shows that protostellar outflows are an integral part of the star formation process. Protostellar outflows significantly impact the multiplicity of stars, how stars accrete and correspondingly their final masses. Therefore it is necessary to consider outflow feedback when modelling star formation. This work especially focuses on episodic outflow feedback. It is advisable to explicitly model episodic outflow feedback if not all relevant episodic accretion trigger are captured self-consistently. Otherwise, relevant characteristics of outflows such as outflow bullets or correspondingly Hubble wedges in position-velocity diagrams will be missed. Especially these outflow bullets carry valuable information about the accretion histories of protostars.

### 7.3

#### OUTLOOK

The simulations presented in this work consist mostly of  $1 M_{\odot}$  dense cores. *Paper II* evaluates the impact of various initial core parameters on the outcome of the simulations. Based on this knowledge, the next step could be to extend the simulation ensemble and re-sample the core mass function. This way, one could comprehensively study the impact of episodic outflow feedback on the stellar initial mass function and its shift compared to the core mass function (Pelkonen et al., 2021). If the core mass is increased such that high-mass star formation occurs, one would need to consider a more sophisticated radiative transfer model. This would then open up the possibility to study the interplay between outflows and radiation with the so-called "flashlight" effect (Kuiper et al., 2015).

Besides sampling the core mass function with a set of isolated cores, it would be insightful to simulate larger-scale simulations, e.g. small molecular clouds containing at least one filament. There, one could study the interplay between outflows and the larger-scale environment. Four open questions that could be investigated using a larger-scale setup are whether episodic outflows cut off accretion flows onto cores, if outflows might trigger star formation, if outflows are capable of sustaining the turbulence within the cloud, and if outflows have a preferred orientation with respect to the filament.

Ideally, these simulations would be performed with a code capable of the new mesh-less finite mass scheme that offers numerous benefits compared to grad-h SPH (Section 2.12). One of the biggest caveats of the simulations presented in this thesis is the missing magnetic fields. Therefore, the selected code should be able to handle MHD simulations.

The simulations presented in this thesis could be further analysed with a focus on the angular momentum carried away by the outflow bullets. The angular momentum of outflow bullets is considered to shed light on the launching mechanism by constraining the corresponding launching region in the accretion disc (Lee, 2020). Since we have a fixed launching model, it would be interesting to see whether we can reconstruct it from the angular momentum in the outflow bullets.

*Paper III* shows that outflows and especially outflow bullets carry fossil information about the accretion history. This information is encoded in position-velocity

---

diagrams, e.g. by Hubble wedges. It might be possible to train a convolutional neural network (e.g. [Dhillon & Verma, 2019](#)) on simulations presented in *Paper II* that takes position-velocity diagrams and predicts the accretion history. I tried to develop and train such a network, but the results are preliminary and not very accurate yet. However, this direction might be worth further investigation.

## BIBLIOGRAPHY

---

- Anderl, S., Maret, S., Cabrit, S., et al., Probing episodic accretion with chemistry: CALYPSO observations of the very-low-luminosity Class 0 protostar IRAM 04191+1522. Results from the CALYPSO IRAM-PdBI survey. 2020, *A&A*, 643, A123
- Anderson, J. M., Li, Z.-Y., Krasnopolsky, R., & Blandford, R. D., Locating the Launching Region of T Tauri Winds: The Case of DG Tauri. 2003, *ApJ*, 590, L107
- André, P., Di Francesco, J., Ward-Thompson, D., et al. 2014, in *Protostars and Planets VI*, ed. H. Beuther, R. S. Klessen, C. P. Dullemond, & T. Henning, 27
- Anglada, G., López, R., Estalella, R., et al., Proper Motions of the Jets in the Region of HH 30 and HL/XZ Tau: Evidence for a Binary Exciting Source of the HH 30 Jet. 2007, *AJ*, 133, 2799
- Anglada, G., Rodríguez, L. F., & Carrasco-González, C., Radio jets from young stellar objects. 2018, *A&A Rev.*, 26, 3
- Arce, H. G., Borkin, M. A., Goodman, A. A., Pineda, J. E., & Halle, M. W., The COMPLETE Survey of Outflows in Perseus. 2010, *ApJ*, 715, 1170
- Arce, H. G. & Goodman, A. A., The Mass-Velocity and Position-Velocity Relations in Episodic Outflows. 2001, *ApJ*, 551, L171
- Arce, H. G., Santiago-García, J., Jørgensen, J. K., Tafalla, M., & Bachiller, R., Complex Molecules in the L1157 Molecular Outflow. 2008, *ApJ*, 681, L21
- Arce, H. G. & Sargent, A. I., Outflow-Infall Interactions in Early Star Formation and Their Impact on the Mass-assembling Process in L1228. 2004, *ApJ*, 612, 342
- Arce, H. G. & Sargent, A. I., The Evolution of Outflow-Envelope Interactions in Low-Mass Protostars. 2006, *ApJ*, 646, 1070
- Arce, H. G., Shepherd, D., Gueth, F., et al., Molecular Outflows in Low- and High-Mass Star-forming Regions. 2007, *Protostars and Planets V*, 245
- Audard, M., Abraham, P., Dunham, M. M., et al. 2014, in *Protostars and Planets VI*, ed. H. Beuther, R. S. Klessen, C. P. Dullemond, & T. Henning, 387
- Audard, M., Stringfellow, G. S., Güdel, M., et al., A multi-wavelength study of the young star V1118 Orionis in outburst. 2010, *A&A*, 511, A63
- Bachiller, R., Martín-Pintado, J., Tafalla, M., Cernicharo, J., & Lazareff, B., High-velocity molecular bullets in a fast bipolar outflow near L1448/IRS3. 1990, *A&A*, 231, 174
- Bally, J., *Protostellar Outflows*. 2016, *ARA&A*, 54, 491
- Banerjee, R., Klessen, R. S., & Fendt, C., Can Protostellar Jets Drive Supersonic Turbulence in Molecular Clouds? 2007, *ApJ*, 668, 1028

- Barnes, J. & Hut, P., A hierarchical  $O(N \log N)$  force-calculation algorithm. 1986, *Nature*, 324, 446
- Bate, M. R., Stellar, brown dwarf and multiple star properties from a radiation hydrodynamical simulation of star cluster formation. 2012, *MNRAS*, 419, 3115
- Bate, M. R., Bonnell, I. A., & Price, N. M., Modelling accretion in protobinary systems. 1995, *MNRAS*, 277, 362
- Bate, M. R., Tricco, T. S., & Price, D. J., Collapse of a molecular cloud core to stellar densities: stellar-core and outflow formation in radiation magnetohydrodynamic simulations. 2014, *MNRAS*, 437, 77
- Bentley, J. L., Multidimensional Binary Search Trees Used for Associative Searching. 1975, *Commun. ACM*, 18, 509â517
- Beuther, H., Gieser, C., Suri, S., et al., Fragmentation and kinematics in high-mass star formation: CORE-extension targeting two very young high-mass star-forming regions. 2021, arXiv e-prints, arXiv:2104.02420
- Bhandare, A., Kuiper, R., Henning, T., et al., First core properties: from low- to high-mass star formation. 2018, *A&A*, 618, A95
- Bjerkeli, P., Ramsey, J. P., Harsono, D., et al., Kinematics around the B335 protostar down to au scales. 2019, *A&A*, 631, A64
- Black, D. C. & Bodenheimer, P., Evolution of rotating interstellar clouds. I. Numerical techniques. 1975, *ApJ*, 199, 619
- Blandford, R. D. & Payne, D. G., Hydromagnetic flows from accretion disks and the production of radio jets. 1982, *MNRAS*, 199, 883
- Bodenheimer, P., Angular Momentum Evolution of Young Stars and Disks. 1995, *ARA&A*, 33, 199
- Bodenheimer, P. H. 2011, *Principles of Star Formation*
- Bonnor, W. B., The Formation of the Nebulae. With 3 Figures. 1956, *ZAp*, 39, 143
- Busch, L. A., Belloche, A., Cabrit, S., Hennebelle, P., & Commerçon, B., The dynamically young outflow of the Class 0 protostar Cha-MMS1. 2020, *A&A*, 633, A126
- Cai, M. J., The X-wind Model. 2009, *Astrophysics and Space Science Proceedings*, 13, 143
- Calvet, N., Hartmann, L., & Kenyon, S. J., Mass loss from pre-main-sequence accretion disks. I - The accelerating wind of FU Orionis. 1993, *ApJ*, 402, 623
- Caratti o Garatti, A., Stecklum, B., Linz, H., Garcia Lopez, R., & Sanna, A., A near-infrared spectroscopic survey of massive jets towards extended green objects. 2015, *A&A*, 573, A82
- Carrasco-González, C., Rodríguez, L. F., Anglada, G., et al., A Magnetized Jet from a Massive Protostar. 2010, *Science*, 330, 1209
- Casse, F. & Ferreira, J., Magnetized accretion-ejection structures. IV. Magnetically-driven jets from resistive, viscous, Keplerian discs. 2000, *A&A*, 353, 1115

- Cerqueira, A. H., Lefloch, B., Esquivel, A., et al., H<sub>2</sub> mass-velocity relationship from 3D numerical simulations of jet-driven molecular outflows. 2021, *A&A*, 645, A135
- Chan, T. K., Theuns, T., Bower, R., & Frenk, C., Smoothed Particle Radiation Hydrodynamics: Two-Moment method with Local Eddington Tensor Closure. 2021, arXiv e-prints, arXiv:2102.08404
- Chandrasekhar, S., The Stability of Non-Dissipative Couette Flow in Hydromagnetics. 1960, *Proceedings of the National Academy of Science*, 46, 253
- Chen, X., Arce, H. G., Zhang, Q., Launhardt, R., & Henning, T., Rotating Bullets from A Variable Protostar. 2016, *ApJ*, 824, 72
- Cheng, Y., Qiu, K., Zhang, Q., et al. 2019, *Molecular Bullets in A High-mass Protostar*
- Clarke, S. D., Whitworth, A. P., Duarte-Cabral, A., & Hubber, D. A., Filamentary fragmentation in a turbulent medium. 2017, *MNRAS*, 468, 2489
- Clarke, S. D., Williams, G. M., & Walch, S., The hierarchical fragmentation of filaments and the role of sub-filaments. 2020, *MNRAS*, 497, 4390
- Commerçon, B., Hennebelle, P., Audit, E., et al. 2012, in *Astronomical Society of the Pacific Conference Series*, Vol. 453, *Advances in Computational Astrophysics: Methods, Tools, and Outcome*, ed. R. Capuzzo-Dolcetta, M. Limongi, & A. Tornambè, 13
- Cortes-Rangel, G., Zapata, L. A., Toalá, J. A., et al., ALMA Observations of the Extraordinary Carina Pillars: HH 901/902. 2020, *AJ*, 159, 62
- Cuello, N., Louvet, F., Mentiplay, D., et al., Flybys in protoplanetary discs - II. Observational signatures. 2020, *MNRAS*, 491, 504
- Cullen, L. & Dehnen, W., Inviscid smoothed particle hydrodynamics. 2010, *MNRAS*, 408, 669
- Cunningham, A. J., Klein, R. I., Krumholz, M. R., & McKee, C. F., Radiation-hydrodynamic Simulations of Massive Star Formation with Protostellar Outflows. 2011, *ApJ*, 740, 107
- Cunningham, A. J., Krumholz, M. R., McKee, C. F., & Klein, R. I., The effects of magnetic fields and protostellar feedback on low-mass cluster formation. 2018, *MNRAS*, 476, 771
- Curtis, E. I., Richer, J. S., Swift, J. J., & Williams, J. P., A submillimetre survey of the kinematics of the Perseus molecular cloud - II. Molecular outflows. 2010, *MNRAS*, 408, 1516
- de Valon, A., Dougados, C., Cabrit, S., et al., ALMA reveals a large structured disk and nested rotating outflows in DG Tauri B. 2020, *A&A*, 634, L12
- Dehnen, W. & Aly, H., Improving convergence in smoothed particle hydrodynamics simulations without pairing instability. 2012, *MNRAS*, 425, 1068
- Dhillon, A. & Verma, G., Convolutional neural network: a review of models, methodologies and applications to object detection. 2019, *Progress in Artificial Intelligence*, 9, 85

- Downes, T. P. & Cabrit, S., Jet-driven molecular outflows from class 0 sources: younger and stronger than they seem? 2007, *A&A*, 471, 873
- Drabek-Maunder, E., Hatchell, J., Buckle, J. V., Di Francesco, J., & Richer, J., The JCMT Gould Belt Survey: Understanding the influence of outflows on Gould Belt clouds. 2016, *MNRAS*, 457, L84
- Drozdovskaya, M. N., Walsh, C., Visser, R., Harsono, D., & van Dishoeck, E. F., The complex chemistry of outflow cavity walls exposed: the case of low-mass protostars. 2015, *MNRAS*, 451, 3836
- Duchêne, G., Bontemps, S., Bouvier, J., et al., Multiple protostellar systems. II. A high resolution near-infrared imaging survey in nearby star-forming regions. 2007, *A&A*, 476, 229
- Duchêne, G., Lacour, S., Moraux, E., Goodwin, S., & Bouvier, J., Is stellar multiplicity universal? Tight stellar binaries in the Orion nebula Cluster. 2018, *MNRAS*, 478, 1825
- Duncan, E. J., Fedriani, R., & Tan, J. C. 2021, in *American Astronomical Society Meeting Abstracts*, Vol. 53, American Astronomical Society Meeting Abstracts, 114.08
- Dunham, M. M., Stutz, A. M., Allen, L. E., et al. 2014, in *Protostars and Planets VI*, ed. H. Beuther, R. S. Klessen, C. P. Dullemond, & T. Henning, 195
- Ebert, R., Zur Instabilität kugelsymmetrischer Gasverteilungen. Mit 2 Textabbildungen. 1957, *ZAp*, 42, 263
- Ellerbroek, L. E., Podio, L., Kaper, L., et al., The outflow history of two Herbig-Haro jets in RCW 36: HH 1042 and HH 1043. 2013, *A&A*, 551, A5
- Evans, Neal J., I., Dunham, M. M., Jørgensen, J. K., et al., The Spitzer c2d Legacy Results: Star-Formation Rates and Efficiencies; Evolution and Lifetimes. 2009, *ApJS*, 181, 321
- Feddersen, J. R., Arce, H. G., Kong, S., et al., The CARMA-NRO Orion Survey: Protostellar Outflows, Energetics, and Filamentary Alignment. 2020, *ApJ*, 896, 11
- Federrath, C., Schrön, M., Banerjee, R., & Klessen, R. S., Modeling Jet and Outflow Feedback during Star Cluster Formation. 2014, *ApJ*, 790, 128
- Fehér, O., Kóspál, Á., Ábrahám, P., Hogerheijde, M. R., & Brinch, C., Interferometric view of the circumstellar envelopes of northern FU Orionis-type stars. 2017, *A&A*, 607, A39
- Fernández-López, M., Zapata, L. A., Rodríguez, L. F., et al., A Ringed Pole-on Outflow from DO Tauri Revealed by ALMA. 2020, *AJ*, 159, 171
- Ferreira, J., Magnetically-driven jets from Keplerian accretion discs. 1997, *A&A*, 319, 340
- Ferrero, L. V., Cappa, C. E., Saldaño, H. P., et al., Multifrequency study of HH 137 and HH 138: discovering new knots and molecular outflows with Gemini and APEX. 2020, *MNRAS*, 496, 4239

- Fischer, W. J., Safron, E., & Megeath, S. T., Constraining the Rate of Protostellar Accretion Outbursts in the Orion Molecular Clouds. 2019, *ApJ*, 872, 183
- Frank, A., Ray, T. P., Cabrit, S., et al. 2014, in *Protostars and Planets VI*, ed. H. Beuther, R. S. Klessen, C. P. Dullemond, & T. Henning, 451
- Fryxell, B., Olson, K., Ricker, P., et al., FLASH: An Adaptive Mesh Hydrodynamics Code for Modeling Astrophysical Thermonuclear Flashes. 2000, *ApJ*, 131, 273
- Gaudel, M., Maury, A. J., Belloche, A., et al., Angular momentum profiles of Class 0 protostellar envelopes. 2020, *A&A*, 637, A92
- Ghosh, P. & Lamb, F. K., Disk accretion by magnetic neutron stars. 1978, *ApJ*, 223, L83
- Gingold, R. A. & Monaghan, J. J., Smoothed particle hydrodynamics: theory and application to non-spherical stars. 1977, *MNRAS*, 181, 375
- Glassgold, A. E., Mamon, G. A., & Huggins, P. J., The Formation of Molecules in Protostellar Winds. 1991, *ApJ*, 373, 254
- Gray, W. J., McKee, C. F., & Klein, R. I., Effect of angular momentum alignment and strong magnetic fields on the formation of protostellar discs. 2018, *MNRAS*, 473, 2124
- Grond, J. J., Woods, R. M., Wadsley, J. W., & Couchman, H. M. P., TREVR: A general  $N \log^2 N$  radiative transfer algorithm. 2019, *MNRAS*, 485, 3681
- Grudić, M. Y., Guszejnov, D., Hopkins, P. F., Offner, S. S. R., & Faucher-Giguère, C.-A., STARFORGE: Toward a comprehensive numerical model of star cluster formation and feedback. 2020, arXiv e-prints, arXiv:2010.11254
- Guszejnov, D., Grudić, M. Y., Hopkins, P. F., Offner, S. S. R., & Faucher-Giguère, C.-A., STARFORGE: the effects of protostellar outflows on the IMF. 2021, *MNRAS*, 502, 3646
- Hansen, C. E., Klein, R. I., McKee, C. F., & Fisher, R. T., Feedback Effects on Low-mass Star Formation. 2012, *ApJ*, 747, 22
- Hartigan, P., Frank, A., Foster, J. M., et al., Fluid Dynamics of Stellar Jets in Real Time: Third Epoch Hubble Space Telescope Images of HH 1, HH 34, and HH 47. 2011, *ApJ*, 736, 29
- Hartmann, L. & Calvet, N., Observational constraints on FU ORI winds. 1995, *AJ*, 109, 1846
- Hillenbrand, L. A., Contreras Peña, C., Morrell, S., et al., Gaia 17bpi: An FU Ori-type Outburst. 2018, *ApJ*, 869, 146
- Hillenbrand, L. A., De, K., Hankins, M., et al., Outbursting Young Stellar Object PGIR 20dci in the Perseus Arm. 2021, *AJ*, 161, 220
- Hirano, N., Ho, P. P. T., Liu, S.-Y., et al., Extreme Active Molecular Jets in L1448C. 2010, *ApJ*, 717, 58
- Hirota, T., Machida, M. N., Matsushita, Y., et al., Disk-driven rotating bipolar outflow in Orion Source I. 2017, *Nature Astronomy*, 1, 0146

- Hone, E., Kraus, S., Davies, C. L., et al., Compact gaseous accretion disk in Keplerian rotation around MWC 147. 2019, *A&A*, 623, A38
- Hopkins, P. F., A new class of accurate, mesh-free hydrodynamic simulation methods. 2015, *MNRAS*, 450, 53
- Hsieh, T.-H., Lai, S.-P., & Belloche, A., Widening of Protostellar Outflows: An Infrared Outflow Survey in Low-luminosity Objects. 2017, *AJ*, 153, 173
- Hsieh, T.-H., Murillo, N. M., Belloche, A., et al., Chronology of Episodic Accretion in Protostars—An ALMA Survey of the CO and H<sub>2</sub>O Snowlines. 2019, *ApJ*, 884, 149
- Hsieh, T.-H., Murillo, N. M., Belloche, A., et al., Probing Episodic Accretion in Very Low Luminosity Objects. 2018, *ApJ*, 854, 15
- Hubber, D. A., Batty, C. P., McLeod, A., & Whitworth, A. P., SEREN - a new SPH code for star and planet formation simulations. Algorithms and tests. 2011, *A&A*, 529, A27
- Hubber, D. A., Rosotti, G. P., & Booth, R. A., GANDALF - Graphical Astrophysics code for N-body Dynamics And Lagrangian Fluids. 2018, *MNRAS*, 473, 1603
- Hubber, D. A., Walch, S., & Whitworth, A. P., An improved sink particle algorithm for SPH simulations. 2013, *MNRAS*, 430, 3261
- Jeans, J. H., The Stability of a Spherical Nebula. 1902, *Philosophical Transactions of the Royal Society of London Series A*, 199, 1
- Jhan, K.-S. & Lee, C.-F., 25 au Angular Resolution Observations of HH 211 with ALMA: Jet Properties and Shock Structures in SiO, CO, and SO. 2021, *ApJ*, 909, 11
- Jiménez-Serra, I., Báez-Rubio, A., Martín-Pintado, J., Zhang, Q., & Rivilla, V. M., The Ionized Warped Disk and Disk Wind of the Massive Protostar Monoceros R2-IRS2 Seen with ALMA. 2020, *ApJ*, 897, L33
- Kadam, K., Vorobyov, E., Regály, Z., Kóspál, Á., & Ábrahám, P., Outbursts in Global Protoplanetary Disk Simulations. 2020, *ApJ*, 895, 41
- Kandori, R., Tomisaka, K., Tamura, M., et al., Distortion of Magnetic Fields in a Starless Core. IV. Magnetic Field Scaling on Density and Mass-to-flux Ratio Distribution in FeSt 1-457. 2018, *ApJ*, 865, 121
- Kenyon, S. J. & Hartmann, L., Pre-Main-Sequence Evolution in the Taurus-Auriga Molecular Cloud. 1995, *ApJS*, 101, 117
- Kenyon, S. J., Hartmann, L. W., Strom, K. M., & Strom, S. E., An IRAS Survey of the Taurus-Auriga Molecular Cloud. 1990, *AJ*, 99, 869
- Kim, W.-T. & Ostriker, E. C., Amplification, Saturation, and Q Thresholds for Run-away: Growth of Self-Gravitating Structures in Models of Magnetized Galactic Gas Disks. 2001, *ApJ*, 559, 70
- Koenigl, A., Disk Accretion onto Magnetic T Tauri Stars. 1991, *ApJ*, 370, L39
- Kölligan, A. & Kuiper, R., Jets and outflows of massive protostars. From cloud collapse to jet launching and cloud dispersal. 2018, *A&A*, 620, A182

- Königl, A., Salmeron, R., & Wardle, M., Wind-driving protostellar accretion discs - I. Formulation and parameter constraints. 2010, *MNRAS*, 401, 479
- Könyves, V., André, P., Arzoumanian, D., et al., Properties of the dense core population in Orion B as seen by the Herschel Gould Belt survey. 2020, *A&A*, 635, A34
- Könyves, V., André, P., Men'shchikov, A., et al., A census of dense cores in the Aquila cloud complex: SPIRE/PACS observations from the Herschel Gould Belt survey. 2015, *A&A*, 584, A91
- Kounkel, M., Covey, K., Moe, M., et al., Close Companions around Young Stars. 2019, *The Astronomical Journal*, 157, 196
- Krumholz, M. R., Bate, M. R., Arce, H. G., et al. 2014, in *Protostars and Planets VI*, ed. H. Beuther, R. S. Klessen, C. P. Dullemond, & T. Henning, 243
- Kuffmeier, M., Frimann, S., Jensen, S. S., & Haugbølle, T., Episodic accretion: the interplay of infall and disc instabilities. 2018, *MNRAS*, 475, 2642
- Kuiper, R., Yorke, H. W., & Turner, N. J., Protostellar Outflows and Radiative Feedback from Massive Stars. 2015, *ApJ*, 800, 86
- Kuruwita, R. L., Federrath, C., & Haugbølle, T., The dependence of episodic accretion on eccentricity during the formation of binary stars. 2020, *A&A*, 641, A59
- Lada, C. J. & Fich, M., The Structure and Energetics of a Highly Collimated Bipolar Outflow: NGC 2264G. 1996, *ApJ*, 459, 638
- Larson, R. B., Numerical calculations of the dynamics of collapsing proto-star. 1969, *MNRAS*, 145, 271
- Lee, C.-F., Molecular jets from low-mass young protostellar objects. 2020, *A&A Rev.*, 28, 1
- Lee, C.-F., Hirano, N., Zhang, Q., et al., Jet Motion, Internal Working Surfaces, and Nested Shells in the Protostellar System HH 212. 2015, *ApJ*, 805, 186
- Lee, C.-F., Ho, P. T. P., Li, Z.-Y., et al., A rotating protostellar jet launched from the innermost disk of HH 212. 2017, *Nature Astronomy*, 1, 0152
- Lee, C.-F., Li, Z.-Y., Codella, C., et al., A 100 au Wide Bipolar Rotating Shell Emanating from the HH 212 Protostellar Disk: A Disk Wind? 2018, *ApJ*, 856, 14
- Lee, C.-F., Li, Z.-Y., & Turner, N. J., Spiral structures in an embedded protostellar disk driven by envelope accretion. 2020, *Nature Astronomy*, 4, 142
- Lee, C.-F., Mundy, L. G., Reipurth, B., Ostriker, E. C., & Stone, J. M., CO Outflows from Young Stars: Confronting the Jet and Wind Models. 2000, *ApJ*, 542, 925
- Lee, C.-F., Mundy, L. G., Stone, J. M., & Ostriker, E. C., CO Outflows from Young Stellar Objects. 2002, *ApJ*, 576, 294
- Lee, C.-F., Tabone, B., Cabrit, S., et al., First Detection of Interaction between a Magnetic Disk Wind and an Episodic Jet in a Protostellar System. 2021, *ApJ*, 907, L41

- Lefèvre, C., Cabrit, S., Maury, A. J., et al., CALYPSO view of SVS 13A with PdBI: Multiple jet sources. 2017, *A&A*, 604, L1
- Leung, P. K. C. & Ogilvie, G. I., Wind-MRI interactions in local models of protoplanetary discs - I. Ohmic resistivity. 2020, *MNRAS*, 498, 750
- Li, P. S., Klein, R. I., & McKee, C. F., Formation of stellar clusters in magnetized, filamentary infrared dark clouds. 2018, *MNRAS*, 473, 4220
- Li, S., Sanhueza, P., Zhang, Q., et al., The ALMA Survey of 70  $\mu\text{m}$  Dark High-mass Clumps in Early Stages (ASHES). II. Molecular Outflows in the Extreme Early Stages of Protocluster Formation. 2020, *ApJ*, 903, 119
- Li, Z.-Y., Magnetohydrodynamic Disk-Wind Connection: Self-similar Solutions. 1995, *ApJ*, 444, 848
- Li, Z.-Y., Magnetohydrodynamic Disk-Wind Connection: Magnetocentrifugal Winds from Ambipolar Diffusion-dominated Accretion Disks. 1996, *ApJ*, 465, 855
- Li, Z. Y., Banerjee, R., Pudritz, R. E., et al. 2014, in *Protostars and Planets VI*, ed. H. Beuther, R. S. Klessen, C. P. Dullemond, & T. Henning, 173
- Lind, S. J., Rogers, B. D., & Stansby, P. K., Review of smoothed particle hydrodynamics: towards converged Lagrangian flow modelling. 2020, *Proceedings of the Royal Society of London Series A*, 476, 20190801
- Liu, T., Lacy, J., Li, P. S., et al., ALMA Reveals Sequential High-mass Star Formation in the G9.62+0.19 Complex. 2017, *ApJ*, 849, 25
- Lomax, O., Whitworth, A. P., & Hubber, D. A., The Role of Discs in the Collapse and Fragmentation of Prestellar Cores. 2016, *PASA*, 33, e004
- Lomax, O., Whitworth, A. P., Hubber, D. A., Stamatellos, D., & Walch, S., Simulating star formation in Ophiuchus. 2014, *MNRAS*, 439, 3039
- López-Vázquez, J. A., Zapata, L. A., Lizano, S., & Cantó, J., ALMA Observations and Modeling of the Rotating Outflow in Orion Source I. 2020, *ApJ*, 904, 158
- Lorenzetti, D., Antonucci, S., Giannini, T., et al., On the Nature of EXor Accretion Events: An Infrequent Manifestation of a Common Phenomenology? 2012, *ApJ*, 749, 188
- Louvet, F., Dougados, C., Cabrit, S., et al., The HH30 edge-on T Tauri star. A rotating and precessing monopolar outflow scrutinized by ALMA. 2018, *A&A*, 618, A120
- Lucas, P. W., Elias, J., Points, S., et al., Discovery of a mid-infrared protostellar outburst of exceptional amplitude. 2020, *MNRAS*, 499, 1805
- Lucy, L. B., A numerical approach to the testing of the fission hypothesis. 1977, *AJ*, 82, 1013
- Lucy, L. B., Spectroscopic binaries with components of similar mass. 2006, *A&A*, 457, 629
- Machida, M. N. & Basu, S., The First Two Thousand Years of Star Formation. 2019, *ApJ*, 876, 149

- Machida, M. N. & Hosokawa, T., Evolution of protostellar outflow around low-mass protostar. 2013, *MNRAS*, 431, 1719
- Machida, M. N. & Matsumoto, T., Impact of protostellar outflow on star formation: effects of the initial cloud mass. 2012, *MNRAS*, 421, 588
- Masunaga, H. & Inutsuka, S.-i., A Radiation Hydrodynamic Model for Protostellar Collapse. II. The Second Collapse and the Birth of a Protostar. 2000, *ApJ*, 531, 350
- Matt, S. & Pudritz, R. E., Accretion-powered Stellar Winds as a Solution to the Stellar Angular Momentum Problem. 2005, *ApJ*, 632, L135
- Matzner, C. D. & Jumper, P. H., Star Cluster Formation with Stellar Feedback and Large-scale Inflow. 2015, *ApJ*, 815, 68
- Matzner, C. D. & McKee, C. F., Bipolar Molecular Outflows Driven by Hydromagnetic Protostellar Winds. 1999, *ApJ*, 526, L109
- Maud, L. T., Cesaroni, R., Kumar, M. S. N., et al., Chasing discs around O-type (proto)stars. ALMA evidence for an SiO disc and disc wind from G17.64+0.16. 2018, *A&A*, 620, A31
- Maury, A. J., André, P., Testi, L., et al., Characterizing young protostellar disks with the CALYPSO IRAM-PdBI survey: large Class 0 disks are rare. 2019, *A&A*, 621, A76
- Maury, A. J., Girart, J. M., Zhang, Q., et al., Magnetically regulated collapse in the B335 protostar? I. ALMA observations of the polarized dust emission. 2018, *MNRAS*, 477, 2760
- McCaughrean, M., Zinnecker, H., Andersen, M., Meeus, G., & Lodieu, N., Standing on the shoulder of a giant: ISAAC, Antu, and star formation. 2002, *The Messenger*, 109, 28
- Millan-Gabet, R., Malbet, F., Akeson, R., et al. 2007, in *Protostars and Planets V*, ed. B. Reipurth, D. Jewitt, & K. Keil, 539
- Mohanty, S. & Shu, F. H., Generalized Multipole X-Wind Model. 2009, *Astrophysics and Space Science Proceedings*, 13, 51
- Molyarova, T., Akimkin, V., Semenov, D., et al., Chemical Signatures of the FU Ori Outbursts. 2018, *ApJ*, 866, 46
- Monaghan, J. J., SPH and Riemann Solvers. 1997, *Journal of Computational Physics*, 136, 298
- Monaghan, J. J., SPH compressible turbulence. 2002, *MNRAS*, 335, 843
- Monaghan, J. J., Smoothed particle hydrodynamics. 2005, *Reports on Progress in Physics*, 68, 1703
- Morris, J. P. & Monaghan, J. J., A Switch to Reduce SPH Viscosity. 1997, *Journal of Computational Physics*, 136, 41
- Moscadelli, L., Beuther, H., Ahmadi, A., et al., Multi-scale view of star formation in IRAS 21078+5211: from clump fragmentation to disk wind. 2021, *A&A*, 647, A114

- Mottram, J. C., van Dishoeck, E. F., Kristensen, L. E., et al., Outflows, infall and evolution of a sample of embedded low-mass protostars. The William Herschel Line Legacy (WILL) survey. 2017, *A&A*, 600, A99
- Movsessian, T. A., Magakian, T. Y., & Dodonov, S. N., New Herbig-Haro objects and outflows in the Mon R1 association. 2021, *MNRAS*, 500, 2440
- Myers, P. C., Protostar Mass due to Infall and Dispersal. 2008, *ApJ*, 687, 340
- Nakamura, F. & Li, Z.-Y., Protostellar Turbulence Driven by Collimated Outflows. 2007, *ApJ*, 662, 395
- Nakamura, F. & Li, Z.-Y., Confronting the Outflow-regulated Cluster Formation Model with Observations. 2014, *ApJ*, 783, 115
- Nony, T., Motte, F., Louvet, F., et al., Episodic accretion constrained by a rich cluster of outflows. 2020, *A&A*, 636, A38
- Offner, S. S. R. & Arce, H. G., Investigations of Protostellar Outflow Launching and Gas Entrainment: Hydrodynamic Simulations and Molecular Emission. 2014, *ApJ*, 784, 61
- Offner, S. S. R. & Chaban, J., Impact of Protostellar Outflows on Turbulence and Star Formation Efficiency in Magnetized Dense Cores. 2017, *ApJ*, 847, 104
- Offner, S. S. R., Klein, R. I., McKee, C. F., & Krumholz, M. R., The Effects of Radiative Transfer on Low-Mass Star Formation. 2009, *ApJ*, 703, 131
- O'Neill, T. J., Cosentino, G., Tan, J. C., Cheng, Y., & Liu, M., The Core Mass Function Across Galactic Environments. III. Massive Protoclusters. 2021, arXiv e-prints, arXiv:2104.08861
- Pascucci, I., Banzatti, A., Gorti, U., et al., The Evolution of Disk Winds from a Combined Study of Optical and Infrared Forbidden Lines. 2020, *ApJ*, 903, 78
- Pawlik, A. H. & Schaye, J., TRAPHIC - radiative transfer for smoothed particle hydrodynamics simulations. 2008, *MNRAS*, 389, 651
- Pelkonen, V. M., Padoan, P., Haugbølle, T., & Nordlund, Å., From the CMF to the IMF: beyond the core-collapse model. 2021, *MNRAS*, 504, 1219
- Pelletier, G. & Pudritz, R. E., Hydromagnetic disk winds in young stellar objects and active galactic nuclei. 1992, *ApJ*, 394, 117
- Pérez, S., Hales, A., Liu, H. B., et al., Resolving the FU Orionis System with ALMA: Interacting Twin Disks? 2020, *ApJ*, 889, 59
- Pineda, J. E., Offner, S. S. R., Parker, R. J., et al., The formation of a quadruple star system with wide separation. 2015, *Nature*, 518, 213
- Plunkett, A. L., Arce, H. G., Mardones, D., et al., Episodic molecular outflow in the very young protostellar cluster Serpens South. 2015, *Nature*, 527, 70
- Podio, L., Codella, C., Gueth, F., et al., The jet and the disk of the HH 212 low-mass protostar imaged by ALMA: SO and SO<sub>2</sub> emission. 2015, *A&A*, 581, A85

- Podio, L., Tabone, B., Codella, C., et al., The CALYPSO IRAM-PdBI survey of jets from Class 0 protostars. Are jets ubiquitous in young stars ? 2020, arXiv e-prints, arXiv:2012.15379
- Podio, L., Tabone, B., Codella, C., et al., The CALYPSO IRAM-PdBI survey of jets from Class 0 protostars. Exploring whether jets are ubiquitous in young stars. 2021, *A&A*, 648, A45
- Price, D. J. & Monaghan, J. J., Smoothed Particle Magnetohydrodynamics - II. Variational principles and variable smoothing-length terms. 2004, *MNRAS*, 348, 139
- Price, D. J. & Monaghan, J. J., An energy-conserving formalism for adaptive gravitational force softening in smoothed particle hydrodynamics and N-body codes. 2007, *MNRAS*, 374, 1347
- Price, D. J., Tricco, T. S., & Bate, M. R., Collimated jets from the first core. 2012, *MNRAS*, 423, L45
- Quinlan, N. J., Basa, M., & Lastiwka, M., Truncation error in mesh-free particle methods. 2006, *International Journal for Numerical Methods in Engineering*, 66, 2064
- Rab, C., Elbakyan, V., Vorobyov, E., et al., The chemistry of episodic accretion in embedded objects. 2D radiation thermo-chemical models of the post-burst phase. 2017, *A&A*, 604, A15
- Raghavan, D., McAlister, H. A., Henry, T. J., et al., A Survey of Stellar Families: Multiplicity of Solar-type Stars. 2010, *ApJS*, 190, 1
- Reipurth, B., Bally, J., & Devine, D., Giant Herbig-Haro Flows. 1997, *AJ*, 114, 2708
- Reipurth, B., Davis, C. J., Bally, J., et al., The Giant Herbig-Haro Flow HH 212 and Associated Star Formation. 2019, *AJ*, 158, 107
- Reipurth, B., Devine, D., & Bally, J., Herbig-Haro Flows from the L1641-N Embedded Infrared Cluster. 1998, *AJ*, 116, 1396
- Reynolds, N. K., Tobin, J. J., Sheehan, P., et al., Kinematic Analysis of a Protostellar Multiple System: Measuring the Protostar Masses and Assessing Gravitational Instability in the Disks of L1448 IRS3B and L1448 IRS3A. 2021, *ApJ*, 907, L10
- Riaz, B. & Bally, J., Accretion and outflow activity in proto-brown dwarfs. 2021, *MNRAS*, 501, 3781
- Riaz, B., Briceño, C., Whelan, E. T., & Heathcote, S., First Large-scale Herbig-Haro Jet Driven by a Proto-brown Dwarf. 2017, *ApJ*, 844, 47
- Rodríguez, T. M., Hofner, P., Araya, E., et al. 2021, in *American Astronomical Society Meeting Abstracts*, Vol. 53, American Astronomical Society Meeting Abstracts, 348.13
- Rosen, A. L., Offner, S. S. R., Sadavoy, S. I., et al., Zooming in on Individual Star Formation: Low- and High-Mass Stars. 2020, *Space Sci. Rev.*, 216, 62
- Safron, E. J., Fischer, W. J., Megeath, S. T., et al., Hops 383: an Outbursting Class 0 Protostar in Orion. 2015, *ApJ*, 800, L5

- Salmeron, R., Königl, A., & Wardle, M., Angular momentum transport in protostellar discs. 2007, *MNRAS*, 375, 177
- Schleuning, D. A., Far-Infrared and Submillimeter Polarization of OMC-1: Evidence for Magnetically Regulated Star Formation. 1998, *ApJ*, 493, 811
- Schulz, N. S. 2012, *The Formation and Early Evolution of Stars*
- Seale, J. P. & Looney, L. W., Morphological Evolution of Bipolar Outflows from Young Stellar Objects. 2008, *ApJ*, 675, 427
- Seifried, D., Banerjee, R., Klessen, R. S., Duffin, D., & Pudritz, R. E., Magnetic fields during the early stages of massive star formation - I. Accretion and disc evolution. 2011, *MNRAS*, 417, 1054
- Seifried, D., Banerjee, R., Pudritz, R. E., & Klessen, R. S., Turbulence-induced disc formation in strongly magnetized cloud cores. 2013, *MNRAS*, 432, 3320
- Seifried, D., Banerjee, R., Pudritz, R. E., & Klessen, R. S., Accretion and magnetic field morphology around Class 0 stage protostellar discs. 2015, *MNRAS*, 446, 2776
- Seifried, D., Pudritz, R. E., Banerjee, R., Duffin, D., & Klessen, R. S., Magnetic fields during the early stages of massive star formation - II. A generalized outflow criterion. 2012, *MNRAS*, 422, 347
- Shan, Y., Yee, J. C., Bowler, B. P., et al., The Multiplicity of M Dwarfs in Young Moving Groups. 2017, *ApJ*, 846, 93
- Shang, H., Allen, A., Li, Z.-Y., et al., A Unified Model for Bipolar Outflows from Young Stars. 2006, *ApJ*, 649, 845
- Shang, H., Krasnopolsky, R., Liu, C.-F., & Wang, L.-Y., A Unified Model for Bipolar Outflows from Young Stars: The Interplay of Magnetized Wide-angle Winds and Isothermal Toroids. 2020, *ApJ*, 905, 116
- Sharma, R., Tobin, J. J., Sheehan, P. D., et al., Constraining the Chemical Signatures and the Outburst Mechanism of the Class 0 Protostar HOPS 383. 2020, *ApJ*, 904, 78
- Shu, F., Najita, J., Ostriker, E., et al., Magnetocentrifugally Driven Flows from Young Stars and Disks. I. A Generalized Model. 1994, *ApJ*, 429, 781
- Shu, F. H., Self-similar collapse of isothermal spheres and star formation. 1977, *ApJ*, 214, 488
- Shu, F. H. & Adams, F. C. 1987, in *IAU Symposium, Vol. 122, Circumstellar Matter*, ed. I. Appenzeller & C. Jordan, 7
- Shu, F. H., Lizano, S., Ruden, S. P., & Najita, J., Mass loss from rapidly rotating magnetic protostars. 1988, *ApJ*, 328, L19
- Shu, F. H., Najita, J., Ostriker, E. C., & Shang, H., Magnetocentrifugally Driven Flows from Young Stars and Disks. V. Asymptotic Collimation into Jets. 1995, *ApJ*, 455, L155
- Shu, F. H., Najita, J. R., Shang, H., & Li, Z. Y. 2000, in *Protostars and Planets IV*, ed. V. Mannings, A. P. Boss, & S. S. Russell, 789–814

- Sicilia-Aguilar, A., Bouvier, J., Dougados, C., Grankin, K., & Donati, J. F., Reading between the lines. Disk emission, wind, and accretion during the Z CMa NW outburst. 2020, *A&A*, 643, A29
- Sijacki, D. & Springel, V., Physical viscosity in smoothed particle hydrodynamics simulations of galaxy clusters. 2006, *MNRAS*, 371, 1025
- Simon, M. & Obbie, R. C., Twins Among the Low-Mass Spectroscopic Binaries. 2009, *AJ*, 137, 3442
- Snell, R. L., Loren, R. B., & Plambeck, R. L., Observations of CO in L 1551 : evidence for stellar wind driven shocks. 1980, *ApJ*, 239, L17
- Sperling, T., Eislöffel, J., Nisini, B., et al., Evolution of the atomic component in protostellar outflows. 2021, arXiv e-prints, arXiv:2105.08410
- Springel, V., Smoothed Particle Hydrodynamics in Astrophysics. 2010, *ARA&A*, 48, 391
- Springel, V. & Hernquist, L., Cosmological smoothed particle hydrodynamics simulations: the entropy equation. 2002, *MNRAS*, 333, 649
- Stamatellos, D. & Whitworth, A. P., The role of thermodynamics in disc fragmentation. 2009, *MNRAS*, 400, 1563
- Stamatellos, D., Whitworth, A. P., Bisbas, T., & Goodwin, S., Radiative transfer and the energy equation in SPH simulations of star formation. 2007, *A&A*, 475, 37
- Stamatellos, D., Whitworth, A. P., & Hubber, D. A., Episodic accretion, protostellar radiative feedback, and their role in low-mass star formation. 2012, *MNRAS*, 427, 1182
- Stock, C., Caratti o Garatti, A., McGinnis, P., et al., Investigating episodic accretion in a very low-mass young stellar object. 2020, *A&A*, 643, A181
- Stone, J. M., Gammie, C. F., Balbus, S. A., & Hawley, J. F. 2000, in *Protostars and Planets IV*, ed. V. Mannings, A. P. Boss, & S. S. Russell, 589
- Szegedi-Elek, E., Abraham, P., Wyrzykowski, L., et al., Gaia 18dvy: A New FUor in the Cygnus OB3 Association. 2020, *ApJ*, 899, 130
- Tabone, B., Cabrit, S., Bianchi, E., et al., ALMA discovery of a rotating SO/SO<sub>2</sub> flow in HH212. A possible MHD disk wind? 2017, *A&A*, 607, L6
- Tabone, B., Cabrit, S., Pineau des Forêts, G., et al., Constraining MHD disk winds with ALMA. Apparent rotation signatures and application to HH212. 2020, *A&A*, 640, A82
- Tafalla, M., Su, Y. N., Shang, H., et al., Anatomy of the internal bow shocks in the IRAS 04166+2706 protostellar jet. 2017, *A&A*, 597, A119
- Takagi, Y., Honda, S., Arai, A., et al., Revealing the Spectroscopic Variations of FU Orionis Object V960 Mon with High-resolution Spectroscopy. 2020, *ApJ*, 904, 53
- Takami, M., Chen, T.-S., Liu, H. B., et al., An ALMA Study of the FU Ori-type Object V900 Mon: Implications for the Progenitor. 2019, *ApJ*, 884, 146

- Takemura, H., Nakamura, F., Ishii, S., et al., The C<sup>18</sup>O core mass function toward Orion A: Single-dish observations. 2021, PASJ
- Tanabe, Y., Nakamura, F., Tsukagoshi, T., et al., Nobeyama 45 m mapping observations toward Orion A. I. Molecular Outflows. 2019, PASJ, 71, S8
- Tanaka, K. E. I., Tan, J. C., Zhang, Y., & Hosokawa, T., The Impact of Feedback in Massive Star Formation. II. Lower Star Formation Efficiency at Lower Metallicity. 2018, ApJ, 861, 68
- Tobin, J. J., Looney, L. W., Li, Z.-Y., et al., The VLA Nascent Disk and Multiplicity Survey of Perseus Protostars (VANDAM). II. Multiplicity of Protostars in the Perseus Molecular Cloud. 2016, ApJ, 818, 73
- Tobin, J. J., Looney, L. W., Li, Z.-Y., et al., The VLA/ALMA Nascent Disk and Multiplicity (VANDAM) Survey of Perseus Protostars. VI. Characterizing the Formation Mechanism for Close Multiple Systems. 2018, ApJ, 867, 43
- Tomida, K., Okuzumi, S., & Machida, M. N., Radiation Magnetohydrodynamic Simulations of Protostellar Collapse: Nonideal Magnetohydrodynamic Effects and Early Formation of Circumstellar Disks. 2015, ApJ, 801, 117
- Tomida, K., Tomisaka, K., Matsumoto, T., et al., Radiation Magnetohydrodynamic Simulations of Protostellar Collapse: Protostellar Core Formation. 2013, ApJ, 763, 6
- Toomre, A., On the gravitational stability of a disk of stars. 1964, ApJ, 139, 1217
- Troland, T. H. & Crutcher, R. M., Magnetic Fields in Dark Cloud Cores: Arecibo OH Zeeman Observations. 2008, ApJ, 680, 457
- Tychoniec, Ł., Hull, C. L. H., Kristensen, L. E., et al., Chemical and kinematic structure of extremely high-velocity molecular jets in the Serpens Main star-forming region. 2019, A&A, 632, A101
- Vaytet, N. & Haugbølle, T., A grid of one-dimensional low-mass star formation collapse models. 2017, A&A, 598, A116
- Vázquez-Semadeni, E., Palau, A., Ballesteros-Paredes, J., Gómez, G. C., & Zamora-Avilés, M., Global hierarchical collapse in molecular clouds. Towards a comprehensive scenario. 2019, MNRAS, 490, 3061
- Vazzano, M. M., Fernández-López, M., Plunkett, A., et al., Outflows, envelopes, and disks as evolutionary indicators in Lupus YSOs. 2021, arXiv e-prints, arXiv:2101.05330
- Velikhov, E. P., STABILITY OF AN IDEALLY CONDUCTING LIQUID FLOWING BETWEEN ROTATING CYLINDERS IN A MAGNETIC FIELD. 1959, Zhur. Eksp'tl. i Teoret. Fiz.
- Velusamy, T., Langer, W. D., & Thompson, T., HiRes Deconvolved Spitzer Images of 89 Protostellar Jets and Outflows: New Data on the Evolution of the Outflow Morphology. 2014, ApJ, 783, 6
- Vorobyov, E. I. & Basu, S., Variable Protostellar Accretion with Episodic Bursts. 2015, ApJ, 805, 115

- Vorobyov, E. I., Elbakyan, V. G., Liu, H. B., & Takami, M., Distinguishing between different mechanisms of FU-Orionis-type luminosity outbursts. 2021, *A&A*, 647, A44
- Vorobyov, E. I., Elbakyan, V. G., Plunkett, A. L., et al., Knotty protostellar jets as a signature of episodic protostellar accretion? 2018, *A&A*, 613, A18
- Wang, L.-Y., Shang, H., & Chiang, T.-Y., Ejection History of the IRAS 04166+2706 Molecular Jet. 2019, *ApJ*, 874, 31
- Wang, L.-Y., Shang, H., Su, Y.-N., et al., Molecular Jet of IRAS 04166+2706. 2014, *ApJ*, 780, 49
- Ward-Thompson, D. & Whitworth, A. P. 2011, *An Introduction to Star Formation*
- Wardle, M. & Koenigl, A., The Structure of Protostellar Accretion Disks and the Origin of Bipolar Flows. 1993, *ApJ*, 410, 218
- Weinberger, R., Springel, V., & Pakmor, R., The AREPO Public Code Release. 2020, *ApJS*, 248, 32
- Whelan, E. T., Riaz, B., & Rouz e, B., The near-infrared outflow and cavity of the proto-brown dwarf candidate ISO-Oph 200. 2018, *A&A*, 610, L19
- Wurster, J. & Bate, M. R., Disc formation and fragmentation using radiative non-ideal magnetohydrodynamics. 2019, *MNRAS*, 486, 2587
- Wurster, J., Bate, M. R., & Price, D. J., There is no magnetic braking catastrophe: low-mass star cluster and protostellar disc formation with non-ideal magnetohydrodynamics. 2019, *MNRAS*, 489, 1719
- Wurster, J. & Li, Z.-Y., The role of magnetic fields in the formation of protostellar discs. 2018, *Frontiers in Astronomy and Space Sciences*, 5, 39
- Wurster, J., Price, D. J., & Bate, M. R., Can non-ideal magnetohydrodynamics solve the magnetic braking catastrophe? 2016, *MNRAS*, 457, 1037
- Xu, W. & Kunz, M. W., Formation and evolution of protostellar accretion discs - I. Angular-momentum budget, gravitational self-regulation, and numerical convergence. 2021, *MNRAS*, 502, 4911
- Yen, H.-W., Gu, P.-G., Hirano, N., et al., HL Tau Disk in HCO<sup>+</sup> (3-2) and (1-0) with ALMA: Gas Density, Temperature, Gap, and One-arm Spiral. 2019, *ApJ*, 880, 69
- Yildız, U. A., Kristensen, L. E., van Dishoeck, E. F., et al., APEX-CHAMP<sup>+</sup> high-J CO observations of low-mass young stellar objects. IV. Mechanical and radiative feedback. 2015, *A&A*, 576, A109
- Zhang, C., Ren, Z., Wu, J., et al., Filament intersections and cold dense cores in Orion A North. 2020, *MNRAS*, 497, 793
- Zhang, Q., Hunter, T. R., Brand, J., et al., Search for CO Outflows toward a Sample of 69 High-Mass Protostellar Candidates. II. Outflow Properties. 2005, *ApJ*, 625, 864
- Zhang, Y., Arce, H., Mardones, D., & Cabrit, S. 2017, in *Star Formation from Cores to Clusters*, 65

- Zhang, Y., Arce, H. G., Mardones, D., et al., ALMA Cycle 1 Observations of the HH46/47 Molecular Outflow: Structure, Entrainment, and Core Impact. 2016, *ApJ*, 832, 158
- Zhang, Y., Arce, H. G., Mardones, D., et al., An Episodic Wide-angle Outflow in HH 46/47. 2019, *ApJ*, 883, 1
- Zhang, Y., Greco, E., Yang, Y., et al. 2021, in American Astronomical Society Meeting Abstracts, Vol. 53, American Astronomical Society Meeting Abstracts, 114.06
- Zhang, Y., Higuchi, A. E., Sakai, N., et al., Rotation in the NGC 1333 IRAS 4C Outflow. 2018, *ApJ*, 864, 76
- Zhu, Z., Hartmann, L., & Gammie, C., Nonsteady Accretion in Protostars. 2009a, *ApJ*, 694, 1045
- Zhu, Z., Hartmann, L., Gammie, C., & McKinney, J. C., Two-dimensional Simulations of FU Orionis Disk Outbursts. 2009b, *ApJ*, 701, 620
- Zhu, Z., Hartmann, L., Gammie, C. F., et al., Long-term Evolution of Protostellar and Protoplanetary Disks. I. Outbursts. 2010, *ApJ*, 713, 1134
- Zinchenko, I. I., Liu, S.-Y., Su, Y.-N., Wang, K.-S., & Wang, Y., Dense Cores, Filaments, and Outflows in the S255IR Region of High-mass Star Formation. 2020, *ApJ*, 889, 43

#### DATA AVAILABILITY

The data underlying this thesis will be shared on reasonable request to the supervisor.

## ACKNOWLEDGEMENTS

Mein größter Dank geht an meine Betreuerin Steffanie Walch-Gassner, die mich nicht nur durch die Doktorphase gebracht hat, sondern auch schon im Bachelor und Master meine Mentorin war. In den Jahren habe ich viel von ihr gelernt und noch mehr fürs Leben mitgenommen. Insbesondere bin ich dankbar für die große Freiheit und das Vertrauen, das mir entgegengebracht wurde. Auch wenn nicht immer alles so funktioniert hat, wie ich mir das vorgestellt habe, hat sie mich immer beraten, unterstützt und mir geholfen, den roten Faden zu finden. Hier möchte ich auch Peter Schilke dafür danken, dass er alle meine Abschlussarbeiten gelesen hat.

Des Weiteren möchte ich mich besonders bei Daniel und Seamus bedanken. Beide sind unglaublich tolle Betreuer, zu denen man mit jeder erdenklichen Frage kommen kann. Daniel danke ich dafür, dass er immer Teil der "Late Group" war und mir auch schon während der Bachelor und Master Zeit sehr geholfen hat. Bei Ant bedanke ich mich ganz herzlich für die Einladung nach Cardiff. Ohne ihn würden die Paper nicht annähernd so gut klingen.

Ich danke Thorsten, Andre, Birka, Shash und Dominik für die vielen "wissenschaftlichen" (und häufiger eher nicht so wissenschaftlichen) Unterhaltungen im Büro. Ohne euch wäre die Zeit bei Weitem nicht so schön gewesen. Spezieller Dank geht dabei noch an Dominik dafür, dass er für wirklich jedes technische Problem eine Lösung parat hatte, an Thorsten dafür, dass er die Magic Runde am Laufen gehalten hat und an Andre für die lebensnotwendige Kaffeemaschine.

Dann möchte ich meinen Eltern und meinem Bruder für die Liebe und Unterstützung danken; nicht nur in dieser Zeit, sondern während meines gesamten Lebens. Ohne euch wäre nichts davon möglich gewesen. Ich danke allen Freunden, die für die nötige Ablenkung gesorgt haben. Insbesondere bedanke ich mich bei Elli und Matthi, die mir in den Corona Monaten in der Ubierring WG viel Kraft gegeben haben und bei Ulle, der die ganze Zeit mitgefiebert hat.

Der mir wichtigste Dank geht an Annika, die durch ihre Liebe diese Zeit erst unvergesslich gemacht hat. Auch nach Wochen vergeblichen debuggens war sie immer an meiner Seite und hat es geschafft, mich wieder zu motivieren. Danke für diese besondere Zeit.

## SELBSTSTÄNDIGKEITSERKLÄRUNG

Hiermit versichere ich an Eides statt, dass ich die vorliegende Dissertation selbstständig und ohne die Benutzung anderer als der angegebenen Hilfsmittel und Literatur angefertigt habe. Alle Stellen, die wörtlich oder sinngemäß aus veröffentlichten und nicht veröffentlichten Werken dem Wortlaut oder dem Sinn nach entnommen wurden, sind als solche kenntlich gemacht. Ich versichere an Eides statt, dass diese Dissertation noch keiner anderen Fakultät oder Universität zur Prüfung vorgelegen hat; dass sie - abgesehen von unten angegebenen Teilpublikationen und eingebundenen Artikeln und Manuskripten - noch nicht veröffentlicht worden ist sowie, dass ich eine Veröffentlichung der Dissertation vor Abschluss der Promotion nicht ohne Genehmigung des Promotionsausschusses vornehmen werde. Die Bestimmungen dieser Ordnung sind mir bekannt. Darüber hinaus erkläre ich hiermit, dass ich die Ordnung zur Sicherung guter wissenschaftlicher Praxis und zum Umgang mit wissenschaftlichem Fehlverhalten der Universität zu Köln gelesen und sie bei der Durchführung der Dissertation zugrundeliegenden Arbeiten und der schriftlich verfassten Dissertation beachtet habe und verpflichte mich hiermit, die dort genannten Vorgaben bei allen wissenschaftlichen Tätigkeiten zu beachten und umzusetzen. Ich versichere, dass die eingereichte elektronische Fassung der eingereichten Druckfassung vollständig entspricht."

Teilpublikationen:

- *Evolution of Hubble wedges in episodic protostellar outflows* (Rohde et al., MNRAS, 483, 2563, 2019)
- *The impact of episodic outflow feedback on stellar multiplicity and the star formation efficiency* (Rohde et al., MNRAS, 500, 3594, 2021)
- *Protostellar Outflows: a window to the past* (Rohde et al., MNRAS, 510, 2552, 2022)

Köln, den 24.05.2021



(Paul Rohde)

## TEILPUBLIKATIONEN

Im Folgenden wird auf die Beiträge der Autorinnen und Autoren zu den, dieser Dissertation zugrundeliegenden, wissenschaftlichen Veröffentlichungen eingegangen. Die folgenden Punkte treffen auf alle drei im Anschluss genannten Veröffentlichungen zu.

- Die zugrundeliegende Forschungsarbeit wurde maßgeblich von P. Rohde durchgeführt.
- Die Manuskripte wurden zum überwiegenden Teil von P. Rohde verfasst.
- S. Walch, D. Seifried und S. Clarke waren von Beginn an bei allen wissenschaftlichen Diskussionen eingebunden und haben ausschlaggebende Ratschläge, Hilfen und Hinweise beigetragen.
- Alle Koautoren haben wertvolle Kommentare zu fortgeschrittenen Versionen der Manuskripte beigetragen.
- A. Whitworth hat alle drei Manuskripte sprachlich überarbeitet.
- Im Prozess des Peer-Review Verfahrens haben anonyme Gutachter\*innen wertvolle Kommentare beigetragen.
- Alle in den Veröffentlichungen präsentierten Simulationen wurden von P. Rohde durchgeführt.
- Das den Simulationen zugrunde liegende numerische Programm GANDALF wurde maßgeblich von D. Hubber entwickelt.
- Die für die Simulationen genutzte Rechenkapazität wurde von dem "Leibniz Supercomputing Centre" am Supercomputer "SuperMuc" im Rahmen des Projekt pr47pi bereitgestellt.

Liste der Publikationen:

*Evolution of Hubble wedges in episodic protostellar outflows* (Rohde et al., MNRAS, 483, 2563, 2019)

- Das für die Simulationen genutzte episodische Akkretionsmodell wurde maßgeblich von D. Stamatellos entwickelt.
- Das oben genannten episodische Akkretionsmodell wurden von P. Rohde zusammen mit einem von P. Rohde entwickelten Ausfluss Modell zu einem episodischen Ausfluss Modell kombiniert, implementiert und getestet. Dieses episodische Ausflussmodell wurde in einer frühen Fassung schon in der Masterarbeit von P. Rohde vorgestellt.

*The impact of episodic outflow feedback on stellar multiplicity and the star formation efficiency* (Rohde et al., MNRAS, 500, 3594, 2021)

- Das für die Simulationen genutzte stellare Evolutionsmodell wurde maßgeblich von S. Offner entwickelt.
- Das oben genannten stellare Evolutionsmodell wurden von P. Rohde zusammen mit dem von P. Rohde entwickelten episodischen Ausfluss Modell kombiniert, implementiert und getestet.

*Protostellar Outflows: a window to the past* (Rohde et al., MNRAS, 510, 2552, 2022)

## CURICULUM VITAE

Paul Rohde  
MSc., BSc.

### PERSONAL DETAILS

Date of Birth 20 September 1991  
Place of Birth Cologne, Germany  
Nationality German



### CONTACT ADDRESS

I. Physikalisches Institut    Email: rohde@ph1.uni-koeln.de  
University of Cologne       Phone: (+49) 151 - 10632168  
Zùlpicher Strasse 77  
50937 Cologne

### EDUCATIONAL QUALIFICATION

21 Jul 2021                      PhD Defense: *Episodic outflow feedback in low-mass star formation*, Supervisor: Prof. Dr. Stefanie Walch-Gassner  
Apr 2017 - 21 Jul 2021        PhD, I. Physikalisches Institut, Universität zu Köln  
Oct 2015 - Mar 2017          Master of Physics, Universität zu Köln  
Oct 2011 - Sep 2015          Bachelor of Physics, Universität zu Köln  
Sep 2002 - Jul 2011          Secondary School, Gymnasium Rodenkirchen, Graduation July 2011

### PUBLICATIONS

Rohde P. F., Walch S., Seifried D., Clarke S. D., Whitworth A. P., and Hubber D. A., *Evolution of Hubble wedges in episodic protostellar outflows*. MNRAS, 483, 2563, 2019

Rohde P. F., Walch S., Clarke S. D., Seifried D., Whitworth A. P., and Klepitko A., *The impact of episodic outflow feedback on stellar multiplicity and the star formation efficiency*. MNRAS, 500, 3594, 2021

Rohde P. F., Walch S., Seifried D., Whitworth A. P., and Clarke S. D., *Protostellar Outflows: a window to the past* (Rohde et al., MNRAS, 510, 2552, 2022)

Köln, den 05.02.2022



(Paul Rohde)